A N N U A L R E P O R T

2006

and list of publications

Bayerisches Forschungsinstitut
für Experimentelle Geochemie und Geophysik
Universität Bayreuth

Bayerisches Geoinstitut
Universität Bayreuth
D-95440 Bayreuth
Germany

Telephone: +49-(0)921-55-3700
Telefax: +49-(0)921-55-3769
e-mail: bayerisches.geoinstitut@uni-bayreuth.de
www: http://www.bgi.uni-bayreuth.de

Editorial compilation by: Stefan Keyssner and Petra Buchert
Section editors: Andreas Audétat, Tiziana Boffa Ballaran, Leonid Dubrovinsky, Dan Frost, Florian Heidelbach, Hans Keppler, Catherine McCammon, Nobuyoshi Miyajima, Dave Rubie, Gerd Steinle-Neumann, Nicolas Walte

Staff and guests of the Bayerisches Geoinstitut in **July 2006**:

Die Mitarbeiter und Gäste des Bayerischen Geoinstituts im **Juli 2006**:

First row, from left (1. Reihe, v. links) Gerd Steinle-Neumann, Innokenty Kantor, Tamara Goldin, Stefanie Japel, Stefan Keyssner

Second row, from left (2. Reihe, v. links) Ashima Saikia, Jun Liu, Enikő Bali, Anke Potzel, Ute Mann, Olga Narygina, Polina Gavrilenko, Eva Holbig, Micaela Longo, Yuki Asahara

Third row, from left (3. Reihe v. links) Petra Buchert, Valeria Misiti, Ahmed El Goresy, Catherine McCammon, Sven Linhardt, Tiziana Boffa Ballaran, Natalia Dubrovinskaia, Jérôme Rouquette, Anastasia Kantor, Serena Tarantino, Wolfgang Böss, Heinz Fischer

Fourth row, from left (4. Reihe v. links) Dean Presnall, Friedrich Seifert, Florian Heidelbach, Patrick Cordier, Alexander Konschak, Leonid Dubrovinsky, Andreas Audétat, Omar Adjaoud, Dan Frost, Dave Rubie, Stefan Übelhack, Jay Melosh

Fifth row, from left (5. Reihe v. links) Silvio Mollo, Nobuyoshi Miyajima, Shantanu Keshav, Nico Walte, Detlef Krauße, Kurt Klasinski, David Dolejš, Alexander Kurnosov, Hans Keppler, Michele Zema, Svyatoslav Shcheka

Absent (Es fehlten) Ulrich Böhm, Gertrud Gollner, Gudmundur Gudfinnsson, Lydia Kison-Herzing, Holger Kriegl, Oskar Leitner, Oliver Rausch, Gerd Ramming, Hubert Schulze

Contents

Foreword

The year 2006 marks a major break in the history of the Geoinstitut with the retirement of Fritz Seifert, its first director. The present structure and the international reputation of the institute were mainly shaped by Fritz in the early years of his tenure in Bayreuth. The decisions made during that time proved to be very fruitful for the further development of the institute. In particular, the decision to have only a small number of permanent staff members, but a flexible program for inviting guest scientist from all over the world was rather unusual at that time, but it turned out to be essential for the success of the institute. The Geoinstitut today still largely lives on the new ideas brought in by external visitors, who spend periods of weeks, months, or years in Bayreuth. On the other hand, many established scientists holding professorships or other senior positions throughout the world have started their career as visiting scientists at Bayerisches Geoinstitut. Many of them returned in June 2006 to celebrate the 20^{th} anniversary of the founding of the Geoinstitut during two sunny days in the new castle and the park of the Eremitage in Bayreuth.

The main research areas of the Geoinstitut are experimental studies in Earth sciences, complemented by computer modeling. While this may perhaps appear to some people as a rather narrow field, one of the great strength of the Geoinstitut is actually that it carries out experimental work in pretty much all fields of Earth science, ranging from studies of surface processes down to investigations of the Earth's core, from geophysics to geochemistry and sometimes extending into neighboring disciplines such as material science and high-pressure physics. The present annual report demonstrates this diversity. Scientific highlights include deformation experiments on the perovskite and post-perovskite polymorphs of $CaIrO_3$, an analogue material for the perovskite and post-perovskite phases of $MgSiO_3$. The experiments show that the transition from perovskite to post-perovskite probably involves a change in deformation mechanism, consideration of which may be essential for understanding the properties of the D" layer at the core-mantle boundary. Optical absorption spectra of ferropericlase have been measured through the spin-pairing transition. They show that ferropericlase remains optically quite transparent even in the lowermost mantle, implying a significant radiative contribution to heat transfer. While these are experiments relevant to the properties of the deep Earth's interior, other studies focus on near surface processes. Using Raman spectroscopy on synthetic fluid inclusions, it was possible to demonstrate that gases released during explosive volcanic eruptions do not only contain H_2S and SO_2, but also species of hexavalent sulfur. This is an important finding for understanding the climatic effects of volcanism – the only natural process that can compensate for global warming. Finally, as an example of high-pressure research that may not be very relevant for Earth science but is quite interesting for chemistry and physics, a phase transition from a cubic to a hexagonal phase was detected in pure gold, at a pressure above 2 megabar.

The experimental facilities of the Geoinstitut have been expanded by the purchase of two new, fully-automated piston cylinder presses and a GC-MS/MS spectrometer for organic analysis. The recently acquired laser ablation ICP-MS is fully operational and has already

been used by guest scientists from abroad. As in almost every year, the achievements of our scientists were recognized by several awards, including both the Mineralogical Society of America Award and the James B. Macelwane Medal of the American Geophysical Union to Dan Frost. The international cooperation of the Geoinstitut with various partners was further enhanced by the new EU Marie Curie Research Training Network "Crust to core – the fate of subducted material" organized by Gerd Steinle-Neumann.

As in previous years, and also on behalf of my colleagues, I would like to thank the *Free State of Bavaria* as represented by the *Bayerisches Staatsministerium für Wissenschaft, Forschung und Kunst* as well as the *Kommission für Geowissenschaftliche Hochdruckforschung* of the *Bavarian Academy of Sciences* for their continuing support and strong commitment to the Bayerisches Geoinstitut. The *President of Bayreuth University*, Prof. Dr. Dr. h. c. Helmut Ruppert always had an open ear for the needs of our institute. We also gratefully acknowledge generous support from external funding agencies, in particular the *Alexander von Humboldt Foundation*, the *European Union*, the *German Science Foundation*, and the *European Science Foundation,* which have also contributed greatly to the development and success of the Institute.

Bayreuth, March 2007 Hans Keppler

Vorwort

Das Jahr 2006 stellt eine Zäsur für das Geoinstitut dar wegen der Emeritierung von Fritz Seifert, seinem ersten Direktor. Die gegenwärtige Struktur und die internationale Reputation des Instituts wurden von Fritz zu Beginn seiner Amtszeit in Bayreuth aufgebaut. Die damals getroffenen Entscheidungen haben sich als richtig und fruchtbar für die weitere Entwicklung des Instituts erwiesen. Die Entscheidung ein Institut aufzubauen, das nur wenige permanente Stellen für Wissenschaftler hat, aber über ein flexibles Programm für Gastwissenschaftler aus der ganzen Welt verfügt, war damals sehr ungewöhnlich, aber entscheidend für den weiteren Erfolg. Das Geoinstitut lebt auch heute vor allem von den neuen Ideen seiner Gastwissenschaftler, die Wochen, Monate oder Jahre in Bayreuth verbringen. Auf der anderen Seite verdanken viele Professoren und andere Wissenschaftler in Führungspositionen auf der ganzen Welt den Beginn ihrer Karriere einem Gastaufenthalt am Bayerischen Geoinstitut. Viele von ihnen kehrten im Juni 2006 nach Bayreuth zurück um an zwei sonnigen Tagen im neuen Schloss und im Park der Bayreuther Eremitage das 20-jährige Bestehen des Instituts zu feiern.

Der Schwerpunkt der Arbeit des Geoinstituts liegt auf der experimentellen Untersuchung geologischer Prozesse, komplementiert durch Computer-Modellierung. Dies mag als ein relativ enges Arbeitsgebiet erscheinen, aber die Stärke des Geoinstituts besteht gerade darin, dass es experimentelle Untersuchungen über fast alle geowissenschaftlichen Fragestellungen durchführt. Untersuchungen zu den Eigenschaften des Erdkerns gehören hier ebenso dazu wie die Simulierung von Prozessen an der Erdoberfläche. Die experimentellen Arbeitsgebiete reichen von Geochemie und Geophysik bis zu Nachbardisziplinen wie Materialwissenschaft und Hochdruck-Physik. Der vorliegende Jahresbericht demonstriert diese wissenschaftliche Breite. Glanzlichter sind Deformationsexperimente an der Perowskit- und Post-Perowskit-Phase von $CaIrO_3$, einem Analog-Material für $MgSiO_3$ mit Perowskit- und Post-Perowskit-Struktur. Die Experimente zeigen, dass der Übergang von Perowskit zu Post-Perowskit wahrscheinlich einhergeht mit einem Wechsel im Deformationsmechanismus, der möglicherweise essenziell ist für die Eigenschaften der D"-Lage an der Kern-Mantel-Grenze. Optische Absorptionsspektren von Ferroperiklas wurden gemessen bis ins Stabilitätsfeld der low-spin-Phase. Sie zeigen, dass Ferroperiklas auch im unteren Mantel optisch recht transparent bleibt, so dass wahrscheinlich der Strahlungsanteil an der thermischen Leitfähigkeit nicht vernachlässigbar ist. Während diese Untersuchungen relevant sind für das tiefe Erdinnere, beschäftigen sich andere Experimente mit oberflächennahen Prozessen. Mit Hilfe von Raman-Spektroskopie an synthetischen Fluideinschlüssen konnte gezeigt werden, dass vulkanische Gase nicht nur H_2S und SO_2 enthalten, sondern auch Verbindungen des sechswertigen Schwefels. Dies ist wichtig für das Verständnis des klimatischen Effekts großer Vulkaneruptionen – die einzige natürliche Kraft, die die globale Erwärmung kompensieren kann. Ein Phasenübergang zwischen der kubischen und einer hexagonalen Phase von metallischem Gold ist schließlich ein Beispiel für ein Resultat aus der Hochdruckforschung, welches für die Geowissenschaften nicht relevant ist, in Chemie und Physik aber sicher auf großes Interesse stößt.

Die experimentellen Möglichkeiten am Geoinstitut wurden ausgebaut durch die Beschaffung von zwei neuen, vollautomatischen Piston-Cylinder-Pressen sowie eines GC-MS/MS-Spektrometers für organische Analysen. Die kürzlich beschaffte Apparatur für laser ablation ICP-MS ist voll in Betrieb und wurde bereits von auswärtigen Gastwissenschaftlern benutzt. Wie fast in jedem Jahr wurden die Leistungen unserer Wissenschaftler anerkannt in mehreren Preisen, darunter der Mineralogical Society of America Award und die James B. Macelwane Medaille der American Geophysical Union an Dan Frost. Die internationale Kooperation des Geoinstituts mit verschiedenen Partnern wurde weiter verstärkt durch das neue EU Marie Curie Research Training Network "Crust to core – the fate of subducted material", welches organisiert wurde von Gerd Steinle-Neumann.

Wie in den vorangegangenen Jahren möchte ich auch im Namen meiner Kollegen dem *Freistaat Bayern*, vertreten durch das *Bayerische Staatsministerium für Wissenschaft, Forschung und Kunst*, als auch der *Kommission für Geowissenschaftliche Hochdruckforschung* der *Bayerischen Akademie der Wissenschaften* meinen Dank für ihre fortwährende Unterstützung und ihre enge Verbundenheit mit dem Bayerischen Geoinstitut aussprechen. Der *Präsident der Universität Bayreuth*, Prof. Dr. Dr. h. c. Helmut Ruppert, hatte immer ein offenes Ohr für die Wünsche des Instituts. Wir sind auch sehr dankbar für die großzügige Förderung durch externe Geldgeber, insbesondere durch die *Alexander von Humboldt-Stiftung*, die *Europäische Union*, die *European Science Foundation* und die *Deutsche Forschungsgemeinschaft*, die ebenfalls wesentlich zur Entwicklung und zum Erfolg des Bayerischen Geoinstituts beigetragen haben.

Bayreuth, im März 2007 Hans Keppler

1. Advisory Board and Directorship

1.1 Advisory Board

The *Kommission für Geowissenschaftliche Hochdruckforschung der Bayerischen Akademie der Wissenschaften* advises on the organisation and scientific activities of the Institute. Members of this board are:

Prof. Dr. U. CHRISTENSEN	Max-Planck-Institut für Aeronomie, Katlenburg-Lindau
Prof. Dr. R. KNIEP	Institut für Chemische Physik fester Stoffe der Max-Planck-Gesellschaft, Dresden
Prof. Dr. H. PALME	Institut für Mineralogie und Geochemie der Universität zu Köln
Prof. Dr. R. RUMMEL	Institut für Astronomische und Physikalische Geodäsie der TU München
Prof. Dr.-Ing. G. SACHS (Chairman)	Lehrstuhl für Flugmechanik und Flugregelung der Technischen Universität München
Prof. Dr. E. SALJE	Department of Earth Sciences, University of Cambridge
Prof. Dr. H. SOFFEL	Emeritus, Institut für Allgemeine und Angewandte Geophysik der Universität München

The Advisory Board held meetings in Bayreuth (11.06.2006) and in Munich (17.11.2006).

1.2 Leadership

Prof. Dr. Hans KEPPLER (Director from 01.10.2006)
Prof. Dr. David C. RUBIE (Director until 30.09.2006)
Prof. Dr. Friedrich SEIFERT (retired 30.09.2006)

2. Staff, Funding and Facilities

2.1 Staff

At the end of 2006 the following staff positions existed in the Institute:

- Scientific staff: **12**
- Technical staff: **13**
- Administrative staff: **2**
- Administrative officer: **1**

During 2006, 14 scientific (100 months) and 1 technical (9 months) positions were funded by grants raised externally by staff members of the institute.

In addition 14 long-term scientific positions (73 months) were funded by the resources of the BGI Visiting Scientists' Program (see Sect. 8) which also supported short-term visits for discussing future projects or presenting research results (see Sect. 6). Positions for 6 young scientists (72 months) were funded under the BGI International Graduate School under the Elitenetzwerk Bayern "Structure, Reactivity and Properties of Oxide Materials" (see Sect. 4). 2 scientists (12 months) were funded by personal grants (stipends).

2.2 Funding

In 2006, the following financial resources were available from the Free State of Bavaria:

- Visiting Scientists' Program: 416.000 €
- Consumables/investment: 1.230.000 €
- Internat. Graduate School/Elitenetzwerk Bayern 129.000 €

The total amount of national/international external funding ("*Drittmittel"*) used for ongoing research projects in 2006 was 644.300 € (Positions: 362.000 €; equipment, consumables and travel grants: 282.300 €).

	positions	**equipment, consumables, travel grants**	**total**
• AvH	51.000 €		51.000 €
• DAAD		1.300 €	1.300 €
• DFG	266.000 €	77.000 €	343.000 €
• EU	45.000 €	180.000 €	225.000 €
• Others		24.000 €	24.000 €
			644.300 €

(AvH = Alexander von Humboldt Foundation; DAAD = German Academic Exchange Program; DFG = German Science Foundation; EU = European Union)

In the following list only the BGI part of the funding is listed in cases where joint projects involved other research institutions. Principal investigators and duration of the grants are listed in brackets.

Funding institution	Project, Funding	Total Project Funding
BCTC [*1)]	Travel funding (G. Steinle-Neumann, S. Akber-Knutson – 7.05 - 12.07) for project "Computer Modelling of Deep Earth Mineralogy and Geochemistry"	6.500 €
BFHZ [*2)]	Travel funding (L.S. Dubrovinsky – 7.05 - 6.06)	4.985 €
DAAD	PPP Schweden (L.S. Dubrovinsky – 1.06 - 12.06) Travel funding:	3.045 €
DFG	Bo 2550/1-1 (T. Boffa Ballaran, D.J. Frost, L.S. Dubrovinsky – 8.05 - 7.07) Positions: BAT IIa/2, 24 months 58.800 € Consumables and travel funding: 6.000 €	64.800 €
DFG	Du 393/4-1 (L.S. Dubrovinsky – 12.05 - 11.07) Positions: BAT IIa, 24 months 117.600 € Consumables and travel funding: 23.000 €	140.600 €
DFG	Du 393/6-1 (L.S. Dubrovinsky, H.F. Braun – 8.06 - 7.08) Positions: BAT IIa/2, 24 months 58.800 € Consumables and travel funding: 8.400 €	67.200 €
DFG	Fr 1555/3-1 (D.J. Frost, D.C. Rubie, F. Langenhorst – 1.06 - 12.07) Consumables and travel funding: 8.000 €	8.000 €
DFG	Fr 1555/4-1 (D.J. Frost, A.B. Woodland, F. Langenhorst, S. Jahn – 10.06 - 9.08) Consumables and travel funding:	10.535 €
DFG	Ja 1122/1-1 (S.D. Jacobsen, L.S. Dubrovinsky – 2.04 - 1.06) Positions: BAT IIa/2, 24 months 58.800 € Consumables and travel funding: 21.000 €	79.800 €
DFG	Ke 501/5-3 (H. Keppler) Positions: BAT IIa, 24 months 117.600 € Consumables and travel funding: 18.700 €	136.300 €
DFG	Gottfried Wilhelm Leibniz-Preis Ke 501/6-1 (H. Keppler – 12.04 - 9.06) Positions, consumables, equipment, travel:	240.000 €
DFG	ESF-Verbundprojekt "Hydrogen in Minerals" KE 1351/1-1 (H. Keppler – 12.05 - 11.08) Positions: BAT IIa/2, 36 months 88.200 € Consumables and travel funding: 15.000 €	103.200 €
DFG	Mc 3/13-3 (C.A. McCammon, L.S. Dubrovinsky – 1.05 - 12.06) Positions: BAT IIa/2, 24 months 58.800 € Consumables and travel funding: 33.810 €	92.610 €

DFG	Mc 3/16-1 (C.A. McCammon, L.S. Dubrovinsky – 10.06 - 9.09) Positions: student assistant, (80 h/month), 36 months 22.570 € Consumables and travel funding: 45.800 €	68.370 €
DFG	Ru 437/6-2 (D.C. Rubie, D.J. Frost, F. Langenhorst, A. Holzheid – 4.04 - 9.07) Positions: BAT IIa, 24 months 117.600 € Consumables and travel funding: 12.100 €	129.700 €
DFG	Ru 437/8-1 (D.C. Rubie, D.J. Frost, F. Langenhorst – 9.06 - 11.07) Positions: BAT IIa/2, 24 months 58.800 € Consumables and travel funding: 12.750 €	71.550 €
DFG	RU 1323/1-1 (D.C. Rubie, D.J. Frost – 5.06 - 4.08) Positions: BAT IIa, 24 months 117.600 € Consumables and travel funding: 12.900 €	130.350 €
EU	Marie Curie Research Training Network "Crust to core: the fate of subducted material" (1.07 - 12.10) G. Steinle-Neumann (coordinator), G. Fiquet (Paris, France), A.I. Beccero (Sevilla, Spain), S. Buiter (Trondheim, Norway), O. Cadek (Prague, Czech Republic), D. Dobson (London, UK), G. Fiquet (Paris, France), F. Langenhorst (Jena, Germany), P. Jochym (Krakow, Poland), S. Poli (Milan, Italy) and M.W. Schmidt (Zurich, Switzerland) BGI funding:	536.000 €
EU	"Research Infrastructures – Transnational Access" Programme (D.C. Rubie – 1.05 - 12.08)	960.000 €
EU	Marie Curie Fellowships (Training Center) (S. Mackwell/D. Rubie – 01.02. - 01.06) Positions, consumables, equipment, travel:	150.000 €
EU	Marie Curie Host Fellowships for Early Stage Research Training (C.A. McCammon – 01.06. - 12.09) Positions, consumables, equipment, travel:	677.952 €
Industry	Unrestricted Industrial grants (N.A. Dubrovinskaia, L.S. Dubrovinsky)	100.000 €

*1) Bavaria California Technology Center

*2) Bayerisch-Französisches Hochschulzentrum
(Centre de Coopération Universitaire Franco-Bavarois)

2.3 Laboratory and office facilities

The institute occupies an area of

ca. 1200 m^2	laboratory space
ca. 480 m^2	infrastructural areas (machine shops, computer facilities, seminar room, library)
ca. 460 m^2	office space

in a building which was completed in 1994.

2.4 Experimental and analytical equipment

The following major equipment is available at Bayerisches Geoinstitut:

I. High-pressure apparatus
- 5000 tonne multianvil press (25 GPa, 3000 K)
- 1200 tonne multianvil press (25 GPa, 3000 K)
- 1000 tonne multianvil press (25 GPa, 3000 K)
- 500 tonne multianvil press (20 GPa, 3000 K)
- 500 tonne press with a deformation DIA apparatus
- 4 piston-cylinder presses (4 GPa, 2100 K)
- Cold-seal vessels (700 MPa, 1100 K, H_2O), TZM vessels (300 MPa, 1400 K, Ar), rapid-quench device
- Internally-heated autoclave (1 GPa, 1600 K)

II. Structural and chemical analysis
- 2 X-ray powder diffractometers
- 1 X-ray powder diffractometer with furnace and cryostat
- Single-crystal X-ray cameras
- 2 automated single-crystal X-ray diffractometers
- High-brilliance X-ray system
- 1 Mössbauer spectrometer (1.5 - 1300 K)
- 3 Mössbauer microspectrometers
- 2 FTIR spectrometers with IR microscope
- FEG transmission electron microscope, 200 kV analytical, with EDS and PEELS
- FEG scanning electron microscope with BSE detector, EDS, EBSD and CL
- 2 Micro-Raman spectrometers
- JEOL JXA-8200 electron microprobe; fully-automated with 14 crystals, 5 spectrometer configuration, EDX, capability for light elements
- Cameca SX-50 electron microprobe
- 193 nm Excimer Laser-Ablation ICP-MS
- ICP-AES sequential spectrometer
- Water content determination by Karl-Fischer titration
- GC/MS-MS for organic analyses

III. *In situ* determination of properties

Diamond anvil cells for powder and single crystal X-ray diffraction, Mössbauer, IR, Raman, optical spectroscopy and electrical resistivity measurements up to at least 100 GPa

Facility for *in situ* hydrothermal studies in DAC

Externally electrically heated DACs for *in situ* studies at pressures to 100 GPa and 1200 K

1-atm furnaces to 1950 K, gas mixing to 1600 K, zirconia fO2 probes

1-atm high-temperature creep apparatus

Gigahertz ultrasonic interferometer and an interface to resistance-heated diamond-anvil cells

Heating stage for fluid inclusion studies

Impedance/gain-phase analyser for electrical conductivity studies

Apparatus for *in situ* measurements of thermal diffusivity at high P and T

Laser-heating facility for DAC

IV. Computational facilities

19 node linux cluster (2x2.4 GHz Xeon, 1 Gb memory), Gb ethernet

16 node linux cluster (2x3.6 GHz Xeon em64t, 4 Gb memory), Gb ethernet

7 node linux cluster (2x3.0 GHz Xeon Woodcrest Dual Core, 8 Gb memory), InfiniBand

RAID System (6 Tb storage)

The Geoinstitut is provided with well equipped machine shops, electronic workshop and sample preparation laboratories. It has also access to the university computer centre.

The picture on page 18 shows the perovskite (Pv) and the post perovskite (Post-Pv) phase of $CaIrO_3$, photographed in the microscope using reflected light and crossed polarizers. Both phases were in equilibrium at 2 GPa and 1250 °C; the orthorhombic post-perovskite phase shows much stronger anisotropy (reflected in the stronger colours) than the perovskite phase (also orthorhombic) which displays abundant twinning. In the light of recent discoveries of the post perovskite transition in $MgSiO_3$, the textures of post perovskite phase are important for the understanding of the structure of the D" layer at the core/mantle boundary. The morphology and defect microstructures (dislocations and polysynthetic twinning) are discussed in this volume under 3.7 c on page 125.

Die Abbildung auf Seite 18 stellt eine Mikro-Aufnahme der Perowskit- und Post-Perowskitphasen (Pv und Post-Pv) von $CaIrO_3$ unter reflektiertem Licht und bei gekreuzten Polarisatoren dar. Beide Phasen befinden sich bei 2 GPa und 1250 °C im Gleichgewicht. Die orthorhombische Post-Perowskitphase weist durch kräftigere Farben eine sehr viel stärkere Anisotropie als die ebenfalls orthorhombische Perowskitphase auf, in der Zwillingsbildungen verbreitet sind (Lamellenmuster). Angesichts der vor kurzer Zeit gemachten Entdeckung des Post-Perowskitüberganges in $MgSiO_3$ sind die Texturen der Post-Perowskitphase wichtig, um die Struktur der D"-Lage an der Kern/Mantel-Grenze erklären zu können. Morphologie und kleinmaßstäbliche Defekt-Strukturen (Gitterversatz, polysynthetische Zwillingsbildung) werden in diesem Bericht unter 3.7 c (Seite 125) beschrieben.

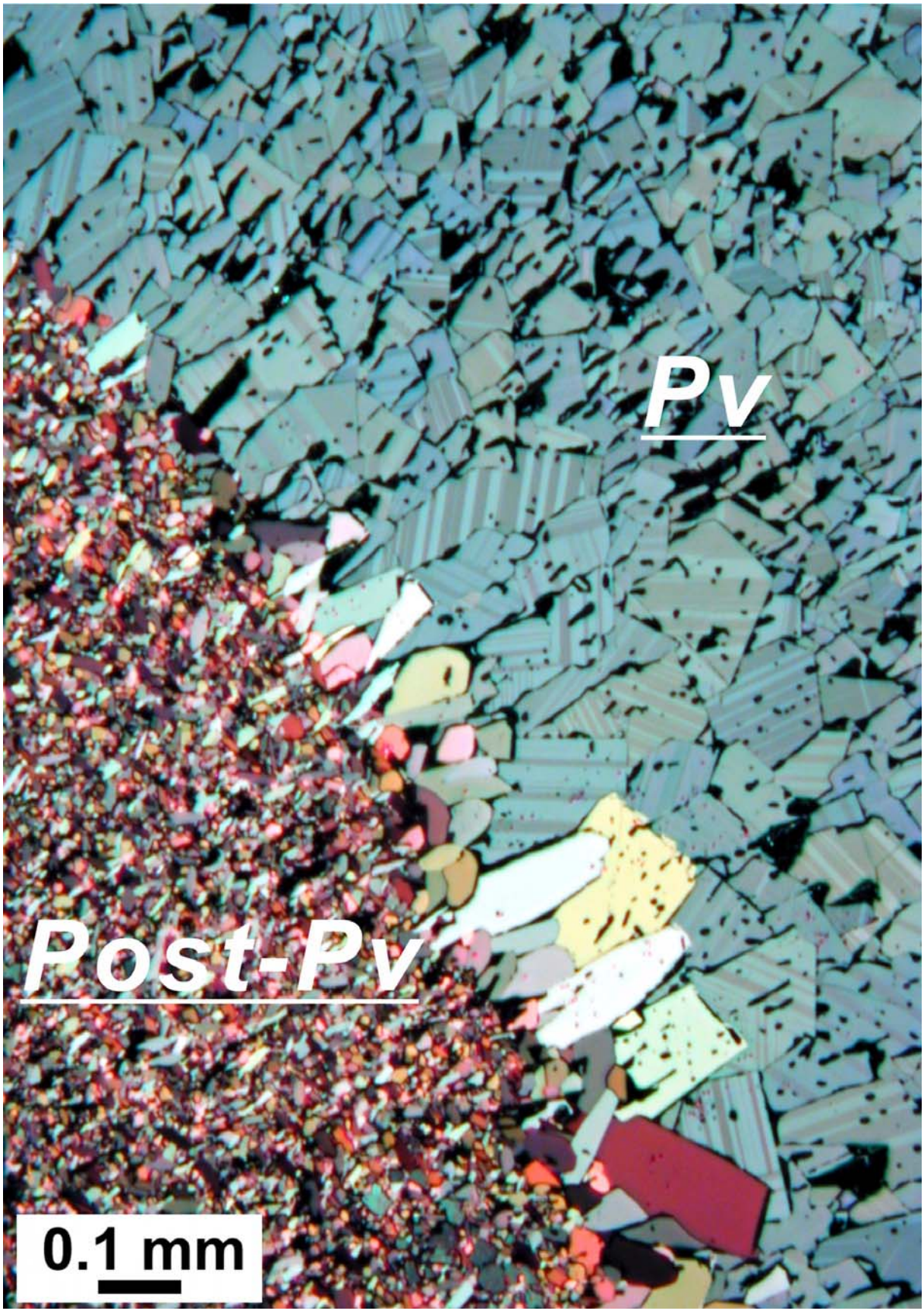
Pv
Post-Pv
0.1 mm

3. Forschungsprojekte

Es wird an dieser Stelle nur über die wichtigsten, derzeit laufenden Projekte berichtet. Informationen über abgeschlossene Teilprojekte sind in den Abschnitten 5.1 und 5.2 in Form von Literaturzitaten angegeben. Die Beiträge des Kapitels 3 sollen nicht zitiert werden.

3.1 Aufbau der Erde und Geodynamik

Während viele Fragen in der Geologie durch die Erforschung von Gesteinsproben an der Erdoberfläche beantwortet werden können, fehlt diese direkte Information über das Erdinnere für Tiefen größer als 200 km. Zum Verständnis des Erdmantels und des Erdkerns werden deshalb hauptsächlich Informationen aus der Geophysik herangezogen: hierbei sind die Inversionsmethoden der Seismologie und der Gravimetrie besonders hilfreich, da sie quantitative Informationen über die Dichte und elastische Struktur des Erdinnern liefern. Durch Fortschritte in Inversionsmethoden sowie einer größeren Datendichte, insbesondere in der Seismologie, haben wir heute ein detailliertes Bild vom Aufbau des Erdinnern mit starken horizontalen Variationen, Anisotropie, sowie einer großen Anzahl von seismischen Diskontinuitäten.

Um die geophysikalische und geochemische Bedeutung dieser seismischen Messungen zu verstehen, müssen sie mit experimentellen Daten zu physikalischen Eigenschaften und Phasenübergängen kombiniert werden. Das Verständnis, dass seismische Diskontinuitäten im Erdmantel von Phasenübergängen im Mineralsystem Mg_2SiO_4 verursacht werden, konnte nur aus der gemeinsamen Betrachtung von Mantelpetrologie und seismischen Daten entstehen. Zusätzlich zur Mg_2SiO_4-Olivin-Komponente enthält der Mantel Mischkristalle die auf $MgSiO_3$- und $CaSiO_3$-Zusammensetzungen basieren (Pyroxene, Granate und Perowskite). Im Gegensatz zu den Phasenübergängen im Mg_2SiO_4-System, die über einen kleinen Druckbereich auftreten, zeigen die Mischkristalle von $MgSiO_3$ graduelle Übergänge. Die Phasenübergänge von Pyroxen zu Granat und von Granat zu Perowskit sind im Gegensatz zu den Übergängen in Mg_2SiO_4 wenig untersucht.

Die ersten zwei Beiträge dieses Kapitels beschäftigen sich mit diesen komplexen Mischkristallen. Im ersten Beitrag wird das Phasengleichgewicht zwischen Pyroxenen und Granaten untersucht, in dem beide Phasen über einen großen Druckbereich existieren. Die Ergebnisse zeigen, dass eine detaillierte Analyse der Kationen im Granat Rückschlüsse auf den Druck zulässt, bei dem sie sich gebildet haben. Kenntnisse über die Aufteilung der Kationen zwischen Pyroxen und Granat fließen in petrologische Modelle zum Mantel ein.

In den vergangenen Jahren haben seismologische Messungen eine komplizierte Verteilung von seismischen Diskontinuitäten im Erdmantel aufgezeigt, vor allem in der Übergangszone zwischen oberem und unterem Erdmantel, in einer Tiefe zwischen 440 und 660 km. Zum Beispiel wird eine Diskontinuität bei 520 km Tiefe nicht global beobachtet, aber zeigt dort, wo sie auftritt, eine große Diversität mit stark variierender Tiefe und manchmal mehreren Reflektoren. Um dieses Verhalten zu verstehen, befasst sich der zweite Beitrag mit der

Entmischung von $CaSiO_3$-Perowskit aus der Granat-Phase des Mantels. Diese Entmischung erlaubt eine alternative Erklärung von Mantel-Diskonituitäten in der Mitte der Übergangszone, zusätzlich zum Phasenübergang von Wadsleyit nach Ringwoodit in Mg_2SiO_4. Ähnlich wie die Diskontinuitäten in Tiefen zwischen 500 und 560 km Tiefe wurde die Diskontinuität in 660 km Tiefe lange Zeit allein mit der Mg_2SiO_4-Komponente des Mantels in Verbindung gebracht. Mit Hilfe eines thermodynamischen Modells wird im dritten Beitrag dieses Kapitels der Effekt von Temperatur und Druck auf alle Phasenübergange in einem Mantelmodell untersucht, die mit der Diskontinuität bei 660 km Tiefe assoziiert sind.

Diese Beiträge zeigen, dass wir mit Hilfe der Mineralphysik auf dem Weg zu einem detaillierten Bild über die Struktur des Erdmantels sind; im Gegensatz dazu ist unser Verständnis des Erdkerns noch sehr unvollständig. Hier stehen grundsätzliche Fragen im Vordergrund wie die kristallographische Struktur von Eisen und seinen Verbindungen bei extremem Druck unter Temperaturen wie sie im Erdkern herrschen, oder die Frage nach dem leichten Element, das im Kern mit Eisen legiert ist und die Menge dieses leichten Elements. Hierbei müssen wir uns auf die Integration von Daten aus verschiedenen Feldern der Geowissenschaften verlassen, z. B. der Kosmo- und Geochemie, sowie Laborexperimenten unter Megabar-Druck in der Diamantstempelpresse. Der vierte Beitrag dieses Kapitels befasst sich mit der Phasenstabilität von reinem Eisen unter Megabar-Druck. Der fünfte Beitrag untersucht die elastischen Eigenschaften einer Fe-Ni-Legierung (22 mol.% Ni) unter Druck, um den Einfluss von Ni auf die Elastizität von Eisen zu verstehen.

In einem weiteren Beitrag zum Erdkern wird die Abspaltung von Eisen durch den Magmaozean des frühen Mantels sowie die daraus resultierende Verteilung von Ni untersucht. Die Eisen-Absonderung wird mit Hilfe eines Finiten Elemente-Programms simuliert, das den Fluss zweier sich durchdringender Flüssigkeiten beschreibt. Dasselbe Programm wird im letzten Beitrag des Kapitels benutzt, um die Ablagerung von Auswurfmaterie in der Erdatmosphäre infolge eines Meteoriten-Einschlags zu untersuchen. Die Resultate aus dieser Simulation werden genutzt, um die Folgen des Chixulub Impakts zu interpretieren, der für das Aussterben der Dinosaurier am Ende der Kreidezeit verantwortlich gemacht wird.

3.2 Geochemie

Die Erde ist ein dynamischer Planet, in dem sich chemische Elemente in stetem Austausch zwischen Reservoiren an der Oberfläche und im Erdinneren befinden. Zahlreiche Beiträge in diesem Kapitel zielen auf ein besseres Verständnis von Prozessen dieser geochemischen Umverteilung, sowohl was die heutige als auch die frühe Erde betrifft. Im Gegensatz zu den dynamischen Prozessen auf der Erde sind Meteoritenbruchstücke über lange Zeit isoliert im eiskalten Weltraum geblieben. Sie haben seit ihrer Entstehung keinerlei Fraktionierung erfahren. Sie stellen Zeitzeugen dar, aus denen sich Prozesse ablesen lassen, die in der Frühgeschichte des Sonnensystems auftraten. Der erste Beitrag dieses Kapitels geht sogar noch einen Schritt weiter in die Vergangenheit zurück. Hier wird über die Suche nach Hinweisen für kurzlebige Isotopen in Meteoritproben berichtet, aus denen möglicherweise Informationen

über die Geschichte des präsolaren Systems abgelesen werden können. Da diese Isotope sehr schnell zerfallen, können lediglich noch ihre Tochterprodukte identifiziert werden. Aus ihnen lassen sich Informationen über nukleare Prozesse ablesen, die in den erloschenen Sternen abgelaufen sind und die alle schwereren Elemente als Wasserstoff im Sonnensystem hervorgebracht haben. Wichtige Voraussetzung für die korrekte Interpretation jeglicher Radio-Isotopenstudie ist eine genaue Kenntnis der Zerfallskonstanten. Mit einer kritischen Bewertung des Druckeinflusses auf die Zerfallskonstante von ^{7}Be befasst sich ein weiterer Beitrag.

Die sich anschließenden sechs Beiträge befassen sich mit experimentellen Untersuchungen zur Zusammensetzung des Erdkerns. Zwei Aufsätze handeln von der Fraktionierung hoch siderophiler Elemente zwischen dem Mantel und dem Kern sowie zwischen dem festen inneren und dem flüssigen äußeren Erdkern. Stark siderophile Elemente haben die Eigenschaft, dass sie sehr effizient in metallisches Eisen fraktionieren. Es stellt sich daher die Frage, wieso stark siderophile Elemente im Erdmantel relativ häufig sind, bzw. wieso sie während der Bildung des Erdkerns nicht stärker abgereichert wurden. Eine experimentell überprüfbare Möglichkeit wäre, dass diese Konzentrationen die Metall-Silikat-Verteilung dieser Elemente unter hohen Drücken und Temperaturen widerspiegelt. Drei weitere Beiträge befassen sich mit der Natur der leichten Elemente im Erdkern, welche nach geophysikalischen Erkenntnissen 10 % des äußeren Erdkerns ausmachen. Eine extreme Herausforderung stellen Experimente zur Reaktion von Wasserstoff und Kohlenstoff mit metallischem Eisen unter hohen Drücken und Temperaturen dar. Hier sind thermodynamische Modelle von Nutzen, mit denen experimentelle Ergebnisse bis zu den extremen Bedingungen während der Erdkern-bildung extrapoliert werden können.

Prozesse der Diamantbildung im Erdmantel werden in zwei weiteren Beiträgen diskutiert. Während viele Diamanten in oberflächennahen Regionen des Erdmantels, in der Lithosphäre, gebildet werden, scheinen einige, wie kürzlich erkannt wurde, aus viel tieferen Stockwerken der Erde zu stammen. Anhaltspunkte zur Diamantbildung lassen sich aus der Aufteilung von Spurenelementen zwischen der Schmelze, aus der sich die Diamanten wahrscheinlich bildeten und in den Diamanten eingeschlossenen Mineralen gewinnen. In ähnlicher Weise könnten auch Untersuchungen zur Fraktionierung stabiler Kohlenstoffisotope während des Diamant-wachstums neue Erkenntnisse zu deren Bildung beitragen.

Einige der Beiträge machen deutlich, wie wichtig es ist, für ein bestimmtes Spurenelement das Wirtsmineral im Erdmantel zu identifizieren. Das gilt besonders für Untersuchungen von Elementfraktionierungen bei Schmelzprozessen. Ein Projekt befasst sich zum Beispiel mit der Frage, ob eine Hochdruck-Modifikation von Rutil (TiO_2) eventuell die Fraktionierung der Elemente Nb und Ta im Erdmantel bewirkt, was erklären würde, warum Nb im Vergleich zu Ta in zahlreichen Mantelgesteinen seltener ist. Änderungen im Oxidationszustand der Elemente können ebenfalls ein recht differenziertes geochemisches Verhalten bei der Aufschmelzung und Kristallisation von Gesteinen bewirken. Für die Petrologie besteht die Herausforderung, Bestimmungsmethoden derart zu verbessern, dass der Oxidationszustand

von Elementen im Maßstab von Mineralkörnern messbar wird. Dort ist die meiste Information über die bei der Mineralbildung abgelaufenen Prozesse gespeichert. Methodische Fortschritte auf diesem Gebiet werden zum Ende dieses Kapitels dargelegt; sie liefern uns ein besseres Verständnis über im Erdmantel und Erdkruste vorherrschende Redox-Verhältnisse, insbesondere bei Fraktionierungsereignissen.

3.3 Mineralogie, Kristallchemie und Phasenübergänge

Untersuchungen darüber, wie sich Veränderungen in Druck, Temperatur, Sauerstofffugazität sowie chemischer Zusammensetzung auf verschiedene Kristallstrukturen auswirken, sind für einen großen Bereich der Materialwissenschaften wichtig. Besonders nützlich sind sie auch in der Physik und Chemie sowie auch in den Ingenieurs- und Geowissenschaften. Zu den markantesten Reaktionen auf Veränderungen der Umgebungsbedingungen gehören Phasenübergänge. Fast jegliche Materie unterliegt in den kritischen Druck- und Temperaturbereichen, die im Erdinneren und im dem Inneren der äußeren Planeten herrschen, Umwandlungsprozessen. In diesem Kapitel werden die Versuche vorgestellt, die dazu dienen sollen, den Beginn von Phasenumwandlungen zu entdecken; der Reaktion verschiedenartiger Materie auf hohen Druck und Temperatur wird mit Hilfe von Röntgenbeugungs- und Spektroskopiemethoden nachgespürt.

Die meisten Beiträge dieses Kapitels ließen sich unter der Hauptüberschrift *Phasenübergänge* einordnen. So unterschiedlich die erforschten Materialien sind, so unterschiedlich sind die Untersuchungsziele: Sie reichen von der Wasserzirkulation in abtauchenden Platten der Erdkruste über das Hochdruckverhalten von im Erdmantel stabilen Mineralen bis zu den äußeren Planeten und deren Eisanteil. Bei diesen Experimenten werden *in situ*-Methoden eingesetzt: Diamantstempelpressen werden mit Einkristall- bzw. Pulverproben bestückt und unter Druck mit Röntgenbeugungsmethoden und/oder der Raman-Spektroskopie untersucht. Der Vorteil der gleichzeitigen Anwendung dieser beiden Methoden beruht darauf, dass die erzielten Ergebnisse sich gegenseitig ergänzen und somit Kristallstrukturen und ihre Veränderungen in unterschiedlichen Maßstäben verständlicher werden. Einige der Untersuchungen zeigen, wie Wissenschaftler durch eine stete Verbesserung der experimentellen Technik zu einer höheren Datengenauigkeit gelangen, wie im Falle der Röntgenbeugungsmessungen an Pulverproben unter hydrostatischem Druck. Mit neu entwickelten Techniken lassen sich die außergewöhnlichen Druck- und Temperaturbedingungen des Erdinneren experimentell nachstellen, um zum Beispiel Phasenübergänge von FeO sowie den *fcc*- nach *hcp*-Übergang in Gold zu untersuchen. Analog-Materie stellt noch immer ein sehr wichtiges Hilfsmittel dar, um das Verhalten ihrer isostrukturellen Verbindungen unter den extremen Bedingungen des tiefsten Erdinneren zu verstehen. So können zum Beispiel Stempelzylinderpressen für Untersuchungen der Phasenbeziehungen Perowskit/Post-Perowskit in $CaIrO_3$ eingesetzt werden. Aus diesen Experimenten lässt sich ableiten, wie der Perowskit/Post-Perowskit-Übergang in $MgSiO_3$ sich an der Grenze unterer Erdmantel/ Erdkern auswirken könnte.

Das Materialverhalten wird nicht nur durch die Art seiner Phasenübergänge bei verschiedenen Drücken und Temperaturen definiert, sondern auch durch eine akkurate Bestimmung seiner Zustandsgleichung (*Equation of state – EOS*). In diesem Kapitel befassen sich zwei Untersuchungen mit dem Effekt von Kationenaustausch und -anordnung auf die Komprimierbarkeit zweier bedeutender gesteinsbildender Minerale: Orthopyroxen und Spinell.

Die beiden letzten Beiträge dieses Kapitels berichten über neue experimentelle und analytische Entwicklungen in der Anwendung der Mössbauer-Spektroskopie bei der Untersuchung orientierter Einkristall-Proben und Gläser. So wurde in einer Studie Einkristall-Almandin untersucht, um eine asymmetrische Quadrupol-Doublette im kubischen Kristall zu erklären. In der anderen Untersuchung wurde die ^{57}Fe-Mössbauer-Spektroskopie für Fe-haltige Alumo-Silikatgläser als komplementäre Methode zu Neutronendiffraktometrie und Computermodellierung eingesetzt, um die Nah-Ordnung um Fe-Atome (d. h. die Fe-Koordinationszahl) zu studieren.

3.4 Physikalische Eigenschaften von Mineralen

Ein primäres Untersuchungsziel der modernen Mineralogie und Mineralphysik sind die physikalischen Eigenschaften von Mineralen unter verschiedenen Zustandsbedingungen. Umfassende Erkenntnisse über Zusammensetzung, Mineralogie und Aufbau des Erdinneren können nicht allein aus direkten geophysikalischen Beobachtungen gewonnen werden; vielmehr müssen die Forschungsansätze interdisziplinär ausgerichtet sein. Am Geoinstitut werden physikalische, mechanische und chemische Eigenschaften von Mineralen, die am Aufbau des Erdmantels beteiligt sind, mit experimentellen und theoretischen Methoden genauer bestimmt. Physikalische Eigenschaften (d. h. elastische, optische und elektronische) werden in Abhängigkeit von Druck, Temperatur, chemischer Zusammensetzung und Mikro-struktur durch Modellierung und experimentell untersucht. Die Ergebnisse ermöglichen die mineralogische und geochemische Modellierung des Erdmantels. Diese Untersuchungen stellen einen signifikanten Anteil der am Geoinstitut durchgeführten Forschungsarbeiten dar und die so gewonnenen Informationen tragen wesentlich zu einem besseren Verständnis der im Erdinneren ablaufenden rheologischen Prozesse bei.

Es werden in diesem Kapitel Untersuchungen über elastische und magnetische Eigenschaften von Mineralen des Erdmantels neben Untersuchungen zum Wärmetransport präsentiert. Der erste Beitrag stellt eine Studie über die Stabilität und elastischen Eigenschaften von kristallinen Fe-Ni-Phasen bei hohem Druck vor. Eine Fe-Ni-Legierung stellt die Hauptkomponente des inneren Erdkerns dar; genaue Informationen über die elastischen Eigenschaften dieser Legierung sind unentbehrlich, wenn man Aussagen zur Mineralogie, Chemie und Temperaturverteilung im inneren Kern aufgrund der Interpretation seismischer Daten treffen will. Bisher wurden derartige Untersuchungen anhand reiner Eisenschmelzen durchgeführt. Diese Studie ist somit ein wichtiger Fortschritt in der Bestimmung des Einflusses von Ni auf Phasenstabilität und elastische Eigenschaften. Der zweite Beitrag

beschreibt Untersuchungen elastischer Eigenschaften von Fe-Al-haltigem Silikat-Perowskit. Silikat-Perowskit ist nicht nur das Hauptmineral des unteren Erdmantels, sondern wahrscheinlich auch das am häufigsten vorkommende Mineral in der Gesamterde. Um die Mineralogie und Zusammensetzung des unteren Erdmantels besser zu verstehen, sollten unbedingt die elastischen Eigenschaften von Perowskit bekannt sein. Bisher konzentrierten sich die Untersuchungen der elastischen Eigenschaften auf das Endglied aus reinem $MgSiO_3$; auch Auswirkungen der Al-Substitution wurden untersucht, jedoch mit gegensätzlichen Ergebnissen. In dieser Studie wurden die elastischen Eigenschaften von Perowskit-Kristallen mit einer dem Erdmantel entsprechenden chemischen Zusammensetzung untersucht, und man kommt zu dem Ergebnis, dass eine Fe- und Al-Substitution in der Kristallstruktur die Zustandsgleichung nur gering beeinflusst. Im Rahmen einer dritten Studie wurden optische Eigenschaften einer weiteren Hauptkomponente des unteren Erdmantels – Magnesiowüstit, (Mg,Fe)O – untersucht. Ein wichtiges Fazit dieser Arbeit ist, dass der Wärmetransport durch thermische Strahlung im unteren Mantel im Gegensatz zu früheren Annahmen eine große Rolle spielen muss. Dieses Ergebnis hat Auswirkungen auf die Modellierung der thermischen Entwicklung der Erde. Ein weiterer Beitrag befasst sich mit Olivin, dem häufigsten Mineral des oberen Erdmantels und druckinduzierten Veränderungen im Spin-Zustand; Kenntnisse darüber sind wichtig, da derartige Wechsel die chemischen und physikalischen Eigenschaften des Minerals beeinflussen. Zum Abschluss des Kapitels werden neue Ergebnisse rechnergestützter Modellierungen von magnetischen und elastischen Eigenschaften zweier nur sehr untergeordnet auftretender Minerale des Erdmantels, Magnetit und Pentlandit, vorgestellt.

3.5 Fluide und ihre Wechselwirkung mit Schmelzen und Mineralen

Fluide sind wichtige Medien des Stofftransports im Erdinnern. Fluideigenschaften unter hohem Druck sind jedoch extrem schwer zu untersuchen. Ein nützliches Hilfsmittel für solche Untersuchungen sind synthetische Flüssigkeitseinschlüsse. Es handelt sich hier um kleine Tropfen von Fluid, die in einem Kristall während des Wachstums eingeschlossen wurden. Alternativ können Fluideinschlüsse auch durch das Ausheilen von Rissen, z. B. in einem Quarzkristall in der Gegenwart von Fluid erzeugt werden. Die Auflösung und Wiederausfällung von Quarz verheilt die Risse. Dabei verbleibt oft ein Teil des Fluids in Form von Einschlüssen im Kristall. Diese Fluideinschlüsse können dann bequem unter Normalbedingungen untersucht werden, um Aufschluss über die Eigenschaften des Fluids bei hohem Druck und hoher Temperatur zu erhalten.

Zwei Projekte in diesem Jahresbericht verwenden im Labor unter definierten Bedingungen erzeugte Flüssigkeitseinschlüsse zur Untersuchung von Fluideigenschaften. Das erste Projekt untersucht den Oxidationszustand von Schwefel in Fluiden, die von kristallisierenden Magmenkörpern in der Erdkruste abgegeben werden. Die Schwefel-Spezies in den Fluiden unterscheiden sich drastisch von bisher allgemein akzeptierten Vorhersagen auf der Basis thermodynamischer Berechnungen. Im Gegensatz zu existierenden Modellvorstellungen ist sechswertiger Schwefel eine wichtige Spezies in magmatisch-hydrothermalen Fluiden. Der

Grund dafür liegt wahrscheinlich in Solvatationseffekten im Fluid. Dies ist eine sehr wichtige Beobachtung, denn die Freisetzung von Schwefel bestimmt die Auswirkung von Vulkaneruptionen auf das Klima und diese Effekte können je nach Art der freigesetzten Schwefelverbindungen sehr unterschiedlich sein.

Die zweite Arbeit mit synthetischen Flüssigkeitseinschlüssen untersucht die Fraktionierung von Kupfer und Gold zwischen Flüssigkeit und Dampfphase. Diese Fraktionierung spielt möglicherweise eine wichtige Rolle bei der Anreicherung bestimmter Metalle in hydrothermalen Erzlagerstätten. Die Experimente deuten darauf hin, dass unter bestimmten Bedingungen Metalle in der Dampfphase konzentriert werden.

Die Eigenschaften von Fluiden in der Übergangzone des Erdmantels sind noch schwieriger zu untersuchen als die Eigenschaften von Fluiden in der Kruste. Unter den reduzierenden Bedingungen in der Übergangszone bestehen die Fluide wahrscheinlich überwiegend aus Methan. Einige vorläufige Experimente deuten darauf hin, dass derartige Fluide Silikate nur in geringem Umfang lösen und daher nur wenig zum Stofftransport im Mantel beitragen. Außerdem ist wahrscheinlich die Löslichkeit von Wasser in Mantelmineralen im Gleichgewicht mit derartigen Fluiden stark reduziert.

Als Teil eines umfangreicheren Programms zur Quantifizierung von Wasserspeicherung und -transport im Mantel wurde schließlich die Löslichkeit von Wasser in Klinopyroxen untersucht. Die Löslichkeit von Wasser steigt stark mit dem Aluminiumgehalt an. Diese Beobachtung könnte bei der Modellierung des Wassertransports in den Mantel im Bereich von Subduktionszonen wichtig sein.

3.6 Physik und Chemie von Schmelzen und Magmen

Die Entstehung von Magma durch Teilaufschmelzungen im Erdinneren begleitet die Evolutionsgeschichte unseres Planeten von Anfang an. Der Magmentransport in der Erde, zum Beispiel an ihre Oberfläche, sowie die Magmenkristallisation gelten als Hauptprozesse, die den Erdkörper im Verlauf seiner Entstehung geformt haben. In der Frühgeschichte der Erde muss es eine Teil- oder Komplettaufschmelzung des Planeten gegeben haben, um die schwerkraftbedingte Trennung von Silikaten und Eisenlegierungen zu ermöglichen, sodass sich ein silikatischer Erdmantel um einen metallischen Erdkern herum ausbilden konnte. Auch im Anschluss stellten fortgesetzte Aufschmelzung, Magmatransport und Magmakristallisation die wichtigsten Prozesse dar, die zur getrennten Ausbildung (Differenziation) der heutigen Erdkruste und des Mantels führten. Die Art des Transports und der Differenziation wird durch die physikalischen und chemischen Eigenschaften eines Magmas bestimmt, die zusätzlich eine wichtige Rolle für die Eigenschaften von vulkanischen Eruptionen an der Erdoberfläche spielen. Bei den gewaltigsten und zerstörerischsten Eruptionen sind Magmen mit einem besonders hohen Anteil leichtflüchtiger Komponenten, zum Beispiel CO_2 und H_2O, beteiligt. Daher sind genauere Kenntnisse über die Löslichkeit von Volatilen in Silikatschmelzen sowie darüber, wie sie im atomaren Maßstab in die Struktur

von Schmelzen eingebaut sind, für das Verständnis von Vulkanismus und vulkanischen Prozessen von primärer Bedeutung. Auch werden ökonomisch interessante Erzlagerstätten primär durch Ausfällungen aus magmatischen, volatilreichen Fluiden gebildet.

Die ersten beiden Beiträge dieses Kapitels befassen sich mit der Aufnahme von Fluiden in Magmen. Die Ergebnisse zur Speziation von gelöstem CO_2 in einer vereinfachten Basaltschmelze sind deswegen bedeutsam, weil CO_2 eine der häufigsten flüchtigen volatilen Komponenten ist, die in Magmen gelöst sind. Frühere Untersuchungen zu diesem Thema wurden an aus Schmelzen abgeschreckten Gläsern durchgeführt, die jedoch nicht immer die gleiche Struktur und Speziation wie die Ausgangsschmelze aufwiesen. Die neuen Fluiduntersuchungen, die an Schmelzen bei hohen Drücken unter Einsatz der *in situ*-Spektroskopie durchgeführt wurden, stellen daher einen großen Fortschritt dar. Zum ersten Mal konnte die Temperaturabhängigkeit der Speziation direkt beobachtet werden. Der zweite Beitrag befasst sich mit der für die Erzlagerstättenbildung wichtigen Frage, wieviel Chlor in der Fluidphase granitischer Magmen enthalten ist. Zur Lösung dieses Problems ist eine Verknüpfung analytischer Daten von Schmelzeinschlüssen mit experimentell gewonnenen Ergebnissen zur Chlorlöslichkeit notwendig. In der vorliegenden Studie wurde zum ersten Mal ein umfassendes thermodynamisches Modell für in Silikatschmelze gelöste Halogene entwickelt. Weiterhin wird gezeigt, dass natürliche Magmen gleichzeitig 2 Fluidphasen entmischen können: Dampf + Sole („*brine*“). Dadurch wird bei Modellierungen die Verwendung experimentell ermittelter Daten zur Elementverteilung erheblich erschwert. Der dritte Beitrag präsentiert Resultate experimenteller Untersuchungen zum Ursprung karbonatreicher Schmelzen durch Teilaufschmelzung des Erdmantels. Es ergeben sich neue Kenntnisse über den Ursprung verschiedener vulkanischer Gesteine, die auf der Erdoberfläche anzutreffen sind (z. B. Karbonatite und Kimberlite) und über den Ursprung von Diamanten. Weiterhin können diese Ergebnisse möglicherweise unsere Kenntnisse des Kohlenstoffkreislaufs zwischen Erdmantel und Erdoberfläche (einschließlich Hydro-, Bio- und Atmosphäre) verbessern. Ein weiterer Beitrag befasst sich mit den Eigenschaften eines Systems, das aus einem kleinen Anteil fein verteilter Schmelze in einer kristallinen Matrix besteht. Geklärt werden soll, ob die Schmelze durch die Matrix perkolieren kann, was für die Materie-Differenziation erforderlich wäre. Das in diesem Beitrag vorgestellte System stellt ein Analogon einer Metallschmelze in einer Silikatmatrix dar und ist somit für Überlegungen zur Bildung des Erdkerns und der Kerne anderer Planeten verwendbar.

3.7 Rheologie

Das Innere der Erde ist durch dynamische Prozesse geprägt, die sich in der Verformung der Gesteine in stark variierenden zeitlichen und räumlichen Maßstäben widerspiegeln. Bei hohen Spannungen und Verformungsraten sowie niedrigen Temperaturen deformieren sich Gesteine durch bruchhafte Prozesse (z. B. Gesteinsverschiebungen, die Erdbeben auslösen), während bei niedrigen Spannungen und Verformungsraten sowie hohen Temperaturen duktile Deformationsprozesse vorherrschen (z. B. Konvektionsfließen der Mantelgesteine). Das rheologische Verhalten der Gesteine wird durch sogenannte Fließgesetze beschrieben, die sich

mittels Verformungsversuchen im Labor konstruieren lassen. Die Anzahl der externen (z. B. Druck, Temperatur, Fugazitäten von Wasser und Sauerstoff) und internen (z. B. Phasengehalt, Mikrostruktur und Textur) Faktoren, die einen Einfluss auf die Gesteinsrheologie haben, ist jedoch relativ groß. Gut kontrollierte Deformationsexperimente unter Druck- und Temperaturbedingungen, die für das Erdinnere relevant sind, stellen nach wie vor eine große technische Herausforderung dar. Jedoch können mit modernen Pressen (z. B. D-DIA-Vielstempelpresse) und durch die Verwendung von Analogmaterialien (z. B. $CaIrO_3$ als Analogon für $MgSiO_3$) Erkenntnisse über das rheologische Verhalten im tiefen Erdinneren gewonnen werden. Ein wichtiger Aspekt der Gesteinsdeformation ist, dass sie das Gestein selber in Bezug auf seine Struktur verändert und dadurch eine Anisotropie physikalischer Eigenschaften (z. B. seismische Wellengeschwindigkeiten oder elektrische Leitfähigkeit) erzeugt, die wiederum *in situ* mit geophysikalischen Methoden gemessen werden kann.

Da die Hauptbestandteile des unteren Erdmantels, $(Mg,Fe)SiO_3$-Perowskit und Post-Perowskit, bei Oberflächenbedingungen relativ instabil sind, ist der Einsatz von Analogmaterialien wie $CaIrO_3$ für die Charakterisierung ihrer Rheologie, und insbesondere, der Änderung ihrer Rheologie mit dem Phasenübergang sehr wertvoll. Verformungs-experimente mit $CaIrO_3$ zeigen, dass der Phasenübergang von Perowskit nach Post-Perowskit sehr wahrscheinlich mit einem Wechsel im Deformationsmechanismus von Korngrenzgleiten (Perowskit) zu Versetzungsgleiten (Post-Perowskit) einhergeht. Das wiederum bedeutet einen Wechsel von isotropem (Perowskit) zu anisotropem (Post-Perowskit) Gefüge, was auch in der D"-Schicht oberhalb der Kern-Mantel-Grenze seismologisch beobachtet wird. Die zweit-häufigste Phase des unteren Erdmantels, Magnesiowüstit, zeigt eine besonders starke Abhängigkeit der Rheologie von der chemischen Zusammensetzung (Fe/Mg-Verhältnis), da ein zunehmender Fe-Gehalt auch eine Zunahme an Punktdefekten (z. B. Gitterleerstellen) bedeutet, die wiederum einen direkten Einfluss auf die mechanische Festigkeit des Materials haben und zudem den aktiven Deformationsmechanismus bestimmen.

Die Übergangszone zwischen oberem und unterem Erdmantel in 410 bis 660 km Tiefe ist ein weiterer Bereich, in dem Phasenübergänge (z. B. Olivin zu Wadsleyit und Ringwoodit) einen entscheidenden Einfluss auf das plastische Fließen der Gesteine haben können. Unter den Bedingungen der Übergangszone erscheint die Olivinstruktur des $MnGeO_4$-Analogmaterials wesentlich weicher zu sein als die entsprechende Wadsleyitstruktur. Das bedeutet, dass dieser Phasenübergang ein Hindernis für die Konvektion zwischen oberem und unterem Mantel darstellt. Im oberen Mantel wird das plastische Fließverhalten und die resultierende physikalische Anisotropie hauptsächlich von der Deformation des Olivin bestimmt; während aber die Rheologie von Olivin selbst relativ gut bekannt ist, ist der Einfluss von partiellen Schmelzen auf das Fließverhalten und insbesondere die Mikrostrukturentwicklung bisher ungeklärt. Dies ist gerade für die Interpretation seismischer Daten und der Fließgeometrie in den Bereichen unterhalb der mittelozeanischen Rücken wichtig, wo partielle Schmelzen auftreten. Rheologie und Verformungsstrukturen der Pyroxene sind kritische Parameter bei der Deformation der unteren Erdkruste, des oberen Erdmantels und insbesondere der subduzierten ozeanischen Lithosphäre. Hier wiederum spielen Phasenübergänge (z. B. Proto- zu Orthoenstatit) und Ordnungsphänomene (z. B. Übergang C2/c → P2/n in Omphazit) eine

wichtige Rolle bei den Deformationsmechanismen und den resultierenden Mikrostrukturen. Deshalb kann eine detaillierte Mikrostrukuranalyse von Pyroxenen dabei helfen, die p,T-Bedingungen der Gesteinsdeformation zu ermitteln. Die Deformation in der Oberkruste wird weitestgehend durch bruchhafte Vorgänge in quarzreichen Gesteinen gesteuert; die Untersuchung kataklastischer Störungszonen in Quarziten, die vermutlich ehemalige Erdbebenherde darstellen, vermittelt daher Einsichten in die Erdbebenherdmechanismen und insbesondere in die Rolle des Wassergehaltes bei diesen Prozessen.

3.8 Metamorphose

Metamorphose ist die Folge veränderter chemischer und physikalischer Bedingungen, denen Gesteine in geologisch aktiven Gebieten der Erde ausgesetzt sind, z. B. in Subduktionzonen, bei der Gebirgsbildung oder in der Tiefe von kontinentalen Grabenbrüchen. Die metamorphen Reaktionen beinhalten eine Umkristallisation des ursprünglichen Mineralbestandes, was durch neue Druck- und Temperaturbedingungen und häufig durch den Einfluss von Fluiden bedingt wird. Da diese Mineralgefüge häufig während des Aufstieges der Gesteinseinheiten an die Eroberfläche (Exhumierung) metastabil erhalten bleiben, können sie genutzt werden, die Geschichte der Gesteine durch Raum und Zeit zu verfolgen und ermöglichen es darüber hinaus, die Bedingungen und Prozesse im tiefen Erdinneren zu erforschen.

Die vier Beiträge dieses Kapitels geben einen Überblick über die große Bandbreite der metamorphen Prozesse und machen die Bandbreite der Themen deutlich, die an metamorphen Gesteinen untersucht werden. Die ersten beiden Beiträge handeln von Schockmetamorphose, d. h. Umbildungen, die durch ein in sehr kurzen Zeiträumen (Sekunden bis Minuten) ablaufendes Ereignis (z. B. einen Meteoriteneinschlag) verursacht werden und die kurzfristig zu extrem hohen Temperaturen und Drücken in der Impaktzone führen können. Derartige charakteristische Umbildungen finden sich nur in den Gesteinen aus Impaktzonen. Im ersten Beitrag wird eine transmissionselektonenmikroskopische (TEM) Untersuchung über die Nukleation von Ringwooditlamellen in Olivin unter hohem Druck präsentiert, die in einem geschockten Chondriten konserviert wurde. Eine neue Verwachsungsorientierung wurde hierbei entdeckt, die aus experimentellen Studien bisher nicht bekannt war. Der zweite Beitrag beschreibt die Ergebnisse einer hochauflösenden TEM-EDXS-Untersuchung von aluminiumhaltigem Akimotoit ($MgSiO_3$), der in Schmelzadern eines geschockten Chondriten entdeckt wurde. Dabei wurde ein ungewöhnlich hoher Fe^{3+}-Gehalt festgestellt, der mit einer gekoppelten Fe^{3+}-Al^{3+}-Substitution zusammenhängt, während sich koexistierender majoritischer Granat und Ringwoodit als relativ Fe^{3+}-verarmt zeigen. Bei Abschätzungen der Sauerstofffugazität (fO_2) unter Verwendung dieser Mineralsysteme muss diese Verarmung berücksichtigt werden. In den zwei folgenden Beiträgen werden verschiedene Aspekte der eklogitfaziellen Metamorphose beleuchtet. In dem dritten Beitrag wird der Einfluss von Subkorngrenzen auf die Diffusion während der Metamorphose in Granat untersucht. Die chemische Zusammensetzung von Granat ist ein wichtiger Indikator zur Bestimmung von Druck-, Temperatur-, Zeitpfaden (PTt-Pfade), die eine Gesteinseinheit durchlaufen hat. Die Ergebnisse der Studie zeigen eine Entkoppelung des Diffusionsverhaltens unterschiedlicher

Elemente abhängig von dem Vorhandensein und der Dichte von Subkorngrenzen im Granat. Eines der wichtigen Themen der Eklogitfaziesmetamorphose ist die Frage, durch welchen Prozess die sehr dichten Eklogite nach ihrer Bildung in der tiefen Erdkruste oder dem Mantel wieder zur Erdoberfläche transportiert werden können. Der letzte Beitrag untersucht in diesem Zusammenhang die Kristallgitterorientierung (LPO) von Omphazitkristallen in Eklogiten des Tauernfensters/Österreich. Die LPO der Omphazite offenbaren Informationen über Intensität und Richtung der Verformung während der Hochdruckmetamorphose. Die Ergebnisse der Studie deuten darauf hin, dass die momentanen Exhumierungsmodelle für das Tauernfenster modifiziert werden müssen.

3.9 Materialwissenschaften

Die Materialwissenschaft versucht, eine Verbindung zwischen der Atom- und Kristallstruktur einer Materie mit Zieleigenschaften und speziellen Anwendungsmöglichkeiten herzustellen. Einen wesentlichen Einfluss auf Gefüge und Eigenschaften eines Stoffes üben seine chemische Zusammensetzung und seine Entstehungsgeschichte aus. Druck gilt generell als Medium, das Volumen, Struktur und elektronische Eigenschaften von Stoffen verändert. Auf diesem Forschungsgebiet zur Entwicklung, Synthese und Analyse neuer Materialien mit einzigartigen und nutzvollen Eigenschaften genießt das Bayerische Geoinstitut aufgrund seiner Ausstattung einen großen Vorteil. Im Fokus der aktuellen Forschungsarbeiten stehen ultraharte Werkstoffe, wobei sich vielversprechende neue Möglichkeiten hinsichtlich nano-Verbundstoffen aus Bornitrid abzeichnen. Nanokristalline Formen bereits bekannter Stoffe können weitaus nützlichere Eigenschaften aufweisen als ihre makrokristallinen Pendants. Das wurde zum Beispiel für Diamant bereits erkannt, und so werden die Forschungsarbeiten zur Synthese und Charakterisierung von nanokristallinem Diamant fortgesetzt. Die Dotierung mit Bor stellt eine weitere Methode dar, mit der die Eigenschaften von Diamant durch Änderungen in der elektronischen Struktur verbessert werden können. Zusätzliche Synthesen bei hohen Drücken in Verbindung mit theoretischen Berechnungen werden Einblicke in das Verhalten von Diamant als Supraleiter liefern. Anwendungsmöglichkeiten von nano-kristallinem Titan- und Zirkonoxid und ihren Mischkristallen beinhalten den Einsatz als Pigmente, Katalysatoren und in der Elektronik. Weitere Untersuchungen zum Kompressions-verhalten und zu Phasenübergängen werden stattfinden, um die Beziehungen zwischen Zusammensetzung, Mikrogefüge und physikalischen Eigenschaften zu verstehen. Mit ähnlichen Themen befassen sich auch die restlichen Beiträge dieses Kapitels, die ein weites Spektrum von Stoffen und Eigenschaften umfassen.

3.10 Methodische Entwicklungen

Die Entwicklung neuer experimenteller und analytischer Techniken stellt die Basis jeglicher wissenschaftlichen Forschung dar; ihre Bedeutung kann nicht überbetont werden. Das Bayerische Geoinstitut weist auf diesem Gebiet eine lange Tradition auf hohem Niveau aus. Zahlreiche im Institut erarbeiteten Innovationen wurden von Labors auf der ganzen Welt

übernommen. Die Konzeption, Erprobung und Durchführung neuer experimenteller und analytischer Methoden stellt eine zeitaufwändige Herausforderung dar, die nur mit sehr guter technischer und finanzieller Ausstattung angenommen werden kann. Diese Bedingungen sind im Geoinstitut glücklicherweise gegeben. Das Jahr 2006 sah sowohl Fortschritte in der Mikro-Röntgen-Absorptionsspektroskopie als auch hinsichtlich der Druckkalibirierung und Druckregelung in Diamantstempelzellen. Ein neu entwickeltes energiedispersives Spektrometer mit fest eingestellter Optik und einer räumlichen Auflösung von 5 µm ermöglicht erstmals eine 2D-Darstellung der röntgenspektroskopischen Eigenschaften von Proben in einer Diamantstempelzelle über eine Fläche von 500x500 µm. Neue Untersuchungen zur Zustandsgleichung von LiF liefern dringend benötigte Informationen für ein Medium zur Druckkalibirierung. Dieses weist eine hohe Fähigkeit zur Druckübertragung, eine niedrige Absorption von Röntgenstrahlen sowie keine Phasenübergänge bis 32 GPa und 720 °C auf. Weiterhin haben neue Entwicklungen zum Einbau von Wegmessern in Diamantstempelzellen den kontrollierten Druckaufbau (und -abbau) in den Zellen stark beschleunigt und sicherer gemacht. Die neuen Möglichkeiten zur Druckeinstellung, ohne die Notwendigkeit, die Zelle zu bewegen und zeitaufwändige Längenmessungen durchzuführen, sind besonders vorteilhaft bei ortsaufgelösten *in situ*-Experimenten.

3. Research Projects

In this section an overview of the most important ongoing projects is given. Information concerning recently-completed projects can be obtained from the publication lists of section 5.1 and 5.2. Please note that the following contributions should not be cited.

3.1 Earth's Structure and Geodynamics

Due to the lack of direct samples from the Earth's interior deeper than ~ 200 km, its study relies primarily on information from geophysical inversion methods. Among them gravitational and seismic observations are most useful for a quantitative understanding of the Earth as they provide information about the density and elasticity of its internal structure. In particular, through advances in seismology we now see an increasingly complex picture of structure in the Earth's interior, with strong lateral variations, anisotropy, and a set of varied seismic discontinuities.

In order to understand the geophysical and geochemical significance of such features, seismic information needs to be combined with experimental data on phase transitions and physical properties that can be used to interpret the geophysical observations. From joint considerations of mantle petrology and seismic data, it has become clear that the major seismic discontinuities in the mantle are associated with phase transitions in the Mg_2SiO_4 olivine based solid solution in the mantle. In addition to olivine, the mantle also contains solid solution minerals that are based on $MgSiO_3$ and $CaSiO_3$ stoichiometry (pyroxenes, garnets, and perovskites). In contrast to the sharp phase transitions in the Mg_2SiO_4 system, the minerals in the $MgSiO_3$ based solid solution show gradual transformations. While the Mg_2SiO_4 based solid solution is well understood in experiments, the dissolution of pyroxenes into garnets or the exsolution of perovskites from the garnet component of the mantle are not extensively studied.

The first two contributions of this section address issues in this more complex solid solution. In the first contribution the phase equilibria between pyroxenes and garnets are considered with both phases coexisting over a wide pressure range. The experiments show that a detailed balance of the cations present in the garnet can potentially be used to infer the pressure of formation. The detailed pressure dependence of partitioning of major cations between pyroxenes and garnets will also influence the petrological models of the mantle, necessary for a detailed analysis of seismic wave velocity profile through the mantle.

In recent years, a complicated distribution and nature of seismic discontinuities has emerged from seismological studies, in particular in the transition zone. For example, the discontinuity near 520 km depth is not globally observed, but – where present – shows a diverse range of behaviour with varying depth and multiple reflectors. To explore this behaviour in terms of the underlying mineral thermodynamics, the second contribution looks into the exsolution of $CaSiO_3$ perovskite from the garnet component of mantle mineralogy. This exsolution provides an alternative interpretation of discontinuity in the mantle, in addition to the phase transition

from wadsleyite to ringwoodite in Mg_2SiO_4. Similar to the discontinuities between 500 and 560 km, the discontinuity near 660 km depth in the Earth has long been attributed to the Mg_2SiO_4 system only. The third contribution in this section explores the effect that temperature has on the location of phase transitions associated with the 660 km discontinuity for a mantle chemical model (pyrolite) using a thermodynamic mineralogical model of mantle mineralogy.

While mineral physics has advanced the understanding of Earth's mantle to a detailed level as illustrated in these contributions, questions regarding the core are still more fundamental, and range from the crystallographic structure of iron or its alloys under the extreme pressure and temperature conditions in the Earth's inner core, as well as the amount and nature of the alloying elements present. The answer to these questions relies on the integration of information from a wide variety of fields in the planetary and Earth sciences, and laboratory experiments in the megabar range in the diamond anvil cell play a central role. The fourth contribution in this section revisits phase stability of pure iron at megabar pressures and the fifth contribution investigates the bulk elastic behaviour of a Ni-Fe alloy (22 mol.% Ni) to study the influence of Ni on the elastic properties of Fe.

In the last contribution of the core part, the settling of iron through a magma ocean in the early Earth and the resulting distribution of Ni between the metallic and the residual silicate melt is studied. The settling of liquid iron droplets through a magma ocean is modelled with a finite difference code that simulates the flow of two interpenetrating fluids. In the final contribution of this section, the same code is used to study the deposition of ejecta through the atmosphere following a meteorite impact. The results are used to improve the understanding of the deposition of ejecta following the Chixulub impact that is thought to be responsible for the extinction of the dinosaurs at the K/T boundary.

a. *Calibration of the pyroxene-garnet transformation in simple and complex systems (D.J. Frost)*

Compositions of garnets recovered from the mantle can be described mainly using $Mg_3Al_2Si_3O_{12}$ (pyrope), $Fe_3Al_2Si_3O_{12}$ (almandine) and $Ca_3Al_2Si_3O_{12}$ (grossular) end members. However, at pressures above 4 GPa the $M_4Si_4O_{12}$ majorite component (where M is a divalent cation, normally Mg, Fe or Ca) becomes increasingly important. As a result, for a given bulk rock composition the proportion of pyroxene formed will decrease with increasing pressure as the proportion of the majorite component in garnet increases. This transformation of pyroxene to garnet has been studied in a few simple systems at low temperatures and some complex bulk compositions have also been examined. However, there have been no studies to calibrate accurately the pressure of this transformation particularly at mantle temperatures and the thermodynamic properties are relatively unknown, as are the effects of the major divalent cation substitutions on the transformation. Knowledge of this transformation is important, however, when developing petrological models for the calculation of sound wave velocities in

the mantle. Also an increasing number of studies are finding evidence of natural majoritic garnets in diamond inclusions and from ultrahigh-pressure metamorphic terrains. A determination of the pressure and temperatures under which these natural garnets formed requires information on the effect of composition, pressure and temperature on the pyroxene to majoritic garnet transition.

In order to measure the pressure of a phase transformation accurately many studies use *in situ* X-ray diffraction at a synchrotron facility, whereby pressure can be determined from unit cell measurements of a pressure standard mixed with or adjacent to the transforming phases. The kinetics of garnet reactions are, however, extremely slow and very few experiments would be possible over the period of most synchrotron beam time allocations. In this study majorite forming reactions have been calibrated by employing multi chamber capsules where samples with compositions along the Mg_2SiO_4-Fe_2SiO_4 join are also included. Phase relations in this "olivine" system are known very accurately as they include a number of divariant phase transformations that are important for the Earth. The olivine to ringwoodite transition in particular involves the formation of a two-phase region where both phases coexist over a pressure range between approximately 5 and 13 GPa. The composition of each phase changes with pressure and temperature such that if both phases are found to coexist the pressure can be accurately determined from the phase diagram using the Fe/(Fe+Mg) ratios of the two phases.

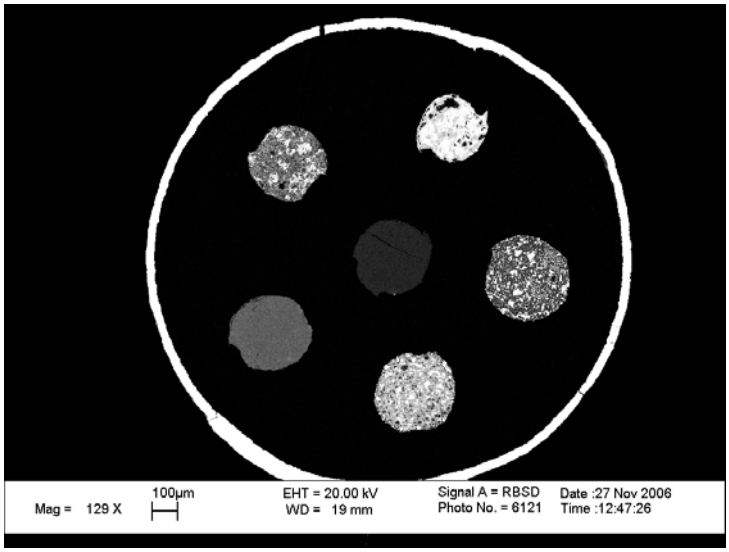

Fig. 3.1-1: Multi-chamber alumina capsule showing 6 samples. 4 samples contain garnet-pyroxene compositions while the other 2 are olivine samples with varying Fe/(Fe+Mg) ratios for the calibration of pressure.

Figure 3.1-1 shows a multichamber alumina capsule from a typical experiment. Six sample chambers are present and two such capsules are run in each experiment. This allows for the presence of several pyroxene-garnet bulk compositions and several pressure calibrant olivine compositions in each experiment. In this way the degree of the majorite forming reaction can be examined in various bulk compositions at an identical and well-known pressure and temperature. Starting bulk compositions are glasses with the general formula $M_{3.5}AlSi_{3.5}O_{12}$ *i.e.*, at the mid point between garnet and pyroxene stoichiometries where M is either Mg, ($Mg_{0.9}$,$Fe_{0.1}$), ($Mg_{0.5}$,$Fe_{0.5}$), Fe, Ca or ($Ca_{0.5}Mg_{0.5}$). Experiments are run at 1400 °C for several

days and recovered samples are analysed using the electron microprobe. Figure 3.1-2 demonstrates how the experimental pressures are calculated in each experiment using the Mg_2SiO_4-Fe_2SiO_4 phase diagram. The effects of Fe-Mg substitution on the pyroxene garnet transformation are demonstrated. Increasing the proportion of Fe decreases the solubility of the majorite component at a given pressure. These and further experiments will allow an accurate and complete thermodynamic model for the pyroxene garnet transformation to be developed.

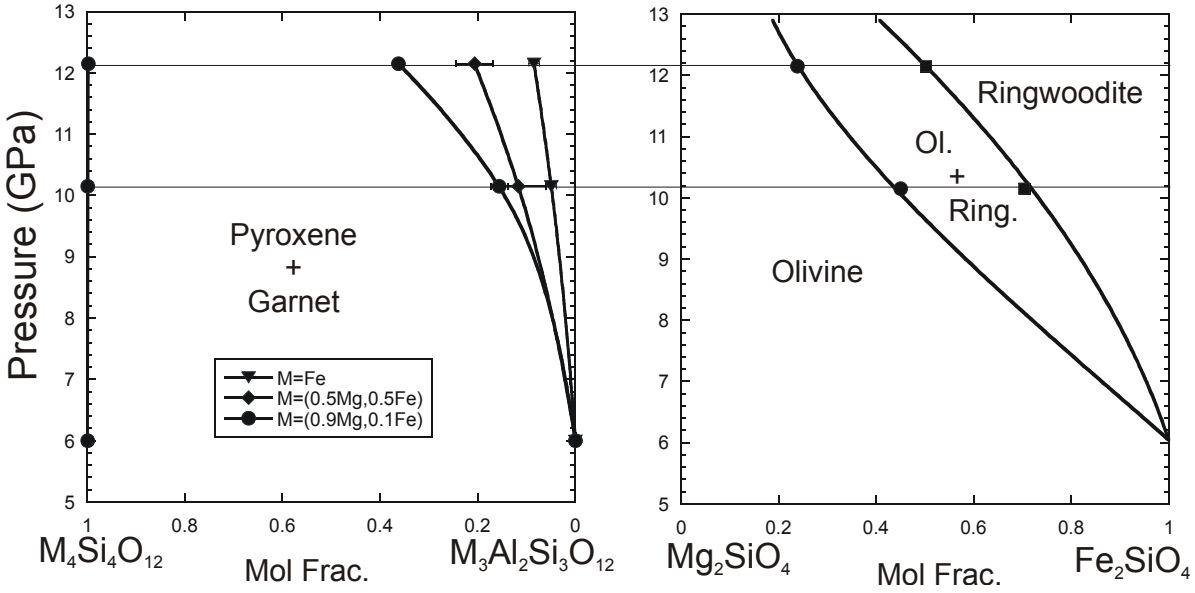

Fig 3.1-2: The proportion of the majorite component ($M_4Si_4O_{12}$) in garnets coexisting with pyroxene as a function of garnet Fe-Mg content is shown in the diagram on the left while the right hand diagram shows how pressure is determined from the Mg_2SiO_4-Fe_2SiO_4 phase diagram using coexisting compositions of olivine (circles) and ringwoodite (squares).

b. *Calculations of sound velocity and seismic discontinuity structure at the base of the transition zone (A. Saikia, D.J. Frost and D.C. Rubie)*

Several studies that have examined different types of reflected seismic waves have observed complexity in the region of the 520 km seismic discontinuity (*d520*). In some regions *d520* seems to split into two separate discontinuities one at approximately 500 km and the other at around 560 km. In addition to the wadsleyite to ringwoodite transition, it has been proposed that the exsolution of $CaSiO_3$ perovskite (*Ca-pv*) from majoritic garnet (*gt*) may be capable of producing a seismic discontinuity. However, to date very little experimental data exist by which to test this latter possibility. Here we study the *Ca-pv* forming reaction to determine if it occurs over a narrow enough pressure interval to cause a discontinuity. We use these results to parameterise a thermodynamic model for this reaction and use this to calculate sound velocity profiles for different plausible bulk compositions at the base of the transition zone.

We examine *Ca-pv* exsolution as a function of *gt* Al/Si ratio (*i.e.*, along the pyrope-majorite solid solution). Experiments are performed by equilibrating Ca free majorite *gt* with *Ca-pv* to determine the saturation level as a function of P, T and *gt* Al content. The experimental data at 1600 °C are shown in Fig. 3.1-3. Increasing the Al content of *gt* (*i.e.*, making it more pyropic as opposed to majoritic) allows more Ca to remain in the *gt* structure at a given pressure. The exsolution of *Ca-pv* can be described by the equation,

$Ca_3Al_2Si_3O_{12}$	+	¾ $Mg_4Si_4O_{12}$	=	$3CaSiO_3$	+	$Mg_3Al_2Si_3O_{12}$
grossular *gt*		majorite *gt*		*Ca-pv*		pyrope *gt*

The experimental results are a thermodynamic model employing this equation. The important variables in this fit are the volume change of the reaction and the non-ideal mixing parameters for majoritic garnet. Because the data cover a range of garnet-majorite compositions the model can be used to calculate the exsolution of $CaSiO_3$ over a range of relevant bulk compositions. The *gt* Ca content calculated for a typical bulk earth composition, peridotite, is shown by the solid curve in Fig. 3.1-3. The exsolution of *Ca-pv* begins quite sharply with increasing pressure, causing the Ca content of *gt* to decrease. As *Ca-pv* exsolves, however, the residual *gt* becomes more Al-rich and thus the *Ca-pv* exsolution starts to level off. The exsolution is therefore inherently nonlinear with pressure.

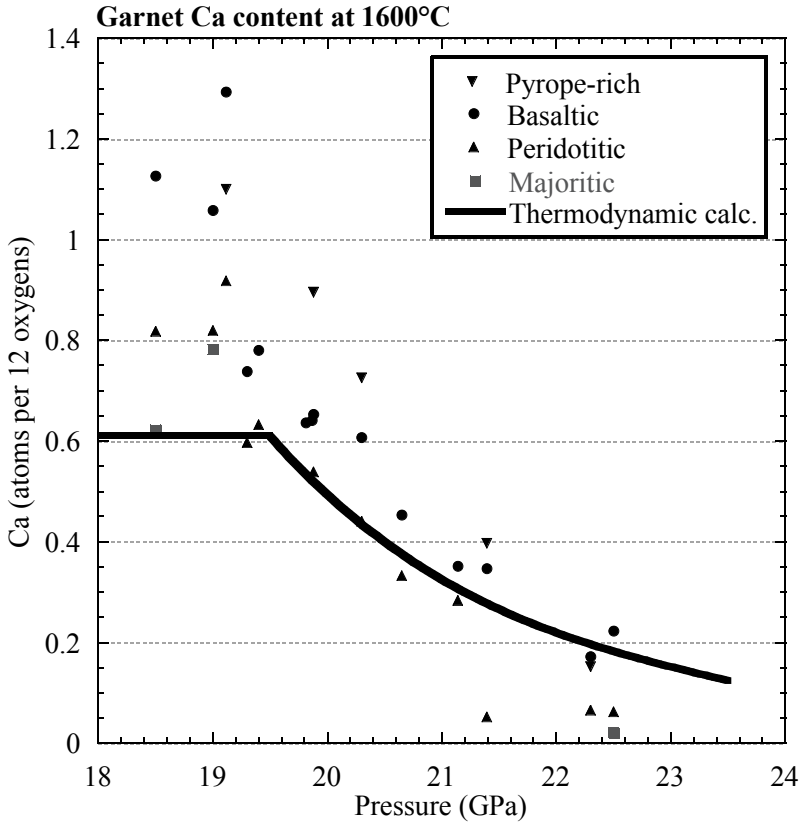

Fig 3.1-3: Concentration of Ca in *gt* coexisting with *Ca-pv* at 1600 °C. Different symbols reflect differing amounts of majorite component. The solid line shows the result of a thermodynamic calculation for peridotite.

Based on elasticity data from the literature we compute the S wave velocity (V_S) at the base of the transition zone for a peridotitic mantle and for a MORB bulk composition. For peridotite

the major jump observable in S velocity results from the wadsleyite to ringwoodite transition and the *Ca-pv* forming reaction produces only a weak increase in the S velocity gradient above this much larger jump. It is unlikely that such a weak gradient would produce a seismically observable discontinuity. For the MORB composition no olivine polymorphs are stable and a strong non linear discontinuity occurs as *Ca-pv* exsolves from *gt* due to the relatively high Ca content of MORB. These results suggest that although we would not expect a split *d520* in peridotite mantle, mantle that was a physical mixture of peridotitic and MORB composition material - as subducting slab material would be at these depths - could produce a split in the seismic discontinuity. Splitting of *d520* may therefore be an indication of the presence of recycled slab material at the base of the transition zone.

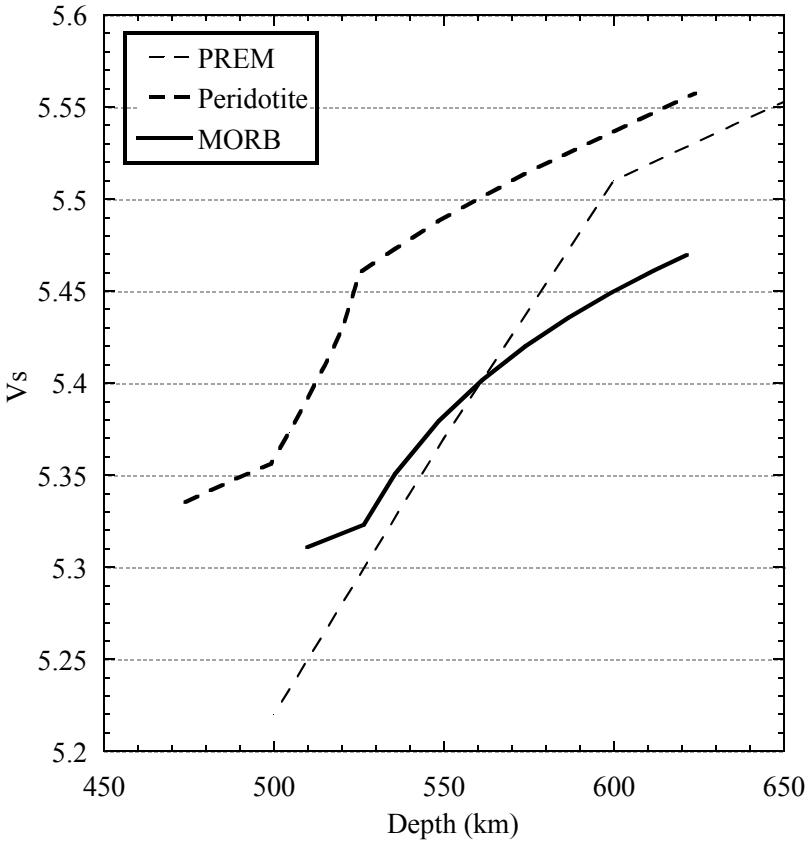

Fig. 3.1-4: Shear wave velocity for peridotite (dashed) and MORB (solid) compositions as a function of depth calculated from a thermodynamic model that was derived from the experimental data. The strong discontinuity for the peridotite curve arises from the wadsleyite to ringwoodite transition while a non linear discontinuity occurs for the MORB curve as a result of $CaSiO_3$ exsolution.

c. *Buoyancy in the mantle near the 660 km discontinuity (S.A. Piazzoni/Munich, G. Steinle-Neumann, H.-P. Bunge/Munich and D. Dolejš)*

The phase transitions in the pressure range of 23 to 25 GPa that give rise to the seismic discontinuity at 660 km, the top of the lower mantle, are of great significance in the dynamics of the Earth's mantle. In particular, the breakdown of Mg_2SiO_4 ringwoodite (γ) to the lower mantle phase, $MgSiO_3$ perovskite (*pv*) and MgO periclase (or rather the solid solution magnesiowüstite *mw*) has a negative Clapeyron slope, and the resulting buoyancy forces act as a barrier to vertical flow. This behaviour has been widely investigated in mantle geodynamics. However, the set of phase transitions occurring at the top of the lower mantle

are more complex than a separate consideration of the Mg_2SiO_4 and $MgSiO_3$ based systems would suggest, changing the influence of these phase transitions on mantle dynamics.

Here we use a thermodynamic model of mantle minerals in the CFMAS system (CaO-FeO-MgO-Al_2O_3-SiO_2) to look at details of the phase transformations leading to the lower mantle phase assemblage. This model is based on laboratory experiments on phase relations, the thermal equation of state, and calorimetric data. The model finds the stable phase assemblage by Gibbs free energy minimization, including end-member compositions as well as solid solutions. Near the 660 km discontinuity this mineralogical model shows that at low temperatures SiO_2 stishovite (*st*) becomes stable. Similarly, at high temperatures (> 2300 K) *γ* does not break down into *pv* and *mw* directly but passes through a majorite garnet (*gt*) stability field, resulting in a transformation of *γ* into *gt* and *mw* (Fig. 3.1-5). At higher pressures, corresponding to the upper boundary of the lower mantle *gt* transforms to *pv*, a transition that has a positive Clapeyron slope.

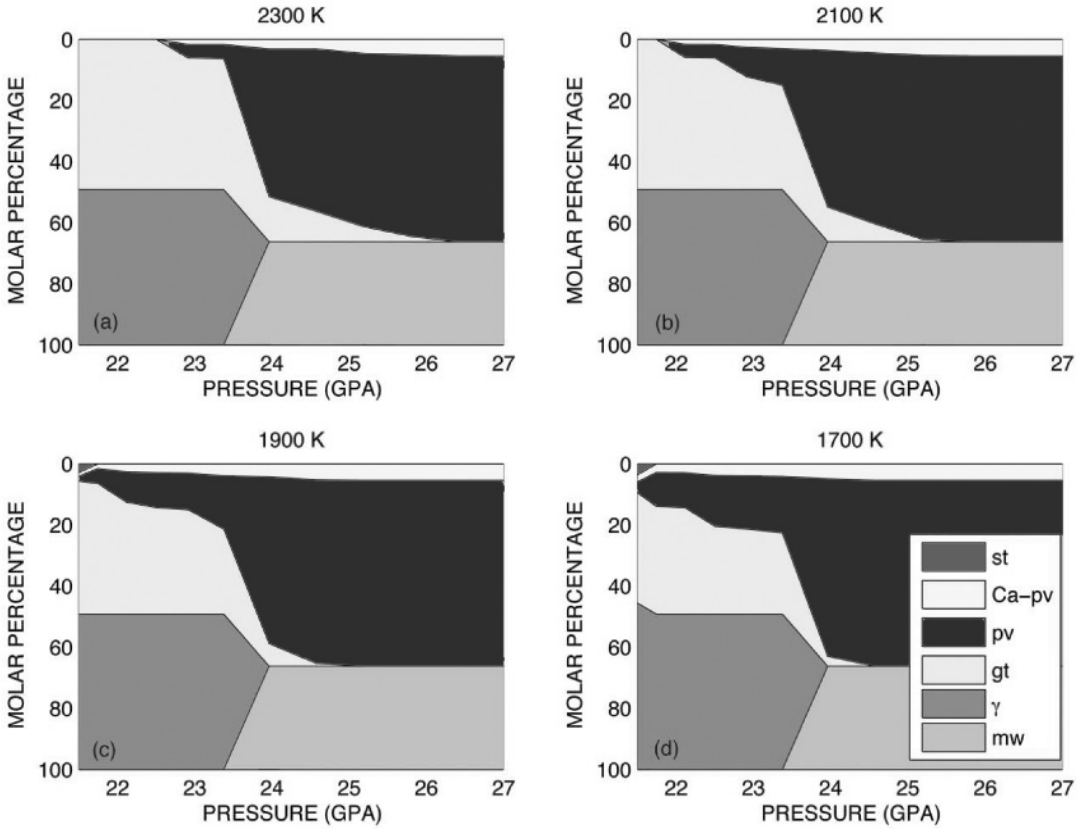

Fig. 3.1-5: Modal abundance of the stable phases for a pyrolitic mantle at different temperatures (1700-2300 K) over the pressure range of the transition zone. At low temperature (panels c and d) *pv*, *mw*, and $CaSiO_3$ perovskite form over a narrow depth interval from *gt* and *γ*, with a negative Clapeyron slope for the post-spinel transition. At high temperatures (panels a and b) *gt* is stable up to lower mantle pressures, transforming smoothly into *pv*, with a positive Clapeyron slope. At high temperature the pressure at which *gt* is completely transformed into *pv* corresponds to about 720 km. We note that the database does not include akimotoite that is expected to be present at the 10 vol.% level at low temperatures.

Recent seismological observations of the splitting of the 660 km discontinuity into two seismic reflections, ranging in depth from 640 to 720 km, require a complex structure of phase transitions as described here. A hot upwelling would experience additional buoyancy from the *pv* to *gt* transformation and penetrate the 660 km discontinuity, becoming part of the upper mantle circulation before it is slowed down by the effects of the negative Clapeyron slope of the *gt* or *pv* plus *mw* to *γ* transition. Similarly, the additional negative buoyancy from dense *st* in a subducting slab will facilitate its sinking into the lower mantle, consistent with global observation in seismic tomography.

d. *γ-Fe at Earth core conditions (L.S. Dubrovinsky and N.A. Dubrovinskaia, in collaboration with A.S. Mikhaylushkin, S.I. Simak and I.A. Abrikosov/Linköping)*

Despite intense experimental efforts over the past decades there are still a number of fundamental questions regarding the structural state and phase relations in pure iron at very high pressures and temperatures. In particular, the location of the ε (hcp) - γ (fcc) - liquid triple point reported in the literature varies between 50 GPa and 2500 K and 100 GPa and 2900 K. In previous experiments γ-Fe was unambiguously detected *in situ* by means of X-ray diffraction at pressures up to about 70 GPa at high temperatures, and results showed that γ-Fe can be stabilized on quenching to ambient temperature. However, so far no reports on the presence of the γ-phase at pressures above 100 GPa were reported, neither *in situ* nor in temperature-quenched experiments.

Here we perform a series of experiments of the structural behaviour of iron and its chemical properties at multimegabar pressure range in the laser-heated diamond anvil cell (DAC). Pieces of iron foil (99.999 % purity, Good Fellow Inc., 2 or 5 μm thickness) were loaded in different experiments in NaCl or MgO pressure-transmitting medium (which also serve as thermal insulator layers) and compressed using 4-pin type DACs equipped with beveled diamonds with culet size of 80 to 150 μm. After the target pressure was reached (in range 100 to 180 GPa) samples were heated to 2500 - 4000 K by double-side laser heating, and temperature-quenched samples were studied by means of X-ray powder diffraction at beamline ID27 at ESRF and at IDD-13 beamline at APS. Although most of diffraction patterns obtained contain only diffraction lines of ε-Fe (Fig. 3.1-6, upper panel), some patterns (particularly those collected from samples heated at temperatures above 3700 K and pressures above 150 GPa) show the presence of both ε- and γ-Fe (Fig. 3.1-6, lower panel). Our observations do not necessarily imply the P-T stability of γ-Fe at very high pressures and temperatures, but suggest that γ-Fe could at least exist as a metastable polymorph, even at pressures above 160 GPa. This is supported by theoretical predictions.

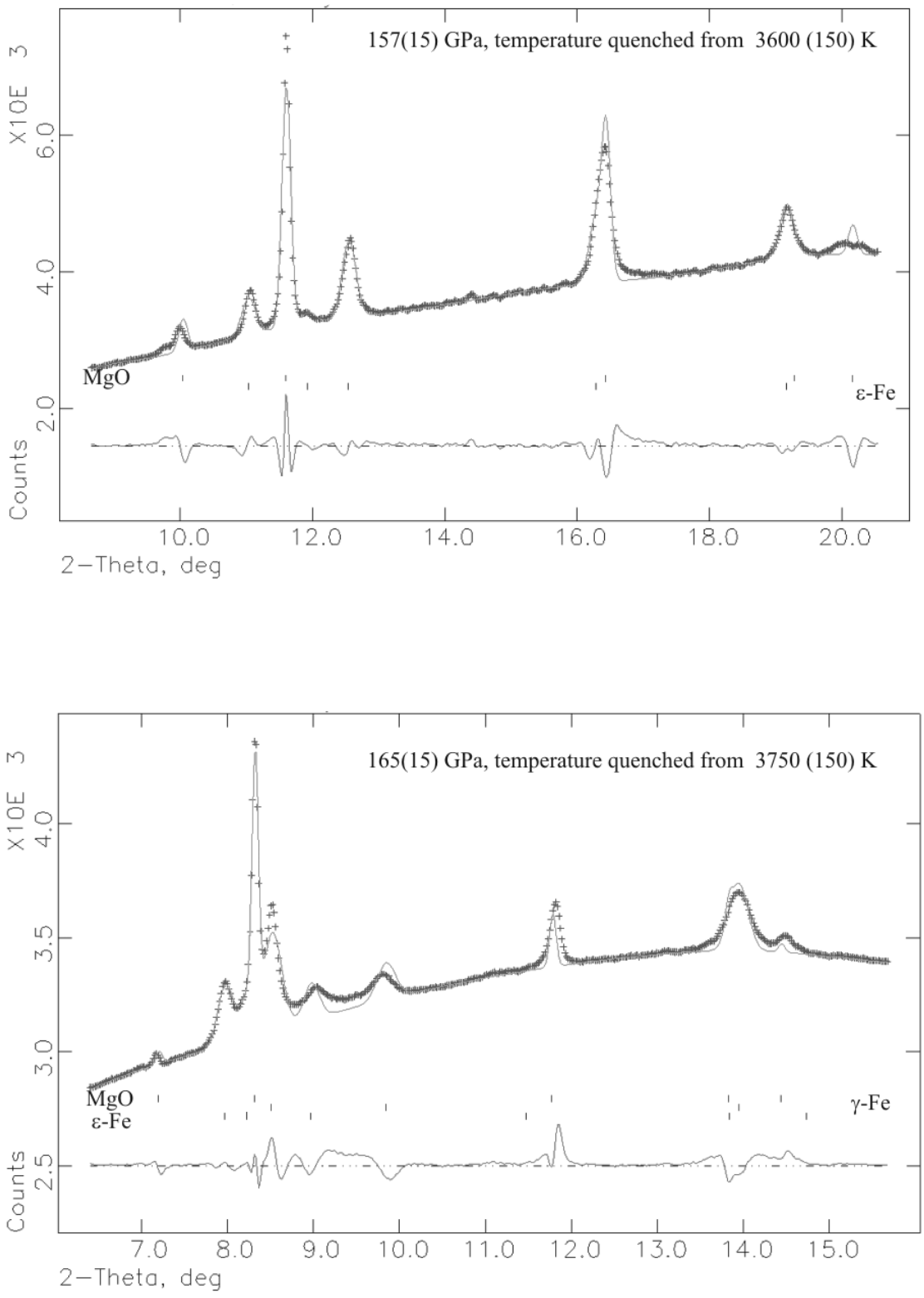

Fig. 3.1-6: Examples of processed full-profile diffraction patterns (GSAS) of iron heated in MgO pressure transmitting media at 157(15) GPa and 3600(150) K (upper panel) and at 165(15) and 3750(150) K (lower panel). Pressure is the ambient temperature pressure derived from the ε-Fe equation, after heating and subsequent cooling of the sample.

e. *Sound wave velocities of fcc Fe-Ni alloy at high pressure and temperature by means of inelastic X-ray scattering (A.P. Kantor, I.Yu. Kantor, A.V. Kurnosov, A.Yu. Kuznetsov, N.A. Dubrovinskaia and L.S. Dubrovinsky, in collaboration with M. Krisch, A.A. Bossak and V.P. Dmitriev/Grenoble)*

High-pressure and high-temperature properties of Fe-Ni alloy with low (5-25 %) Ni content are essential for interpreting seismic and geomagnetic observations and for computer modeling of the Earth's deep interior. We performed a study of a FeNi alloy with 22 at.% of Ni up to 72 GPa and 715 K, using inelastic X-ray scattering and X-ray powder diffraction from polycrystalline material. The X-ray diffraction study revealed stability of the face centered cubic (*fcc*) over the hexagonal close packed (*hcp*) phase in the whole investigated pressure-temperature range. The study presents the first investigations of elasticity of *fcc* phase of iron-nickel $Fe_{0.78}Ni_{0.22}$ alloy.

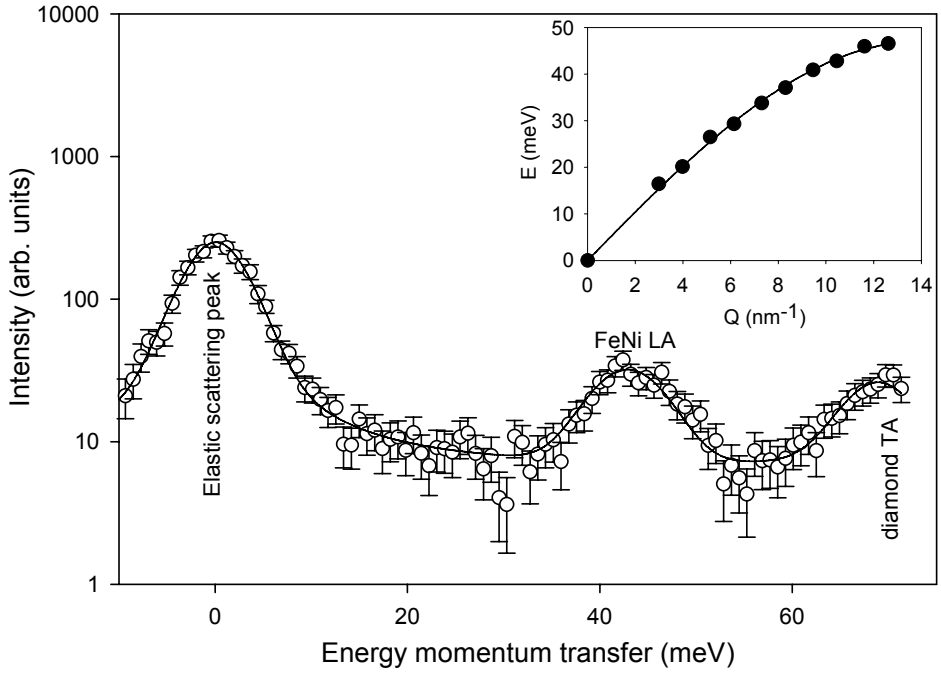

Fig. 3.1-7: Representative IXS spectrum of polycrystalline $Fe_{0.78}Ni_{0.22}$ alloy, collected at 71.7 GPa and 715 K (Q=10.45). Inset: an example of the sinusoidal fit to the experimental $E(Q)$ relation.

The isothermal equations of state were derived at room temperature and at 715 K (K_{300}=162(1) GPa, K'_{300}=4.97(1), V_{300}=6.89(1) cm^3/mole; K_{715}=160(1) GPa, K'_{715}=4.97(2), V_{715}=6.96(1) cm^3/mole). X-ray inelastic scattering measurements from polycrystalline material allow the determination of the longitudinal acoustic wave velocity V_L (Fig. 3.1-7), and provide, combined with the measured equations of state, the full isotropic elasticity of the material. We did not observe a significant deviation of the elastic properties from those of pure ε-iron (Fig. 3.1-8) and furthermore no deviation from Birch's law. Although the bulk

elasticity of *fcc* Fe-Ni alloy and ε-Fe appear to be very similar, the elastic anisotropy of hexagonal and cubic phases should be quite different. If a metal phase in the inner core is not hexagonal, but cubic (or a mixture of two coexisting phases), the understanding of inner core anisotropy should be revised.

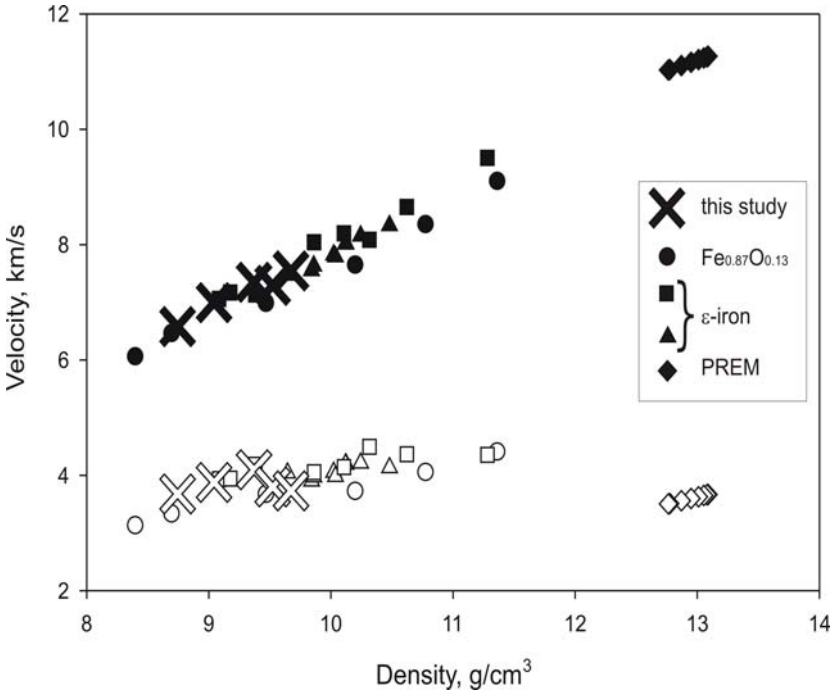

Fig. 3.1-8: Longitudinal V_L (filled symbols) and transverse V_T (open symbols) wave velocities of $Fe_{0.78}Ni_{0.22}$ alloy at ambient and high temperature in comparison with data for $Fe_{0.87}Ni_{0.13}$ alloy (from Lin *et al.*, Geophys. Res. Lett. 30, p. 2112, 2003), pure ε-iron (from Lin *et al.*, Science 308, p. 1892, 2005, triangles and from Antonangeli *et al.*, Earth and Planet. Sci. Lett. 225, p. 243, 2004, squares), and PREM.

f. *Fe segregation and Ni partitioning in the terrestrial magma ocean: a polybaric numerical model (H.J. Melosh and D.C. Rubie)*

Current models of the Earth's formation recognize the importance of large impacts in the early history of the planet, and the fact that such impacts lead inevitably to the production of large volumes of melt. The formation and evolution of such "magma oceans" has become a standard part of the discussion of the early history of the Earth as well as the other terrestrial planets. The partitioning of siderophile elements between silicate liquid and a metal phase during core formation played an important role in establishing the observed siderophile element abundance in the Earth's mantle; an understanding of these abundances depends crucially on the thermodynamics of element partitioning between a silicate melt and metal phase as a function of temperature, pressure, oxygen fugacity and melt structure. Experiments now provide a good understanding of how partition coefficients of many elements depend on these parameters. However, the mechanics of iron segregation from the silicate strongly

controls how much of the metal and silicate react together and produce current element abundances: If iron sinks through the mantle in masses that are large, little chemical equilibration will occur between the two phases. Even when the masses are smaller, as may occur for surface-tension-controlled droplets, the strong depth and temperature dependence of the partition coefficients is a major factor in determining the final siderophile element abundances in the mantle. Iron masses, in whatever form, do not sink quietly through a magma ocean: Their density variations drive vigorous convection currents that themselves tend to suspend and disperse the masses of iron. In addition, thermal convection may also stir the ocean. A simple Stokes-flow model of iron settling cannot resolve the full complexity of iron segregation and the resulting siderophile element partitioning. Although thermal convection in planets has been intensively studied, much less is understood of the dynamic interactions between a convecting fluid and a second fluid that can separate from the first.

Here we have begun with a model for pyroclastic flows developed at Los Alamos. This model is based on a computer code called KFIX that incorporated the ability to compute the flow of two interpenetrating fluids that may move at any speed, ranging from slow subsonic to supersonic. HJM and T. Goldin have adapted this code to the problem of the interaction of planetary ejecta with the Earth's upper atmosphere and magma ocean differentiation (see also next contribution). The code is fully implicit, solving a pressure and mass balance constraint with velocities computed on a staggered mesh. We added subroutines to implement chemical exchange of trace chemical species (Ni in this case) between liquid magma and molten iron. The magma equation of state is based on komatiite liquid, while the equation of state for the iron is derived from shock wave measurements on iron. In our preliminary calculations, partition coefficients from the literature have been taken to allow direct comparison with previous results.

A 1,000 x 1,000 km computational mesh was constructed. Iron metal, in weight ratio between 0.10:1 and 0.32:1 of silicate, was uniformly distributed as 1 cm diameter droplets throughout the mesh at the beginning of the computation. The magma viscosity is taken to be 0.01 Pa-s as a rough average of the likely viscosity variation. We also added a mesh size-dependent macroscopic eddy viscosity to simulate sub-mesh scale turbulence of 10^8 Pa-s. The initial concentration of Ni in the iron is 2.27 wt.% and in the silicate 42 ppm. Initial temperature is uniform at 2,000 K which is thus a highly stable configuration from the point of view of thermal convection; an adiabatic temperature profile might have been a more realistic choice. In our initial runs the resolution is very coarse; we chose only 15 x 15 computational cells. Nevertheless, a number of prominent features can be readily observed from these runs.

The most obvious feature is that, although the droplets initially began to fall in an orderly array at the Stokes velocity of about 0.3 m/sec, after no more than a few hours irregularities develop, creating compositional density currents that quickly dominate the flow. These currents reach up to 50 m/s and completely overwhelm thermal convection. The falling droplets are swept upwards and downwards by this flow as they continue to settle with respect to the fluid. The net result of this vigorous motion is adiabatic cooling of the upper part of the mesh and heating of the lower mesh. In addition, the potential energy of the descending iron

droplets is converted into heat, which greatly raises the temperature in the lower part of the magma ocean and may have a strong effect on the partition coefficient, beyond that previously considered in partitioning computations. These currents continue to stir the magma ocean as the droplets separate, slowly converting their gravitational potential energy to heat and warming the lower part of the ocean. Nevertheless, over a period of months the lower part of the magma ocean is strongly stirred by currents originating from compositional density differences. Thermal convection velocities in the upper, magma-dominated part of the magma ocean reach about 7 m/s, small compared to those driven by compositional convection. Within about half a year, in this low-resolution model, most of the iron has settled to the bottom of the magma ocean. At this time, the average Ni concentration in the separated iron divided by that in the silicate magma is 15, in good agreement with previous simple considerations for a 1000 km deep magma ocean. Figure 3.1-9 shows a snapshot of the iron tracer particle locations 25 days after the beginning of the computation. About half of the iron has fallen out at this stage.

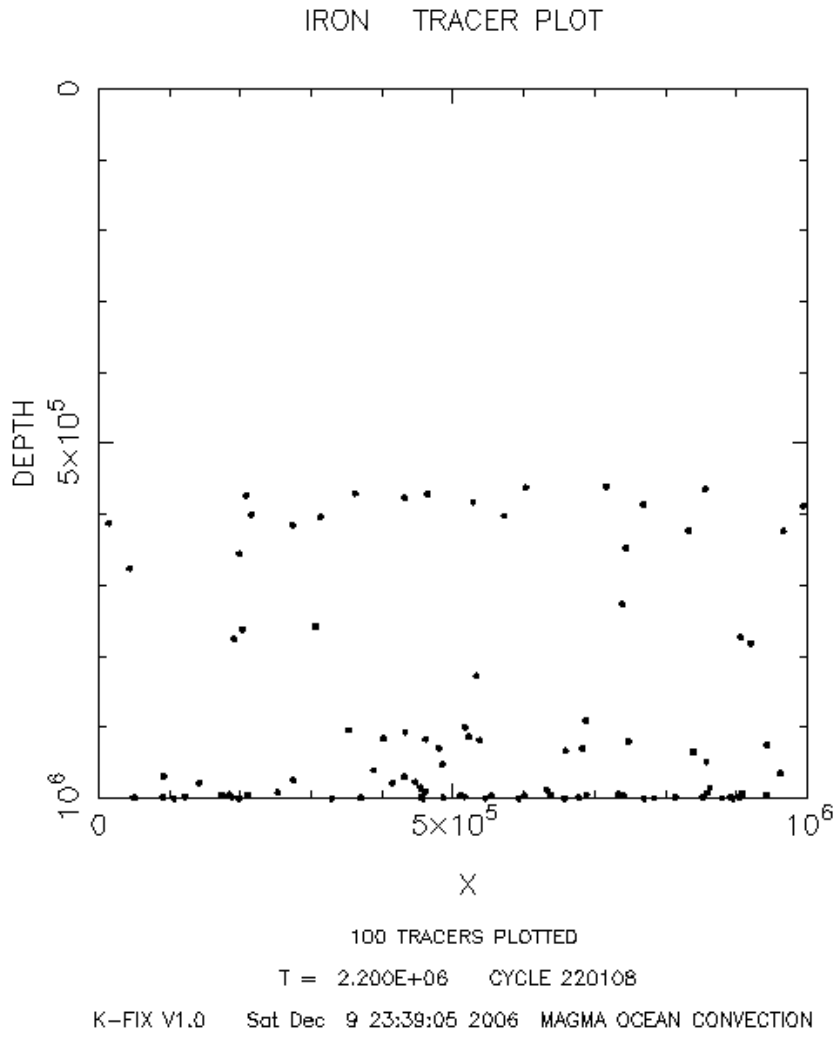

Fig. 3.1-9: Iron droplet tracer particles showing the distribution of iron in a magma ocean 1000 km deep after about 25 days of settling. The ratio of metal to silicate was 0.32 in this run, similar to that in the present Earth.

g. *Interactions between falling Chicxulub impact ejecta and the atmosphere (T.J. Goldin and H.J. Melosh)*

The mechanics of impact ejecta deposition are not well understood, especially for impacts onto planets with atmospheres, such as Earth, where complex interactions occur between the ejected particles and the surrounding atmosphere. Current models of ejecta emplacement, which rely on the fact that material is ejected from craters on ballistic trajectories, are unable to account for multiple layers of ejecta deposited around some terrestrial craters such as Chicxulub, where a dual ejecta layer is observed in North America. Studying the interactions between Chicxulub impact ejecta and the atmosphere is particularly important for understanding the environmental effects of this catastrophic impact.

The ejecta layer at the K/T boundary has been linked to the 65-Ma Chicxulub impact off the coast of the Yucatan, Mexico. The distal ejecta layer, which is found world-wide at sites more than 7000 km from the crater, has a fairly constant thickness of 2-3 mm. In general, the distal ejecta layer, the "fireball layer", consists of densely packed spherules (average diameter of 250 μm) with a spherule area density of ~ 20,000 cm^{-2}. The layer is also enriched in Iridium, an impact indicator, which suggests an impact vapor plume origin. At sites of intermediate distance (2000-4000 km) from the crater in continental North America, the Chicxulub impact ejecta consists of two layers: In addition to the ~ 3 mm thick upper layer containing the Iridium anomaly and spherules, there is a lower, thicker (*i.e.*, ~ 2 cm thick) layer consisting of mainly terrestrial claystone. It has been suggested that the upper layer is equivalent to the distal fireball layer and the lower layer represents material from the ejecta curtain, but the mechanics of producing two distinct layers is unclear. The dual-layer stratigraphy has led to the argument of a second impact event, but it is also possible that atmospheric interactions can explain the emplacement of two distinct ejecta layers. Additionally, soot has been identified at the K/T boundary, suggesting the impact triggered global wildfires. The heating is linked to ejecta re-entry, but models are needed to determine the distribution of this heat within the atmosphere.

In order to model the impact sedimentation the finite-difference code KFIX-LPL is used, which has been modified to suit the problem of impact sedimentation. The code models two-dimensional, two-phase fluid flow allowing us to examine the interactions between the atmosphere and ejected particles (spherules). We modeled a simplified distal Chicxulub scenario of the injection of uniform sized (250 μm diameter) spherules into the atmosphere at 8 km/s, at an altitude of 200 km and with an inflow density consistent with the volume of spherules observed in outcrops. The initial mesh approximates the Earth's atmosphere and employs an exponential pressure gradient, constant temperature (although, in reality, there is some temperature variation in the atmosphere), and standard gravity of 9.8 m/s^2. Air is modeled using the equation of state of a perfect gas and the spherules are modeled as a simple incompressible fluid with the properties of basaltic glass. The particles fall through the thin upper atmosphere, pushing the atmosphere downwards until the particles decelerate due to drag and increasing atmospheric pressure. As can be observed in Fig. 3.1-10, the particles

accumulate a dense layer at ~ 50 km altitude. The deceleration of spherules heats the atmosphere (> 700 K) around the particles causing expansion of the atmosphere, creating a sharp boundary between hot dense atmosphere below the spherules and cool thin atmosphere above.

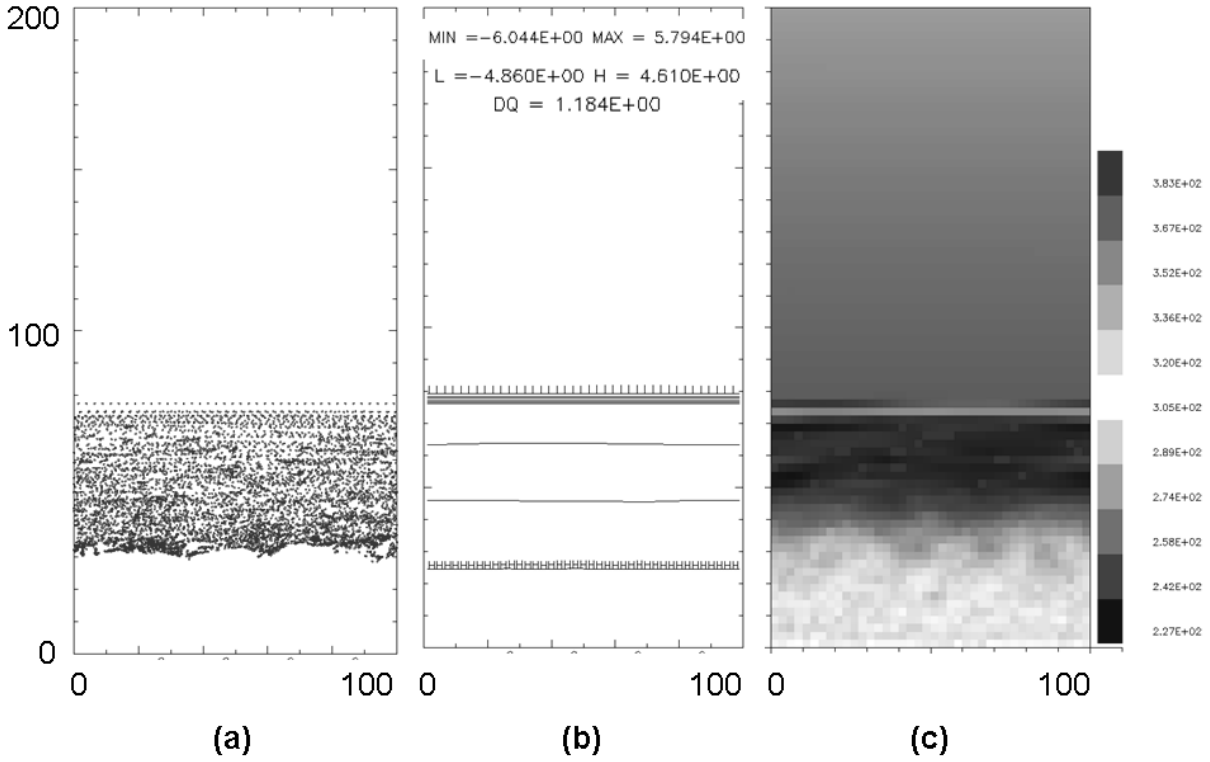

Fig. 3.1-10: Plots showing (a) the positions of injected liquid tracers (fireball spherules), (b) log pressure contours where pressure is measured in bars, and (c) temperature contours in Kelvin after 80 minutes (assuming simple black body thermal radiation) for the distal fireball layer model. Injection angle is 45 degrees and all axes are labeled in kilometers.

Deposits from the ejecta curtain are expected to extend to the intermediate distances (2000-4000 km from Chicxulub) where the double layer is observed. Thus, we employed an initial brief injection of terrestrial ejecta into our model atmosphere in addition to the more prolonged flux of fireball material. The compression of the atmosphere by the terrestrial material alters the structure of the atmosphere causing the fireball material to fall separately and resulting in the deposition of two distinct layers. Deposition of the lower terrestrial layer on the ground begins at ~ 80 minutes and that of the upper fireball layer begins at ~ 130 minutes.

In conclusion, results from KFIX-LPL models suggest that the influx of distal ejecta spherules into the upper atmosphere following the K/T impact event compressed the upper atmosphere, disrupted the normal pressure gradient, and heated the atmosphere at an altitude ~ 50 km,

causing expansion of the lower atmosphere. It has been proposed that thermal energy radiated from ejecta reentering the atmosphere caused global wildfires and our models, which include thermal radiation, provide support for significant atmospheric heating. Such extreme changes to the atmosphere also explain the deposition of the vapor plume and ejecta curtain material as two distinct layers at intermediate distances from Chicxulub and our models suggest that deposition of both layers occurred over a timescale of hours.

3.2 Geochemistry

The Earth is a dynamic planet where chemical elements are constantly in flux as they exchange and cycle between reservoirs both at the surface and in the deep interior. Many of the contributions in this section are aimed at understanding the processes of chemical differentiation that take place as elements move between these reservoirs both in the present day Earth and during its formation. Most meteorite samples, on the other hand, have remained cold and isolated in space and have not undergone fractionation events since their formation. They are time capsules that preserve evidence of processes that occurred during the early history of the solar system. The first contribution in this section, however, goes one step further back in time even than this, as it details the search for evidence of short-lived isotopes in meteorite samples, which can shed light on pre-solar system history. As such isotopes decay rapidly only the daughter products can now be identified, but their identity can yield information on the nuclear processes that took place in the expired stars that produced all elements heavier than hydrogen in the solar system. An important requisite for the correct interpretation in any radiogenic isotope study is that the decay constant is accurately known. A critical evaluation of the effect of pressure on the decay constant of ^{7}Be can be found in the subsequent contribution.

The following six contributions in this section focus on experimental studies performed to understand the composition of the Earth's core. Two of these deal with the partitioning of highly siderophile elements between the mantle and core and between the solid inner and liquid outer core. Highly siderophile elements strongly partition into metallic Fe over silicates but a question remains as to why the concentrations of highly siderophile elements in the Earth's mantle are quite as high as they are. An experimentally testable possibility is that these concentrations reflect metal-silicate partitioning at high pressures and temperatures. Three contributions deal with the nature of the 10 % light-alloying element(s), which are known to exist in the outer core from geophysical constraints. Experiments on oxygen and carbon reactions with Fe-metal at high pressure and temperature are extremely challenging and benefit from the support of thermodynamic models that can then be refined and used to extrapolate the results to the extreme conditions that prevailed during core formation.

The processes that lead to the formation of diamond in the mantle are the focus of two reports this year. It has been recently recognised that while many diamonds form in the upper regions of the Earth's mantle *i.e.*, the lithosphere, some appear to have formed at much deeper levels. Clues to the formation of diamond can be gained by studying trace element fractionation between the melts from which diamonds likely formed and mineral inclusions trapped inside diamonds. Similarly, studying the fractionation of stable carbon isotopes during diamond formation may also help to constrain the processes.

A recurrent theme in several of the reports is the importance of identifying the host mineral in the mantle for a particular minor or trace element. Such studies are crucial when it comes to

understanding the fractionation of elements during melting processes. One study for example examines whether a high-pressure form of rutile (TiO_2) might cause fractionation of the elements Nb and Ta in the mantle and thus explain why Nb seems to be depleted in comparison to Ta in many mantle rocks. Changes in element oxidation state can also lead to quite different geochemical behaviour during the melting and crystallisation of rocks. The challenge for petrology is in refining techniques that can analyse element oxidation states on the grain scale, where most of the important information is recorded during these processes. Advances in these techniques detailed towards the end of this section give us a better understanding of the redox state that prevails in the mantle and crust, particularly during fractionation events.

a. *Search for extinct ^{36}Cl in a Ca- and Al-rich inclusion from the Vigarano carbonaceous chondrite (D. Nakashima and U. Ott/Mainz, in collaboration with A. El Goresy)*

Now extinct short-lived radionuclides with half lives of 10^5 to 10^8 years may serve as sensitive chronometers and tracers for processes in the early solar system and can provide constraints for models of nucleosynthesis. Radioactive ^{36}Cl ($T_{½} = 3\times10^5$ years) has been suspected to be extant in the early solar system. Its actual detection, however, has proven to be difficult. Part of the problem is that Cl-rich phases such as sodalite tend to be alteration products rather than primary phases and that the decay of ^{36}Cl primarily leads to volatile ^{36}Ar. There has been no clear evidence about ^{36}Ar excesses induced by ^{36}Cl decay in sodalite in Ca- and Al-rich inclusions (CAIs; presumably the first solids in the solar system), which may be due to ^{36}Ar loss. Although only 1.9 % of decays lead to ^{36}S, it was found that ^{36}S excesses correlate with Cl/S in sodalites from a CAI in the Ningqiang meteorite, corresponding to $^{36}Cl/^{35}Cl \sim 5\times10^{-6}$ at the time of sodalite formation. A similar ratio was found in sodalites in the Pink Angel CAI from the Allende meteorite. On the other hand, we ourselves found no evidence for extinct ^{36}Cl in our study of another fine-grained Allende CAI.

Continuing this work, we searched for sodalite in a CAI from the Vigarano carbonaceous chondrite by using a field emission SEM at BGI. The CAI consists mainly of coarse-grained gehlenitic melilite (20-100 μm) and is rimmed by monomineralic layers of, from inside outward, spinel (~ 10 μm wide), fassaite (~ 2 μm wide), and diopside (~ 8 μm wide). Sodalite and nepheline grains (5-20 μm) occur as mixtures along cracks within melilite (Fig. 3.2-1a) and probably formed from melilite via reaction with nebular gases bearing Na, K, and Cl.

The Cl and S isotopic analysis in the sodalite grains were performed with the NanoSIMS at Mainz, which has a high lateral resolution and high sensitivity. Sulfur isotopes 32, 34, and 36 as well as ^{37}Cl were measured in multicollection ion counting as negative ions produced by a Cs^+ primary beam of ~ 25 pA (~ 1 μm in diameter). Obtained $^{37}Cl/^{34}S$ ratios were converted

into $^{35}Cl/^{34}S$ ratios using a ratio of 3.13 for the $^{35}Cl/^{37}Cl$. Mundrabilla troilite and FeS grains neighboring the CAI were used as standards.

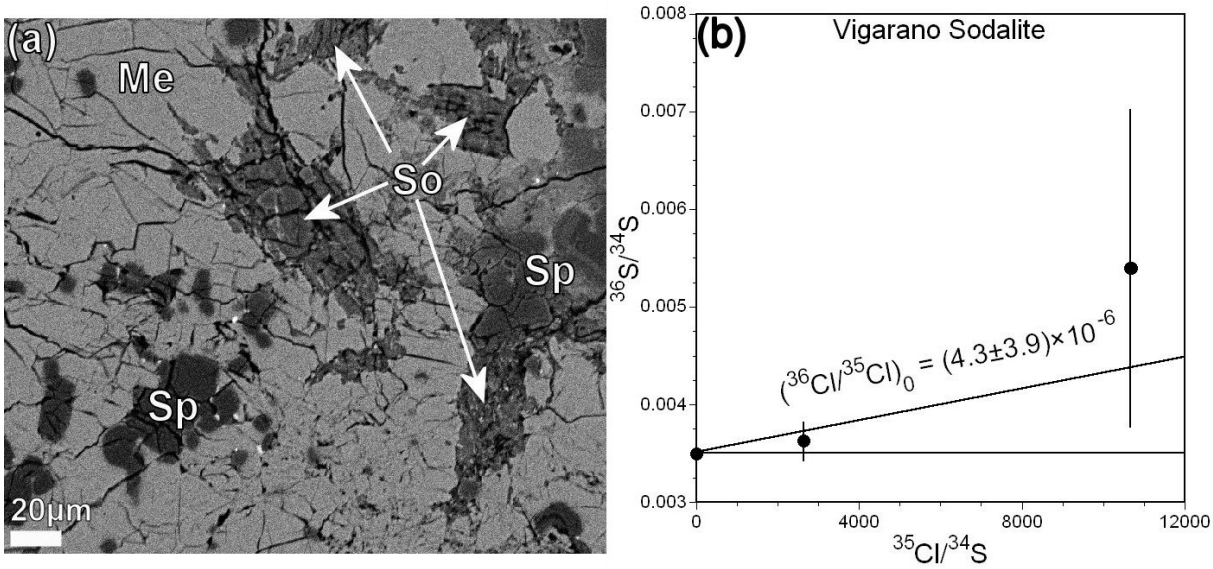

Fig. 3.2-1: (a) Back-scattered electron image of the Vigarano CAI, showing melilite (Me), spinel (Sp), and sodalite (So). Sodalite occurs as an alteration phase mixed with nepheline. (b) Plot of $^{36}S/^{34}S$ vs. $^{35}Cl/^{34}S$. The horizontal line corresponds to normal $^{36}S/^{34}S$ as deduced from standards ($^{35}Cl/^{34}S \sim 0$). A weighted fit line yields a $^{36}Cl/^{35}Cl$ ratio of $(4.3\pm3.9)\times10^{-6}$.

Most of the data have comparably low $^{35}Cl/^{34}S$ ratios (~ 3000). Some show ^{36}S excesses. Only one datum has a high $^{35}Cl/^{34}S$ ratio (~ 10000) and shows a large ^{36}S excess, however, with a large error. The ^{36}S excesses suggest that at least some of the sodalite grains in the Vigarano CAI formed while ^{36}Cl was alive. However, considering the data showing no ^{36}S excess, sodalite formation may have occurred also after ^{36}Cl extinction. It is also possible that ^{36}Cl-^{36}S system in sodalite was disturbed by later parent body processes. Except for the datum showing a high $^{35}Cl/^{34}S$ ratio, the data were combined into a single data point (Fig. 3.2-1b). A weighted fit yields $^{36}Cl/^{35}Cl = (4.3\pm3.9)\times10^{-6}$ (Fig. 3.2-1b), which is comparable with the previous results but with a very large error. The $^{36}Cl/^{35}Cl$ ratio corresponds to the value at the time of sodalite formation. Based on the time interval between sodalite formation and CAI formation ($\geq 1.5\times10^6$ years estimated from ^{26}Al-^{26}Mg systems), the $(^{36}Cl/^{35}Cl)_0$ ratio at CAI formation is deduced to be $\geq 1.6\times10^{-4}$. Then, the following questions arise: What is the origin of ^{36}Cl? Where did the alteration leading to sodalite formation occur?

Origin of ^{36}Cl: There are three possible origins of ^{36}Cl; supernovae (SN), asymptotic giant branch (AGB) stars, and spallation reactions by energetic particle bombardment by the active early sun. The $(^{36}Cl/^{35}Cl)_0$ ratio ($\geq 1.6\times10^{-4}$) is too high to be produced by SN or AGB stars. It is likely that ^{36}Cl was produced by spallation reactions by energetic particle bombardment by the active early sun, which is also important for ^{10}Be. However, ^{10}Be is observed in all CAIs

studied in roughly equal abundance, whereas our results suggest that ^{36}Cl abundance appears to be variable. A larger database for ^{36}Cl is required to establish its relation to other radionuclides.

Sodalite formation location: An early study on the Allende meteorite came to the conclusion that sodalite probably formed in the nebula, as no sodalite grains were found in the matrix surrounding the Pink Angel CAI. However, in our previous studies, we found numerous sodalite grains in the Allende matrix, which may argue for parent body alteration instead. In the case of Vigarano, CAI fragments next to the sodalite bearing CAI do not contain sodalite. If alteration occurred after fragmentation, all the CAI fragments should contain sodalite. It is therefore likely that Vigarano sodalite formed before CAI fragmentation. Since the fragmentation should have occurred on the parent body, Vigarano sodalite may have formed in the nebula. Thus, multiple alteration episodes need to be considered.

b. *Ab-initio predictions of pressure- and chemistry-dependent electron-capture radioactive decay of ^{7}Be (K.K.M. Lee, in collaboration with G. Steinle-Neumann)*

Radioactivity plays a central role in planetary science as appropriate decay schemes are used to date geological and astronomical processes at all time and length scales. Additionally, radioactivity provides an important source of heat in planetary bodies. Since radioactive decay is a nuclear process, it is often considered to be insensitive to external factors, such as ionization, temperature, pressure, or chemical environment. This is due to the screening provided by the orbital electrons surrounding the nucleus and has been shown to be essentially true for α and positive and negative β decays. However, for electron-capture processes, external forces can influence the stability of an unstable nuclide because the decay rate is directly related to the electron density at the nucleus.

The electron-capture decay constant ($\lambda_{ec} = \ln 2/\tau_{1/2,ec}$, where $\tau_{1/2,ec}$ is the electron-capture half-life) is proportional to the total electron charge density ρ_e at the nucleus. Thus any external effects that disturb the total electron density at the nucleus will perturb the electron capture rate, thereby changing the value of the isotope's half-life. The change in electron-capture decay constant, $\delta\lambda_{ec}$ is described as:

$$\delta\lambda_{ec} = \left| \frac{\rho_e}{\rho_{e,ref}} - 1 \right| \lambda_{ec,ref} \qquad (1)$$

where $\lambda_{ec,ref}$ is the reference decay constant for electron-capture decays and $\rho_{e,ref}$ is the corresponding charge density, *i.e.*, at zero pressure.

Here we investigate the change in decay constant for the electron-capture ^{7}Be decay due to pressure and chemistry by means of ab-initio computations of the electron charge density at

the nucleus as for Be metal, oxide and chloride. In order to accurately model the electronic charge density ρ_e, we employ state-of-the-art all-electron first-principles computations. We use the linearized augmented plane wave (LAPW) method with an atomic like orbital basis set around the nuclei, as implemented in the Wien2k package.

^{7}Be is naturally produced by cosmic ray bombardment of atmospheric nitrogen and oxygen and decays completely by electron capture to ^{7}Li with a $\tau_{1/2}$ of ~ 53.3 days. Once formed, ^{7}Be is removed from the atmosphere and is incorporated into forming sedimentary material and water. The short half-life, rapid removal from the atmosphere and affinity for the sediments make this nuclide useful in determining recent sediment formation.

A rather large effect on λ_{ec} for different environments is expected for ^{7}Be due to its few electrons that prohibits much electronic shielding of the nucleus. Indeed ^{7}Be has been shown to exhibit changes up to ~ 1.5 % in decay constant for chemically different compounds, including Be, $Be(OH_2)_4^{2+}$, BeO and BeF_2, with $\lambda_{ec}[Be(OH_2)_4^{2+}]<\lambda_{ec}[Be]\leq \lambda_{ec}[BeO]< \lambda_{ec}[BeF_2]$. Additionally, some computational studies have also predicted a decrease in half-life of ^{7}Be with the application of pressure and measured up to ~ 1 % decrease in the half-life with the application of a pressure of ~ 40 GPa.

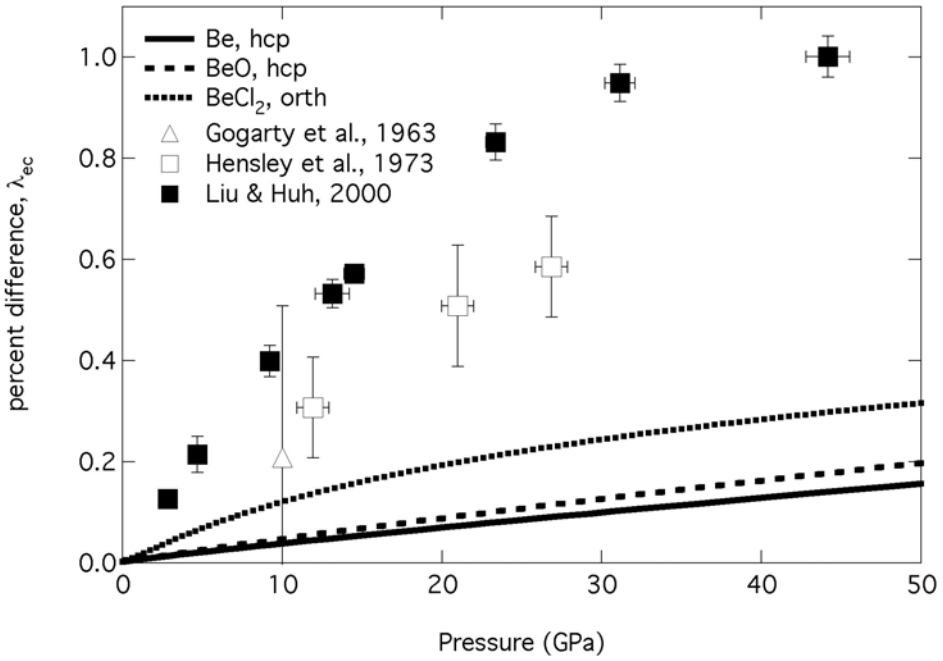

Fig. 3.2-2: Percent change λ_{ec} for hcp Be (solid line), BeO (dashed line) and $BeCl_2$ (dotted line). An increase in the decay constant λ_{ec} corresponds to a decrease in the half-life $\tau_{1/2,ec}$. Each percent difference in λ_{ec} is referenced from the zero pressure $\lambda_{ec,0}$ for either Be, BeO or $BeCl_2$ respectively. To compare, experimental determination of the change in λ_{ec} is shown for $BeCO_3 \cdot Be(OH)_2$ (triangle, Gogarty *et al.*, in *Office of Naval Research Technical Report No. VII*, 1963), BeO (open squares, Hensley *et al.*, *Science*, *181*, 1164, 1973), and $Be(OH)_2$ (full squares, Liu & Huh, *EPSL*, *180*, 163, 2000).

We have computed the charge density ρ_e of Be, BeO, and $BeCl_2$ in low- and high-pressure crystal structures where known (Fig. 3.2-2), and have evaluated the change in electron capture decay constant both with chemical form and pressure. For changes in the chemical environment we find that total differences are within ~ 0.15 %, with the order $\lambda_{ec}[BeO] \leq \lambda_{ec}[Be] < \lambda_{ec}[BeCl_2]$, where the difference between Be and BeO is less than 0.03 %. While the order is somewhat different from the experiments, it is consistent with previous density functional based computations. The fact that the small differences in decay constants between the various chemical forms are predicted with reasonable accuracy give confidence for the prediction of pressure induced changes. Over a pressure range of 50 GPa both Be and BeO exhibit an increase in λ_{ec} of ~ 0.2 %. For $BeCl_2$ we predict a slightly stronger effect with an ~ 0.3 % increase in λ_{ec} at 50 GPa. The increase is consistent with previous experimental measurements on crystalline BeO and $Be(OH)_2$ gel, our predicted values are, however, smaller by a factor of 2-6. Our results confirm previous computations that have raised doubts about the experiments.

c. *How much potassium is in the Earth's core? (A. Corgne/Sydney, S. Keshav, Y. Fei/ Washington DC and W. McDonough/College Park)*

The Earth's magnetic field is generated by a dynamo process that is maintained by a constant motion of the electrically highly conducting fluid of the outer core. A significant amount of the energy, required to drive Earth's magnetic field, comes from the latent heat of crystallization of the inner core and from the gravitational energy released by the production of a buoyant residual liquid caused by exclusion of a light element component from the solid inner core. Although the basic mechanisms of magnetic field generation are apparently understood, there remain three important unanswered questions: (1) How much power is required to sustain the geodynamo? (2) Is an inner core required to establish a geodynamo? (3) Is a radioactive energy source in the core needed? Accurately describing the power requirement of the geodynamo depends on an accurate estimate of the core's ohmic dissipation (D_{ohm}, loss due to electrical resistance), for which recent estimates give a wide range of values, from 0.1 to 3.5 TW. Thermal modelling predicts an inner core age of ~ 4 Ga for D_{ohm} = 0.1 TW and less than 1 Ga for D_{ohm} = 3.5 TW. The observation of a geomagnetic field of roughly present-day strength in rocks as old as 3.5 Ga would thus be consistent with low power consumption of the geodynamo. However, major disagreements have emerged between low- and high-dissipation based theories because of uncertainties in the different physical parameters involved. Standard models of Earth's thermal history have difficulty explaining how the inner core has existed for more than 1-2 Ga or so. Driving a dynamo without an inner core seems difficult. It would require the heat flux, hence the ohmic dissipation, to be high enough to allow the necessary convection, but not too high to prevent the core from freezing too quickly. Alternative heat sources could have slowed down the growth of the inner core and reduce the demands on primordial heat.

One possibility is for the core to have sequestered a significant amount of radioactive elements such as K, U, and Th. These three elements are generally considered lithophile and are not predicted to have an affinity for core forming materials. U and Th have estimated concentrations, absolute and relative, in the bulk silicate Earth (BSE) that are consistent with the chemical budget of the Earth if it is assumed to be of chondritic composition. Hence, this estimate leaves little room to store U and Th in the Earth's core. In contrast to U and Th, K is depleted in the silicate Earth relative to CI-chondrite (on an anhydrous basis) by about 80 %. This has been generally interpreted as a result of significant volatilization in the solar nebula prior to Earth's accretion. This argument has also been proposed to explain the depletion of Li, B, Na, Rb, F, Zn, and Ga. Most of these elements plot on a single trend, known as the volatility trend. One should ask the question whether K, which plots on the low side of the volatility trend, becomes siderophile or chalcophile (assuming S is present in the core) at high temperatures and/or high pressures.

Here, we report results of silicate melt-liquid alloy partitioning experiments of K to 2200 ºC and 7.7 GPa (corresponding to depths of ~ 250 km deep in the Earth) on a model CI-chondrite composition relevant to model bulk Earth's differentiation. The data reported here for potassium (K) between chondritic silicate melt and Fe-Ni-S-C-O molten alloy at 1650-2200 °C and 1.0-7.7 GPa reveal a negligible effect of pressure on K partitioning, at least up to 7.7 GPa. No evidence for a systematic increase of K solubility in the alloy with temperature or pressure and S or C contents in the alloy was found. Having said that, there appears to be possible increase in the K partition coefficient with increasing O content in the molten alloy; however, this relationship is not very clear at present, and hence, should be considered, at best tentative. Our results, which are appropriate to model core formation in a shallow magma ocean, suggest it is unlikely to sequester even a few tens of ppm of K into Earth's core during a magma ocean event.

d. *Core-mantle exchange: experimentally determined fractionation of Re-Os-Pt in sulphur-bearing solid/molten iron metal at 3.3-22 GPa and 1300-1775 °C (S. Keshav, in collaboration with J.A. Van Orman/Cleveland and Y. Fei/ Washington DC)*

Coupled enrichments of $^{186}Os/^{188}Os$ and $^{187}Os/^{188}Os$ in mantle-derived materials have been suggested to reflect material contributions from the outer core. This process requires significant fractionation of Pt, Re and Os during crystallization of the inner core; and because the inner core is small, differences in solid/liquid metal partition coefficients among these elements must be large. The exchange is proposed to be a consequence of fractionation of different siderophile elements between solid (inner core) and molten iron (outer core) metal, and thus the parameters influencing this fractionation, are the most crucial to understand the above mentioned chemical exchange. To this end, we report partitioning ($D_{solid\text{-}metal/liquid\text{-}metal}$) of Re, Os, and Pt between sulphur-bearing solid and liquid iron metal at 3.3-22 GPa and

1300-1775 °C in the iron rich portion of the Fe-S system. Pressure and temperature, besides the bulk composition, are perhaps important factors in controlling the partitioning systematics, and experiments were designed to cover a wide, and so far the largest pressure and temperature range.

The experiments were performed in split-cylinder multianvil modules and concentrations of Fe, S, Re, Os, and Pt in the run products were obtained using electron microprobe. To ensure bulk homogeneity, each experimental charge was taken above the total melt region in the relevant portion of the Fe-S phase diagram, and was kept there for at least 15-30 mins. By varying the temperature of the experiments, molten iron metal with different (9-20 wt.%) sulphur contents, within the range proposed to be in the Earth's outer core, could be produced. Analyses were performed within 10-15 μm of the interface between solid and quenched liquid metal. At a constant pressure, the partition coefficients show a strong, positive dependence on the sulphur content of the metallic liquid, suggesting a very strong effect of dilutant on the partitioning systematics.

Significantly, even though it is necessary to know the absolute D values, it is the moderate to strong fractionation of Pt and Re from Os required in the geochemical models that call for isotopic and elemental transfer from the Earth's outer core to the silicate mantle. The experimental data have been parameterised, in order to isolate the effects pressure might have on partitioning and relative fractionation between Re, Os, and Pt. For a constant liquid composition, the partition coefficients for all three elements decrease significantly with increasing pressure. The relative values and pressure dependences of the partition coefficients are consistent with elastic strain considerations. At the maximum light element concentration in the outer core (~ 10 wt.%) and pressures beyond, Os, Re and Pt are insufficiently compatible in solid iron to be fractionated significantly by inner core crystallization. From these results it is also clear that at a given sulphur content in the liquid metal, both D_{Os}-D_{Pt} and D_{Os}-D_{Re}, parameters that indicate fractionation expressed as differences in partition coefficients and thus mimicking fractional crystallization, decrease with increasing pressure. The results above are exactly the opposite to what is envisaged in almost all the geochemical models that call for a core contribution in lavas from the Earth's mantle. Hence, an outer core, Os isotopic component in basaltic lavas is questioned. In our view, possible future endeavours to more critically address the Os signals should focus on cautiously pushing the limits of the multianvil modules to higher pressures by using sintered diamond cubes.

e. *Constraints on core formation in terrestrial planets from the HP-HT partitioning behaviour of the highly siderophile elements (Ru, Rh, Pd, Re, Ir, Pt) (U. Mann, D.J. Frost, A. Audétat and D.C. Rubie, in collaboration with H. Becker/Berlin)*

The term 'highly siderophile' for the platinum group elements (Ru, Rh, Pd, Os, Ir, Pt) and Re categorizes their geochemical character observed in 1 atm partitioning experiments, which is

extremely metal loving. As a consequence, these elements have metal-silicate partition coefficients of > 10^4. Therefore one would expect them to be completely stripped from a molten silicate mantle equilibrating with a molten metal phase forming the core of a planetary body. However, in today's Earth's mantle low concentrations of these highly siderophile elements (HSE) are present. This overabundance as well as the fact that they occur in roughly chondritic abundances relative to each other cannot be achieved by low P (1 bar) and moderate T (1300-1550 °C) metal-silicate equilibration. A plausible core-formation hypothesis should be able to explain the observed HSE abundance patterns in the Earth's mantle. Many recent studies have proposed that core-mantle equilibration at high pressures and temperatures may explain the mantle abundances of many siderophile elements. There is currently too little data to assess whether mantle HSE abundances can also be explained in this way. The aim of this study is to evaluate accretion scenarios for the Earth's by studying the metal-silicate partitioning of the HSE over a range of high pressures (> 2 - 25 GPa), high temperatures (> 2000 °C) and redox conditions and employing a peridotitic composition for the silicate phase.

Liquid metal liquid silicate partitioning experiments for the highly siderophile elements Ru, Rh, Pd, Re, Ir and Pt have been performed at 2200 °C and at high pressures of 6 and 18 GPa using a multianvil apparatus. As starting material we employed powders comprising a mixture of 60 wt.% silicate (primitive mantle [PM] composition with FeO ~ 8 wt.%) and 40 wt.% of metal (metallic Fe and HSE). In order to provide relatively oxidising conditions in our initial experiments, two different Fe/HSE proportions with 75 wt.% and 90 wt.% HSE were chosen. The individual HSEs were present in equal proportions. The samples were run in MgO single crystal capsules employing run times of 70 - 90 s. In the experiments both silicate and Fe-HSE alloy were molten such that equilibration should have been very rapid.

In the run products the quenched liquid metal is separated from the silicate phase forming several spheres varying in number and size. A typical example is shown in Fig. 3.2-3a. The metallic liquid quenches to a polycrystalline aggregate displaying various coarse textures (2 - 50 μm scale) including dendritic crystals and zoned grains. Quench crystals also form from the silicate melt (Fig. 3.2-3a, b). The back scattered electron (BSE) image of Fig. 3.2-3b shows the texture of a run product recovered from 6 GPa, which is dominated by very large skeletal forsterite crystals. The interstitial spaces show a brighter silicate phase in the centre and a metallic phase accumulated on the surface of the forsterite crystals. We interpret this as a quench phenomenon and therefore assume that this metal had been dissolved in the silicate melt previous to quench. The disadvantage of using MgO capsules is the reaction of MgO with the silicate sample material. Small patches of MgO can be found between the silicate quench crystals and in some places an MgO envelope started forming around some of the metal blebs (Fig. 3.2-3). However, as it is not entirely enclosing the metal equilibration between silicate and metal phase was not prevented.

The metal phase was analysed with an electron microprobe. To account for the coarse quench textures a defocused electron beam (10 - 30 μm) was used and the single analysis points were set along rectangular grids with some overlap of the excited areas. In order to accurately

measure the extremely low concentrations of the HSE in the quenched silicate melt, analyses were carried out with the new LA-ICP-MS facility at BGI. Due to a lack of appropriate standards for analysing HSE-bearing silicates we synthesized silicate glass standards of eutectic diopside-anorthite bulk composition doped with Ru, Rh, Pd, Re, Ir and Pt in the range of 4-120 ppm. The HSE concentrations of the standard glasses were determined by isotope dilution ICP-MS analysis in cooperation with Prof. H. Becker at the Freie Universität in Berlin. Additionally we employed NIST 610 glass as an external standard for Fe, Ti, Mn and Cr. To account for the coarse quench textures (Fig. 3.2-3b) a spot size of 70 µm was employed.

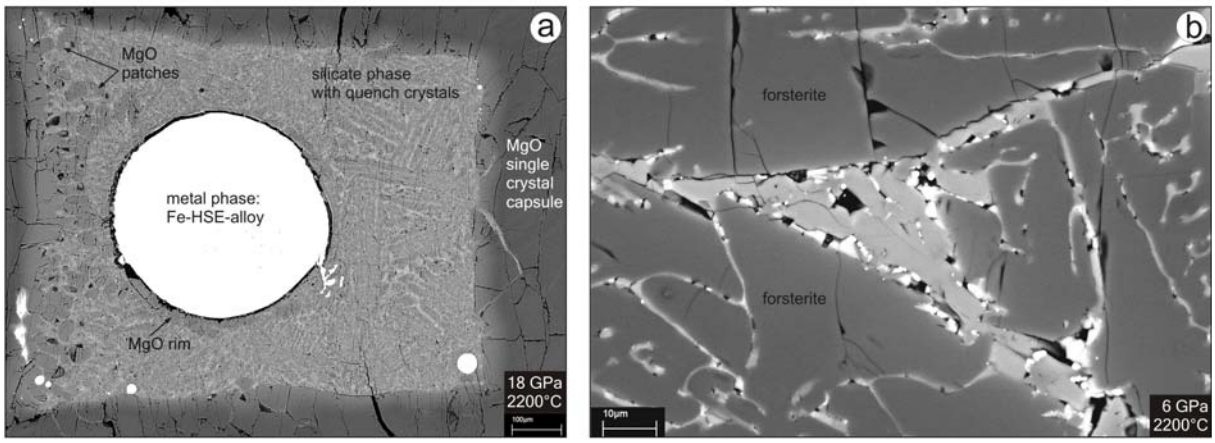

Fig 3.2-3: BSE images of typical run products of the liquid metal - liquid silicate partitioning experiments. a) The metal phase has separated forming a sphere; the silicate phase has crystallized on quenching. MgO from the single crystal capsule starts dissolving in the silicate phase and forms a discontinuous rim around the big metal bleb. b) Detail of the quenched silicate phase showing an interstitial pocket between large skeletal forsterite crystals (6 GPa, 2200 °C). The white phase is metal that was most likely dissolved in the silicate phase.

In Figure 3.2-4 the logarithmic values of the Ru, Rh, Pd, Re, Ir and Pt metal- silicate concentration ratios (D) at 2200 °C and at an oxygen fugacity of 2.3 log units above the Fe-FeO equilibrium (Δ IW +2.3) are plotted as a function of pressure. The solubility in the silicate melt is highest for Pd and lowest for Ir at both pressures. Except for Ir, the proportion of all elements in the silicate melt increases with increasing P, which is most distinct for Pd, Rh and Ru. When compared to the 1 bar partition coefficients calculated for Rh and Pt from literature data, pressure seems to decrease the partition coefficients by more than one order of magnitude. Moreover, with the exception of Pd the difference between the HSE partition coefficients is much smaller at both 6 and 18 GPa compared to the 1 bar values for Pt and Rh, which differ by two orders of magnitude. Even though the redox conditions of this study are relatively high, we might expect a similar pressure effect at an oxygen fugacity more realistic for core formation. These data imply, therefore, that in general there is some tendency for HSE to become less siderophile with increasing pressure.

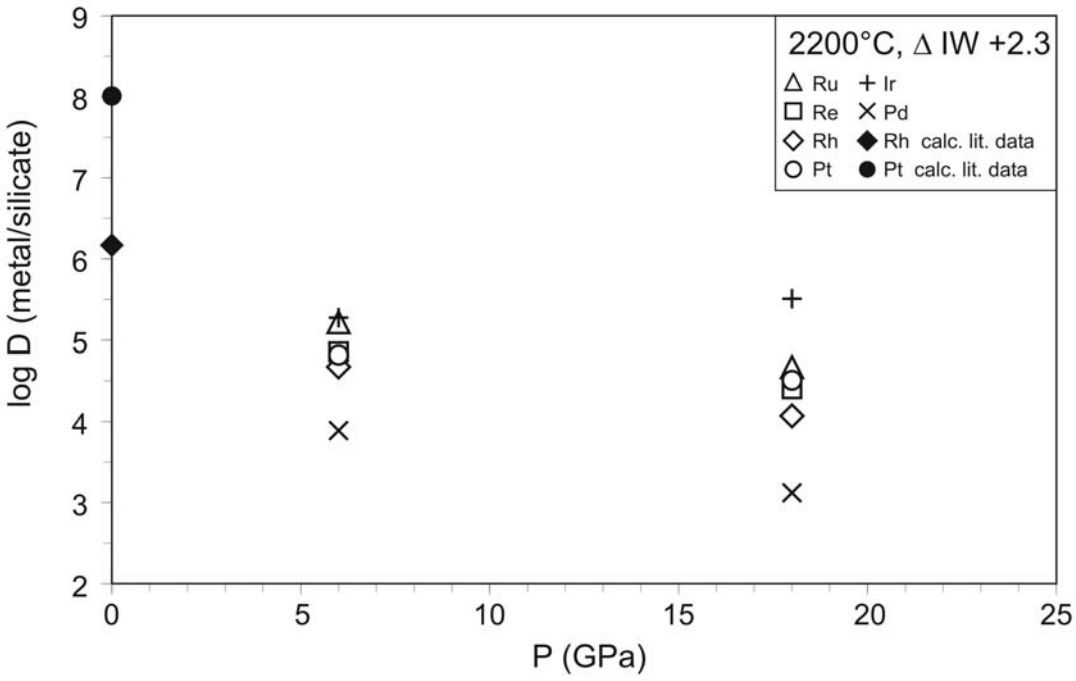

Fig 3.2-4: Logarithmic values of the Ru, Rh, Pd, Re, Ir and Pt metal- silicate concentration ratios (D) plotted against pressure (P) at 2200 °C and 2.3 log units above the iron-wüstite buffer (Δ IW +2.3). Data for Rh and Pt at 1 bar are calculated from the literature.

f. *The effect of pressure on the miscibility gap between metallic and ionic liquids in the system Fe-O (Y. Asahara/Hyogo, D.J. Frost and D.C Rubie)*

The Earth's outer core is mainly composed of liquid metallic Fe but is also known to contain up to 10 % of a light-alloying element or elements with the most likely candidates being O, Si, and S. For a particular light element to be present in the core it must have been sufficiently abundant during the accretion of the Earth and it must have suitably partitioned between Fe-rich liquid metal and the silicate mantle at the conditions that prevailed during core formation. We have studied extensively the partitioning of oxygen between liquid Fe metal and analogue mantle materials over a range of conditions but in order to build thermodynamic models to accurately extrapolate and interpret these data we need a better understanding of the thermodynamics of oxygen solubility in liquid Fe metal. Such additional fundamental thermodynamic data can be gained by studying the solubility of oxygen in liquid Fe metal in equilibrium with coexisting FeO liquid.

We have performed multianvil experiments to determine the effect of pressure on the miscibility gap between Fe metal and FeO liquid at 2100 °C. Starting materials were ground mixtures of FeO and Fe with varying Fe/O ratios. Two-hole alumina capsules were employed such that two starting materials with different Fe/O ratios could be run in a single experiment to check that consistent results were obtained with the different starting mixtures at identical

conditions. Samples were melted for a few minutes then quenched rapidly and recovered for examination with the electron microprobe and scanning electron microscope.

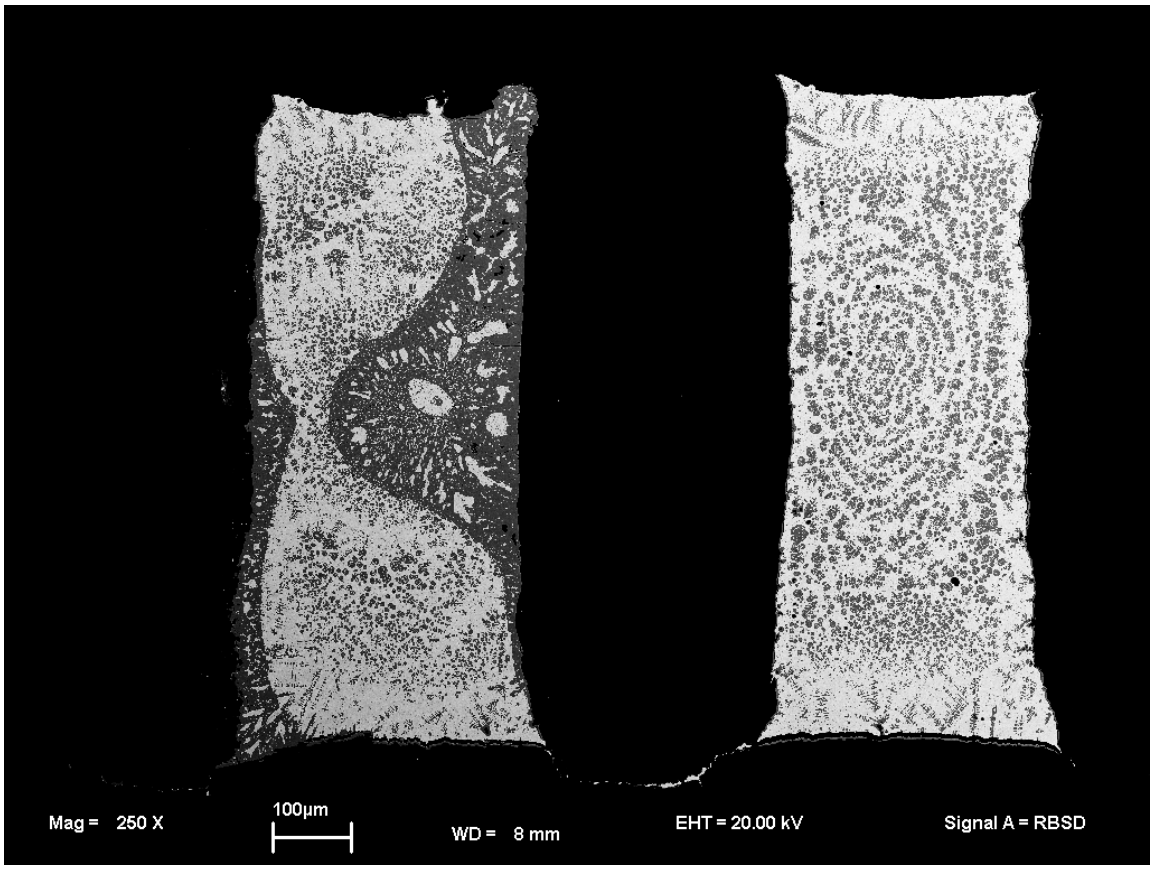

Fig. 3.2-5: Scanning electron microscope images of two samples inside a single alumina capsule from an experiment performed at 20 GPa and 2100 °C. The sample on the left shows a texture consistent with the coexistence of Fe-rich and FeO-rich liquids while that on the right is interpreted to have been entirely Fe-rich liquid at conditions of the experiment.

Typical run products are shown in Fig. 3.2-5. The sample on the left shows an FeO-rich liquid surrounding an Fe-rich liquid forming an hourglass structure. Although major boundaries can be seen between the two liquids significant exsolution occurs from both phases during quenching. FeO exsolves from the Fe metal while Fe metal exsolves from the FeO liquid. The compositions of quench crystals are analyzed in each phase then image analysis is used to integrate the bulk composition of each liquid. Experimental results are shown in Fig. 3.2-6. At 2100 °C the solubility of oxygen in liquid Fe metal stays fairly constant up to approximately 12 GPa but then starts to rise coincident with an increase in the Fe-metal content of the FeO liquid. The miscibility gap between the two liquids would likely close at pressures between 25 and 30 GPa. As the miscibility gap also closes with temperature complete miscibility of Fe and FeO likely also occurs by 2200 °C at 25 GPa. This implies that immiscibility is not likely to be a barrier to oxygen being the light element in the core. These results will be used to

refine thermodynamic data for Fe-O liquids for use in extrapolations to pressures and temperatures higher than those currently feasible in an experiment.

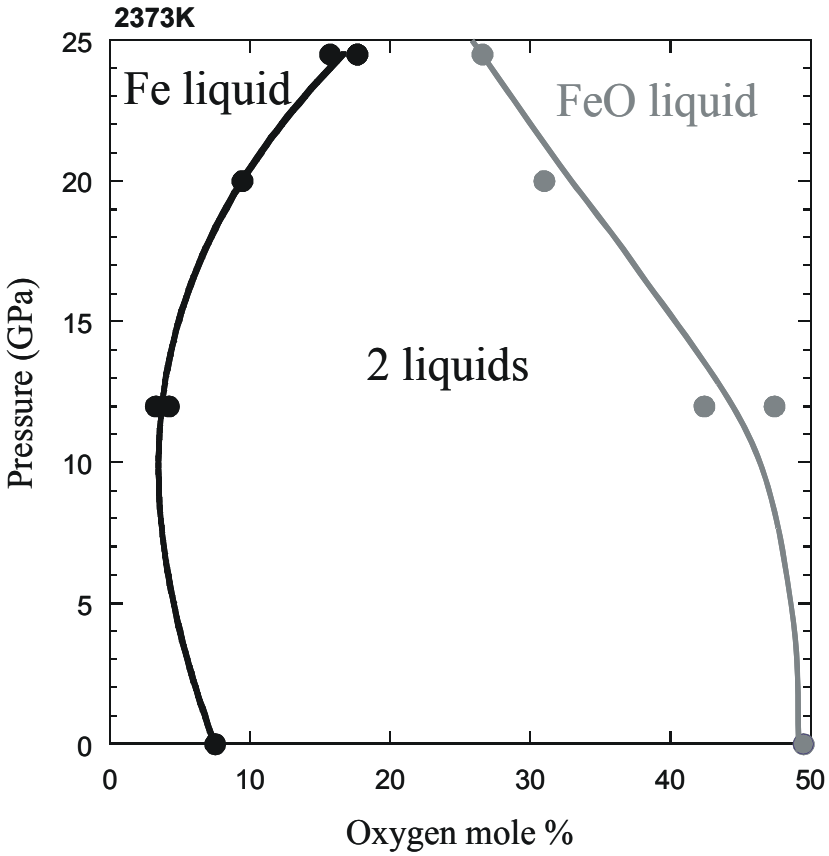

Fig 3.2-6: The coexisting oxygen contents of metallic (Fe-rich) and ionic (FeO-rich) liquids in the system Fe-O as a function of pressure. The miscibility gap between the two liquids closes with pressure such that a single liquid field is probably reached at pressures below 30 GPa at 2373K.

g. *Iron-carbon interactions at high pressures and temperatures (J. Rouquette, D. Dolejš, I.Yu. Kantor, C.A. McCammon, D.J. Frost and L.S. Dubrovinsky)*

Phase relations in the iron-carbon system at one atmosphere have been the subject of a number of investigations for metallurgical applications. This system contains intermediate phases, *e.g.*, Fe_3C (cementite), that are metastable with respect to α-iron and graphite. In nature, Fe_3C (cohenite) occurs as a minor constituent in iron meteorites. At pressures up to 25 GPa and temperatures to 2200K, iron and carbon react and produce several carbides (Fe_3C, Fe_7C_3). Since it has been suggested in the literature that iron carbide may be stable in the Earth's inner core, the physical properties of Fe_3C have been intensely studied. Recent experimental and theoretical investigations on Fe_3C provide new constraints on its geochemical significance. The stability of cementite at high pressures implies incompatibility of the iron-diamond assemblage. On the other hand, the Fe_3C phase has not yet been found in

inclusions in diamonds from the deep mantle; whereas diamond and metallic iron have been observed to coexist. The cementite-diamond relationship has been proposed in the literature as an incongruent transformation, Fe_3C = Fe-rich phase + C, that occurs at 1630 K and 5.3 GPa. In this study, evidence from experiments and thermodynamic calculations (see following contribution by D. Dolejš) is presented for the stability of Fe_3C at high pressures.

For multianvil press (MAP) experiments the starting material, a mixture of ^{57}Fe + C with a molar ratio 3/1 was introduced in a graphite capsule. High-pressure high-temperature experiments were undertaken at approximatly 25 GPa and 2200 K. For diamond anvil cell (DAC) experiments, we used diamonds with 300-250 μm culet size and a Re gasket that was pre-indented to ~ 40-25 μm and then drilled with a 150-125-μm-hole. Powdered samples were loaded (^{57}Fe and/or ^{57}Fe-enriched starting materials) together with ruby under an argon atmosphere to avoid oxidising conditions. Neither NaCl nor any pressure transmitting media were used. Pressures were measured based on the ruby R_1 and R_2 fluorescence lines. Pressure gradients were evaluated to be less than 10 % of the mean reported pressure.

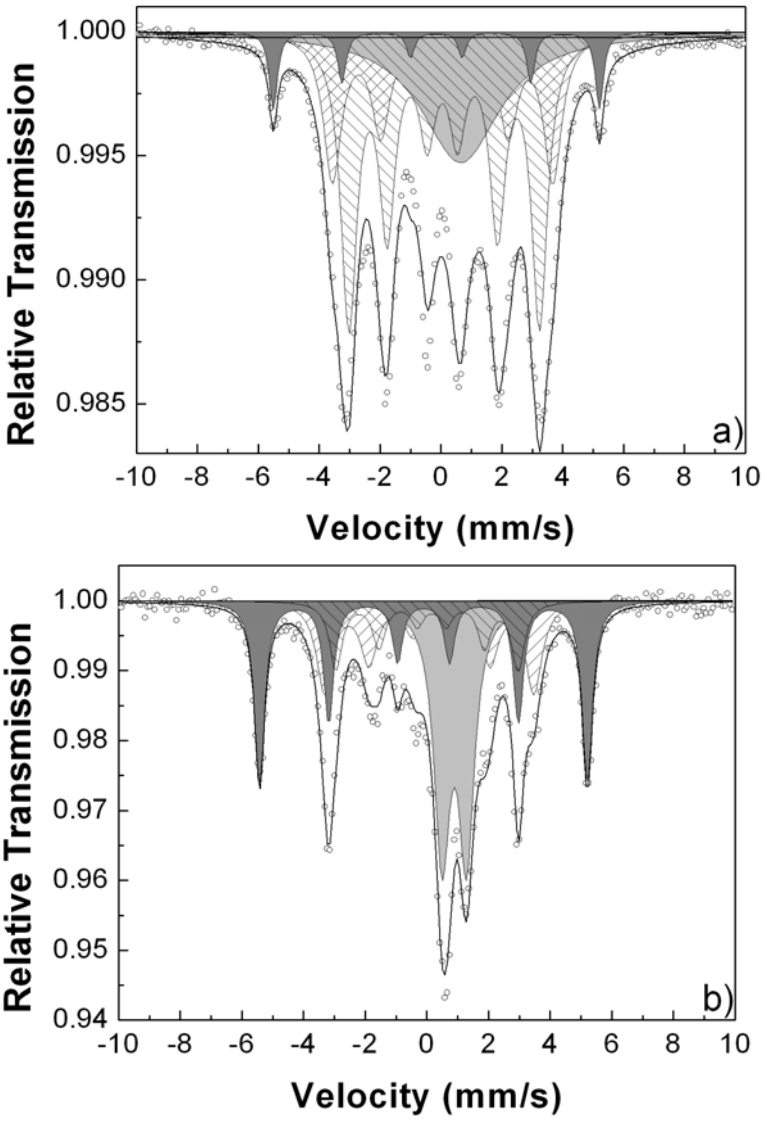

Fig. 3.2-7: Room temperature Mössbauer spectra of the recovered sample from:
a) Fe+C, 25 GPa 2200K (MAP),
b) Fe+$Mg_{0.92}Fe_{0.08}O$, 70 GPa 3400K (DAC).
Components are shaded as follows: metallic iron (dark grey), wüstite or magnesio-wüstite (light grey) and two Fe_3C components (striped in opposite directions).

The Mössbauer spectrum resulting from MAP ^{57}Fe + C synthesis (3/1 ratio) is shown in Fig. 3.2-7a. It was successively fitted using 4 components: one singlet corresponding to octahedral Fe^{2+} in the wüstite form (light grey), one sextet associated to the non-reacting iron (dark grey) and two Fe_3C components (striped in opposite directions). As already proposed in the thermodynamic approach, iron carbide is stable at high pressure high temperature.

Additionally, experiments in the laser-heated DAC using metallic iron as a starting material yielded iron carbide through a reaction between iron and the diamond enclosure (Fig. 3.2-7b). This unusual reactivity between metallic iron and the diamond form of carbon has significant importance for DAC experiments in general, and should be routinely considered in all experiments using iron-based compounds in the laser-heated DAC.

h. *The system Fe-C-O at high pressures: Thermodynamic constraints on carbon occurrence and the redox state in the Earth's interior (D. Dolejš, J. Rouquette and L.S. Dubrovinsky)*

Carbon is a light element in the Earth's interior that is relatively abundant but exhibits negligible solubility in silicate phases. Moreover, it is a potential constituent of the Earth's core that can explain its lower density. Recent studies have revealed progressively reducing nature of the deep mantle and this finding is corroborated by the occurrence of carbon in both carbonate and element form. Under these conditions, intermetallic compounds, Me_xC_y, may become stable and have significant implications for geochemistry of the deep Earth's interior. Intermetallic phases can (1) act as phase divides between iron-rich alloys and diamond, (2) buffer the carbon solubility in iron-rich alloys and liquids, and (3) buffer the mantle redox state.

We present a new thermodynamic model for phase equilibria in the system Fe-C-O. Thermodynamic data for pure solid and liquid phases and mixing properties are based on the SGTE database. Volumetric behaviour is described by the third-order Birch-Murnaghan equation of state utilizing temperature-dependent bulk moduli. Properties of CO and CO_2 end-member fluids are described by the Belonoshko and Saxena (1991, Geochim. Cosmochim. Acta 55, 3191-3208) equation of state, which was calibrated by molecular dynamic simulations to 50 GPa. Excess mixing properties of fluids resulting from attractive and repulsive interactions were estimated from the Lennard-Jones potential. This thermodynamic calibration of solid-liquid-gas equilibria reproduces available experimental data from 1 bar to 5 GPa and it allows us to evaluate high-temperature phase stabilities and compatibilities as a function of pressure and oxygen fugacity.

The system Fe-C is characterized by several intermediate compounds (Fe_3C, Fe_7C_3, Fe_5C_2 etc.) but none of them are stable at 298.15 K and 1 bar. Cementite, Fe_3C, occurs above 730 °C at 1 bar and its stability field significantly expands with increasing pressure. Stable Fe_3C represents a divide between iron-rich alloys and carbon polymorphs. That is, iron-rich alloys

and diamond are not compatible at high-pressure subliquidus conditions. This behaviour is a consequence of the volume change for the equilibrium $Fe_3C(s) = Fe_3C(l)$ and, more importantly, of the relatively low bulk modulus of cementite (174 GPa) in comparison to that of iron and diamond. The relatively high compressibility of Fe_3C appears to exert a major control on its stability in the Earth's interior.

Figure 3.2-8 shows phase diagrams for the Fe_3C-bulk composition at 1 bar and 25 GPa, respectively, with increasing oxygen fugacity. At 1 bar, cementite melts incongruently to produce iron-rich liquid saturated with graphite. Oxidation of cementite leads to several different assemblages depending on temperature: wüstite + graphite (below ~ 770 °C), iron-rich alloy + CO_{1-2}-fluid (770-1050 °C), and iron-rich melt + CO_{1-2}-fluid. At 1 bar, the stability of Fe_3C requires strongly reducing conditions, up to 7 log units below the iron-wüstite buffer. At 25 GPa, cementite is stable over the entire temperature range (500-3500 °C) and its oxidation leads to the formation of wüstite and diamond. The ternary assemblage cementite, wüstite and diamond represents the lowest attainable oxygen fugacity and it is located 2 log units above the iron-wüstite buffer.

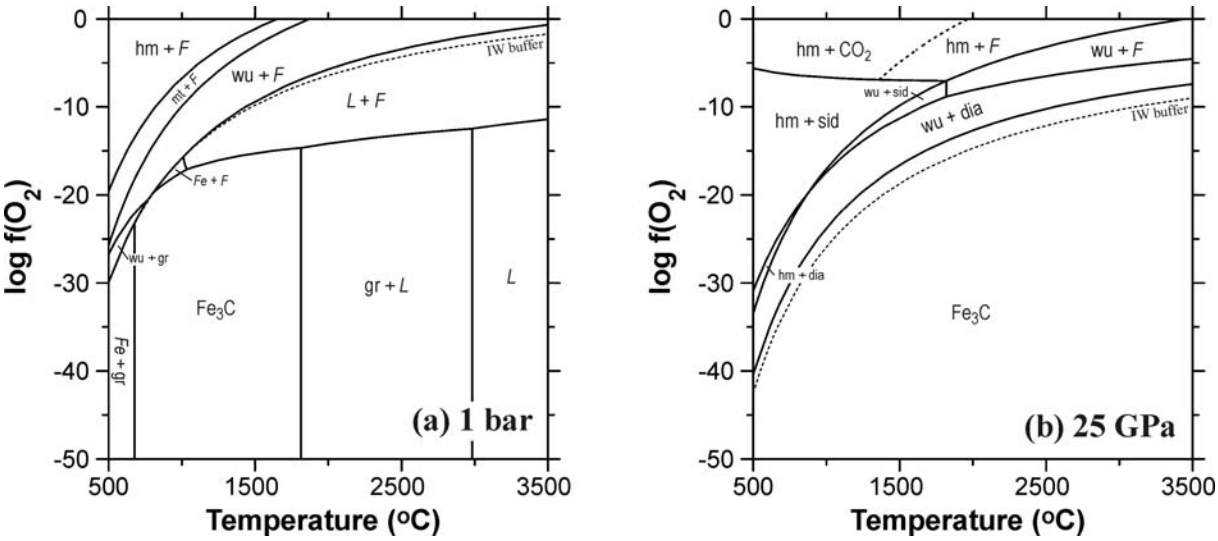

Fig. 3.2-8: Temperature-log $f(O_2)$ diagrams at (a) 1 bar and (b) 25 GPa. Abbreviations: gr – graphite, dia – diamond, wu – wüstite, mt – magnetite, hm – hematite, sid – siderite, *L* – (Fe,C)-liquid, *F* – CO_{1-2}-fluid. Phases shown in italic face are solutions. Liquid becomes rich in carbon with increasing temperature. Fluid is CO_2-rich and approaches pure CO_2 at the highest oxygen fugacity and low temperatures.

The increasing stability of iron carbide at extreme pressures has direct consequences for carbon solubility in (Fe,C)-liquids. Fe_3C is the solid formed upon carbon saturation and its progressively negative energy of formation shifts the solubility of carbon in iron-rich liquids to small values. Figure 3.2-9 illustrates carbon solubility in (Fe,C)-liquids between 1 bar and 25 GPa. At 10 GPa, a rapid increase in carbon solubility above 2500 °C results from a change

between peritectic and congruent melting behaviour of Fe_3C. At extreme pressure, carbon solubility remains lower than 2 wt.%.

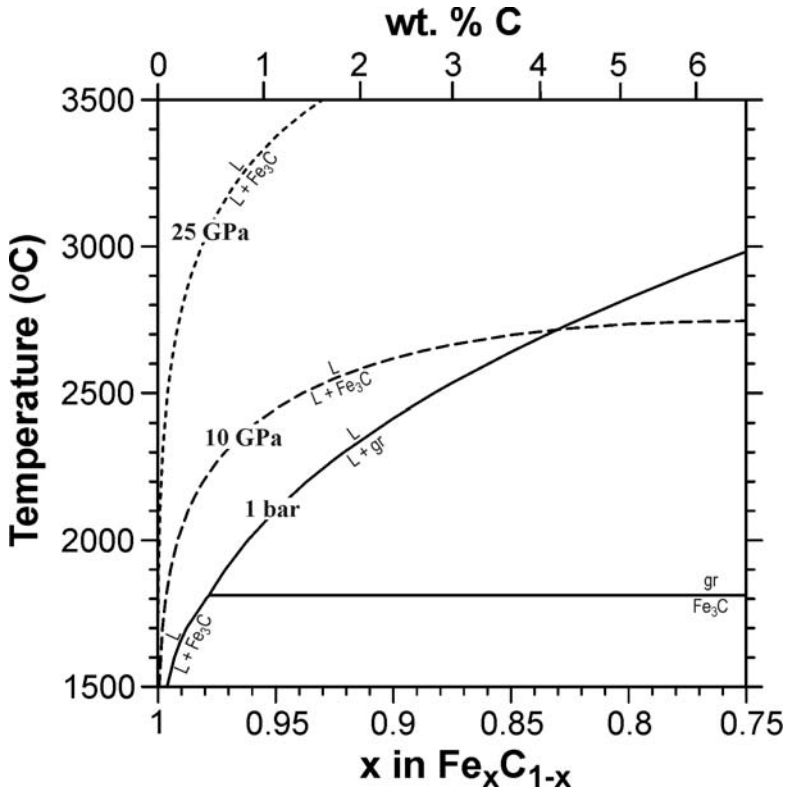

Fig. 3.2-9: Carbon solubility in iron-rich liquids from 1 bar to 25 GPa.

The present thermodynamic calculations reveal the need for additional, more accurate, constraints on the equation of state of iron carbide phases. Figure 3.2-10a shows the difference between the Gibbs free energy of formation for Fe_3C from the elements using different models at 1 bar. Despite the discrepancy between the models of Gustafson (1985, Scand. J. Metall. 14, 259-267) and Wood (1993, Earth Planet. Sci. Lett. 117, 593-607) at greater than 2000 K, both calibrations predict Fe_3C stability at high pressures and little effect on the cementite-wüstite-diamond equilibrium or on the trend of decreasing carbon solubility in iron-rich liquids. Figure 3.2-10b demonstrates the effect of the compressibility of Fe_3C-liquid on the energetics of the solid-liquid transition. If the Fe_3C-liquid has a high bulk modulus, *i.e.*, small compressibility, due to its carbon component, the contribution to the system energy via the VdP-integral is high and the stability of cementite is promoted. Better constraints on compressibility of (Fe,C)-liquids are needed in order to permit extrapolation to core conditions. In summary, the thermodynamic computations reveal that (1) cementite is stable in the Earth's interior, (2) it significantly reduces carbon solubility in iron-rich liquids, and (3) the cementite-wüstite-diamond equilibrium is located 2 log units above the iron-wüstite buffer. These results are in agreement with our current experimental studies in the system Fe-C-O.

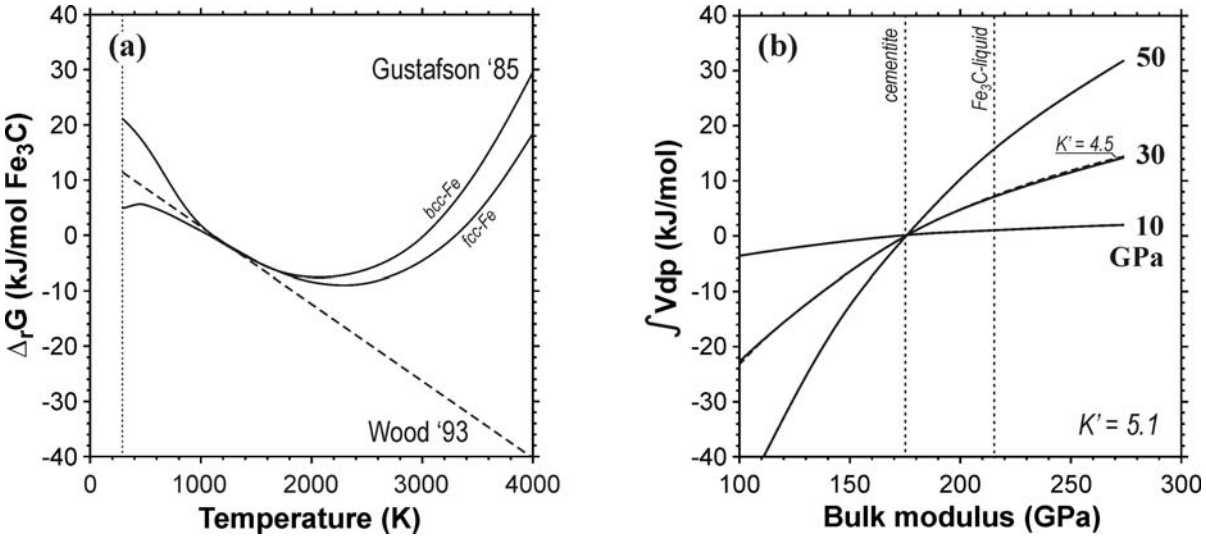

Fig. 3.2-10: (a) Gibbs-free energy of the solid-state equilibrium 3 Fe + C = Fe3C at 1 bar showing the difference between Gustafson's and Wood's model due to the heat-capacity effects; (b) effect of bulk modulus on the Gibbs free energy via the Vdp-integral of the Fe_3C phases. Stiffer behaviour of the Fe_3C-liquid promotes the stability of cementite.

i. *Investigation of the effect of oxygen fugacity on carbon isotopic fractionation during diamond formation (S.S. Shcheka, C.A. McCammon and M. Wiedenbeck/Potsdam)*

Diamonds formed in the Earth's mantle are generally divided into two distinct groups based on the mineralogy of inclusions – "peridotitic" (P-type) and "eclogitic" (E-type). P-type diamonds contain inclusions of an olivine-enstatite-garnet-clinopyroxene assemblage and are characterized by a relatively narrow range of $\delta^{13}C$ (+1 to -10 ‰, with a mean of -5 ‰). Inclusions in E-type diamonds are represented by the association of garnet and clinopyroxene and carbon isotopic signatures of eclogitic diamonds vary in a wider range (+3 ‰ to -35 ‰).

Observed differences in the distribution of carbon stable isotopes have been explained by three main models: (1) involving metasedimentary carbon-bearing material (organic matter and carbonates); (2) primordial isotopic variability of carbon; and (3) isotopic fractionation at mantle conditions. However, the first two models are not fully consistent with all existing geochemical data. According to the third model it would be hypothetically possible to achieve more than 40 ‰ variability in $\delta^{13}C$ in an open system where continuous partial removal of material occurs, even if the fractionation of stable isotopes between carbon-bearing species at the mantle conditions is very small. Theoretical calculations show that most peridotitic samples record values of fO_2 which fall into the region of zero carbon isotopic fractionation between fluid and diamond, but some eclogitic assemblages are more oxidized and imply higher carbon isotope fractionation. Here we have experimentally studied the influence of oxygen fugacity on the carbon isotopic exchange between carbon-bearing fluid and growing diamond.

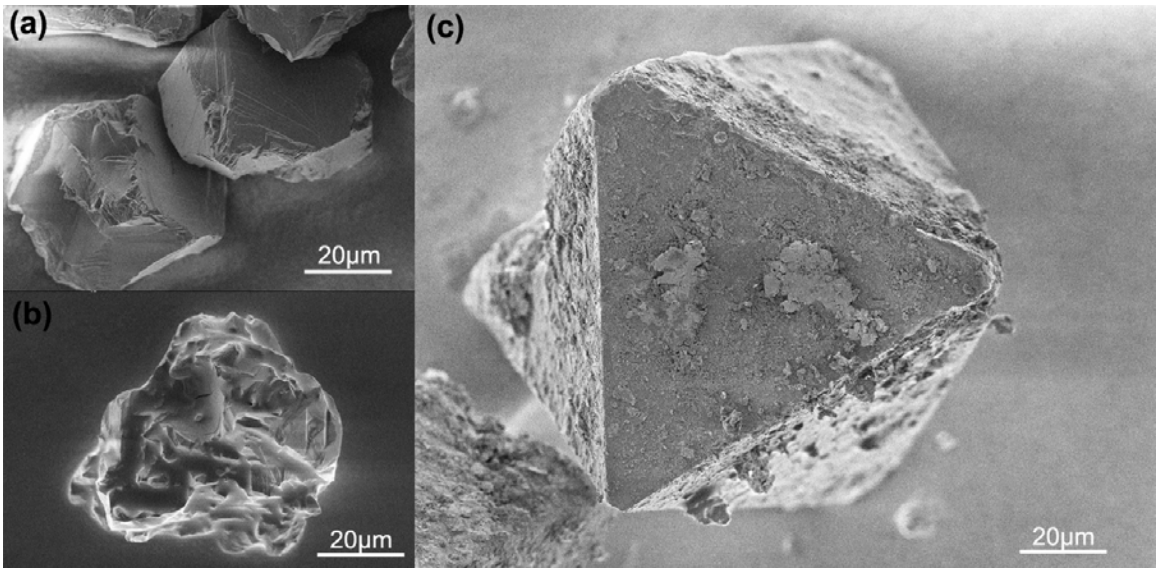

Fig. 3.2-11: SEM images of diamond seeds before (a) and after (b,c) experiments.

Diamond growth experiments were carried out using 1000 t and 1200 t multianvil presses (P = 8-10 GPa; T = 1100-1300 °C). The starting material was a mixture of 60 mol.% of carbonates, 12.5 mol.% clinopyroxene, 12.5 mol.% pyrope garnet and 15 % KCl aimed to reduce the temperature of diamond formation. A carbon-bearing fluid is expected to be formed due to decomposition of carbonates. Four to eight diamond seeds with diameter 35-40 µm (Fig. 3.2-11a) were added in each run. Oxygen fugacity was controlled by the capsule material. Molybdenum, cobalt, iron, nickel and vanadium were used, providing fO_2 in the range 1-8 log units below FMQ.

Up to now, large (up to 150 µm) diamonds (Fig. 3.2-11c) have successfully been synthesized only at 1300 °C, 10 GPa and fO_2 corresponding to the reaction $Mo+O_2=MoO_2$ (~ 3 log units below FMQ). No growth of diamonds was observed at temperatures below 1300 °C, independent of oxygen fugacity. Moreover, in most cases diamond seeds were strongly resorbed (Fig. 3.2-11b). Further efforts are underway to grow diamonds at different oxygen fugacities, and to understand the influence of the composition of the starting material.

j. *Melting in the transition zone and the Earth's lower mantle: a record buried in diamonds (S. Keshav, G.H. Gudfinnsson and D. Presnall/Richardson)*

Even though less voluminous than basalts, kimberlites and carbonatites have been found on almost every continent, and their presence in the sub-oceanic mantle (more specifically ocean-island basalt localities, OIB) has been inferred from studies of mantle xenoliths. Kimberlites, however, are particularly special, as in these rocks pieces of mantle material, either in the form of xenoliths, xenocrysts, or silicate inclusions in diamonds, have often been observed

leaving no doubt regarding the mantle parentage of kimberlites. From various studies it appears that beneath ancient cratonic regions of the continents, the lithosphere may extend down to depths of ~ 200-220 km. Mineral samples derived from even deeper parts are very rare and are found almost exclusively in diamonds. One of the most exciting developments in the last two decades has been the growing realization that some diamonds and thus their inclusions may originate from well below the lithosphere (> 230 km). These inclusions are dominantly of majoritic garnet composition (> 3.04 Si pfu; 3.04-3.50 Si pfu range so far seen) and on the basis of experimentally determined phase relations, these garnets have been interpreted to originate from depths of 300-400 km. Jagersfontein, Sao Luiz, Monastery, and Kankan are the only known diamond source areas with a significant population of majoritic garnets. These majoritic garnet inclusions in diamonds provide a unique means to test models for the petrological, geochemical, and thermal state of the deeper mantle, although there is the potential for overprinting by the diamond-forming environment, *i.e.*, they may not be typical samples of the deeper mantle.

The interpretations regarding the ultimate petrological origin of majoritic garnets are presently hotly debated and fall into two main categories; (1) these garnets (and their diamond hosts) are intimately related to CO_2-rich alkaline melts, similar to carbonatites, kimberlites, and alkalic lavas, where the ultimate source of the diamond host is carbon from various within-mantle and primordial sources; (2) they represent recycled oceanic crust, which is an increasingly popular model. This latter model has the attractive aspect of potentially also providing information on past subduction processes. In order to better understand the connection between CO_2-rich alkaline melts and majoritic garnet inclusions in diamonds (also clinopyroxene inclusions) we have examined the trace element partitioning between these phases.

Experimentally determined trace-element partitioning data have been collected in the CaO-MgO-Al_2O_3-SiO_2-CO_2 (CMAS-CO_2) system. In this system, melts resembling kimberlites coexist with a garnet lherzolite assemblage (forsterite + orthopyroxene + clinopyroxene + garnet) along a P-T divariant surface. The experiments were performed in the pressure range of 8-14 GPa. Significantly, the majoritic character of garnets in the experimental run products here allows one to quantitatively evaluate the link mentioned above. The results reported here are also directly applicable to modeling CO_2-rich melts in the Earth's mantle, melts that have been reported to occur very commonly in diamonds from various continents.

For cpx, all the trace elements are highly-to-moderately incompatible. For majoritic garnets, barring Lu, the trace elements are also highly-to-moderately incompatible. The data obtained here have been inverted to calculate the trace element composition of melts presumed to be in equilibrium with the majoritic garnets (and in the case of Kankan, also two different cpx crystals in two different diamonds) found as inclusions in diamonds. The modeling results suggest that all the calculated melts resemble sampled carbonatites, kimberlites, and alkalic

lavas on the continents. Calculated melts in equilibrium with two different cpx crystals from Kankan yield similar results and the melt compositions resemble carbonatites and kimberlites, indicating that both majoritic garnets and cpx were last in equilibrium with very CO_2-rich melts. On this basis, we conclude that the suggestion that these high-pressure silicates and the associated diamonds are related to former oceanic crust is unsubstantiated.

k. *The location of uranium and thorium in a pyrolitic lower mantle (L. Gautron and S. Greaux/Marne-la-Vallée; D.J. Frost)*

Uranium and thorium are the two main heat-producing elements in the Earth's mantle. A knowledge of the phases into which these elements partition in the mantle is important for understanding the thermal behaviour of the Earth and the geodynamic processes that result. It is possible, for example, that certain processes could have led to the formation of a dense, radiogenic layer in the bottom half of the Earth's mantle. In previous studies $CaSiO_3$ perovskite has been identified as a likely repository for U and Th in the mantle, however most previous studies have examined partitioning only at the silicate liquidus and not at typical temperatures for the lower mantle. The substitution mechanism by which U and Th enter the perovskite structure is poorly understood.

In this study we have examined the solubility of U and Th in minerals forming from a pyrolitic bulk composition at pressures and temperatures corresponding to the Earth's lower mantle. Starting materials comprised oxide mixtures with a pyrolitic bulk composition with varying proportions of UO_2 and ThO_2. These materials were sealed in Re foil capsules. All experiments were performed at 26 GPa and 1700 °C using a 10/4 multianvil assembly. In order to allow for the slow solid-state diffusion of U and Th, run durations of 12 hours were employed over which time the experimental temperature remained perfectly stable. Recovered capsules were mounted in epoxy resin and sectioned for microprobe analysis.

At all conditions $(Mg,Fe)(Si,Al)O_3$ perovskite and $CaSiO_3$ perovskite were found to crystallise in addition to majorite-garnet (Fig 3.2-12). The Al concentration of $(Mg,Fe)(Si,Al)O_3$ perovskite was over 5 wt.% indicating that pressures were indeed around 26 GPa over the duration of the experiments. Preliminary electron microprobe measurements indicate that U and Th both strongly partition into $CaSiO_3$ perovskite at these conditions. In some samples that were highly doped with U and Th $CaSiO_3$ perovskite contained up to 25 wt.% Th and 6 wt.% U. Interestingly the presence of Th and U strongly increases the solubility of Al in $CaSiO_3$ at these conditions, which in some samples was up to 11 wt.%, compared with less that 1 % in typical pyrolite. The results clearly indicate that $CaSiO_3$ perovskite is likely to be the only host of any significance for U and Th in the Earth's lower mantle. Further study will lead to a full understanding of the substitution mechanism by which these elements enter the perovskite structure.

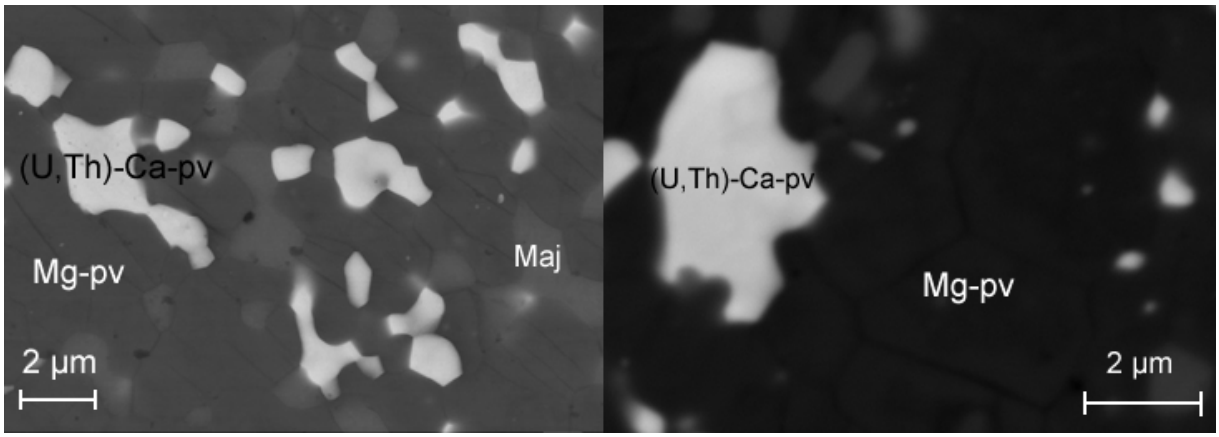

Fig. 3.2-12: A backscattered image of the phases present in a typical run product. Grains of $CaSiO_3$ perovskite (ligth grey) in contact with grains of $MgSiO_3$ perovskite (dark grey or black in the right image).

l. *Slab-derived melts from the Earth's lower mantle: possible plume sources and the global Nb budget (G.D. Bromiley and S.A.T. Redfern/Cambridge; D.J. Frost)*

Subduction of oceanic crust is a key part of plate tectonics, and represents the main mechanism for recycling material back into the deep Earth interior. However, beyond the depths of sub-arc magmatism, our understanding of the fate of subducted material is extremely limited. It has been suggested that melting of ancient subducted slabs deep in the mantle could provide source material for mantle plumes. Here we investigate, for the first time, what geochemical signatures we would expect following slab melting under such conditions. Experiments have been performed to determine what effects the presence of TiO_2 phases in residual material [rutile and its high-pressure polymorph TiO_2 II, Fig. 3.2-13a] have on the behaviour of the geochemical 'twins' Nb and Ta, and Hf and Zr during large-degree partial melting of a typical basaltic composition. Run products from such an experiment are shown in Fig. 3.2-13b.

Results from detailed electron microprobe examination show that the rutile-TiO_2 (II) transition has a controlling influence on the relative partitioning of Nb and Ta. At pressures below 6 GPa, Nb and Ta both partition strongly into rutile. However, there is a slight tendency for rutile to partition Ta relative to Nb (as has been noted in numerous previous investigations). At pressures above 6 GPa, where TiO_2 (II) is the stable form of TiO_2, the relative behaviour of Nb and Ta is altered. Under these conditions, Nb and Ta again strongly partition into the stable TiO_2 phase over coexisting melt. However, in contrast to rutile, TiO_2 (II) favours Nb relative to Ta, such that Nb is partitioned into the crystal relative to Ta. This implies that melts derived from deeply subducted crust will be Nb and Ta deficient, but should also have a unique Nb/Ta ratio, with Nb depleted relative to Ta, which will distinguish them from melts derived from all other sources.

Samples are currently being studied using the Ion Microprobe facility at the University of Edinburgh to accurately measure trace element contents of melts and garnets. Data from this study will be used to elucidate possible slab-derived signatures in plume source material (*e.g.*, oceanic island basalts), using existing geochemical data. Data will also be used to model the role that deep melting of oceanic crust could have had in continental crust formation early in Earth's history.

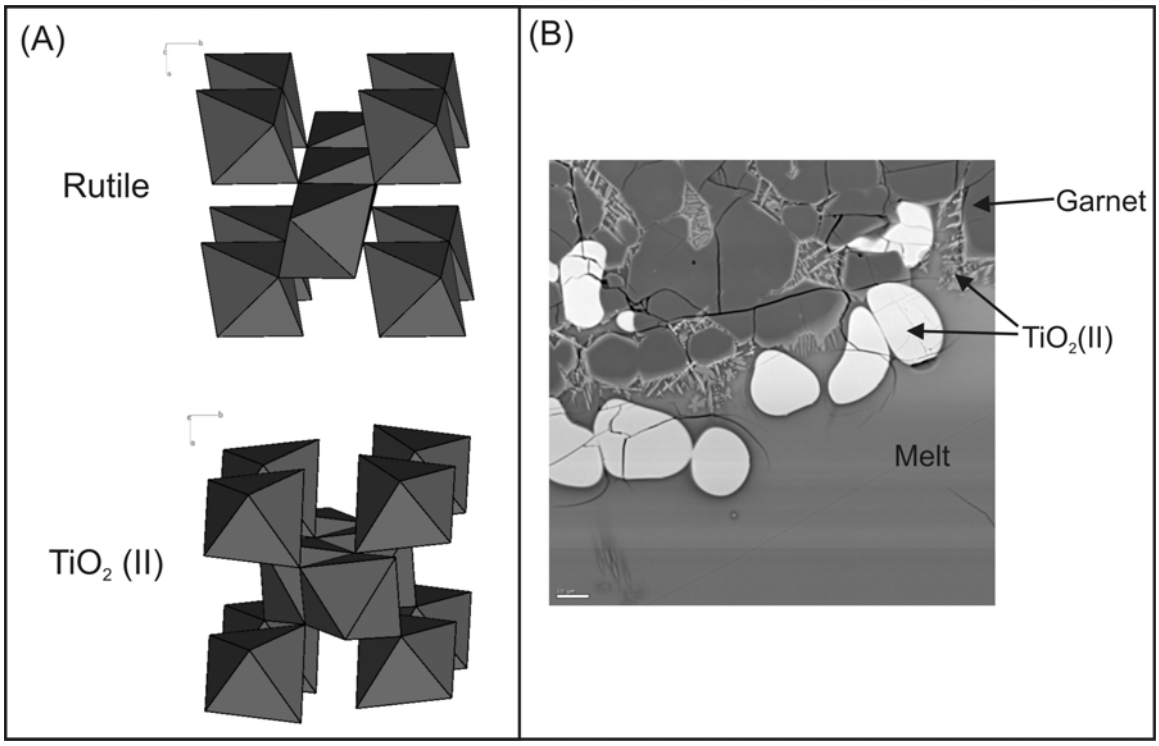

Fig. 3.2-13: (A) structures of rutile and its high-pressure polymorph TiO_2 (II). The Ti^{4+} site in rutile is quite close to a regular octahedra. This site is much more distorted in TiO_2 (II), which could explain changes in trace element partitioning behaviour between the two polymorphs. (B) SEM secondary electron image of part of a multianvil run (8 GPa, 1800 °C) showing large TiO_2 (II) crystals in equilibrium with melt. Grey crystals are garnet, which crystallises in cooler parts of the capsule. Scale bar is 10 microns long.

m. *Transport and storage of phosphorus in lherzolitic and eclogitic assemblages under upper mantle P-T conditions – the role of apatite and garnet (J. Konzett/Innsbruck and D.J. Frost)*

Phosphorus is an important minor constituent of virtually all magmatic rocks albeit with concentrations usually < 0.2 wt.% P_2O_5. In lamproites, kimberlites and alkaline lamprophyres, however, this element is frequently present at a weight % level and may exceed the concentration of Na, testifying to significant phosphorus contents of deep-seated lithospheric and asthenospheric magma sources in spite of the fact that the phosphorus concentration of

primitive mantle is assumed to be only around 100 ppm. The major phosphorus-bearing phase stable under P-T conditions of the crust and upper mantle is apatite $Ca_5(PO_4)_3(OH, F, Cl)$ appearing as an extremely common accessory phase in both metabasaltic and metapelitic bulk compositions. In peridotites, apatite is more rarely encountered and restricted to environments metasomatized by hydrous fluids or melts and often associated with hydrous silicates such as phlogopite and/or amphibole. Experiments with pure OH- and F-apatite have shown that these phases are stable to pressures in excess of 10 GPa. Aside from its role as a phosphorus carrier, apatite is a major host for REE and some LILE such a Sr, U and Th and it is important in understanding the transport and residence of halogens. Although virtually phosphorus-free at pressures < 2-3 GPa, garnet is able to incorporate significant amounts of phosphorus under upper mantle P-T conditions through a number of coupled substitutions involving Na, (Mg,Ca) and Al such as $(Mg,Ca)PAl_{-1}Si_{-1}$ or $NaP(Mg,Ca)_{-1}Si_{-1}$, the latter exchange leading to a complete solid-solution between $Mg_3Al_2(SiO_4)_3$ and $Na_3Al_2(PO_4)_3$ with garnet like structure. Garnet thus may act as an alternative storage site for phosphorus under high P-T conditions and limit the stability field of apatite by preferential partitioning of phosphorus. Based on the present knowledge on the ability of garnet to incorporate phosphorus under high P and T, this study was undertaken (1) to evaluate the phosphorus partitioning between garnet and coexisting OH-apatite, (2) to re-evaluate the P-T stability field of OH-apatite in metabasaltic and peridotitic bulk compositions and (3) to place constraints on the P-T stability of OH-apatite in the presence of garnet for a given bulk phosphorus content.

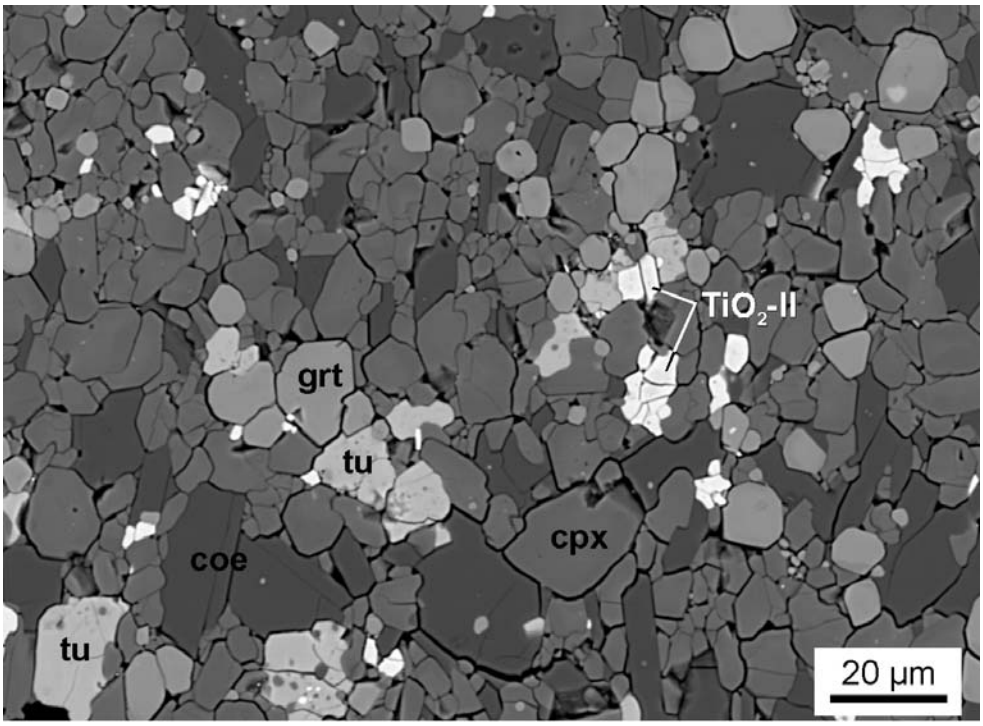

Fig. 3.2-14: Backscattered electron photomicrograph of an assemblage garnet (grt) + omphacitic clinopyroxene (cpx) + coesite (coe) + TiO_2-II + tuite (tu) stable in the MORB bulk composition at 7.5 GPa and 950 °C.

Experiments were carried out in a multianvil press with 18/11 and 14/8 assemblies between 7 and 15 GPa and temperatures in the range of 950 to 1450 °C using welded platinum capsules with inner graphite liners. An average MORB and a fertile spinel-lherzolite composition doped with 3 % synthetic OH-apatite were used as a starting material. The results of the experiments done so far in the MORB bulk composition show that the stability field of OH-apatite is restricted to much lower pressures than previously assumed. This phase was found to < 7.5 GPa at 900 °C and to < 8.0 GPa at 1050 °C in an assemblage garnet + clinopyroxene + SiO_2 + TiO_2. At higher pressures OH-apatite breaks down to an anhydrous Ca-phosphate coexisting with the same eclogitic assemblage (Fig. 3.2-14). Both compositional data and Raman spectra (Fig. 3.2-15) indicate that this phosphate phase is identical to γ-$Ca_3(PO_4)_2$ that was recently described from the Suizhou chondrite and named tuite. γ-$Ca_3(PO_4)_2$ was observed to 1050 °C at 8.0 GPa and to 1200 °C at 11.0 GPa but was absent from experiments at higher P and T where phosphorus is mainly stored in garnet ± quenched fluid/melt.

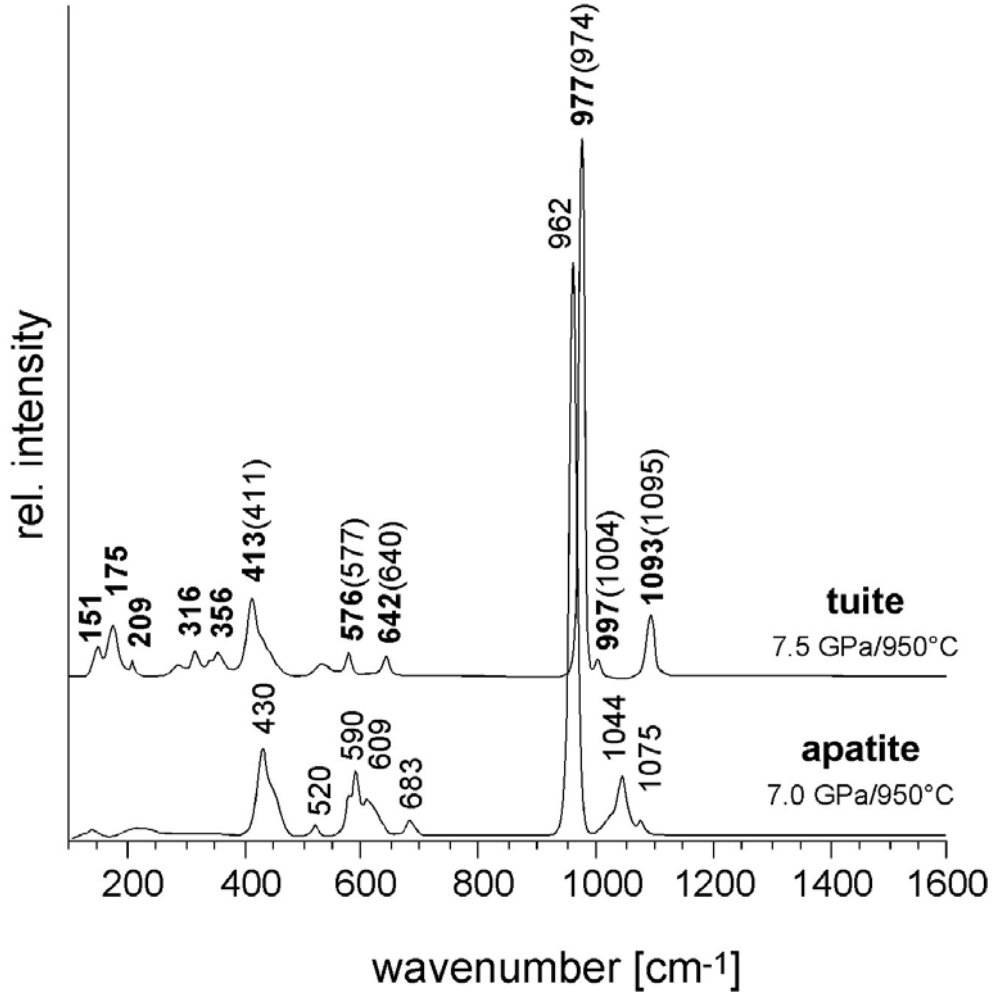

Fig. 3.2-15: Unpolarized Raman spectra of apatite and tuite, showing the diagnostic shift of the ν_1 PO_4 vibrational mode from 962 cm^{-1} in apatite to 977 cm^{-1} in tuite. Wavenumbers in brackets for the tuite spectrum are those identified in natural tuite from the Suizhou chondrite.

In the MORB bulk composition, the P_2O_5-contents of garnet buffered by apatite, tuite or quenched melt/fluid is in the range of 0.2-0.3 wt.% but may rise to values of 0.6-0.8 wt.% in the absence of a phosphate phase (Fig. 3.2-16). Preliminary results at 8 GPa and temperatures of 1050 °C and 1200 °C using the lherzolite bulk composition indicate a similar P-T stability field of OH-apatite but show significantly higher P_2O_5 contents in garnet in the range of 1.0 to 1.2 wt.% P_2O_5. Therefore, at these P-T conditions, < 3 % modal garnet in a lherzolite could accommodate the entire primitive mantle phosphorus budget of 90-100 ppm and prevent the stability of apatite. Thus it is only if sufficient phosphorus is present to saturate garnet that apatite is likely to be stable in a mantle lherzolite, but to a depth not exceeding 200-220 km.

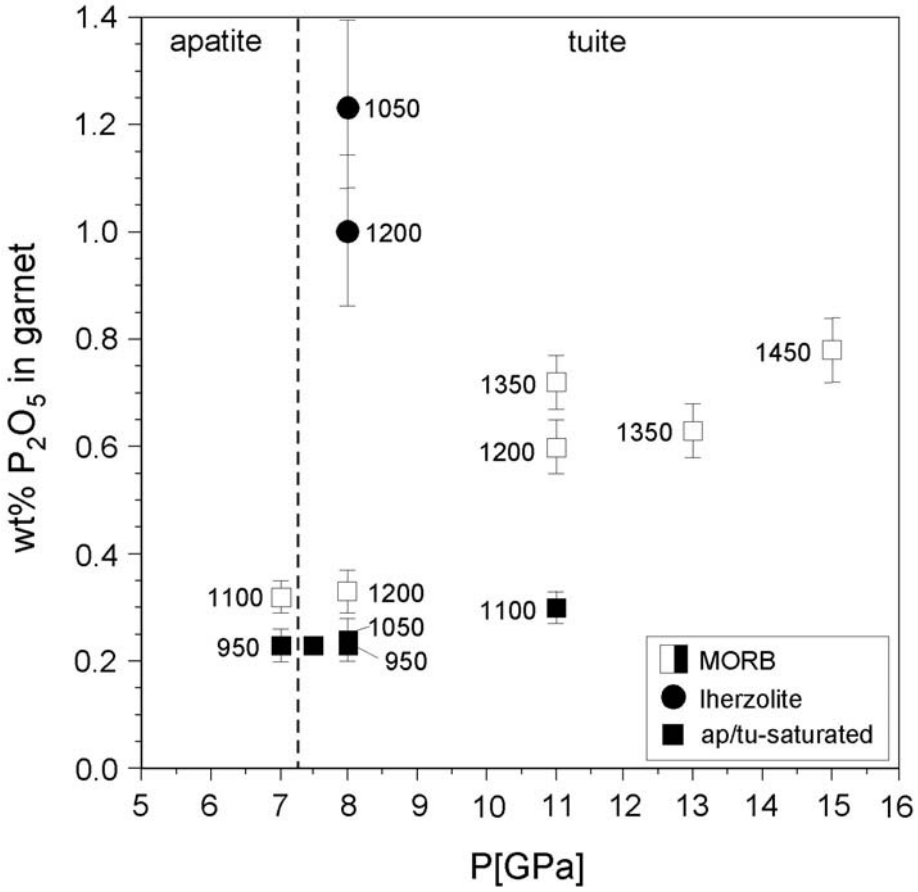

Fig. 3.2-16: The concentration of P_2O_5 in garnet as a function of P, T and coexisting assemblage in the lherzolite and MORB bulk compositions

n. *Iron oxidation state in (Mg, Fe)O: Calibration of the "flank method" on synthetic samples using the electron microprobe (M. Longo and C.A. McCammon)*

One of the important parameters involving phase equilibria and geochemical kinetics is the oxygen fugacity, and during the last twenty years this parameter has been comprehensively investigated. Recently the focus has intensified due to developments in new techniques that

allow the collection of more accurate data at higher spatial resolution. Basically, the aim is to reconstruct the redox conditions that characterize the formation of rock-forming minerals from the crust to the deep Earth's interior, with implications for physical and chemical properties and geochemical behaviour. Measuring the original oxygen fugacity under which the natural rock assemblage formed is difficult to realise. One approach in estimating the oxygen fugacity consists of determining the valence states of multivalent elements, in particular iron. However, only a few techniques allow a measurement of this ratio with sufficient accuracy. The problems related to this measurement are numerous, including small sample dimensions and destructive sample preparation. For these reasons, the improvement of techniques is of critical importance. One promising method is X-ray emission spectroscopy using the electron microprobe, the so-called "flank method" developed by H. Höfer and G. Brey at the University of Frankfurt, who have been able to calibrate $Fe^{3+}/\Sigma Fe$ with a precision of ±0.02 (1σ). The basic principle is that in the X-ray emission spectra of transition metals, the Lα and the Lβ peaks and also the Lα/Lβ intensity ratio shift with a change in oxidation state, and this has been exploited to determine $Fe^{3+}/\Sigma Fe$. Since the low energy Fe Lα and the Fe Lβ X-ray emission lines are also affected by bulk chemistry and crystal structure, it is necessary to correct for self-absorption effects and to establish separate calibration curves for each mineral group.

Ferropericlase (Mg,Fe)O and $(Mg,Fe)(Si,Al)O_3$ perovskite are believed to form the bulk of the Earth's lower mantle, and one of the currently interesting questions in geoscience concerns the reconstruction of redox conditions within the lower mantle. Since studies have shown that the Fe^{3+} concentration in $(Mg,Fe)(Si,Al)O_3$ perovskite is essentially insensitive to oxygen fugacity (see previous BGI Annual Reports), our attention is turned to (Mg,Fe)O. The goal of the current project is to calibrate the "flank method" for synthetic (Mg,Fe)O, with eventual application to ferropericlase inclusions from lower mantle diamonds. So far samples with different iron content (15 and 30 at.%) and variable $Fe^{3+}/\Sigma Fe$ ratios (1-7 at.%) have been synthesised at controlled oxygen fugacity and Fe^{3+} has been measured using Mössbauer spectroscopy. In addition to electron microprobe measurements including the "flank method" calibration, samples will also be investigated using X-ray powder diffraction in order to obtain cell parameters, and transmission electron microscopy in order to check for possible dislocations or cation vacancies that could influence the "flank method" calibration.

o. *XANES study of the oxidation state of Cr in lower mantle phases (C.A. McCammon, S. Eeckhout/Grenoble, N. Bolfan-Casanova and E. Amiguet/Clermont-Ferrand, S. Klemme/ Edinburgh)*

Previous trace-element studies report that minor amounts of Cr are present in the Earth's mantle in an oxidised form, mostly as Cr^{3+} and Cr^{6+} in Earth materials. However, recent literature results on melts have shown that in the presence of Fe at high temperatures, Cr^{2+} is

not quenchable because of electron charge transfer with Fe^{3+} upon cooling. Changes in the oxidation state of transition elements have been predicted to be induced by high pressure, but have not been verified experimentally, even though such changes would be critical for their partitioning behaviour during differentiation processes. Also, the valence state of transition elements in ferropericlase is important because these elements play a role in numerous physical and chemical properties. To better understand the factors controlling the incorporation of Cr in mantle materials, we investigated the crystal chemistry of Cr in synthetic high-pressure (Mg,Cr)O periclase, (Mg,Fe,Cr)O ferropericlase and $(Mg,Cr)SiO_3$ perovskite using X-ray Absorption Near-Edge Structure (XANES). We focused on pre-edge features, which strongly depend on the valence state and coordination number of transition elements, and ^{57}Fe Mössbauer spectra were performed on the Fe-containing samples. The aim of the study was to determine the Cr oxidation state in phases found in the Earth's lower mantle, and to examine the possible relationship with the Fe oxidation state in the same materials.

Two samples of (Mg,Cr)O periclase, three samples of (Mg,Fe,Cr)O ferropericlase, and one sample of $(Mg,Cr)SiO_3$ perovskite were synthesized at high pressure and high temperature for the investigation. Run products were characterised using the electron microprobe and scanning electron microscopy. Cr *K*-edge XANES spectra were recorded in fluorescence mode at room temperature at the European Synchrotron Radiation Facility on the undulator beamline ID26. Reference XANES spectra were recorded on powder pellets of synthetic Cr-bearing enstatite ($^{[6]}Cr^{2+}$ in $Mg_{0.90}Cr_{0.10}SiO_3$), chromite ($^{[6]}Cr^{3+}$ in $FeCr_2O_4$) and crocoite ($^{[4]}Cr^{6+}$ in $PbCrO_4$). For the XANES spectra a linear pre-edge background was subtracted followed by normalisation to the edge jump. To extract the pre-edge features, the contribution of the edge jump to the pre-edge was modelled using a sum of Gaussian functions. Gaussian profiles were used to determine the energy position of the pre-edge components, and the amount of Cr^{2+} was calculated using methods described in the literature. Room temperature Mössbauer spectra were collected on all Fe-containing phases using the same samples disks used to collect XANES data.

Results show the presence of measurable amounts of Cr^{2+} in all samples, where Fe-free (Mg,Cr)O contains significantly higher $Cr^{2+}/\Sigma Cr$ values (34-41 %) compared to (Mg,Fe,Cr)O (2-12 %), even under similar conditions of pressure, temperature and probably oxygen fugacity. The most likely reason for this difference in relative Cr^{2+} content is the loss of Cr^{2+} during cooling according to the reaction $Cr^{2+} + Fe^{3+} \rightarrow Cr^{3+} + Fe^{2+}$, which is supported by the magnitudes of Fe^{3+} concentrations measured using Mössbauer spectroscopy. Compared to (Mg,Cr)O, $(Mg,Cr)SiO_3$ perovskite has a much higher relative Cr^{2+} content, ~ 70 % $Cr^{2+}/\Sigma Cr$, even though the sample was synthesised under relatively oxidising conditions. It is likely that under the more reducing conditions believed to exist in the lower mantle, the valence state of Cr in magnesium silicate perovskite is mainly divalent.

p. *The relation between Li and Fe^{3+} during igneous fractionation: A case study from the peralkaline Ilímaussaq igneous complex, south Greenland (C.A. McCammon, in collaboration with M. Marks and G. Markl/Tübingen, R. Rudnick/College Park, T. Vennemann/Lausanne)*

Lithium generally behaves as an incompatible element during igneous fractionation and is observed to preferentially partition into an aqueous fluid phase during mineral-fluid equilibria. Thus, lithium is fluid-mobile and can be transported during magmatic alteration, magmatic fluid exsolution or hydrothermal circulation. The Ilímaussaq complex in Greenland is a world-famous example of magmatic layering and is the type locality for agpaitic rocks, which are peralkaline nepheline syenites containing complex Ti-Zr silicates. Based on indicators of differentiation (*e.g.*, Fe/Mg, (Na + K)/Al, Ca/(Na + K), Rb/Sr, Mg/Li) in whole-rocks and minerals, Ilímaussaq is the most fractionated alkaline igneous rock suite yet documented. Since crystallisation occurred over an extensive temperature range (1000 to 300 °C), including orthomagmatic and late-stage hydrothermal crystallization, the Ilímaussaq suite can offer unique insights into the behaviour of lithium during magmatic differentiation and fluid exsolution in a peralkaline system.

The petrology and mineral chemistry of the Ilímaussaq rocks are already well documented in the literature. Li concentrations of carefully hand-picked mineral separates were measured using a Nu Plasma multicollector Inductively Coupled Plasma Mass Spectrometer installed at the University of Maryland, which was also used to measure Li isotopic compositions as part of a larger study. Room temperature Mössbauer spectra were collected on nineteen representative amphibole separates to determine $Fe^{3+}/\Sigma Fe$, where values were determined based on relative area ratios corrected for thickness and recoil-free fraction effects.

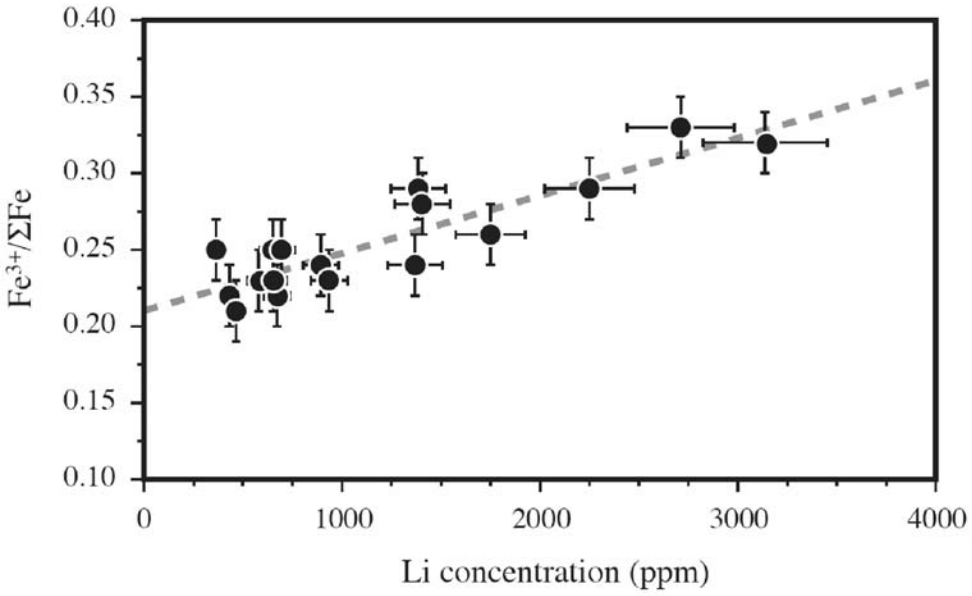

Fig. 3.2-17: Li concentration *versus* $Fe^{3+}/\Sigma Fe$ for representative alkali amphiboles from the agpaitic Ilímaussaq rocks (Greenland).

Li concentrations in amphibole are highly variable and increase systematically with ongoing fractionation from ~ 10 to > 3100 ppm, while Li contents in clinopyroxene are generally low, ranging between 15 and 84 ppm, with no systematic differences between the different intrusive units, hence degree of fractionation. In Na-amphiboles, Li occupies the M3 site, where it mainly substitutes for Fe^{2+} via the coupled substitution $Li^{+} + Fe^{3+} \leftrightarrow 2\ Fe^{2+}$; hence Li may play a role in charge balance during iron oxidation. As shown in Figure 3.2-17, $Fe^{3+}/\Sigma Fe$ increases with increasing Li concentration in the Ilímaussaq Na-amphiboles. If relative Fe^{3+} concentrations in amphibole reflect the magmatic redox state as suggested in the literature, Li concentrations are also correlated with oxygen fugacity. Such an increase in oxygen fugacity from early to late agpaitic rocks and even more oxidised conditions during the hydrothermal stage is consistent with previous petrological studies on the peralkaline igneous rocks of South Greenland. In clinopyroxene, Li and Na likely compete for the same crystallographic site (M2), in contrast to Na-amphiboles where they likely occupy different sites (M3 *versus* M4). The high Na concentrations in the Ilímaussaq clinopyroxenes (typically around 12 wt.% Na_2O) coupled with very low Li may therefore be a consequence of charge balance during iron oxidation occurring primarily through coupled substitution of Na and Fe^{3+}, which is consistent with the strong correlation previously reported between the concentrations of those two cations. Hence the increase in oxygen fugacity from early to late agpaites and the associated increase of the $Fe^{3+}/\Sigma Fe$ ratio in the melt apparently does not affect the Li concentration in clinopyroxene, but induces incorporation of Li into the amphibole structure to accomplish charge balance and may be an important factor influencing the distribution of Li between amphibole and pyroxene.

q. *Global Na8-Fe8 systematics of MORBs: implications for mantle heterogeneity, temperature, and plumes (D.C. Presnall/Richardson and G.H. Gudfinnsson)*

A major development in the characterization of mid-ocean ridge basalt (MORB) glass compositions was the discovery (Langmuir *et al.*, 1992, AGU Geophys. Monog. 71, 183-280. hereafter LKP) that Na8 and Fe8 (Na_2O and FeO, normalized to a constant MgO value of 8 %) show systematic variations when plotted against each other and against axial ridge depth. Axial ridge depth was used as a proxy for crustal thickness, and normalization to MgO = 8 % was a procedure intended to remove the variations created by low-pressure crystallization so that the chemical systematics produced at the depth of separation from the mantle source would be revealed. To explain the Na8-Fe8 variations, LKP developed a model involving melting columns that start at varying depths, require large variations in initial temperature and pressure of melting, extend to low pressures near the base of the crust, and produce oceanic crust of variable thickness.

In a global examination using the Smithsonian database of MORB glass analyses, we find that correlations of Na8 and Fe8 with axial ridge depth are inconsistent and not reliable, an observation originally acknowledged by LKP, but nevertheless incorporated as a critical aspect of their modeling. They mentioned the Galapagos Ridge and the Azores region of the Mid-Atlantic ridge as major exceptions to their modeling, but we find that the situation is much worse. We show that Na8-Fe8-depth variations do not support the LKP modeling for

any ridge segment, short or long, in the Atlantic, Pacific, and Indian Oceans for which data exist in the Smithsonian database. Unfortunately, axial ridge depth was a critical part of their modeling. We ignore axial ridge depth and focus instead on the Na8-Fe8 variations. The Na8-Fe8 variations are in excellent agreement with an estimate of the systematics of solidus melts in the plagioclase/spinel lherzolite transition in the CaO-MgO-Al_2O_3-SiO_2-Na_2O-FeO (CMASNF) system at 0.93-1.5 GPa. This estimate is based on interpolations between the limiting boundaries of the CMASN and CMASF systems. Full determination of the solidus for the CMASNF system in this pressure range is currently in progress at BGI. This system contains all the major minerals of the mantle and 99 % of the compositions of both basaltic melts and their source. Therefore, it provides very robust chemical constraints on melting processes. From these phase relations, temperatures of magma generation for MORBs are estimated to be uniformly low at about 1240-1260˚C. Inverse Na8-Fe8 variations for solidus melts at constant pressure are explained by mantle heterogeneity (the regional trends of LKP), whereas positive variations superimposed on the inverse variations (the local trends of LKP) are consistent with progressive extraction of melts from short, ascending melting columns. The melts that have the highest MgO/FeO ratio are extracted at the tops of these columns. Remarkably, comparison of the observed global variations of Na8 and Fe8 with the solidus phase relations indicates that the temperature variation for magma generation along ridges is no more than about ± 10˚C, and the pressure variation is no more than about ± 0.15 GPa. There are no inconsistencies at all in the modeling, and we are able to extract a crude mapping of the oceanic lithosphere (< ~ 65 km depth) from the data. In a ridge-by-ridge examination, we find that the southern Atlantic lithosphere from Bouvet to about 26˚N is relatively homogeneous, whereas the Atlantic lithosphere north of about 26˚N shows significant long-range heterogeneity. The lithosphere between the Charlie Gibbs and Jan Mayen fracture zones is strongly enriched in FeO/MgO, perhaps by a trapped fragment of basaltic crust in a Caledonian suture. Iceland is explained as the product of this enrichment, not a hot plume ascending from great depths. The East Pacific Rise and Galapagos Ridge sample lithosphere that is heterogeneous over short distances. The lithosphere beneath the northern part of the Indian Ocean is fairly homogeneous and is depleted in FeO/MgO relative to the lithosphere beneath the Red Sea. In this modeling, hot plumes at or near ridges and large variations in temperatures of magma generation are replaced by mantle heterogeneity and consistently low temperatures of magma generation.

r. *Monazite solubility in granitic melts and the lanthanide tetrade effect (T. Quach-Duc/ Tübingen and H. Keppler)*

Rare earth elements or lanthanides are a group of elements with very similar geochemical behaviour. In general, their partitioning between various phases varies smoothly with ionic radius and therefore, with atomic number. Accordingly, rare earth abundance patterns in various rocks are usually smooth curves.

There are, however, some striking exceptions from this rule. In some highly fractionated, often fluorine-rich granites, the rare earth patterns are far away from being smooth. Rather,

they show the selective enrichment of some rare earth elements relative to their neighbors in the periodic table and this enrichment appears to show some periodicity with atomic number. Often, the enrichment pattern can be divided into four segments (the four tetrades), with the basic pattern being repeated in each tetrade. This effect is also known from the fractionation of rare earth elements involving organic solvents and it is probably related to crystal field effects involving the partially filled f-orbitals.

The origin of the lanthanide tetrade effect in granites remained enigmatic. Various models have been suggested, involving for example rare earth fractionation by aqueous fluids or by fluoride melts. The main carriers of lanthanides in felsic rocks, however, are the rare earth phosphates, monazite and xenotime, and the lanthanide content of felsic melts is usually controlled by the equilibrium of the melt with these phases. We therefore carried out a systematic study of monazite and xenotime solubility in granitic melts. Crystals of the phosphate phase of each rare earth element were first synthesized separately and then the solubility of each of these synthetic minerals was measured by month-long dissolution experiments in haplogranitic melts of variable composition. In order to demonstrate equilibrium, some reversed runs have been carried out as well.

The results of these experiments show some spectacular tetrade effects (Fig. 3.2-18), with the solubilities of some of the rare earth elements being twice higher than the solubilities of the two neighboring rare earth elements in the periodic table. In particular, for the peralkaline compositions, where the solubilities are high, this effect is much larger than the analytical or experimental uncertainty. Lanthanide tetrade effects are probably also present in the subaluminous and peraluminous compositions, but because of the much lower bulk solubilities and associated higher analytical errors, the effects are more difficult to observe.

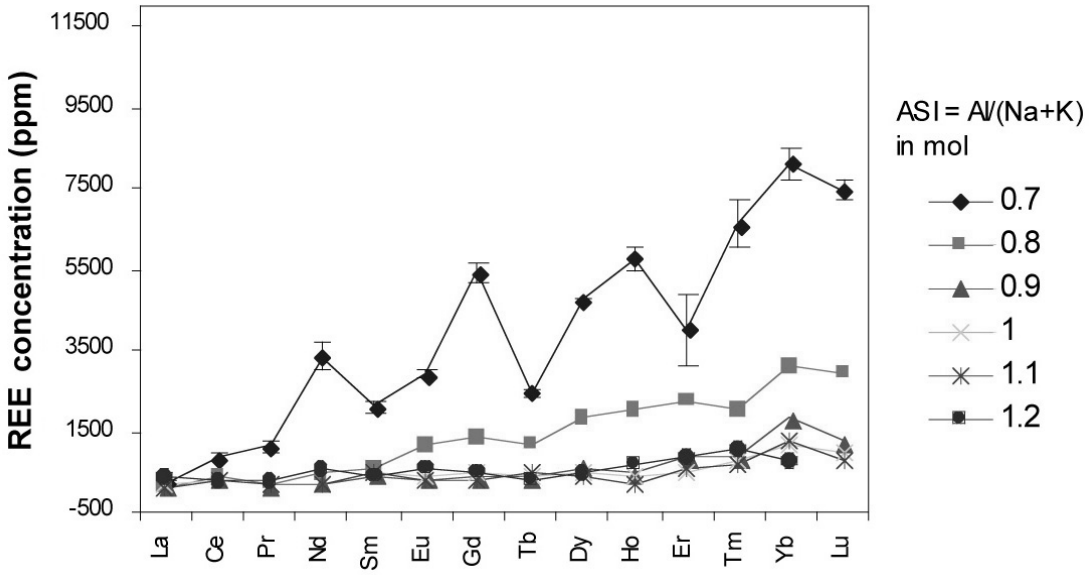

Fig. 3.2.-18: Experimentally determined solubility of the rare earth phosphates monazite (La – Gd) and xenotime (Gd – Lu) in haplogranitic melts of variable alumina saturation index (ASI). The initial P_2O_5 concentration in the melt was 0.1 wt.%.

The appearance of the tetrade effect may be related to the unusual 9- or 8-fold coordination geometry of rare earth elements in monazite and xenotime, which is perhaps different from the coordination of these elements in the silicate melt. In any case, our experiments show that tetrade effect in granitic magmas can be produced simply by the fractionation of monazite and xenotime. The fact that these effects are only observed in some volatile-rich, highly fractionated granites may be related to the low viscosity of the corresponding magmas, that allows an efficient settling out of monazite or xenotime crystals.

3.3 Mineralogy, Crystal Chemistry and Phase Transformations

Studies of the response of a crystal structure to changing conditions of pressure, temperature, oxygen fugacity and chemical composition are fundamental to a large area of material sciences, particularly to physics, chemistry, engineering, and Earth science. One of the most drastic responses is "phase transformation". Almost all materials are strongly affected by transformation processes in the critical range of pressures and temperatures corresponding to the Earth and the outer planets' interior. In this chapter, we focus on the intensive efforts to detect the onset of phase transformation and to understand the responses of different materials at high pressures and temperatures by means of diffraction and spectroscopic techniques.

Most of the reports included in this section can be grouped under the main topic of *Phase transformations*. The materials investigated are as different as the objectives of the studies: from water circulations in subducting slabs and the high-pressure behaviour of minerals stable in the Earth's mantle to the understanding of the outer planets and their planetary ices. These studies use *in situ* techniques combining diamond anvil cells (DACs) loaded with single-crystal or powder samples and X-ray diffraction and/or Raman spectroscopy. The advantage of using these two methods simultaneously is that one obtains complementary results and, hence, a better understanding of the crystal structure and its changes at both macroscopic and local scales. Some of these studies show how the constant improvement of the experimental techniques provides scientists with more accurate data as in the case of powder X-ray diffraction under hydrostatic conditions or allows them to reach the extreme conditions present in the Earth's lower mantle in order to study the phase transformations of FeO and the *fcc* to *hcp* transition in gold. Analogue materials, however, are still a very important tool for understanding the behaviour of their isostructural compounds stable at the extreme conditions of the deepest Earth. For example, the perovskite - post-peroskite phase relations in $CaIrO_3$, which can be studied using a piston-cylinder apparatus, may give an indication of what to expect for the $MgSiO_3$ perovskite to post-perovskite transition which occurs near the Earth's lower mantle-core boundary.

The behaviour of a material is not only defined by the characterisation of its phase transformation with pressure and temperature, but also by the accurate determination of its *Equation of state (EOS)*. Two studies in this section investigate the effect of cation substitution and ordering on the compressibility of two important rock-forming minerals: orthopyroxene and spinel.

The last two reports of this section have developed new experimental and analytical methods to adapt *Mössbauer spectroscopy* to the study of oriented single-crystals and of glasses. One has embarked on a single-crystal Mössbauer study of almandine to clarify an asymmetric quadrupole doublet for the cubic crystal. The other has conducted a ^{57}Fe Mössbauer spectroscopy in Fe-bearing alumino-silicate glasses as a complementary method to neutron

diffraction and computation studies, to examine the short-range order around Fe atoms (*i.e.* Fe-coordination numbers).

a. *Raman spectroscopy of the 10-Å phase at simultaneously high pressure and high temperature (P. Comodi, F. Cera and S. Nazzareni/Perugia; L.S. Dubrovinsky)*

Several studies have shown that the 10-Å phase [$Mg_3Si_4O_{10}(OH)_2.H_2O$], represents an important phase for storage, transport and release of water in subducting slabs to depths exceeding the stability field of talc. This phase forms from talc at pressures between 3-5 GPa through the reaction: talc + H_2O = 10-Å phase and, at higher pressures, through the fluid absent reaction: talc = 10Å + enstatite + coesite. Petrologic experiments indicated that the 10-Å phase forms by breakdown of antigorite between 5.5 and 6.5 GPa, and recently a real-time XRD study showed that dehydration of antigorite, above 550 °C and between 1 and 5 GPa, induces the nucleation of a phyllosilicate close to the talc structure. The occurrence of this phase is not restricted to the ternary MgO-SiO_2-H_2O system, but an aluminous 10-Å phase has been found in peridotitic systems. In complex ultramafic systems with compositions approaching those of natural lherzolite, a 10-Å phase structure forms at the expense of chlorite and, depending on the amount of H_2O under saturation and on the thermal structure of the slab, the 10-Å phase stability region may reach that of phase A and transfer water deep into the mantle. If the 10-Å phase stability field does not reach that of phase A in the subducting slab, devolatilization may occur, influencing metasomatic processes in the mantle wedge and retro-arc magmatism.

Raman and X-ray diffraction data demonstrated that the 10-Å phase is stable up to 42 GPa at room temperature and that water molecules remain between the sheets, forming hydrogen bonds. Details of the evolution of 10-Å phase with temperature at high pressure are, however, almost unknown. In order to study the *P* and *T* behaviour of the 10-Å phase and to understand how the interaction between water molecules and silicate framework evolves, we carried out Raman spectroscopy experiments simultaneously at high pressure (up to 27 GPa) and high temperature (up to 776 K) in electrically heated diamond anvil cells (Figs. 3.3-1 and 3.3-2). The Raman frequencies of all lattice modes increase monotonically with pressure and slightly decrease with temperature along different isobars. The intensities of the 359 and 679 cm^{-1} bands change in opposite directions with *P* and *T*: the differences in relative intensities increase with pressure, whereas decrease with temperature. The stretching bands of H_2O show different behaviours with *P* and *T*: the frequency of the 3597 cm^{-1} mode decreases with pressure ($d\nu/dP$ = -0.81 cm^{-1} GPa^{-1}) and increases with temperature ($d\nu/dT$= 0.025 cm^{-1} K^{-1}), the frequency of the 3672 cm^{-1} mode increases with P($d\nu/dP$ = 1.38 cm^{-1} GPa^{-1}) and decreases with T ($d\nu/dT$= -0.011 cm^{-1} K^{-1}) and the hydroxyl stretching frequency at 3622 cm^{-1} increases with both *P* and *T,* as observed in other dense hydrous magnesium silicates (DHMS). The full width at half maximum (FWHM) of the low-frequency lattice modes is independent of

temperature, and increases linearly with pressure up to 22 GPa, pressure at which the Raman signals disappear. However, the reversible behaviour and recovery of the signals during decompression suggest that the metastability limit is reached, but no amorphization occurs. Temperature strongly affects the FWHM of the 3597 cm^{-1} mode, which disappears at 770 K and about 9 GPa, whereas at room temperature it may be followed to about 12 GPa. These observations indicate that temperature favors hydrogen bond formation, as a consequence of the higher thermal motion.

The frequency shifts were used to determine isothermal and isobaric Gruneisen mode parameters, which are significantly larger than those of talc. The small values of the calculated average of the intrinsic anharmonic parameters, $\langle a_i \rangle$, of 0.52 10^{-5} K^{-1}, also indicate that a quasi-harmonic vibrational model may be used to describe the thermochemical properties of the 10-Å phase. Finally, H*P*-H*T* Raman spectra indicate that the 10-Å phase can host water at high *P*/*T* gradients and that it may be a good candidate for transferring water in the mantle beyond the antigorite stability field.

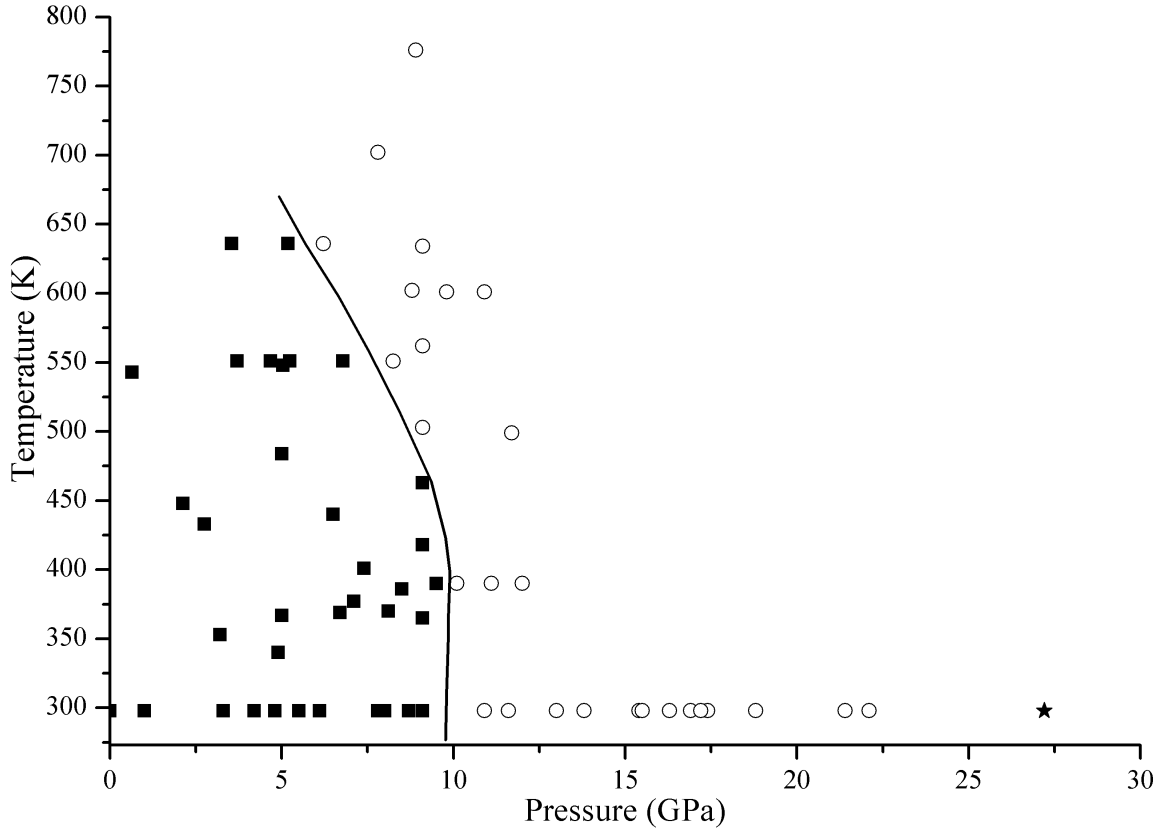

Fig. 3.3-1: *P-T* conditions of the collected Raman spectra. Filled symbols: *P-T* conditions in which three vibrational bands were observed in the OH stretching region; open symbols: *P-T* conditions in which only two bands were observed in the OH stretching region. Star: pressure at which all stretching frequencies disappeared.

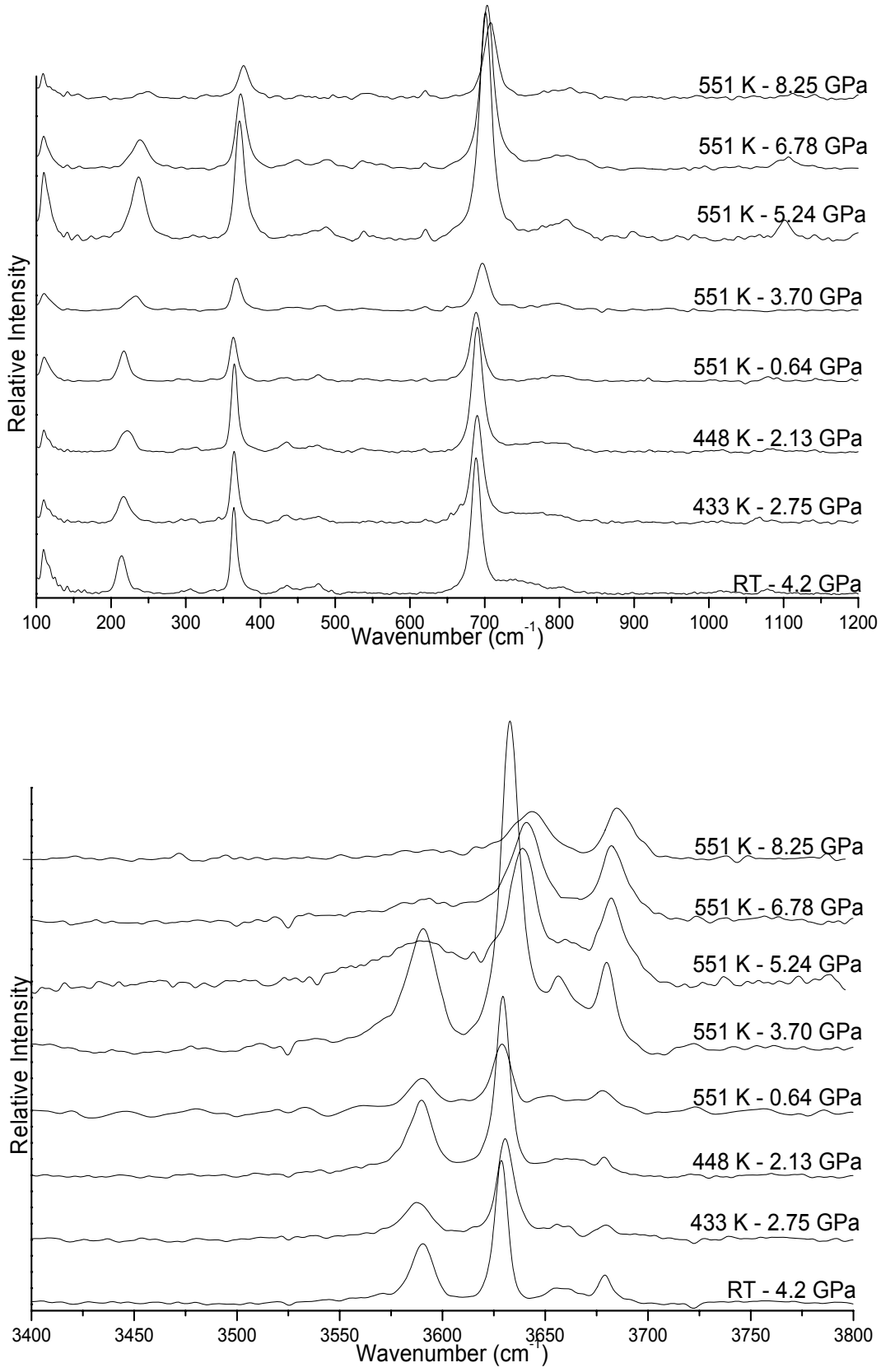

Fig. 3.3-2: Low-frequency (top) and high-frequency (bottom) regions of the Raman spectra collected at different pressures and temperatures.

b. *Is the P-induced inverse-to-direct spinel phase-transition in magnetite real? (G.D. Gatta/Milano, T. Boffa Ballaran, I.Yu. Kantor, L.S. Dubrovinsky and C.A. McCammon)*

Magnetite, $Fe^{3+}(Fe^{2+}Fe^{3+})O_4$, is one of the most studied minerals belonging to the spinel group. With magnesioferrite and maghemite, magnetite represents one of the few spinels with the "inverse" structure. Magnetite is of great importance for petrology, being a common mineral and important phase for geothermometry and oxygen barometry (for example, magnetite/ilmenite geothermometer and oxygen barometer). The presence of magnetite in rock assemblages indicates certain reducing/oxidizing condition, since at high oxygen fugacity magnetite transforms to hematite Fe_2O_3, and at low oxygen fugacity to wüstite FeO. In the past years, there have been a number of reports suggesting a phase transformation in magnetite at about 8 GPa. These previous studies, based on high-pressure synchrotron powder diffraction data and on Mössbauer data, suggest a change of tetrahedra and octahedra relative volumes in the spinel structure and a spinel coordination crossover. The data, however, are not enough accurate to properly constraint such transformation. Therefore, we performed a H*P* single-crystal diffraction experiment aimed at exploring the 0-13 GPa range.

Magnetite single crystals of ~ 200 μm size have been synthesized in a gas-flowing furnace at Bayerisches Geoinstitut. Crystals were enriched with ^{57}Fe to make further high-pressure Mössbauer spectroscopic studies possible. The crystal structure of the synthetic magnetite sample at room conditions (in terms of atomic position, thermal displacement parameters, bond distances and angles) is in agreement with data already published. A single-crystal of magnetite, 22(1) μm thick, was loaded in a BGI-type DAC with ruby micro-spheres for *P*-calibration and a mixture of ethanol:methanol:water=16:3:1 as pressure medium. Accurate cell parameters were measured with a Huber four-circle diffractometer and data collections for structural refinements were performed with a Xcalibur four-circle diffractometer equipped with CCD at different pressures.

The evolution with *P* of the unit-cell volume of magnetite is shown in Fig. 3.3-3a. The lattice is metrically cubic and no violation of the reflection conditions for the $Fd\bar{3}m$ space group was observed within the pressure range investigated. The Eulerian finite strain *vs* Normalized pressures (*fe-Fe* plot) is shown in Fig. 3.3-3b. The evolution of the ruby R_1-fluorescence line with *P* shows that at *P*>9.5 GPa the *P*-medium is not hydrostatic. This is clearly visible in Fig. 3.3-3b where the *Fe* data point at the highest pressure plots off the trend defined by the other data. The structural refinements performed at 0.0001, 4.99(3) and 9.21(8) GPa show that the oxygen *u*-parameter is practically constant in the pressure range investigated, suggesting that no phase transformation occurs within the *P*-range investigated. On the basis of these preliminary data, we suggest that the elastic behaviour of magnetite may depend on the experimental (hydrostatic or non-hydrostatic) conditions.

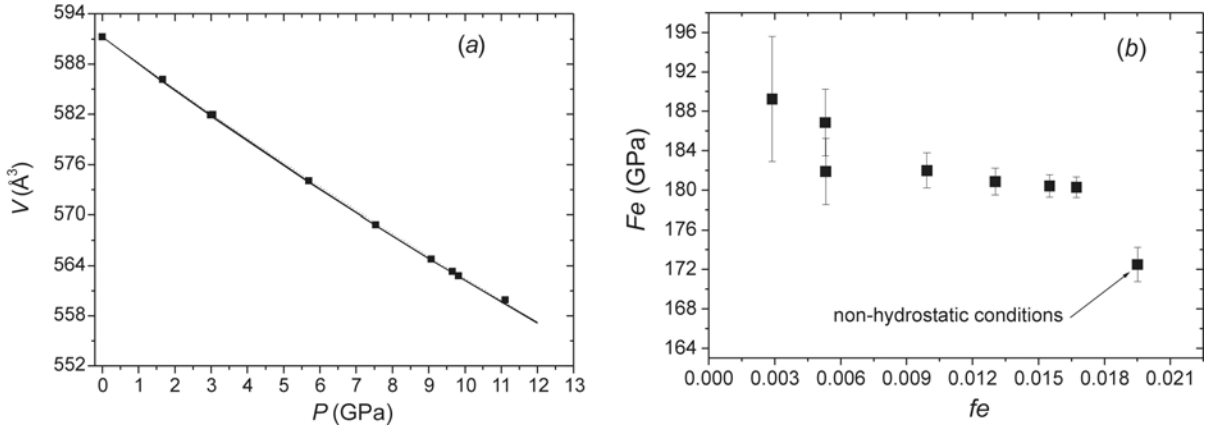

Fig. 3.3-3: *a*) Evolution of the unit-cell volume of magnetite with pressure. The solid line represent the refined II-BM-EoS fit (K_{T0}=179.6(9)GPa). The dotted line (which is almost identical to our fit) represents the II-BM-EoS fit reported by Reichmann and Jacobsen, 2004, Am Min 89, 1061-1066. *b)* Finite Eulerian strain *vs* Normalised pressure (*fe-Fe* plot).

c. *The high-pressure phase transformation of $Na_{0.2}K_{0.8}AlSi_3O_8$ hollandite (J. Liu, T. Boffa Ballaran, L.S. Dubrovinsky, in collaboration with W.A. Crichton/Grenoble*)

Hollandite-type aluminosilicate materials have been a source of renewed interest due to the recent discovery of $(Na,K)AlSi_3O_6$ hollandite-type structure in shocked melt veins of meteorites. Their natural occurrence supports the suggestion of the existence of these minerals as possible hosts of K and Na in the Earth's mantle. However, although the $KAlSi_3O_8$ hollandite end-member is stable over a large *P-T* range, the stability field of $NaAlSi_3O_8$ appears to be very limited (between 20 to 23 GPa and relatively high temperatures). The mixing behaviour of the $(Na,K)AlSi_3O_8$ hollandite system has been investigated (see annual report 2005) and at 1700 °C we observe that up to 50 mol.% of Na can be accommodate into the $KAlSi_3O_8$ hollandite end-member, but no $NaAlSi_3O_8$ hollandite is stable at those conditions. Structural refinements of data collected for $KAlSi_3O_8$ and $Na_{0.2}K_{0.8}AlSi_3O_8$ single-crystals have shown that Na and K are differently accommodated into the cavities of the silicate hollandate octahedral framework, with part of the Na occupying a split position closer to the octahedral walls. This suggests that the ionic radius of Na is too small to stabilise the hollandite structure even at high temperature and pressure. The large amount of possible substitution of Na into the $KAlSi_3O_6$ hollandite end-member, however, may have important effects on the high-pressure behaviour of this mineral and in particular on the tetragonal to monoclinic phase transformation which occurs at high pressure. To characterise such effect we have study the high-pressure behaviour of a sample with composition $Na_{0.2}K_{0.8}AlSi_3O_8$ by means of X-ray powder diffraction with synchrotron radiation.

High-pressure experiments were performed at the beam line HD27 of the ESRF synchrotron facility using a sample of composition $Na_{0.2}K_{0.8}AlSi_3O_8$ loaded in a membrane diamond anvil

cell with He as pressure medium and a ruby as internal pressure standard. The hydrostaticity of the pressure medium allowed the observation of clear splitting of several diffraction lines due to the tetragonal to monoclinic phase transition. The variation with pressure of the *a* and *b* unit-cell parameters are reported in Fig. 3.3-4. The tetragonal *I*4/*m* to monoclinic *I*2/*m* transition is proper ferroelastic with negligible volume strain and with symmetry breaking strains $e_1 - e_2 = (a\sin\gamma - b)/a_0$ and $e_6 = a\cos\gamma/a_0$ following a second order behaviour. The transition pressure P_c = 17.5(5) GPa is 3 GPa lower than that reported for $KAlSi_3O_8$ hollandite end-member. Na substitution, thus, stabilise the monoclinic phase, likely because the framework walls are more distorted than in the tetragonal phase and therefore more apt to accommodate the small Na. Na substitution also affects the high-pressure behaviour of the tetragonal hollandite. Although the bulk modulus of our sample is practically similar to that of the $KAlSi_3O_8$ hollandite end-member considering the uncertainties, the anisotropy of $Na_{0.2}K_{0.8}AlSi_3O_8$ is much larger. The increased compressibility of the *a* axis can be explained by the fact that part of the Na atoms occupy a split position not at the center of the cavity but closer to the wall in the (100) plane.

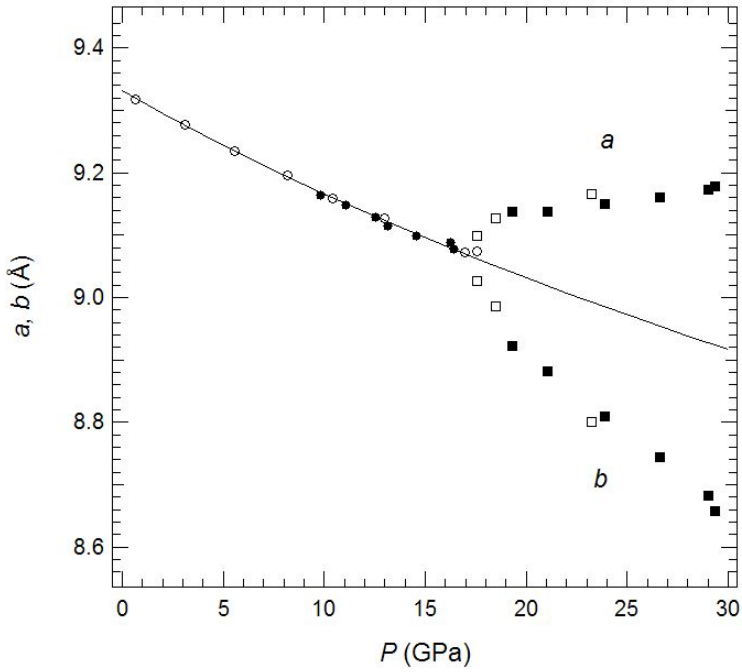

Fig. 3.3-4: Variation as a function of pressure of *a* and *b* unit-cell parameters of hollandite. Filled symbols: data collected under compression; open symbols: data collected under decompression.

d. *The perovskite to post-perovskite transition in $CaIrO_3$ (R.G. Trønnes and S. Stølen/Oslo, in collaboration with D.J. Frost and T. Boffa Ballaran)*

The discovery of a phase transition of $MgSiO_3$-perovskite (Pbnm) to a post-perovskite phase with a $CaIrO_3$-type structure (Cmcm) in the deep mantle has important implications for the

core-mantle boundary heat flux and Earth's dynamics. The Clapeyron slope of the phase boundary is a critical parameter in geodynamical models but cannot be determined very accurately in laser-heated diamond anvil cell experiments. Experiments using suitable analogue compositions where the perovskite to post-perovskite (Pv-PPv) transition can be studied within the pressure ranges of the piston cylinder or multianvil apparatus may therefore be useful.

In a previous study (Hirose and Fukita 2005; Geophys. Res. Lett. 32:L13313) the $CaIrO_3$ Pv-PPv transition was investigated between 1-3 GPa and 1350-1550 °C. The Clapyron slope was found to be between 14-20 MPa/K. We have investigated this transition in order to place narrower constraints on this slope and performed reversal experiments such that the equilibrium boundary could be checked. Experiments were performed in a piston cylinder apparatus using Pt capsules. In addition to the reversal experiments, we also investigated the potential effect of different starting materials including CaO + IrO_2 oxide mixes and oxide mixes reacted at 850-900 °C. The starting material issue is important for $CaIrO_3$, because CaO is hygroscopic and minor amounts of reduced Ir starts to form even in air at temperatures above about 800 °C. Special care was taken to minimize these effects. Figure 3.3-5 shows our results compared with those of the previous study. Our results located the transition at somewhat higher temperatures of 1458-1513 °C at 1-2.5 GPa, with a slightly larger dp/dT-slope of 24-26 MPa/K in comparison to the previous study.

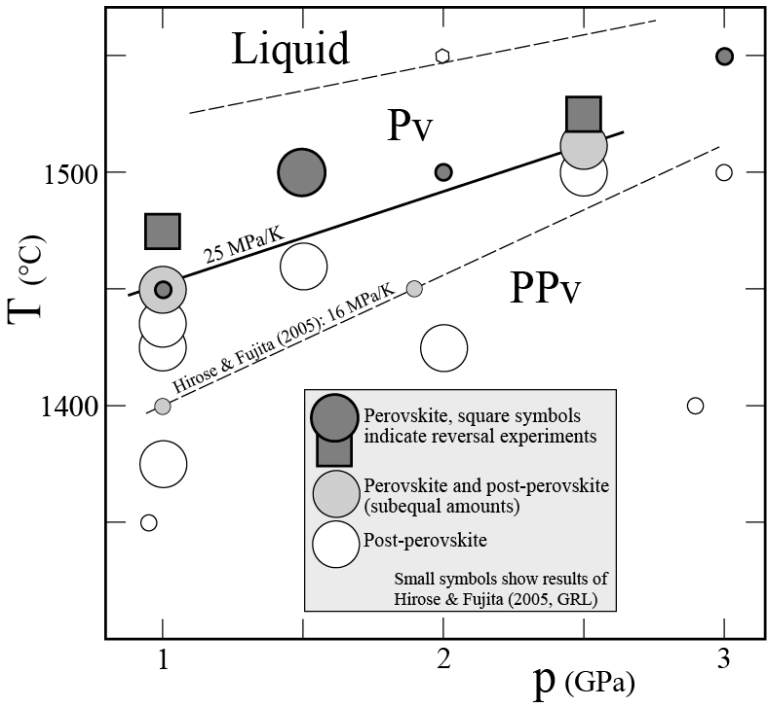

Fig. 3.3-5: $CaIrO_3$ perovskite to post perovskite phase transformation from synthesis and reversal experiments performed in a piston cylinder apparatus. Small symbols refer to the work of Hirose and Fukita (2005, Geophys. Res. Lett. 32:L13313).

The Clapeyron slopes determined for the Pv-PPv transformation in the $CaIrO_3$ system are considerably larger than those estimated for $MgSiO_3$ from first principles and ab-initio models and from modelling of the topography of the upper and lower D"-discontinuities, assuming that these discontinuities are caused by the Pv-PPv transition. Clapeyron slopes ranging from 6 to 10 MPa/K have been used in such geodynamic modelling. Further characterization of the $CaIrO_3$ perovskite and post perovskite phases synthesised in this study is currently underway. Single-crystal XRD, combined with ambient temperature compression and ambient pressure heating experiments are being performed in order to determine the ambient temperature crystallographic structures and elastic properties of these phases. Relaxation calorimetry is being performed to determine thermodynamic properties of the phases.

e. *Monoclinic FeO under high pressure (I.Yu. Kantor, L.S. Dubrovinsky, and C.A. McCammon)*

FeO (mineral wüstite) is the end-member of the (Mg,Fe)O solid solution, the second most abundant phase of the Earth's lower mantle. Its high-pressure and high-temperature properties are important for understanding the structural and physical properties of the Earth. FeO also belongs to the group of strongly correlated transition metal monoxides, some of the most interesting compounds for theoretical studies.

Under ambient conditions FeO is cubic with a NaCl-like structure. At high pressure FeO is known to undergo a symmetry-breaking transition to a trigonal structure. However, above ~ 50 GPa the observed diffraction line positions showed large deviations from those calculated for the trigonal structure, but it was not clear whether the deviations are due to elastic strains under non-hydrostatic stress or to further symmetry reduction.

We performed a high-pressure single-crystal angle-dispersive X-ray diffraction experiment on a $Fe_{0.94}O$ sample using diamond anvil cell up to 80 GPa at ID09 beam line at the European Synchrotron Radiation Facility (ESRF). Based on diffraction line splitting, two transitions were observed in FeO: (1) cubic to trigonal; and (2) trigonal to monoclinic distortion (Fig. 3.3-6). The comparison of our data with that previously reported for the cubic to trigonal transition shows that the transition is first-order in hydrostatic pressure and second-order in non-hydrostatic conditions. Moreover, non-stoichiometry of FeO stabilises the cubic structure. The exact transition pressure for the monoclinic phase could not be established, but at 75 GPa after laser annealing a clear splitting of diffraction lines was observed, fully consistent with a monoclinic lattice distortion. Experimental X-ray diffraction pattern at 75.5 GPa was indexed as monoclinic with the space group $P2_1/m$ (Fig. 3.3-7). Lattice parameters a = 4.630(41) Å, b = 2.929(26) Å, c = 2.735(4) Å, and γ = 58.4(7)º were calculated from 12 diffraction peak positions.

This study shows the first unambiguous experimental observation of the monoclinic phase of FeO under high pressure.

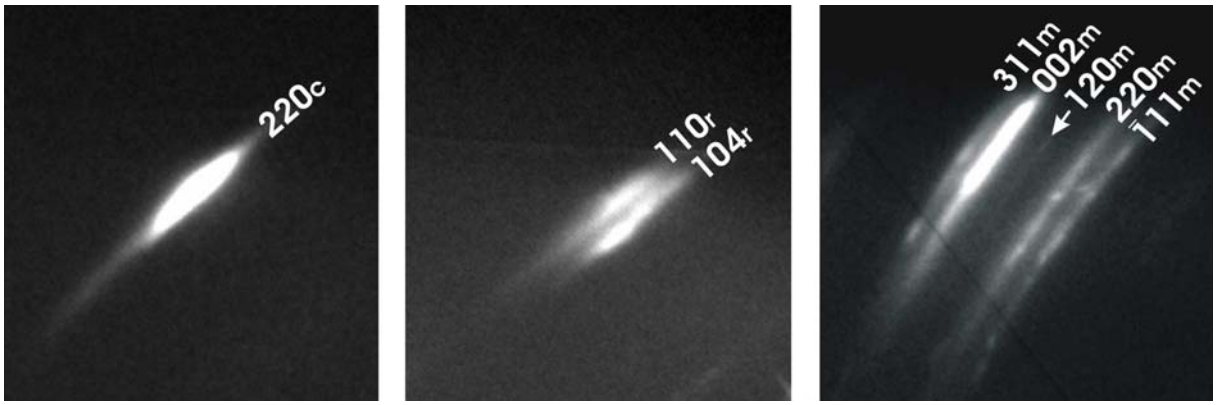

Fig. 3.3-6: Pressure evolution of the FeO cubic 220 reflection. Cubic phase at 11.6 GPa, just below the trigonal distortion (left). Trigonal phase at 24.6 GPa with two reflections, 104 and 110 in trigonal setting (middle). Monoclinic phase at 75.5 GPa with five reflections, -111, 220, 120, 002, and 311 in monoclinic rational ($\gamma \neq 90^{o}$) cell setting (right).

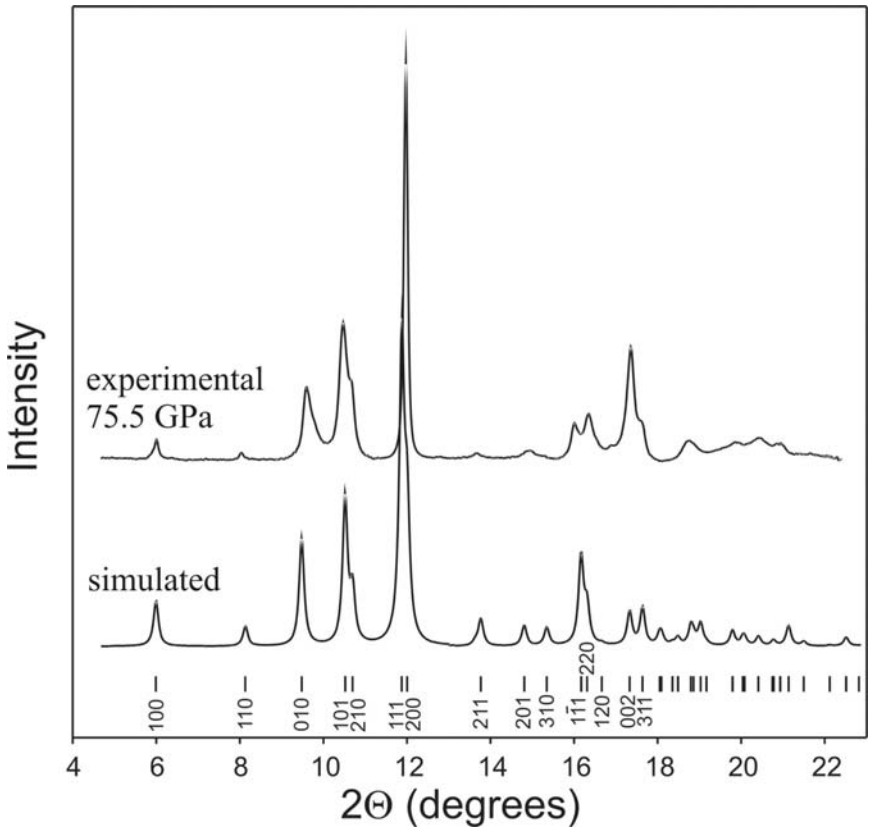

Fig. 3.3-7: Integrated X-ray diffraction pattern of FeO at 75.5 GPa (top) and simulated with the monoclinic space group $P2_1/m$ (bottom).

f. *Phase transition in gold at multimegabar pressures (L.S. Dubrovinsky and N.A. Dubrovinskaia, in collaboration with W.A. Crichton/Grenoble, and A.S. Mikhaylushkin, S.I. Simak, I.A. Abrikosov, J.S. de Almeida, R. Ahuja, W. Luo and B. Johansson/Uppsala)*

The uniqueness of gold and its special role in human society throughout the whole history is closely related to its exceptional stability to chemical reactions at extreme pressures and temperatures. The stability of the solid phase of gold in its *face-centered cubic cell* (*fcc*) structure at pressures up to at least 180 GPa has been reported. Gold has been the subject of many high-pressure research studies for several decades as a primary equation of state (EOS) standard since the large pressure and temperature stability ranges of the *fcc* phase and its large isothermal compressibility make it a very attractive material to be used as a pressure marker above 100 GPa. However, possible pressure-induced phase transition in gold will place a "natural" limit on the application of *fcc* Au as a standard. Laser-driven shock wave experiments did not detect any transitions along the Hugoniot curve up to 10 TPa. Theoretical calculations, however, predict a *fcc*-to-*hcp* phase transformation at pressures between 2 Mbar and 4.1 Mbar (difference in the transition pressure depends on methods and details of calculations). There is also a theoretical possibility of structural phase transformations in complex structure(s) triggered by electronic $s \rightarrow p$ or $s \rightarrow d$ transitions.

We studied experimentally the behaviour of gold at pressures above 270 GPa and temperatures between ambient and 1100 K in externally electrically heated diamond anvil cells (DACs) where temperature gradients within the pressure chamber are practically absent and accuracy in temperature measurements with a thermocouple is within 20 K. Laser-heating was used for relaxing stresses, and X-ray patterns were taken from temperature-quenched samples at high pressure. However, attempts to conduct laser-heating experiments at pressures above 180 GPa failed due to high reflectivity of the gold and/or small thickness of the sample. The *in situ* X-ray high-pressure experiments were conducted at the Bayerisches Geoinstitut (BGI, Germany) and at ESRF (France). At the BGI we obtained powder X-ray diffraction data with a system consisting of Rigaku FRD high-brilliance generator (90 kW) and APEX CCD Area Detector. The MoK_α radiation (tube voltage 60 kV, tube current 55 mA, cathode gun 0.1×0.1 mm) was focused with MaxFlux X-ray optics and further collimated down to 30 μm FWHM beam size. All experiments at pressures above 150 GPa were conducted at the Bayerisches Geoinstitut and, to the best of our knowledge, it is one of the first applications of in-house X-ray facilities at a multimegabar pressure range. The collected images were integrated using the Fit2D or GADDS programs in order to obtain a conventional diffraction pattern.

We conducted three experiments at pressures above 150 GPa and high temperature on pure gold. Upon heating up to 1070 K at pressures below ~ 230 GPa we observed only *fcc* Au. On compression at room temperature *fcc* Au phase was stable at least up to 275(20) GPa (Fig. 3.3-8a). Upon heating the pressure decreased to 248(20) GPa at 860(10) K and we detected

the appearance of new diffraction lines (Fig. 3.3-8b) which could be easily indexed in a framework of the *hcp* structure with lattice parameters a=2.490(2) Å and c=4.060(10) Å, V=6.56(2) cm^3/mol (the coexisting *fcc*-phase has the lattice parameter a=3.520(1) Å and V=6.57(1) cm^3/mol). By slow cooling (over about 8 hours), we observed a gradual increase of the amount of *hcp*-phase, and at room temperature and 236(20) GPa the content of the remaining *fcc*-phase was less than 10 % (Fig. 3.3-8c). The *hcp*-phase could then be compressed up to 270 GPa at ambient temperature (on an attempt of increasing further the pressure the diamonds failed), and on decompression at ~ 230 GPa it transformed back to the *fcc*-phase. Heating the *hcp*-phase-predominate samples at pressures above ~ 230 GPa resulted in transformation to the *fcc*-phase (Fig. 3.3-8d), indicating a positive Clapeyron slope. Investigation of the samples quenched to ambient conditions using SEM and microprobe with a resolution down to sub-micrometers proved the absence of chemical reaction(s), confirmed also by the values of the lattice parameters of Au which resulted to be the same before and after the DAC experiments. In summary, our data indicates that *fcc*-Au transforms to *hcp*-Au and that the transition pressure increases with increasing temperature, in agreement with theoretical predictions.

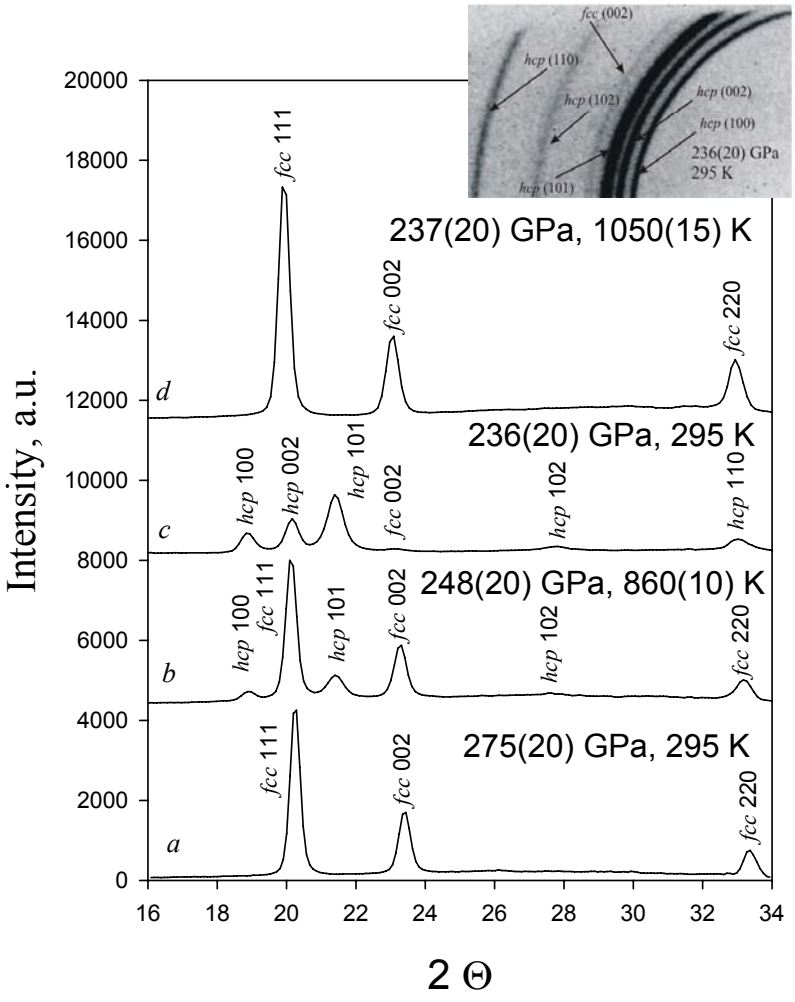

Fig. 3.3-8: Examples of diffraction patterns collected from gold (a) compressed at ambient temperature to 275(20) GPa, (b) heated at 860(10) K at 248(20) GPa, (c) slowly cooled down to room temperature at 236(20) GPa, and (d) heated up to 1050(15) K at 237(20) GPa. Inset shows part of the 2D diffraction image of the sample at 236(20) GPa and room temperature. The pattern is dominated by diffraction lines of the high-pressure *hcp*-Au phase.

g. *A Raman study of methane clathrate hydrates at high pressures (A.V. Kurnosov and L.S. Dubrovinsky)*

"Planetary ices" – H_2O, CH_4, NH_3 – are believed to be the most abundant compounds in the outer solar system after hydrogen and helium. Mixtures of these compounds can form other phases with properties which may differ significantly from the properties of the simple ices. As we have recently shown (see also the last year report), at low ammonia concentrations and over a wide pressure range methane clathrate hydrates are the most stable phases, in the water-methane-ammonia system. Systematic study of these phases will help to understand processes of formation, evolution, internal structure, mechanisms of heat transfer etc. of outer planets and of their satellites.

Here we present the room-temperature high-pressure Raman measurements of three methane hydrate phases as well as two water-saturated methane solid phases. The results are important for understanding the methane-water interactions and give some insight into "anomalous" methane hydrate stability at high pressures. Our observations for hydrates h_1 and h_2 are in good agreement with published literature data. However, at pressures above 2 GPa we found that the spectra previously published should be attributed not to clathrate hydrate phase h_3 but to water-saturated solid methane phase resulted from decomposition of methane hydrate h_2 (Fig. 3.3-9). In the Raman spectra of methane clathrate hydrate h_3, obtained in our experiments and confirmed by X-ray diffraction obtained with the high-brilliance system at the Bayerisches Geoinsitut, the C-H stretching mode is significantly shifted to larger wavenumbers in comparison to the pure methane phase at the same pressures. This indicates the presence of stronger intermolecular interactions in the hydrate phase. In the other hand, the position of the C-H stretching mode of the methane phase (not a hydrate) shows good agreement with the data of Shimizu *et al.* (2002, J Phys Chem B 106, 30-33) mistakenly attributed to the hydrate h_3 by the authors. However at 3-4 GPa these wavenumbers are slightly larger than those reported by Herbert *et al.* (1987, Phys Rev B 36, 9196-9201) for pure methane phase, suggesting in our case the dissolution of some water in the methane phase at these pressures. The pressure dependence of the C-H stretching mode of methane show a break at ~ 4.5 GPa, slightly lower than the transition pressure reported for pure methane. For the methane phase A stable above 5.1 GPa, the positions of the methane stretching mode is very close to those reported by Herbert *et al.* (1987). This is a strong evidence that water can be dissolved in the voids of the I *fcc* structure of solid methane but not in the higher-pressure phase A.

Comparing the Raman spectra of the water-saturated methane in liquid phase and solid phase-I with the literature data of pure methane at the same conditions we can suggest a possible mechanism of water dissolution in methane. The spectra of the liquid phase in the methane-water system are shifted to lower wavenumbers indicating a substitution of methane molecule by water molecule with consequent reduction of the "effective pressure" on the CH_4 molecule. For solid methane phase-I the situation is opposite – our spectra are shifted to larger wavenumbers implying an "inclusion" mechanism, *i.e.* small water molecules occupy the

voids of the *fcc* methane phase. Our spectra of methane phase A stable above 5 GPa do not differ significantly from the spectra of a pure methane system. This indicates that this phase has no more suitable voids to host the water molecules.

In a narrow pressure interval at ~ 2 GPa we found a new methane hydrate phase whose Raman spectrum is similar to that of clathrate phase h_3, but is shifted to lower wavenumbers (see circled area in Fig. 3.3-9). We attribute this to a new methane clathrate phase with one type of cavities. The effective pressure on the methane molecules is intermediate between the pressure in the small cages of structure h_2 and that in the channels of structure h_3.

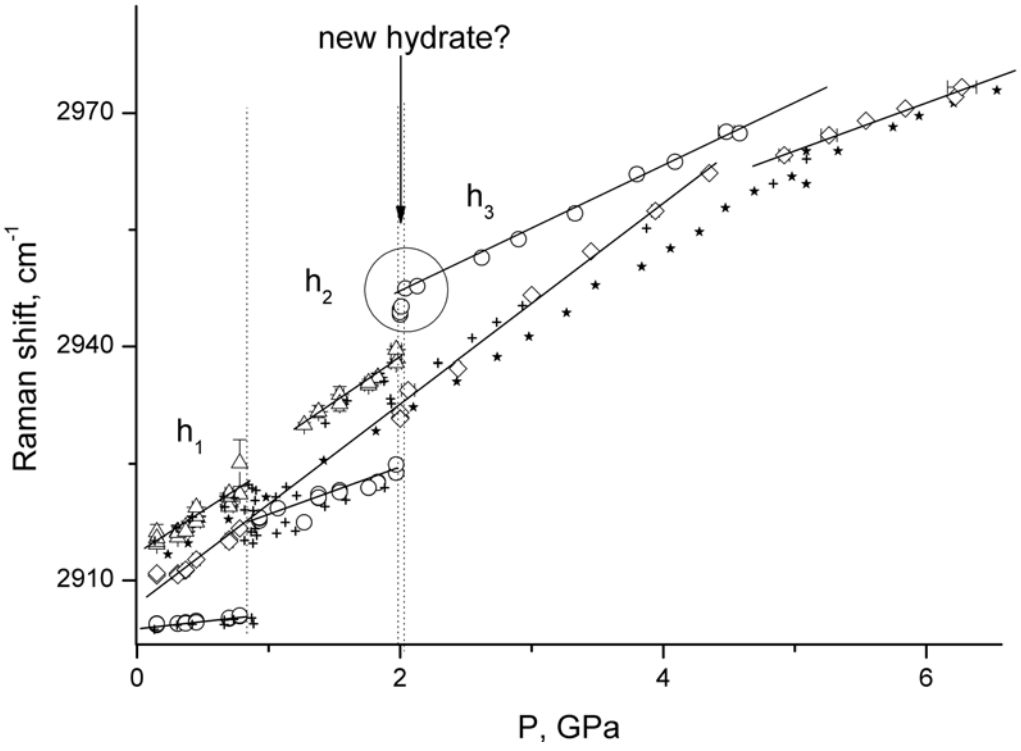

Fig. 3.3-9: Pressure dependence of methane stretching mode in three methane hydrate phases as well as liquid and two solid methane-rich phases in methane-water system. Open circles correspond to methane molecules in large cavities of clathrates hydrates, open triangles: methane molecules in small cavities of hydrate framework; solid stars: pure methane (Herbert *et al.*, 1987, Phys Rev B 36, 9196-9201); pluses: data of Shimizu *et al.*, (2002, J Phys Chem B 106, 30-33) attributed to methane clathrate hydrates.

h. *The effect of Al and water substitution on the high-pressure behaviour of orthoenstatite (T. Boffa Ballaran, in collaboration with F. Nestola/Padova, T. Balic-Zunic/Copenhagen and R. Stalder/Göttingen)*

Next to olivine, pyroxenes are the most abundant constituent of the upper mantle and as such have been investigated intensively. As a result, the compressional behaviour of pure orthoenstatite ($MgSiO_3$, OEN) has been, over the years, well constrained. Natural

orthoenstatite, however, contains usually minor amounts of FeO, CaO and Al_2O_3 which can affect its behaviour at the Earth's mantle conditions. It has been found that Fe substitution has little effect on the equation of state of $MgSiO_3$, whereas Ca substitution stiffens the orthoenstatite structure, and substantially reduces its bulk modulus first derivative *K*'. Al substitution, however, is more complex because it can be associated with incorporation of significant amounts of water which also may modify substantially the physical properties of orthoenstatite.

The compression behaviour of a single-crystal of a synthetic Al-rich orthoenstatite (Al-OEN) with ~ 1400 ppm of water has been investigated up to 9 GPa. The crystal was loaded in a diamond anvil cell with a mixture of 4:1 methanol:ethanol as pressure medium and with few rubies as pressure standard. The variation of the unit-cell volume with pressure (Fig. 3.3-10) reveals that this sample is significantly stiffer than pure $MgSiO_3$, Ca-rich orthoenstatite and natural orthopyroxenes investigated so far. In anhydrous orthoenstatite, Al substitution occurs as Tschermak's component, *i.e.* Al substitutes both at the tetrahedral and octahedral sites according to: $Mg^{VI} + Si^{IV} \rightarrow 2Al$. Two mechanisms of water incorporation have been suggested for orthoenstatite: one involving the substitution of 2H for Mg with consequent formation of a vacancy at the octahedral site, the other involving a coupled substitution of $Al^{3+} + H^{+}$ for Si^{4+} at the tetrahedral site. These two mechanisms might have opposite effects on the high-pressure behaviour of orthoenstatite, since the presence of vacancies is expected to softness the structure of a given material, whereas the $Al^{3+} + H^{+}$ substitution should decrease its compressibility. Our preliminary results suggest that there is, indeed, a marked decrease in compressibility associated with the Al and water substitution in our synthetic sample. However, in order to better constrain the individual effect of Al and water on the OEN structure, further studies of a completely anhydrous Al-OEN and of a more water rich sample are planned.

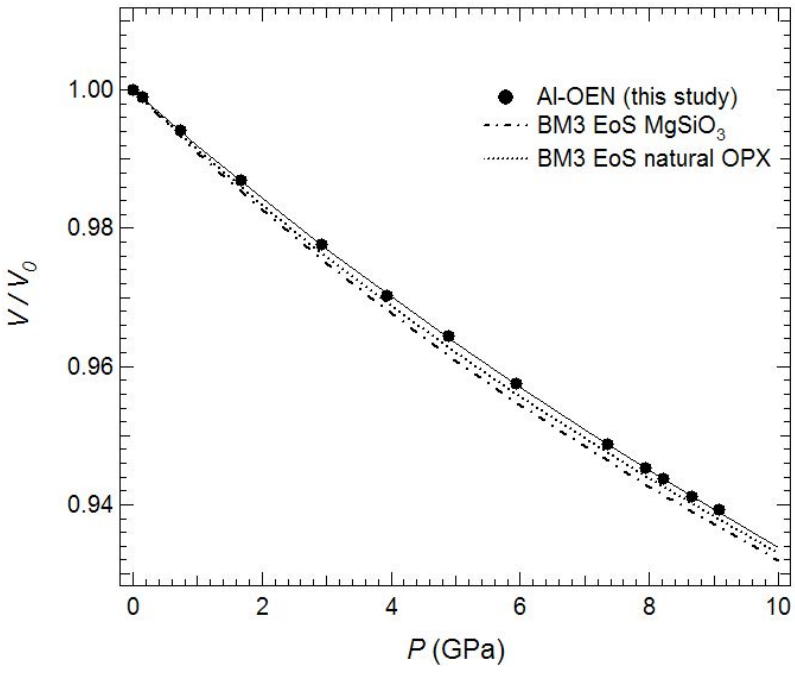

Fig. 3.3-10: Comparison of the unit-cell volume variations of Al-OEN (this study) and the 3rd -order Birch-Murnaghan equtions of state of MgSiO3 orthoenstatite (Angel and Jackson, Am. Mineral., 87, 558-561, 2002) and of a natural orthopyroxene (Hugh-Jones *et al.*, Phys Chem. Minerals, 24, 301-310, 1997).

i. *The effect of cation ordering on the high-pressure crystal structure behaviour of natural spinel $MgAl_2O_4$ (F. Nestola/Padova, T. Boffa Ballaran, T. Balic-Zunic/Copenhagen, F. Princivalle/Trieste, L. Secco/Padova and A. Dal Negro/Padova)*

Spinels, with general chemical formula AB_2O_4 (with A a divalent and B a trivalent cation) are among the most studied oxide phases in Earth Sciences. This mainly is due to the fact that they are used as petrogenetic indicators as well as structural models for minerals stable at pressure/temperature of the Earth mantle. Spinel *sensu strictu*, $MgAl_2O_4$, is one of the most common spinels and has been over the year the subject of many studies. However, although its high-temperature behaviour is well established, the same cannot be said about its high-pressure behaviour. Only four investigations report high-pressure data of $MgAl_2O_4$. These are in general agreement about the bulk modulus value, which varies between 190 and 194 GPa, but do not complete clarify the crystal structure behaviour at high-pressure especially in terms of different cation order or stoichiometry effects.

In order to characterise the high-pressure behaviour of spinel $MgAl_2O_4$ with different degree of order we have performed a comparative study *in situ* at high pressure on two natural single-crystals of pure and stoichiometric $MgAl_2O_4$. The two samples studied were cut from a larger single crystal and one of them was disordered at high-temperature. The two crystals, showing an inversion parameter x of 0.27 and 0.15 at ambient conditions, were loaded together in a diamond anvil cell and their unit-cell edge was measured up to about 7.5 GPa at 14 different pressures (Fig. 3.3-11). The unit-cell volume, V_0, the bulk modulus, K_{T0}, and its first pressure derivative, K', were simultaneously refined using a third-order Birch-Murnaghan equation of state, giving the following coefficients: V_0 = 529.32 (2) Å^3, K_{T0} = 193(1) GPa, K' = 5.6 (3) for the ordered sample and V_0 = 528.39(2) Å^3, K_{T0} = 192 (1) GPa, K' = 5.4 (3) for the disordered one.

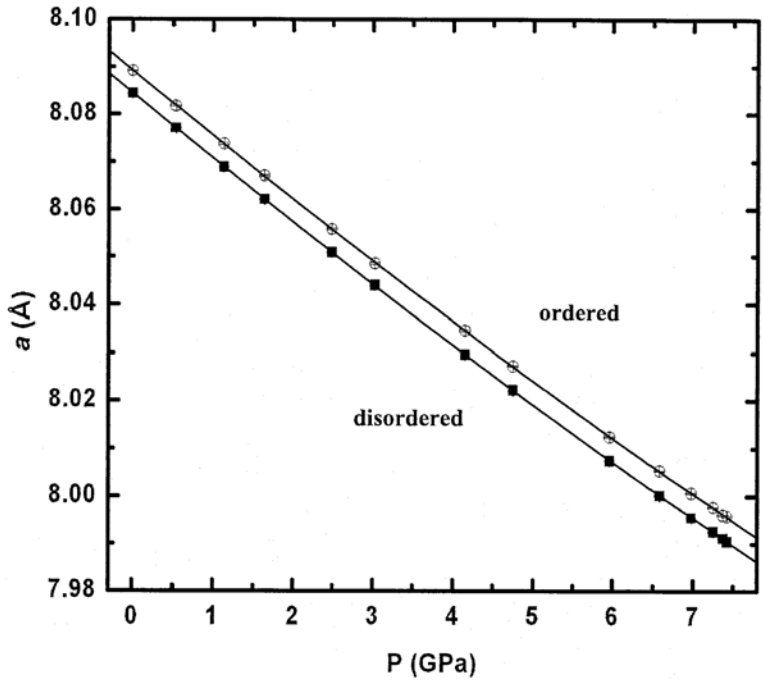

Fig. 3.3-11: Evolution of the unit-cell edge with pressure for ordered (open circles) and disordered (filled squares) spinels studied in this work. Standard deviations are smaller than the symbols used.

Complete intensity data were collected at 0, 0.44, 2.92, 7.34 and 8.03 GPa. For the ordered and disordered samples the oxygen atomic coordinate *u* at room pressure is 0.26331(5) and 0.26168(6), respectively, and remains constant up to high pressure for both samples (Fig. 3.3-12). As a consequence, the polyhedral compressibilities are similar and the Mg/Al distribution over the two crystallographic sites does not vary as a function of pressure. Our data, measured on single-crystals, allowed us to confirm that for spinel structures pressure only does not promote any cation intracrystalline process.

Ringwoodite (Mg_2SiO_4), the most abundant phase of the transition zone, has a spinel structure. Investigations on the high-pressure, high-temperature behaviour of such phase normally are carried out on synthetic samples which may show some disorder of Mg/Si. From the results of this study it appears, however, that such disorder has practically little effect on the compressibility of ringwoodite.

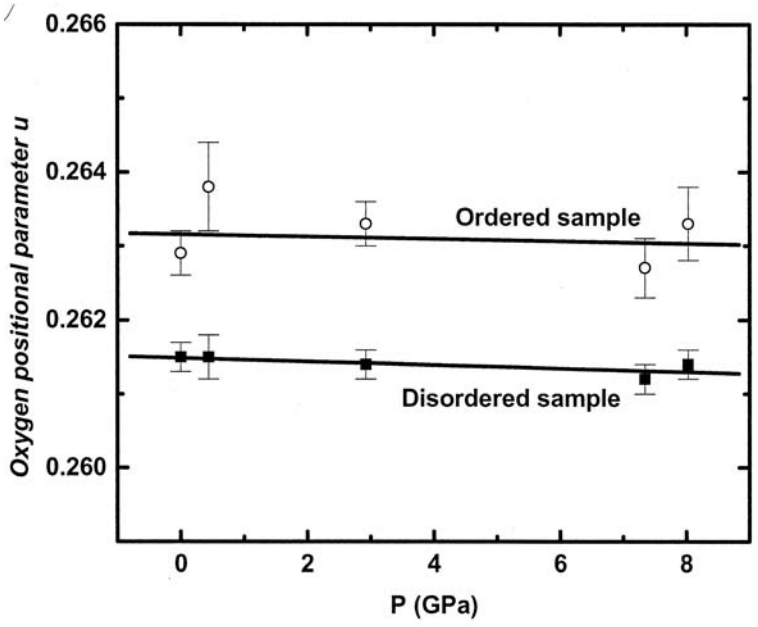

Fig. 3.3-12: Oxygen coordinate *u* as a function of pressure for ordered (open circles) and disordered (filled squares) spinels investigated in this study.

j. *Recoil-free fraction anisotropy in single-crystal almandine (C.A. McCammon, in collaboration with C. Tennant/Christchurch, F. Nestola/Padova and H. Spiering/Mainz)*

Mössbauer spectroscopy measurements of single crystals of pyrope-almandine garnet, obtained as inclusions from diamonds, have been commonly observed to give an asymmetric quadrupole doublet, which is a surprising result for a cubic crystal. The mineral has also been widely studied in polycrystalline form using Mössbauer spectroscopy, and the results also invariably show an asymmetry in the quadrupole doublet. A number of different reasons have been suggested in the literature to account for the asymmetry, including anisotropic recoil-free fraction, spin-spin relaxation, and closely overlapping doublets with slightly different hyperfine parameters. To resolve this question, we embarked on a single-crystal Mössbauer

study of single crystal almandine in conjunction with theoretical calculations of the angular dependence of the component intensity ratios.

The single crystal chosen for this study was selected from a set of near end-member naturally-occurring almandine, originally characterised and reported by A. Woodland and colleagues. We broke the crystal into three pieces, and used one to obtain a full structure refinement using X-ray data, one to perform electron microprobe analysis, and one to collect Mössbauer data. The latter crystal was oriented using X-ray crystallography and a slice taken perpendicular to [101] which was doubly polished to a plate of roughly 400 × 300 μm dimension with thickness 199 μm. We used a crystal orientation technique reported in the literature that rotates the crystal about a fixed axis oriented at 45° to the gamma beam. The gamma beam then traces out a cone in the crystal, enabling a large number of observations in a general set of crystal orientations, so that the extraction of Mössbauer parameters is over determined. A description of the construction and testing of the stage is given in BGI Annual Report 2005. Mössbauer spectra were collected using a point source ("milliprobe" technique) in 20° intervals around the 360° rotation of the stage and processed using two separate analysis procedures: first, a fit to background-corrected area ratios and second a full transmission integral fit.

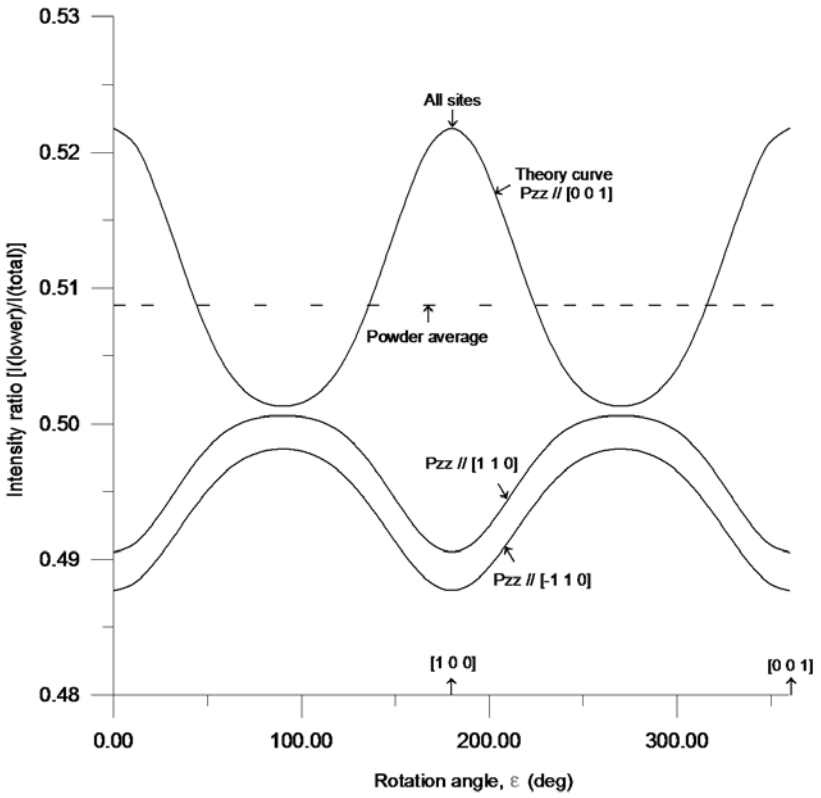

Fig. 3.3-13: Theoretical calculation of the angular dependence of intensity ratios of quadrupole doublet components in the room temperature Mössbauer spectra of almandine. The principal axis of the intensity tensor, P_{zz}, is taken to lie along the *c*-axis, as both the mean squared displacement and electric field gradient tensors are close to uniaxial.

The theoretical angular dependence of intensity ratios was calculated based on the electric field gradient and mean squared displacement tensors using the X-ray determined mean-square displacements and hyperfine parameters from earlier polycrystalline Mössbauer studies of almandine. Calculations were made for each of the six symmetry-related sites occupied by Fe^{2+} in the garnet structure, which were summed since all six symmetry-related tensors contribute to the same quadrupole doublet (marked "All sites" in Fig. 3.3-13). Also, the intensities were summed over all single crystal orientations to obtain the powder average (marked "Powder average" in Fig. 3.3-13). Preliminary fits of the experimental Mössbauer data to the theory curve in Fig. 3.3-13 show several encouraging features: (1) the intensity ratio always exceeds 0.5 as predicted; and (2) the periodicity and general shape of the plot match the theory curve extremely well. Further analysis using a program to refine data simultaneously from all angular-dependent Mössbauer spectra is underway.

k. *^{57}Fe Mössbauer spectroscopy in alumino-silicate glasses (C. Weigel and C.A. McCammon, in collaboration with G. Calas/Paris and S. Rossano/Marne La Valée)*

Despite the growing number of studies performed to determine the structure of iron-bearing silicate glasses, the nature of the environment surrounding iron is still debated. Fe^{3+} and Fe^{2+} are reported to be 4-, 5- or 6-coordinated, but no consensus has been found. To provide new insight to this problem, we have investigated glasses along the join $NaAlSi_2O_6$-$NaFeSi_2O_6$ using Mössbauer spectroscopy. In our glasses Fe^{3+} was found to be the dominant species (~ 84 % of total Fe using wet chemistry). Al^{3+} is known to act as a network former in these sodo-silicate glasses: $[AlO_4]$ tetrahedra are corner-linked to $[SiO_4]$ tetrahedra to form a fully-polymerised network. This work was performed in the context of a larger study involving a number of complementary methods to determine whether Al^{3+} and Fe^{3+} showed the same structural behaviour along the join. Within this larger study, a neutron scattering experiment with isotopic substitution of Fe was performed in combination with numerical simulation on the $NaFeSi_2O_6$ glass. This study revealed the presence of two populations of Fe^{3+} sites: 95 % of Fe^{3+} is in tetrahedral sites (d_{Fe3+-O}=1.866±0.001 Å), and the remainder of Fe^{3+} and Fe^{2+} (~ 20 % of total Fe) is 5-coordinated. We used Mössbauer spectroscopy as a complementary method to examine the short-range order around Fe atoms.

Glasses are structurally characterised by a lack of long-range order. Site geometries are distributed, so hyperfine parameters in Mössbauer spectroscopy are distributed, too. Hence the methods used to extract site parameters from Mössbauer spectra cannot directly be transferred from minerals to glasses, but need to be adapted to the case of glasses. In this study we used the extended Voigt Based Fitting (x-VBF) method, which assumes that hyperfine parameters are distributed according to a two-dimensional Gaussian distribution. All the spectra were corrected for thickness effects before fitting, and are illustrated in Fig. 3-3.14. The figure shows that the intensity of the Fe^{3+} contribution (and thus redox ratio) increases with increasing total iron content. This observation is independent of the fitting model, and provides a criterion by which the validity of fitting models can be tested. Using the x-VBF method, we were able to reproduce the same trend (Fig. 3-3.15), in support of the

fitting approach. Moreover, we found hyperfine parameters for the different samples that were consistent across the composition join, further supporting the validity of the fitting model. The x-VBF fits show that the average centre shift (CS) of the Fe^{2+} and Fe^{3+} distributions are independent of the total Fe content with values CS (Fe^{2+}) ~ 0.85 mm/s and CS (Fe^{3+}) ~ 0.24 mm/s (both relative to α-Fe). According to the literature, CS (Fe^{3+}) ~ 0.24 mm/s is consistent with 4-coordinated Fe^{3+}, which agrees with our previous neutron scattering data. However CS (Fe^{2+}) ~ 0.85 mm/s would be assigned to 4-coordinated Fe^{2+} according to ranges given in the literature, in disagreement with our observation of 5-coordinated Fe^{2+} in the $NaFeSi_2O_6$ glass according to neutron scattering experiments. Since the CS ranges in the literature are often assigned to coordination numbers solely on the basis of empirical observations, there can be limitations. In our previous neutron and computation study we demonstrated that Fe^{2+} is 5-coordinated in these glasses, and if this coordination number is confirmed, it would provide a means to refine the Mössbauer centre shift ranges for a given coordination number.

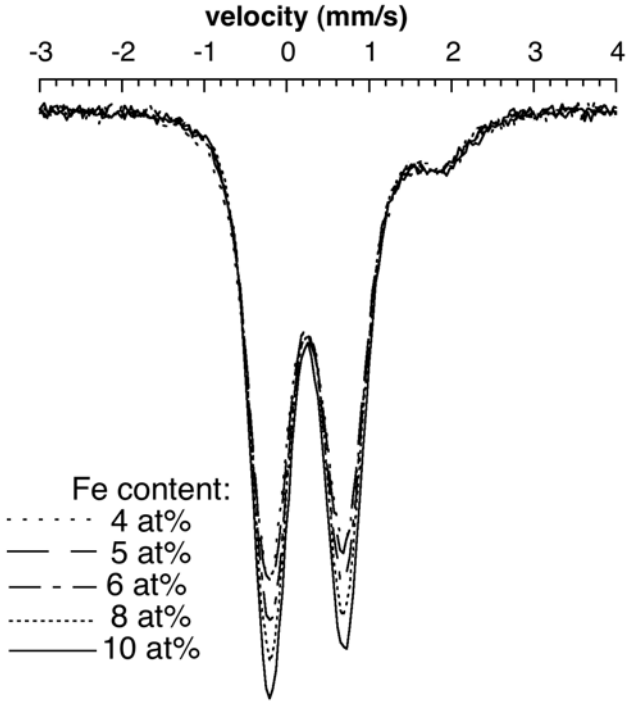

Fig. 3.3-14: Influence of the iron content on thickness-corrected room temperature Mössbauer spectra of $NaAlSi_2O_6$-$NaFeSi_2O_6$ glasses showing the increase in relative Fe^{3+} concentration as a function of increasing total iron content.

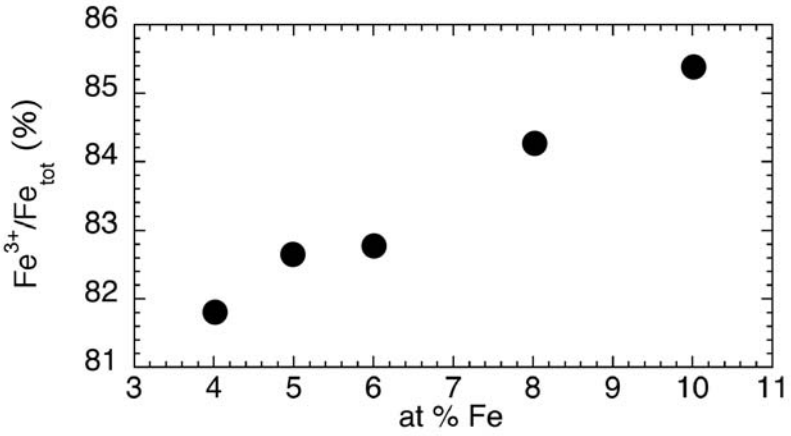

Fig. 3.3-15: Fe^{3+}/Fe_{tot} ratio determined from room temperature Mössbauer spectra of $NaAlSi_2O_6$-$NaFeSi_2O_6$ glasses using the x-VBF method.

3.4 Physical Properties of Minerals

Understanding the physical properties of minerals is a primary goal of modern mineralogy and mineral physics. A full understanding of the composition, mineralogy and structure of the Earth's interior cannot be obtained from direct geophysical observations alone; instead it must come from a combination of disciplines. Researchers at the Geoinstitut seek to constrain the physical, mechanical and chemical properties of the minerals that are occur within the Earth's mantle through experimental and theoretical studies. Theoretical modeling and laboratory measurements of the physical properties (*e.g.*, elastic, optical, and electronic properties of mantle minerals investigated as a function of pressure, temperature, composition and microstructure) provide the information necessary to derive mineralogical and geochemical models of the Earth's mantle. These types of measurements, which form a significant component of the work performed within the Geoinstitut, are also crucial in providing us with information that will lead to an improved understanding of the rheological behaviour of the Earth's interior.

In this annual report, we present results of investigations of the elastic, magnetic and heat-transport properties of mantle minerals. In the first contribution, the stability and elastic properties of Fe-Ni crystalline phases have been investigated at high pressure. Fe-Ni alloy is the main constituent of the Earth's inner core and understanding its elastic properties is essential for establishing the mineralogy, chemistry and temperature of the inner core through the interpretation of seismic data. In the past, most studies have been performed on pure iron and this study represents an important advancement in determining the effects of Ni on phase stability and elastic properties. In the second contribution, the elastic properties of Fe-Al-bearing silicate perovskite have been studied. Silicate perovskite is the main mineral of the Earth's lower mantle and is believed to be the most abundant mineral in the Earth. Understanding its elastic properties is therefore essential for constraining the mineralogy and composition of the lower mantle. Previous studies of elastic properties have concentrated on the pure $MgSiO_3$ end member and the effect of Al substitution has also been investigated but with conflicting results. In the present study, the elastic properties of perovskite crystals with compositions that are appropriate for the mantle have been investigated. The conclusion is that substitution of Al and Fe in the structure has only a small effect on the equation of state. In the third contribution, the optical properties of the other main mineral of the lower mantle, (Mg,Fe)O magnesiowüstite, have been investigated. An important conclusion of this study is that radiative heat transport must be important in the lower mantle, in contrast to previous ideas. This important result will have implications for modeling the thermal evolution of the Earth. The contribution on olivine, the most abundant mineral of the Earth's upper mantle, is concerned with a pressure-induced spin state transition, which is important to understand because of the effects of such transitions on chemical and physical properties. Finally, new results on the magnetic and elastic properties, respectively, of two important accessory

minerals of the Earth's mantle, magnetite and pentlandite, are presented, based on computational studies.

a. *Equation of state of bcc-, fcc-, and hcp-structured phases of iron-nickel alloy $Fe_{0.9}Ni_{0.1}$ (O. Narygina, I.Yu. Kantor, L.S. Dubrovinsky, N.A. Dubrovinskaia)*

As the most abundant constituent of the Earth's core, Fe and its alloys are of great geophysical importance. The density of solid iron at pressures ~ 350 GPa and temperatures of 5000-7000 K may be as much as 5 % lower than the density of the inner core as inferred from geophysical observations. This difference indicates that one or more light elements are dissolved in the Earth's inner core. In addition, nickel (Ni) is also one of the main components of the core, with about 5.5 wt.% being present according to geochemical models. Therefore, investigations of the effects of Ni on the physical properties of Fe alloy under core conditions are essential for geophysical and geochemical models of Earth's deep interior.

The phase diagram and physical properties of Fe as well as alloying effects of Ni on the crystal structure and equation of state have been extensively studied. At ambient conditions the stable phase of Fe is the body-centered cubic (bcc) structure (α-Fe). This phase transforms into a face-centered cubic (*fcc* or γ-Fe) phase upon increasing temperature above 1185 K. At high pressure both *bcc* and *fcc* Fe phases transform into a hexagonal close-packed (*hcp* or ε-Fe) phase, which has a broad *P-T* stability region. However, it has been suggested that, because high pressure stabilizes the face-centered cubic (*fcc*) phase of Ni, γ Fe-Ni alloy may be present in the Earth's inner core.

We have investigated phase transitions in $Fe_{0.9}Ni_{0.1}$ samples by monitoring changes in the X-ray diffraction pattern of laser-heated samples in the pressure range from 0.4 up to 30 GPa. LiF was used as a thermal insulator, pressure transmitting medium and internal pressure standard. Angle-dispersive X-ray diffraction measurements (XRD) were performed at beamline ID27 at the European Synchrotron Radiation Facility (ESRF). The MAR 345 image-plate system, located at a distance of 450 mm from the sample, was used as a detector. The size of the beam on the sample was approximately 10 μm x 9 μm.

We observed that after laser heating of the *hcp* phase at 30 GPa and 1600-1800 K, the *fcc* and *hcp* phases coexist on decompression down to 6 GPa. At lower pressures, both *fcc* and *hcp* phases transform to a single *bcc* phase. Using the GSAS package for a full-profile treatment of the XRD patterns (Fig. 3.4-2) we have refined lattice parameters and molar volumes of the *hcp*, *fcc*, and *bcc* phases as a function of pressure (Fig. 3.4-3). The Birch-Murnagan equation of state was fitted to the data the assuming $K'_0=5$ (Fig. 3.4-3). The obtained values of the bulk modulus K and V_0 for α-, γ- and ε-$Fe_{0.9}Ni_{0.1}$ are presented in Table 3.4-1.

Table 3.4-1: Refined parameters in the third-order Birch-Murnagan equation of state for the α-, γ- and ε-phases of $Fe_{0.9}Ni_{0.1}$.

	K, GPa	K', GPa	V_o, cm^3/mol
Hexagonal close-packed (*hcp*) phase	168.0(3.1)	5	6.875(0.009)
Face-centered cubic (fcc) phase	132.9(3.7)	5	7.107(0.018)
Body-centered cubic (bcc) phase	213.1(20.0)	5	7.094(0.012)

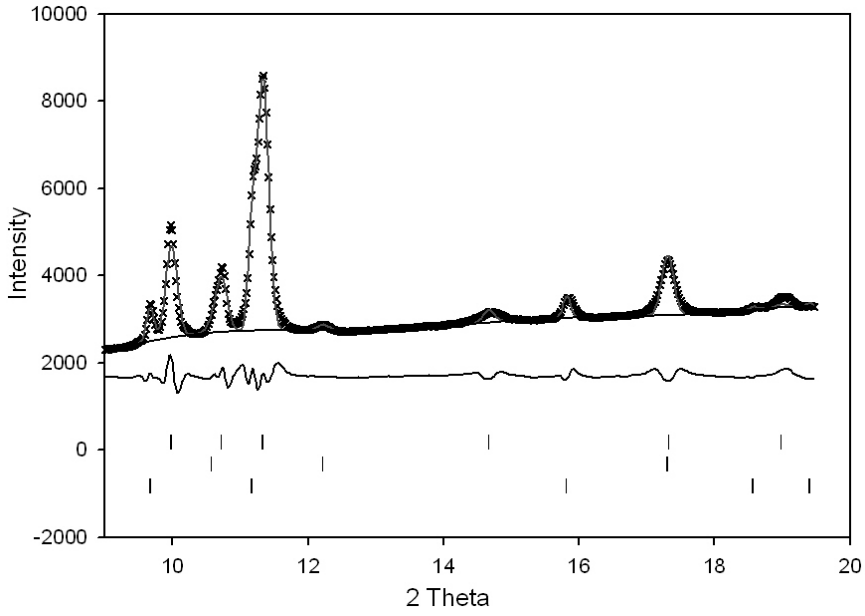

Fig. 3.4-2: Typical example of a fitted X-ray diffraction pattern collected at 15.5 GPa and ambient temperature for $Fe_{0.9}Ni_{0.1}$ alloy. GSAS program package was used to fit the data.

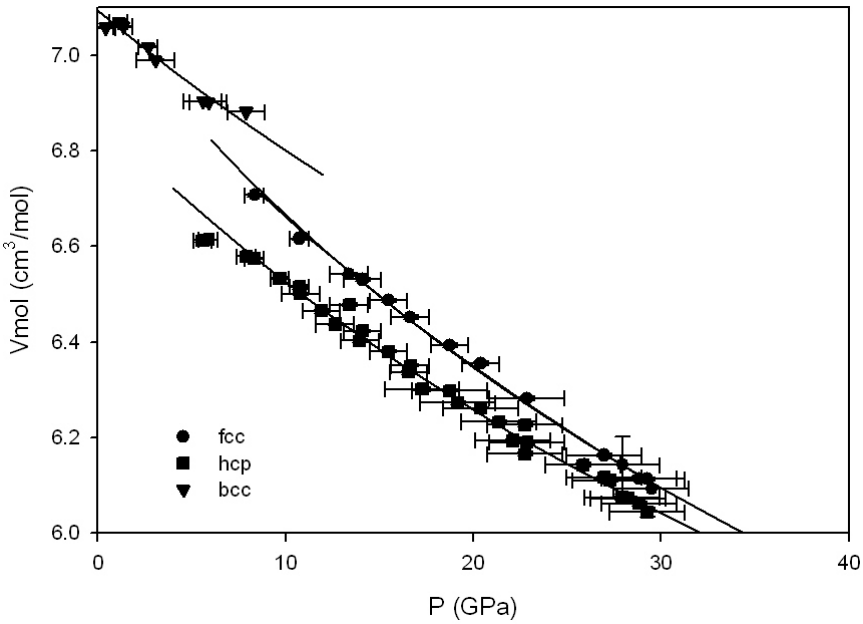

Fig. 3.4-3: Compression curves of the *hcp*, *bcc* and *fcc* $Fe_{0.9}Ni_{0.1}$ phases. Solid lines represent the fitted equations of state (see Table 3.4-1).

b. *The equation of state of (Mg,Fe)(Al,Si)O_3-perovskite as a function of bulk Fe content (A. Saikia, T. Boffa Ballaran, D.J. Frost, D.C. Rubie)*

Magnesium silicate perovskite containing significant amounts of aluminium, ferric and ferrous iron substituted into the structure is considered to be the dominant phase in the Earth's lower mantle. The presence of Fe and Al in perovskite must, to some degree, influence the elasticity, rheology and bulk seismic properties of the lower mantle. Previous studies have proposed that the influence of Al substitution on the equation of state properties of perovskite may depend on the substitution mechanism (*i.e.*, either charge coupled substitution or oxygen vacancy mechanism) by which it is incorporated. In the lower mantle the solubility of Al in perovskite is likely to be charge coupled with ferric iron but changes in Fe partitioning between perovskite and magnesiowüstite could potentially result in conditions where insufficient Fe may be available to balance all Al. Some seismic studies have also argued that there may be regions of the lower mantle that have high Fe concentrations. Previous studies carried out to understand the effects of elements like Al and Fe on perovskite elasticity have reported bulk moduli values ranging from 235 to 265 GPa. This range may well result from different substitution mechanisms that take place when concentrations of trivalent cations are varied. No systematic trends can be observed from previous studies however.

This study was carried out to address the effect of bulk iron content on the equation of state of Al-bearing silicate perovskite using single crystal X-ray diffraction in a diamond anvil cell. Well characterized (Mg,Fe)(Al,Si)O_3 perovskite crystals were employed and measurements were made up to 10 GPa at ambient temperature.

(Al,Fe,Mg)SiO_3 perovskite samples relevant for the mantle were synthesized at 25 GPa and 1800-2000 °C in a multianvil press. Reduced glass powders of the desired composition were loaded into Re and Au foil capsules of 2 mm length and 1 mm diameter and were compressed to 25 GPa using a special 8/3 pressure assembly. Water was added to some experimental runs to promote growth of large crystals. Single crystals with a maximum dimension of 150 microns were recovered on decompression. Compositional characterization was carried out using the electron microprobe and Fe^{3+} and Fe^{2+} ratios were obtained using the Mössbauer milliprobe.

Two high quality crystals were identified with the bulk compositions:
Crystal 1: $(Mg^{2+}_{0.872},Fe^{3+}_{0.088},Fe^{2+}_{0.042},Al^{3+}_{0.007})(Si^{4+}_{0.892},Al^{3+}_{0.108})O_3$; X_{Fe}=0.13
Crystal 2: $(Mg^{2+}_{0.93},Fe^{3+}_{0.035},Fe^{2+}_{0.036},Al^{3+}_{0.012})(Si^{4+}_{0.89},Al^{3+}_{0.097})O_{2.96}$; X_{Fe}=0.07

Room temperature diamond anvil cell compression experiments were carried out in a BGI designed diamond anvil cell with diamond culets of 600 μm. A steel plate indented to a thickness of 90 microns with a 300 micron hole was used as a gasket. A 4:1 mixture of methanol and ethanol was used as a pressure transmitting medium and quartz was used as an internal pressure standard. Unit cell parameters were collected on a four circle Huber

diffractometer using an 8 position centering technique. The unit cell volumes of both crystals are reported as a function of pressure in Fig. 3.4-4. The *P-V* data were fitted with a third-order Birch-Murnaghan equation of state using the "EoS fit 52" software written by R. Angel.

The following EoS parameters were obtained: V_0 = 164.56(1) Å^3, K_0 = 241(2) GPa and K' = 6.4(6) for Crystal 1 and V_0 = 163.688(9) Å^3, K_0 = 240(2) GPa and K' = 6.1(6) for Crystal 2. In order to compare our results with literature data for $MgSiO_3$ perovskite, we also fitted our P-V data with a second-order BM EoS (*i.e.*, K' fixed to 4). The resulting bulk moduli are slightly larger with K_0 = 251(1) GPa for Crystal 1 and K_0 = 252(1) GPa for Crystal 2. This compares with K_0 = 251(2) for $MgSiO_3$ perovskite from the literature. This means that if K' is assumed to be 4 for these perovskite samples then the addition of Al and Fe seems to have no effect on the bulk modulus. However, our data can only be adequately fit by using values of K' that are greater than 4. This implies that the addition of Al and Fe actually lowers the bulk modulus of perovskite and raises K'.

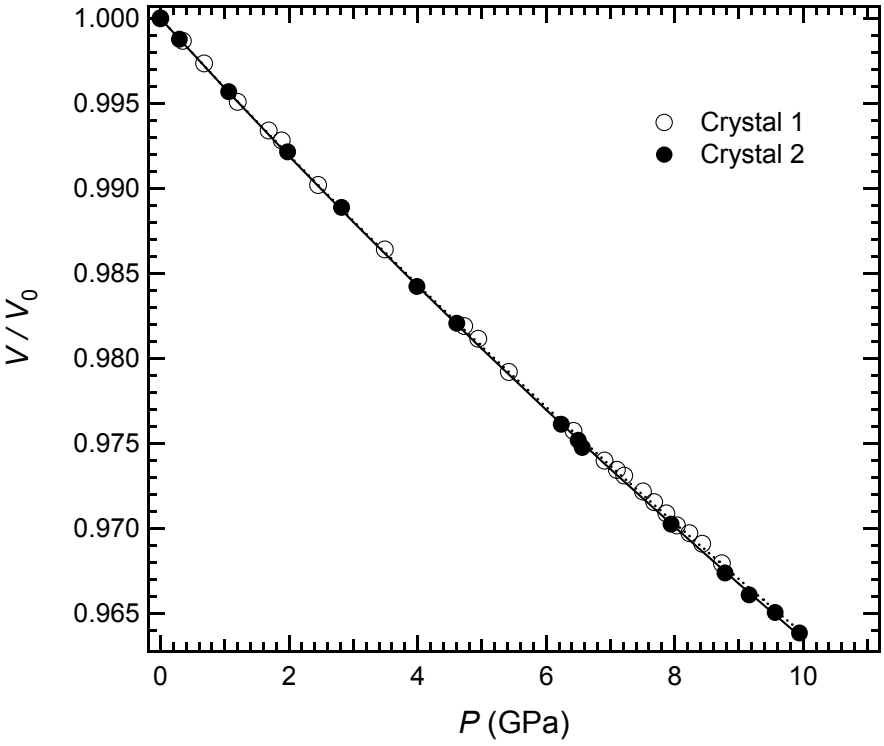

Fig. 3.4-4: Reduced unit cell volumes as a function of pressure for the two (Fe,Mg)(Si,Al)O_3 perovskite crystals investigated in this study.

c. *Optical absorption spectra of ferropericlase to 84 GPa (H. Keppler, I.Yu. Kantor and L.S. Dubrovinsky)*

At the high temperatures prevailing in the Earth's mantle, it would normally be assumed that heat transfer by radiation should be very significant. However, radiative heat transport is

usually completely neglected in models of the temperature distribution in the mantle, because until recently, it was generally assumed that all iron-bearing minerals become optically opaque at high pressures. However, this effect may be due to the fact that the samples investigated in earlier studies contained unrealistically high concentrations of ferric iron.

We therefore studied the optical absorption spectrum of ferropericlase, one of the main constituents of the lower mantle up to 84 GPa using a diamond anvil cell with argon as the pressure medium. The sample we used was synthesized in equilibrium with metallic iron and it was annealed at 25 GPa and 1800 ˚C in order to obtain defect populations and ferric iron contents realistic for the lower mantle.

Typical optical spectra are shown in Fig. 3.4-5. Ferropericlase remains quite transparent up to the highest pressures studied. In particular, there is a pronounced minimum in absorbance in the near infrared region, which pretty much coincides with the maximum of blackbody radiation at lower mantle temperatures. Radiative thermal conductivity is therefore likely to be significant in the lower mantle.

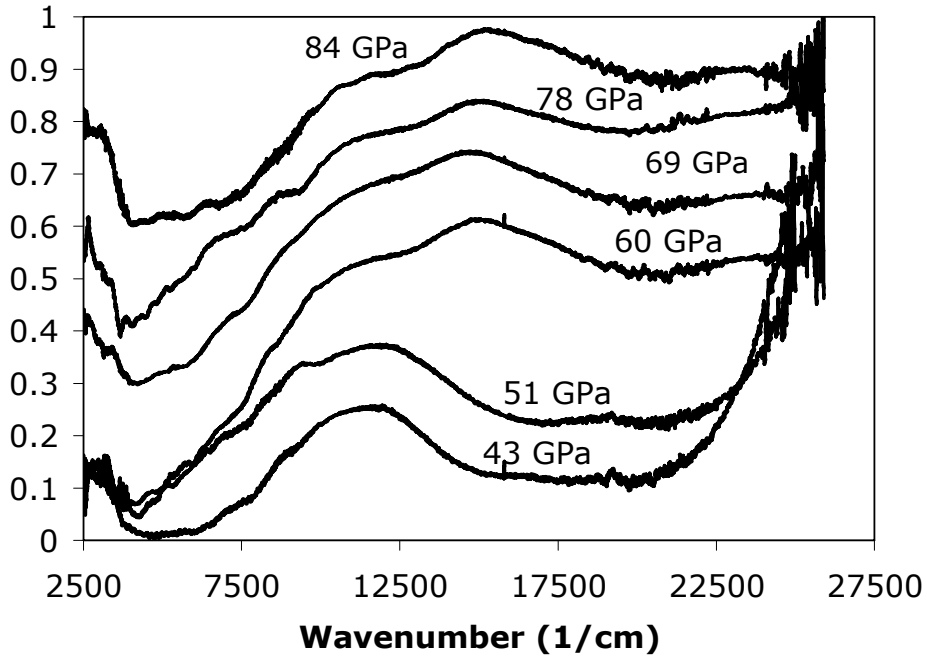

Fig. 3.4.-5: Optical absorption spectra of ferropericlase $Fe_{0.12}Mg_{0.88}O$ to 84 GPa. Thickness is 21 µm. Spectra are offset vertically for clarity. Note the drastic change in the absorption spectrum between 51 and 60 GPa. The slight oscillations below 10,000 cm^{-1} are artifacts (interference fringes).

The spectra also show a major discontinuity between 51 and 60 GPa where a prominent new band appears at about 14500 cm^{-1}. If the change occurring in the spectra between 51 and 60 GPa is interpreted as being due to spin-pairing, *i.e.*, the transition from a high-spin to a low-

spin state, the band positions at 60 GPa allow the crystal field parameters of low-spin Fe^{2+} in ferropericlase to be calculated for the first time. This calculation yields a crystal field splitting Δ of 10,546 cm^{-1} and a Racah parameter B of 376 cm^{-1}. The value of Δ is not very different from that observed for many Fe^{2+}-bearing minerals at ambient conditions. This is a surprising result, as it would imply that spin-pairing, if it indeed occurs around 60 GPa, would not be triggered by an increase in the crystal field splitting Δ, but by a strong reduction of the Racah parameter B far below its free-ion value, implying a higher covalency of the Fe-O bond.

d. *Pressure-induced spin crossover in $(Mg_{0.9}Fe_{0.1})_2SiO_4$ olivine (J. Rouquette, I.Yu. Kantor, C.A. McCammon, L.S. Dubrovinsky and V. Dmitriev/Grenoble)*

Mg-Fe-silicate olivine, $(Mg_{1-x}Fe_x)_2SiO_4$ with x ~ 0.1-0.2, is one of the main constituent minerals in the Earth's crust and upper mantle. Its structural and physical properties are therefore of fundamental importance in geophysics. $(Mg_{1-x}Fe_x)_2SiO_4$ olivine forms a solid solution between the two end-members fayalite (Fe_2SiO_4) and forsterite (Mg_2SiO_4), has the orthorhombic structure (*Pbnm* space group) and contains two types of [Mg,Fe] sites (M1 and M2). In addition to the crystal structure, the electronic configuration of mantle minerals is important because the physical properties of the mantle, such as density, elasticity, rheology and transport properties, are dependent on the electronic states of the constituent minerals at high pressure. Pressure is well known to alter the magnetism of transition metal oxides due to Mott and spin-state transitions. The latter results from spin pairing and occurs when the crystal-field splitting dominates over the exchange energy. The $(Mg_{1-x}Fe_x)_2SiO_4$ solid solution consists of Fe^{2+} ions surrounded octahedrally by ligand ions. The octahedral ligand field gives rise to two possible ground states: the high spin (HS) state ${}^5T_{2g}(t_2^4e^2)$ and the low spin (LS) state ${}^1A_{1g}(t_2^6)$. Numerous spin pairing transitions have already been observed in iron oxide minerals, such as FeO and (Mg,Fe)O, and iron-bearing silicates, such as $(Mg,Fe)SiO_3$ perovskite, using either Mössbauer spectroscopy or X-ray emission spectroscopy. In this study, a $(Mg_{1-x}Fe_x)_2SiO_4$ olivine solid solution (with x = 0.1) was studied at room temperature using Mössbauer spectroscopy, Raman spectroscopy and X-ray diffraction as a function of pressure to provide a more accurate understanding of its electronic state and structural behaviour.

We found evidence for the first time of a transformation in $(Mg_{0.9}Fe_{0.1})_2SiO_4$ olivine at ambient temperature to a metastable spinel structure coupled with a spin pairing transition of Fe^{2+}. Our structural results are consistent with the partial phase transition reported previously in the literature (Fig. 3.4-6), and we observed a transformation in $(Mg_{0.9}Fe_{0.2})SiO_4$ olivine using Mössbauer spectroscopy which we interpreted to be the onset of spin-crossover (Fig. 3.4-7). Based on this phase transition to a metastable form, we infer that only local changes of the olivine structure have occurred that affect the isotropic Fe-O and Si-O bonds with a progressive change of Si coordination from 4 to 6. This is clearly seen in data from the

recovered sample after decompression: 1) no changes in the X-ray diffraction patterns compared to the original ones, and 2) a distribution of quadrupole splitting in the Mössbauer spectrum (Fig. 3.4-7d), implying that high-pressure compression resulted in different local environments for Fe^{2+}. The spin transition occurs over a wide pressure range (Fig. 3.4-8), as observed in other iron-oxide materials, and can be explained by means of interactions between Fe^{2+} clusters due to locally different environments induced by the transformation to the metastable high-pressure spinel form. Such a scenario provides an explanation of pressure-induced amorphisation observed for both Mg_2SiO_4 and Fe_2SiO_4 at higher pressures.

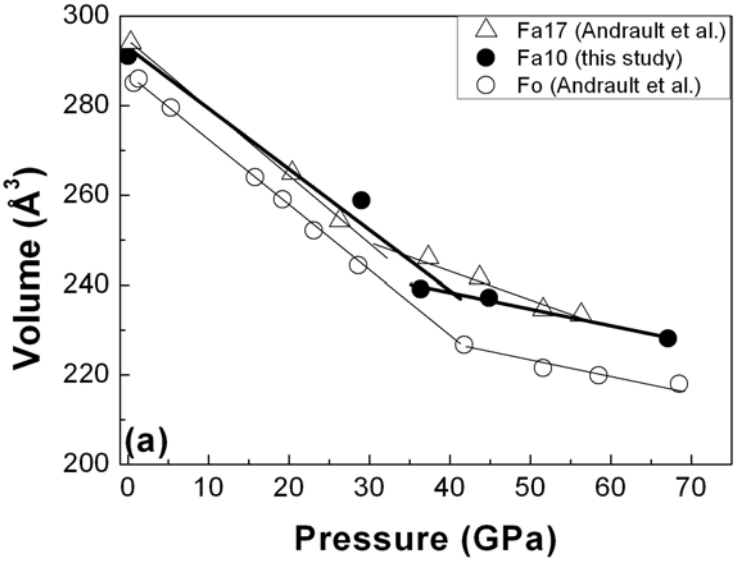

Fig. 3.4-6: Pressure dependence of the unit-cell volumes of $(Mg_{0.9}Fe_{0.1})_2SiO_4$ (Fa_{10}) compared with data of Andrault *et al.* (Phys. Chem. Minerals, 22, 99, 1995) (Fo for x = 0 and Fa_{17} for x = 0.17 in $(Mg_{1-x}Fe_x)_2SiO_4$).

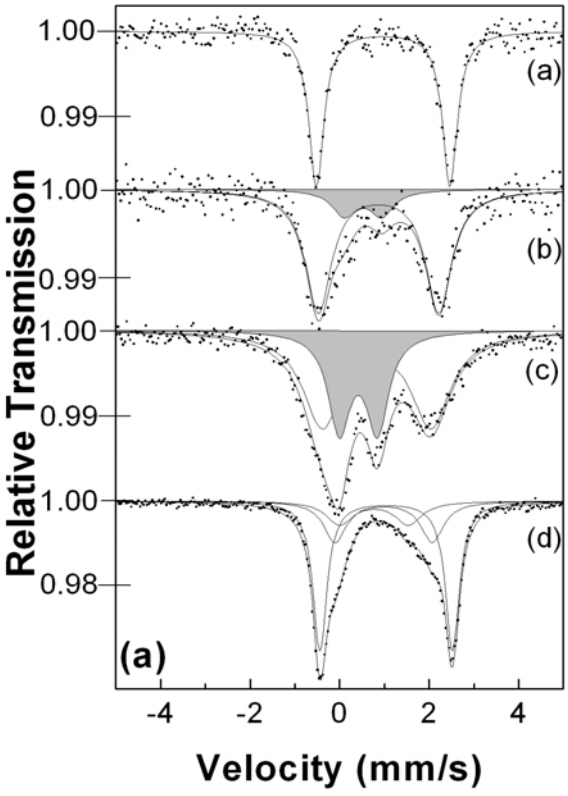

Fig. 3.4-7: Room temperature Mössbauer spectra of $(Mg_{0.9}Fe_{0.1})_2SiO_4$ synthetic olivine in the DAC at: (a) 12 GPa, (b) 52 GPa, (c) 75 GPa and (d) atmospheric pressure after decompression. Components are shaded as follows: high-spin Fe^{2+} (unshaded); low-spin Fe^{2+} (grey). The additional peaks in spectrum (d) are due to high-spin Fe^{2+} in a range of different environments due to the presence of a phase transition associated with strains induced during (de)compression.

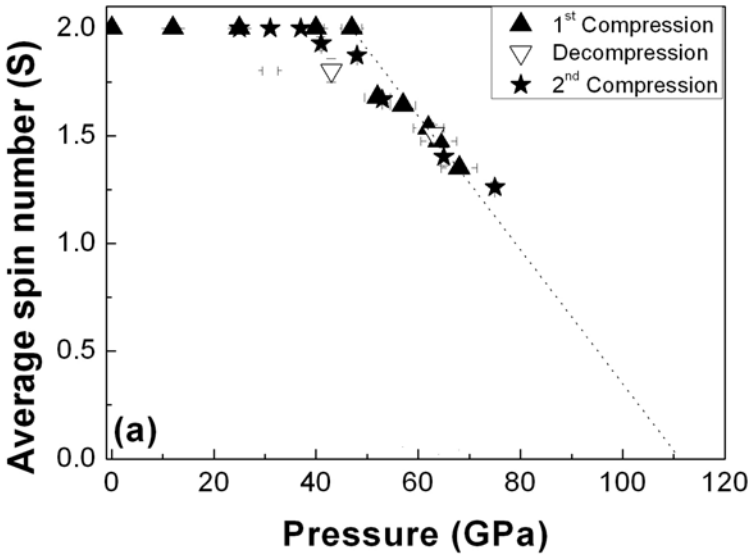

Fig. 3.4-8: Average spin number *S* of $(Mg_{0.9}Fe_{0.1})_2SiO_4$ as a function of pressure from Mössbauer spectroscopy measurements on initial compression (triangles), decompression (inverted open triangles) and subsequent compression (stars).

e. *Nonequivalence of the octahedral sites of cubic Fe_3O_4 magnetite (M.J. Wenzel/Berkeley and G. Steinle-Neumann)*

The magnetic properties of lodestone, Fe_3O_4 magnetite, were first recorded more than 3500 years ago and have been of technological and scientific interest ever since. Quantitative scientific investigation has been ongoing since Gilbert's experiments on the magnetic properties of lodestone and the Earth. At ambient conditions magnetite crystallizes in the cubic inverse spinel structure (Fd-3m). There, Fe^{3+} ions occupy one tetrahedral (A) site and two octahedral (B) sites, with randomly distributed Fe^{3+} and Fe^{2+} ions, in a cubic close packed array of O atoms. Magnetite is ferrimagnetically ordered with the Fe atoms on the A sites having spin opposite to that on the B sites. While experiments at room temperature have demonstrated equivalence between the B sites, with an effective occupation of $Fe^{2.5+}$, electronic ground-state calculations on the cubic structure draw a complex picture: standard approximations to density functional theory (DFT) find equivalency of the B sites while computations using LDA+U on a supercell of the cubic structure yield charge ordering, but differ in the fact that some predict insulating and others metallic behaviour.

Here we use DFT with the GGA and GGA+U approximations to the exchange and correlation potential and investigate the magnetic and electronic structure of Fe_3O_4 magnetite, to explore equivalence in the Fe B sites. We use an all-electron DFT method, the linearized augmented plane wave (LAPW) method as implemented in the Wien2k code. For all calculations we include spin-orbit coupling with magnetization along the *z*-axis. We consider $0<U<4.6$ eV, consistent with previous work on Fe-oxides. For GGA+U computations we start with a case converged in GGA and graduate U in increments of 0.136 eV (10 mRy), converging the result

before increasing U again. For 2.4 eV<U<2.6 eV increments of U as small as $1.36x10^{-4}$ eV are required to converge the results.

Computations are performed for a cell setup in which the two B Fe sites are split, resulting in an orthorhombic description of the magnetite structure, space group Imma, with 3 inequivalent Fe sites (1 A and 2 B sites). This allows charge transfer to take place between the two B sites. We keep the atomic positions and the cell shapes fixed, and perform the computations for the experimental zero-pressure volume. Computations are considered to be converged when in five iterations the magnetic moment and magnitude of the EFG (the largest principal axis component V_{zz} change by less that 0.005 Bohr magnetons (μ_B) and $0.1x10^{21}Vm^{-2}$, respectively.

As the integrated difference between spin up and spin down density of states, the magnetic moment provides a first indication of charge disproportionation. Using GGA we obtain 3.33 μ_B for the A site. The B sites are equivalent with a moment of -3.45 μ_B. The net magnetic moment is -4.00 μ_B per formula unit. The magnitude of the magnetic moment on the A and both B sites shows an increase with increasing U (Fig. 3.4-9), by up to 0.6 μ_B. Due to the canceling effects, the total magnetic moment for the unit cell remains constant, in good agreement with the experimental value of 4.1 μ_B. For U<2.5 eV the B sites are identical. At larger values of U, however, the magnetic moments of the B sites diverge (Fig. 3.4-9).

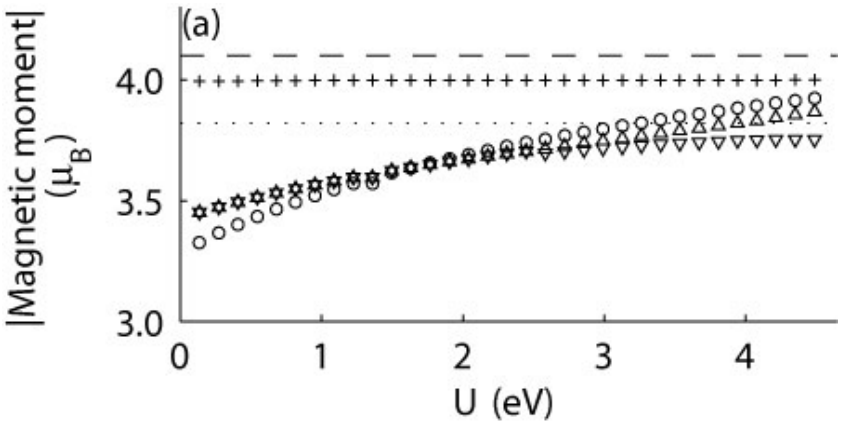

Fig. 3.4-9: Absolute value of magnetic moments of the A site and different B sites (upwards-pointing and downwards-pointing triangles). Crosses show the total moment for the unit cell. The dashed line is the experimental value of the total moment. The dotted line is the experimental value of the A-site magnetic moment.

The EFG tensor is a critical and sensitive indicator of the electron density near the nucleus, reflecting the local structure (anisotropy) of the charge density. As a traceless second rank tensor the EFG is characterized by five elements in the principal axis (PA) system: the largest PA value V_{zz}; the asymmetry ratio $\eta = (V_{xx}-V_{yy})/V_{zz}$; and the three Euler angles of rotation with respect to the global coordinate system. Site symmetry can decrease the number of

elements necessary to characterize the EFG fully. In the Fd-3m structure for Fe_3O_4 the B site has a threefold axis and the EFG is fully characterized by a single principal component V_{zz} ($\eta = 0$). Introducing spin-orbit coupling reduces the symmetry, and the B site EFG PA's may be rotated with respect to the global coordinate system, but due to a twofold rotation axis a rotation is allowed about only one axis. At low U, V_{zz} and the angle of rotation of the PA's are equivalent for the Fd-3m and both Imma B sites. However, the B sites in Imma show some asymmetry at low U while V_{xx} and V_{yy} are approximately the same for Fd-3m up to a U of ~ 2.5 eV. In the Imma case η increases rapidly for U > 1 eV, and reaches a maximum near 2.5 eV. At 2.6 eV, the B sites in the Imma structure become nonequivalent, and show a discontinuous change in *Vzz*, η and rotation angle. It is notable that the cubic case starts to develop asymmetry at the same U of 2.6 eV where the Imma B sites show the discontinuity in EFG (Fig. 3.4-10).

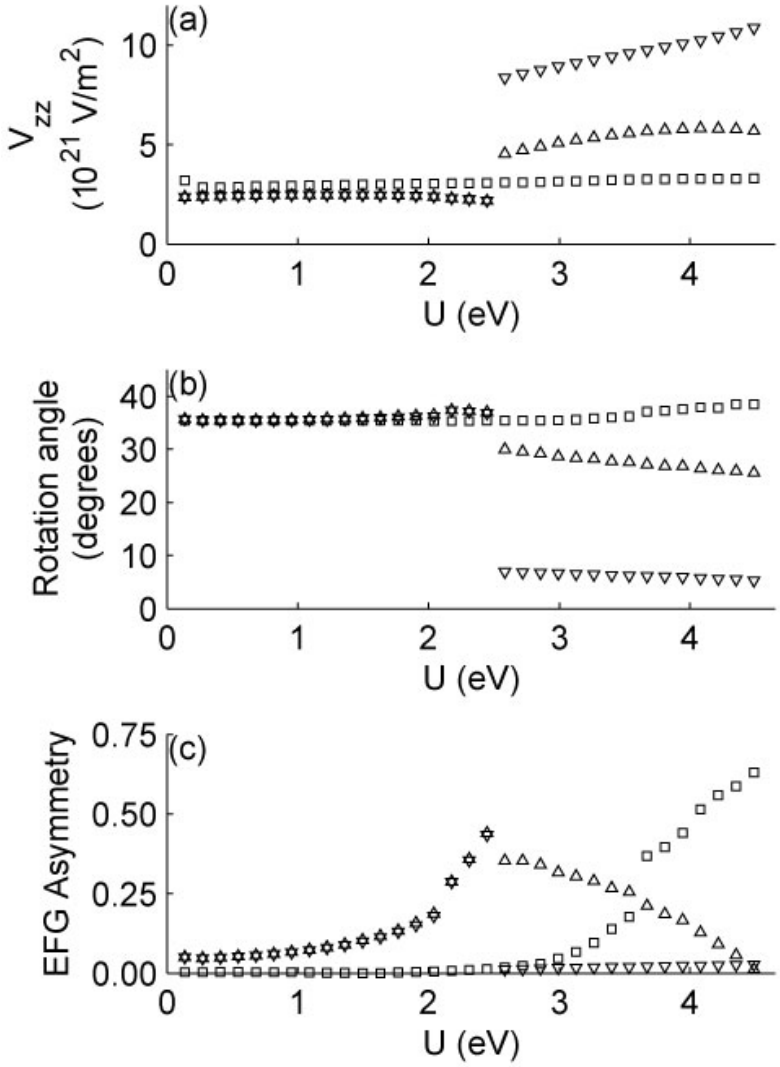

Fig. 3.4-10: (a) Magnitude of the maximum principal axis of the EFG tensor. (b) Rotation angle of the EFG tensor with respect to the global coordinates. (c) EFG tensor asymmetry factor η. Upwards-pointing and downwards-pointing triangles are Imma structure B sites; Squares are Fd-3m B site.

We have shown that for widely accepted values of U there is a clear difference between the two B sites of magnetite in the Imma structure. The equivalence or non-equivalence of the B sites in experiments in the low temperature structure, below the Verwey transition of 120 K, is strongly contested. Above the Verwey temperature the experimental evidence is for equivalence of the B sites. Hence our calculations suggest that the high-temperature cubic phase has intrinsically nonequivalent B sites and thermal activation results in dynamical equivalence. Alternatively, the computed non-equivalence could stem from a too-strong on-site correction, questioning computational results on magnetite and potentially other strongly correlated Fe compounds using the DFT+U formalism.

f. *Compressibility and elasticity of pentlandite $(Fe,Ni,Co)_9S_8$ (R. Caracas)*

Upper mantle xenoliths often contain sulphide inclusions along grain boundaries and within fractures in the silicates. These sulphides belong mainly to the Fe-Ni system and are represented by pentlandite, pyrrhotite and chalcopyrite. They influence the transport properties of the upper mantle, such as electrical conductivity and heat transport and might contribute to the lowering of shear wave velocities. We perform first-principles calculations, based on standard density-functional theory as implemented in the ABINIT package, to determine the compressibility and the elasticity of the bulk materials. We use the generalized gradient approximation with planewaves and pseudopotentials. We start with cation-excess sulfides in the Fe-Ni-Co-S system. Pentlandite is the mineral of choice as it is the main sulphide mineral present in the Earth's upper mantle. The complete Fe-Co-Ni solid solution allows a continuous description of the physical properties to be made in terms of the number of *d* electrons present in the $(Fe,Ni,Co)_9S_8$ system, which varies from 54 for Fe to 63 for Co and 72 for Ni. We perform calculations in the primitive cubic unit cell with 17 atoms for several ordered Fe-Ni-Co substitutions: Fe_9S_8, Fe_8NiS_9, $Co_4Fe_5S_8$, $Fe_5Ni_4S_8$, Co_9S_8, $Fe_4Ni_5S_8$, $Co_4Ni_5S_8$, $FeNi_8S_9$, and Ni_8S_9. Preliminary data show slight increases in volume and compressibility as a function of the number of *d* electrons. Third-order Birch-Murnagham equation of state fits of the P-V data for Fe_9S_8 yield V_0=992.4 $Å^3$, K=130 GPa and K'=4.72 and for Ni_9S_8: V_0=1018.7 $Å^3$, K=134 GPa and K'=4.07. We also envisage investigating properties of Fe-Co-Ni melts, such as density, viscosity and electrical conductivity as a function of pressure and temperature using similar techniques.

3.5 Fluids and their interaction with melts and minerals

Fluids are essential agents of chemical transport in the Earth's crust and mantle. Their properties are, however, notoriously difficult to study. One convenient method for investigating fluids involves the use of synthetic fluid inclusions. These are small droplets of fluid that are trapped in a growing crystal. Alternatively, they may be generated by the healing of fractures, *e.g.*, in a quartz crystal, in the presence of a fluid. Dissolution and reprecipitation of the quartz closes the fracture and traps some of the fluid as inclusions in the crystal. These fluid inclusions can then be conveniently analyzed under ambient conditions, since they act as completely sealed containers of the fluid.

Two studies in this year's annual report make use of synthetic fluid inclusions generated in the laboratory under defined conditions in order to study fluid properties. The first study looks at the oxidation state of sulfur in the fluids evolving from a crystallizing magma in the Earth's crust. The sulfur species detected are very different from those predicted from thermodynamic calculations, probably due to solvation effects in the fluid. In particular, it is found that contrary to predictions, species of hexavalent sulfur are major components in the fluid under conditions typical for many subduction zone volcanoes. This is important, because the sulfur release during eruptions determines the effect of volcanism on climate and this effect can be very different depending on the actual sulfur species present.

The second study using synthetic fluid inclusions looks at the fractionation of copper and gold between liquid and vapor, an effect that may be quite important for enriching some metals in hydrothermal ore deposits. The experiments suggest that under some conditions, metals may become concentrated in the vapor phase.

The properties of fluids in the Earth's transition zone are even more difficult to study than fluids in the crust. Under the reducing conditions in the transition zone, the fluids may consist predominantly of methane. Some preliminary experiments reported in this chapter suggest that such fluids dissolve only very little silicate material and, therefore, are not efficient agents of chemical transport in the mantle. Also, the solubility of water in mantle minerals in equilibrium with such fluids may be strongly reduced.

Finally, as part of continuing efforts at Geoinstitut to quantify the transport and storage of water in the Earth's mantle, water solubility in clinopyroxene has been studied. Water solubility increases strongly with alumina content. These results could be quite important for modeling the recycling of water back into the mantle in subduction zones.

a. *The speciation of sulfur in magmatic-hydrothermal fluids (B. Binder/Tübingen and H. Keppler)*

Sulfur compounds are usually minor constituents of magmatic-hydrothermal fluids. Nevertheless, they control the effects of major volcanic eruptions on climate as well as the

enrichment of various metals in hydrothermal ore deposits. Surprisingly little is known about the type of sulfur species present in hydrothermal fluids at magmatic pressure and temperature conditions. Thermodynamic calculations suggest that H_2S and SO_2 should be the major sulfur species in the fluid, depending on oxygen fugacity, while species of hexavalent sulfur (SO_3 or its hydrated forms such as H_2SO_4) should be negligible.

We trapped sulfur-bearing aqueous fluids as synthetic fluid inclusions in quartz at 0.5-3 kbar, 700-950 °C and oxygen fugacities ranging from the Ni-NiO to the Re-ReO_2 buffer. Oxygen fugacities were controlled by external buffers or by a hydrogen-permeable Shaw membrane. After rapid quench, the fluid in the fluid inclusions was quantitatively analyzed by Raman spectroscopy (Fig. 3.5-1). For the quantification of the Raman signal, standard solutions of known concentrations were measured. Although the sulfur speciation in the quenched fluid not necessarily equals the speciation in the high-temperature fluid, the oxidation state of sulfur can be accurately determined, since the equilibrium concentrations of oxygen and hydrogen in the fluid are too small to significantly change the sulfur redox state by chemical reactions during quenching.

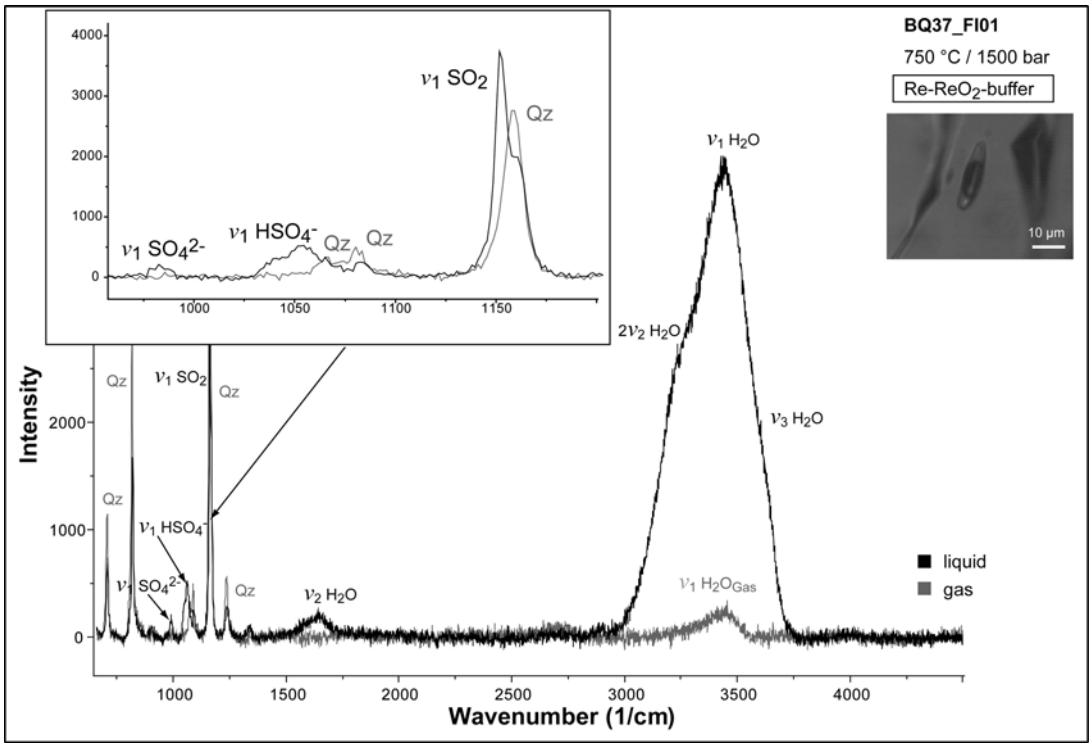

Fig. 3.5-1: Raman spectra of the gas phase and liquid phase of a sulfur-bearing hydrous fluid trapped in a synthetic fluid inclusion in quartz at 750 °C, 1500 bar and Re-ReO_2 buffer conditions. The Raman spectra of the quenched fluid show bands due to SO_2, SO_4^{2-} and HSO_4^-, indicating the presence of sulfur in the oxidation state + 4 and + 6.

Experimental results for 2 kbar are summarized in Fig. 3.5-2. Essentially, H_2S, SO_2 or compounds of hexavalent sulfur (SO_3 or H_2SO_4) are the main sulfur species in the fluid

depending on temperature and oxygen fugacity. The curve describing the conditions where SO_2 and H_2S are equally abundant is shifted downward almost two log units in oxygen fugacity as compared to the predictions from thermodynamic calculations from standard state data of gases. This is probably due to the stabilization of SO_2 by interactions with the solvent. Very surprising is the predominance of species of hexavalent sulfur in the fluid under oxidizing conditions. Throughout the literature, it has almost universally been assumed that SO_2 is the major sulfur species in magmatic-hydrothermal fluids even under rather oxidizing conditions. This would be in agreement with thermodynamic calculations of the equilibrium between SO_2 and SO_3. However, in the fluid probably hydrated forms of SO_3, such as H_2SO_4 dominate. For these compounds, there are no high-temperature thermodynamic data available that would allow the equilibrium between SO_2 and various species of hexavalent sulfur to be calculated. Also, at ambient pressure, H_2SO_4 dissociates into H_2O and SO_3 upon heating to more than 300 °C. This was assumed to imply that H_2SO_4 is not stable at magmatic temperatures. However, our data suggest that this dissociation is suppressed at higher pressures.

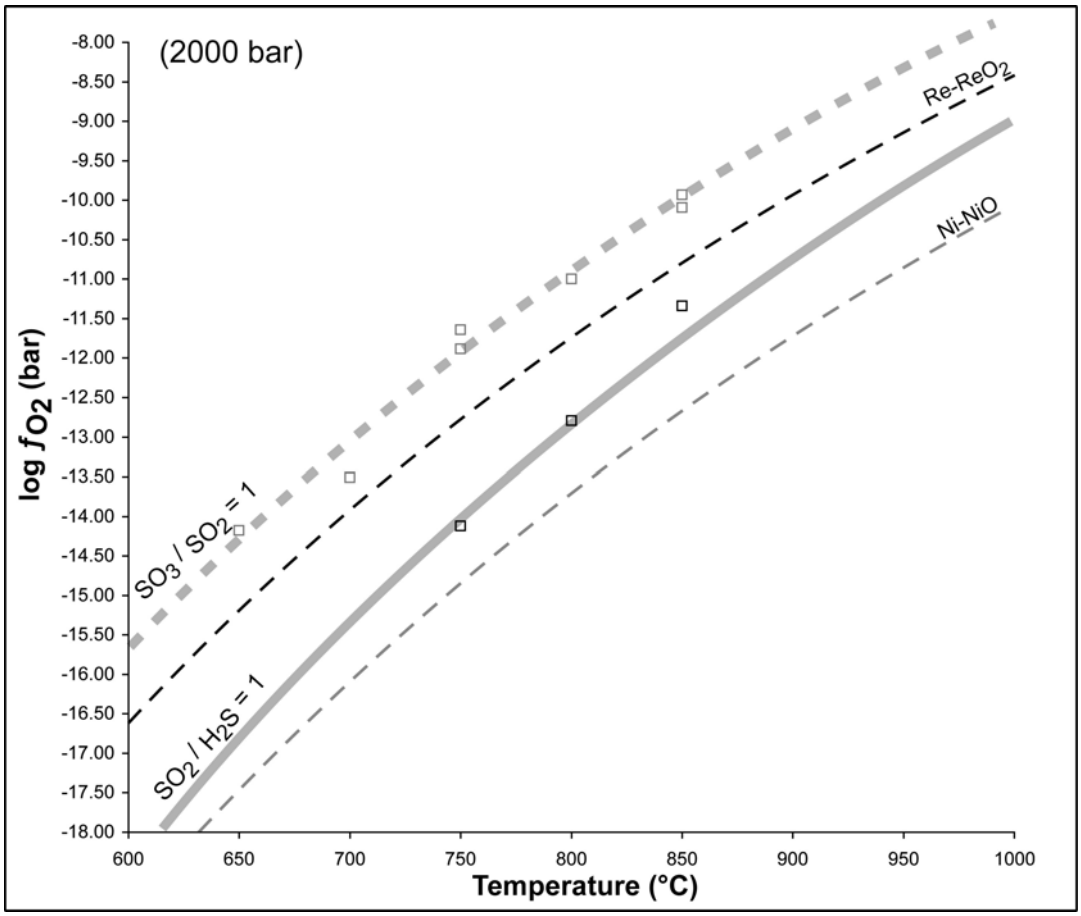

Fig. 3.5-2: Experimentally determined sulfur speciation in aqueous fluids at 2000 bar. Depending on temperature and oxygen fugacity, H_2S, SO_2 and SO_3 or its hydrated forms (H_2SO_4) are stable. The curves show the conditions under which the concentration of H_2S in the fluid equals that of SO_2 and the conditions under which SO_2 and SO_3 (or its hydrated forms) are equally abundant.

The predominance of hexavalent sulfur in the fluid under reasonably oxidizing conditions has some major geologic implications. It suggests that remote sensing of volcanogenic sulfur from satellites, which only detects SO_2, may seriously underestimate the sulfur release during explosive eruptions. Moreover, the kinetics of the formation of sulfate aerosols in the stratosphere may strongly depend on the original oxygen fugacity prevailing in a magma chamber before an eruption. The existence of hexavalent sulfur species in the fluid also means that models of hydrothermal alteration around degassing magma bodies need to be reevaluated. Since sulfuric acid is a much stronger acid than aqueous solutions of SO_2, it may lead to a much stronger leaching and mobilization of metals around a magma body than predicted by existing models.

b. *Partitioning of Cu and Au between vapor and brine in two-phase aqueous fluids (A. Audétat)*

Magmatic-hydrothermal fluids play a central role in the formation of porphyry copper deposits and epithermal gold deposits. Although a link between these two types of deposits has been suspected for a long time, it was not clear what caused this spatial and chemical separation. About 15 years ago, new developments in microanalytical techniques such as SXRF, PIXE and LA-ICP-MS made it possible to analyze concentrations of ore-forming elements in individual fluid inclusions. On coexisting vapor and brine inclusions in natural samples one could demonstrate that most elements strongly partition into the chloride-rich brine, as was expected from mineral solubility experiments. However, there were also some surprises. Copper, gold, arsenic and boron were found to display a much smaller affinity to the brine, and in many cases even were present in higher concentrations in the vapor. Because vapor is the dominant fluid phase in many magmatic-hydrothermal systems it is of prime importance to understand the mechanisms of ore metal complexing in low-density fluids. It is believed that the partitioning of copper and gold into the vapor phase is due to the formation of stable hydrosulfide complexes. Several experimental studies have been conducted in the past few years to test this hypothesis. So far only one group successfully reproduced the fractionation of copper into the vapor phase, although the fugacities of oxygen and sulfur-bearing species were not controlled in that study. Clearly, more experimental studies are needed to understand the behaviour of ore-forming metals in two-phase fluids.

Synthetic fluid inclusions in quartz were produced in the two-phase region of the system H_2O-NaCl-Cu-S at 700 °C / 100 MPa and 800 °C / 120 MPa, at oxygen fugacities buffered by either Ni-NiO or Co-CoO. Uncracked quartz cores measuring 3 x 3 x 10 mm were loaded together with 30 mg silica glass and 80 µl of an aqueous solution containing 10 wt.% NaCl and 12.5 wt.% $CuSO_4$ into gold capsules of 25 mm length, 5.0 mm outer diameter and 4.6 mm inner diameter. The capsules were placed together with 20-40 mm long filler rods made of Ni or Co into rapid-quench cold-seal pressure vessels pressurized with water. After 6-7

days of equilibration, the capsules were rapidly dragged with the aid of a magnet to the cold end of the pressure vessel and then moved back to the hot end, which caused numerous small cracks to develop in the quartz core. The capsules were then held for another 5-7 days at high pressure and temperature to allow healing of the cracks and concomitant fluid inclusion formation. Resulting fluid inclusions typically measure about 10-20 µm, with a few reaching sizes of 30-40 µm (Fig. 3.5-3).

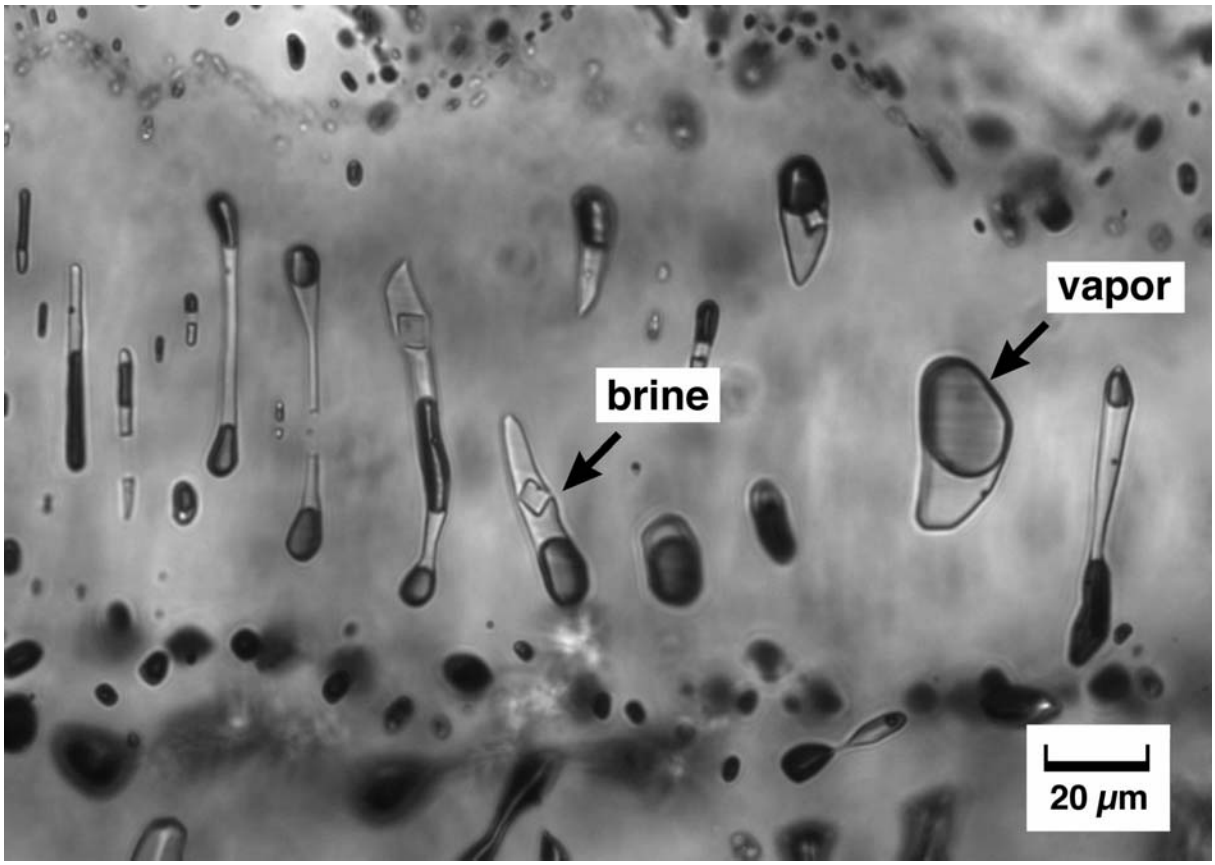

Fig. 3.5-3: Coexisting vapor and brine inclusions trapped at 800 °C and 120 MPa along a former fracture in quartz. The loaded bulk fluid contained 10 wt.% NaCl and split into a brine phase of 55 wt.% NaCl salinity and a vapor phase of 4 wt.% NaCl salinity at these conditions. Note the presence of a small black daughter crystal in both types of inclusions.

Individual vapor and brine inclusions were analyzed by LA-ICP-MS at the Bayerisches Geoinstitut, using a Geolas M 193nm ArF excimer laser (Coherent / Lambda Physik) attached to a Elan DRC-e quadrupole mass spectrometer (Perkin Elmer Instruments). External calibration was performed on a NIST SRM 610 glass, whereas Na was used as internal standard. From each experiment, between 5 and 10 inclusions of each inclusion type were measured. A typical signal of a brine inclusion is shown in Fig. 3.5-4. Signals from vapor inclusions are characterized by much lower intensities, with Au and Cu only seldom being above the detection limit.

Results are summarized in Table 3.5-1. Copper and gold were found to fractionate into the brine phase in all runs except maybe for run VB4, in which a high copper content was observed in a vapor inclusion. However, this latter inclusion was the only vapor inclusion of run VB4 that produced a reasonable copper signal. Therefore, this result has to be regarded with caution. If the concentrations listed in Table 3.5-1 are compared to the copper content of the starting fluid, it becomes evident that more than 99 % of the loaded copper must have been lost to the gold capsule before the fluid inclusions formed. Despite this severe loss of copper there seems to be a trend of higher copper concentrations in fluids equilibrated at Co-CoO than in fluid equilibrated at Ni-NiO (except maybe Cu in run VB4). The same trend is seen in the gold concentrations. This may imply that Cu and Au formed more stable complexes under reducing conditions than under oxidized conditions. However, the data set definitively is too limited for firm conclusions. Further experiments will be conducted at lower pressure and temperature to increase the physical and chemical contrast between vapor and brine, and to reduce the loss of copper to the capsule walls. Because the equilibration of hydrogen through the gold capsule is very slow at temperatures below 600 °C it will be necessary to use internal rather than external fO_2-buffers. Geologically realistic buffer assemblages could be hematite-magnetite-pyrite and pyrite-pyrrhotite-magnetite.

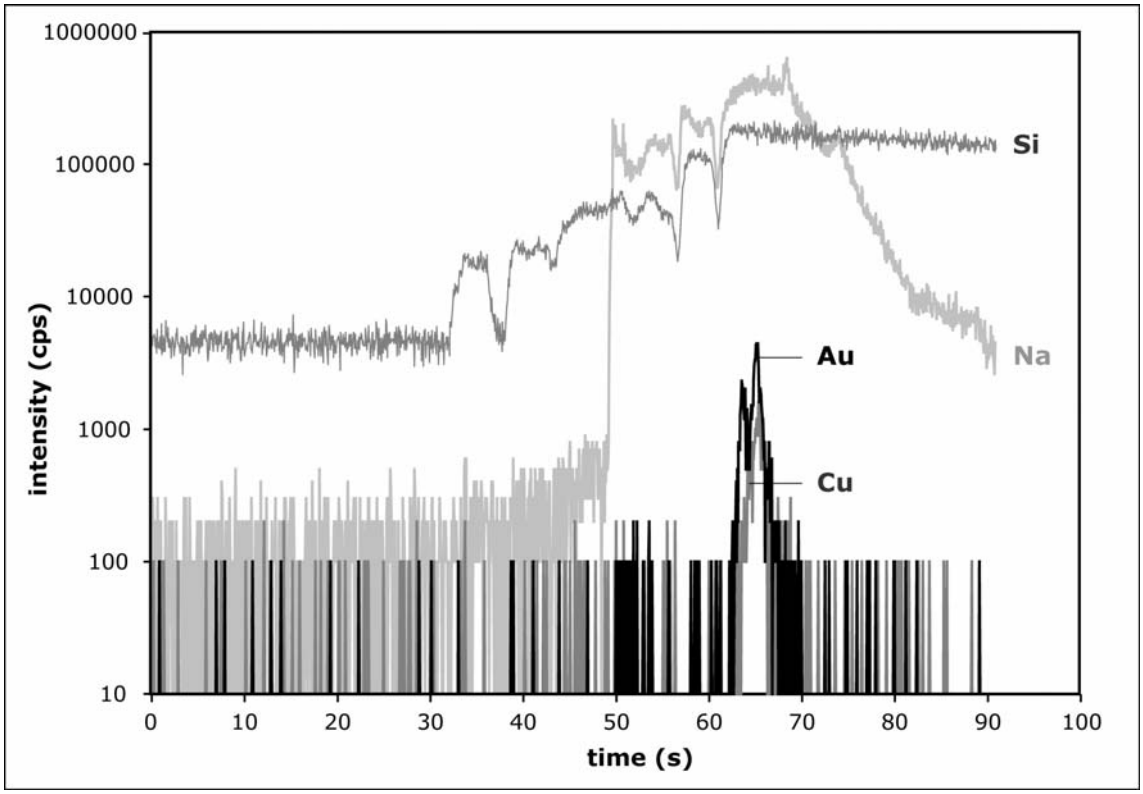

Fig. 3.5-4: LA-ICP-MS signal obtained from a 30 µm-sized brine inclusion in run VB10. Note the isolated appearance of Au and Cu compared to Na, which suggests that these metals are concentrated in the small, opaque daughter crystals visible in Fig. 3.5-3. Calculated concentrations of Au and Cu in this inclusion are 175 and 213 ppm, respectively.

experimental conditions	fO_2-buffer		NaCl (wt.%)	Cu (ppm)	Au (ppm)
700 °C / 100 MPa	NiNiO	vapor	4	298 [1)]	<33
		brine	48	10 ± 4	4 ± 1
700 °C / 100 MPa	CoCoO	vapor	4	<241	32 ± 8
		brine	48	177 ± 27	163 ± 58
800 °C / 120 MPa	NiNiO	vapor	4	18 [1)]	53 ± 8
		brine	55	67 ± 3	123 ± 5
800 °C / 120 MPa	CoCoO	vapor	4	24 ± 1	21 ± 8
		brine	55	234 ± 42	188 ± 24

[1)] only 1 analysis available

Table 3.5-1: Summary of LA-ICP-MS results

c. *Investigation of the behaviour of reduced C-O-H fluids at conditions of the Earth's transition zone (D. J. Frost)*

The oxygen fugacity in the transition zone is likely to be quite low. This arises from the fact that ferric iron is highly soluble in both wadsleyite and garnet, which are the main phases in the transition zone. Ferric Fe components will therefore be fairly dilute which will drive the oxygen fugacity down to levels several orders of magnitude below those of the upper mantle. Calculations suggest that at these oxygen fugacities a C-O-H fluid, although still quite rich in H_2O, will also contain CH_4 and minor H_2. The lower activity of H_2O in the fluid should lower the equilibrium OH^- content of coexisting nominally anhydrous minerals such as wadsleyite. Experiments have been performed to study the properties of such reduced fluid phases and to examine whether they are likely to form at plausible mantle redox states and if they influence the OH^- contents of mantle minerals in the transition zone.

Experiments are performed using double capsules with an inner 1.5 mm diameter Pt sample capsule inside an outer thick walled 4 mm diameter Ag capsule that contains a redox buffer. H_2O is added to the outer capsule while the inner capsule contains a sample of olivine in a graphite liner and some $C_6H_{10}O_4$ (adipic acid) as a fluid source. The outer redox buffer is either Co-CoO or Mo-MoO_2 and the buffer fixes the fH_2 in the outer capsule. Because the outer capsule is much larger than the inner and H_2 passes easily through the thin Pt wall of the inner, the fH_2 is also fixed in the inner capsule. This imposes a fixed C-O-H fluid composition in the inner capsule that can be calculated using equations of state for the gas species. Experiments are performed in the wadsleyite stability field in the 5000 tonne press at approximately 15 GPa.

At 1400 °C the outer redox buffer becomes exhausted (*i.e.*, the metal is totally oxidised) very quickly and the inner capsules show evidence for higher oxygen fugacities. Oxygen fugacities

in the inner capsule can be estimated by including a small amount of Ir metal just below the wadsleyite sample and analysing the amount of Fe that dissolves in this metal. At 1200 °C experiments can be run for several hours, however, without the redox buffer expiring.

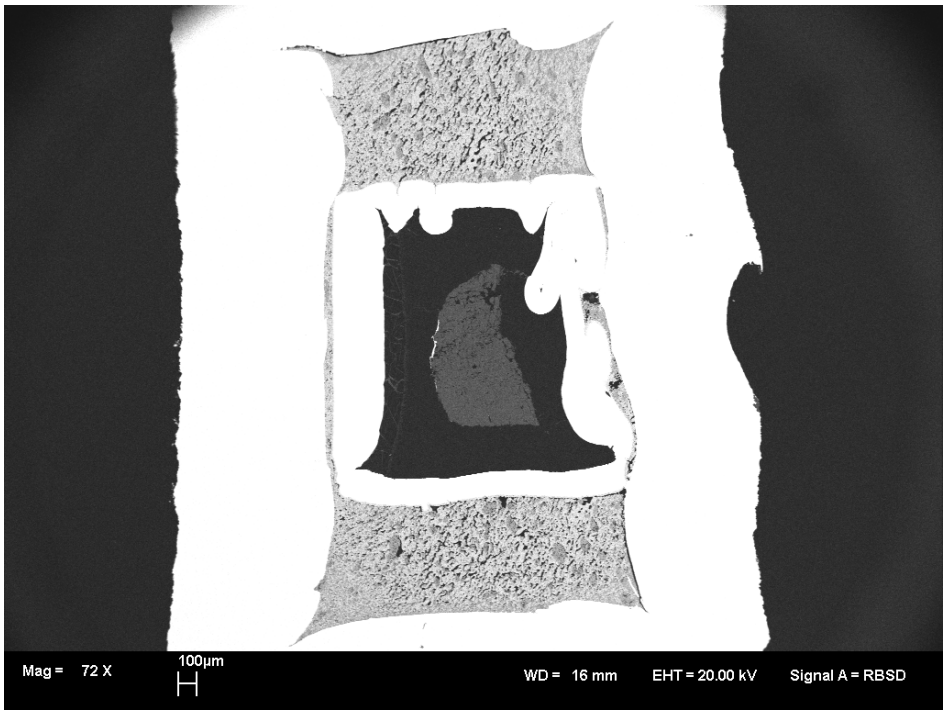

Fig. 3.5-5: Double 4 mm diameter capsule from an experiment performed at 15 GPa and 1200 °C. The outer Ag capsule contains a Co-CoO redox buffer and H_2O. The inner Pt capsule contains a graphite sleeve surrounding a sample of wadsleyite. The outer redox buffer fixes the hydrogen fugacity, which imposes the C-O-H fluid composition in the inner capsule. The fluid was dominated by H_2O but also contained dissolved silicates. A small strip of Ir metal can be seen at the left hand side of the silicate sample, which was included to enable the oxygen fugacity to be estimated.

H_2 is lost continuously from the outer capsule during the experiment as a hydrous product can be found that builds up on the outside of the $LaCrO_3$ furnace. If experiments are run for less than two hours, however, significant fluid is still retained in the outer capsule. Figure 3.5-5 shows a typical run product from 15 GPa and 1200 °C using Co-CoO as the external redox buffer. At these conditions a C-O-H fluid will be comprised almost totally of H_2O. Only the residue from the $C_6H_{10}O_4$ fluid source transforms to diamond in the experiment, the graphite sample holder is untransformed. The silicate sample contains areas of quenched fluid that had a considerable Mg-silicate content dissolved in it. Incongruent dissolution results in the formation of clinoenstatite throughout the sample. In experiments at identical conditions but employing the Mo-MoO_2 buffer the entire graphite capsule transforms to a porous mass of crystals that have been identified by X-ray diffraction as lonsdaleite, the hexagonal polytype of diamond. At these conditions the fluid phase should comprise approximately equal

proportions of CH_4 and H_2O. The porosity of the transformed lonsdaleite assemblage suggests that there was a significant fluid content in the inner capsule during the experiment. The silicate sample is comprised almost completely of wadsleyite, however, and shows no evidence of dissolution or of a quenched fluid phase. Throughout the sample tiny blebs of Ni-Fe alloy can be seen that have exsolved from the wadsleyite. The alloy is Ni rich and the wadsleyite is not significantly depleted in Fe. Calculated oxygen fugacities are within the plausible range for the transition zone. The results indicate that the presence of a CH_4-rich fluid in the transition zone is quite consistent with the likely oxygen fugacity in this region. Such a fluid phase does not seem to contain a significant dissolved silicate component as H_2O-rich fluids do at these conditions. Moreover, the water content of minerals in equilibrium with such fluids is likely to be smaller than in equilibrium with a water-rich fluid.

d. *Water solubility in Al-bearing diopside (P. Gavrilenko and H. Keppler)*

Natural clinopyroxenes from mantle xenoliths show the highest water contents among all nominally anhydrous minerals. In particular, Al-rich omphacitic clinopyroxenes often have exceptionally high water contents. Due to its low modal abundance, clinopyroxene is probably not a major reservoir for water in the upper mantle. However, omphacitic clinopyroxene in subducting slabs may be the main carrier for recycling water from the Earth's surface back into the mantle. Therefore, we are carrying out a systematic study to investigate the water solubility in clinopyroxenes as a function of pressure, temperature and bulk composition. Some preliminary experiments showed that the water solubility in pure diopside is rather low. However, the solubility was found to strongly increase with aluminium content. Accordingly, we systematically studied the influence of aluminium on the water solubility in diopside.

The synthesis of water-saturated aluminous diopside was carried out in an end-loaded piston-cylinder apparatus at 1.5 - 2.5 GPa and 1000-1100 °C. The starting material was a mixture of high-purity $Mg(OH)_2$, $Ca(OH)_2$, $Al(OH)_3$ and SiO_2 with excess water. The composition of the starting mixtures was along the join diopside ($CaMgSi_2O_6$) – Ca-Tschermak's component ($CaAl_2SiO_6$) with different ratios of these two end members. The water concentration in diopside was determined from infrared measurements on perfectly clear single crystals. Water contents were calculated from integral absorbances using published infrared extinction coefficients for water in diopside.

Our preliminary results on water solubility in Al-bearing diopside are presented in figures 3.5-6 and 3.5-7. All infrared spectra of the Al-containing diopside crystals show only one main absorption band at 3650 cm^{-1}, implying one single defined substitution mechanism for water. Interestingly, the infrared bands in pure diopside are different and they disappear once aluminium is added to the system, implying that Al does not only generate new hydrous defects but it also destabilizes the hydrous defects present in pure diopside. According to the unpolarized measurements the water solubility increases strongly with aluminium.

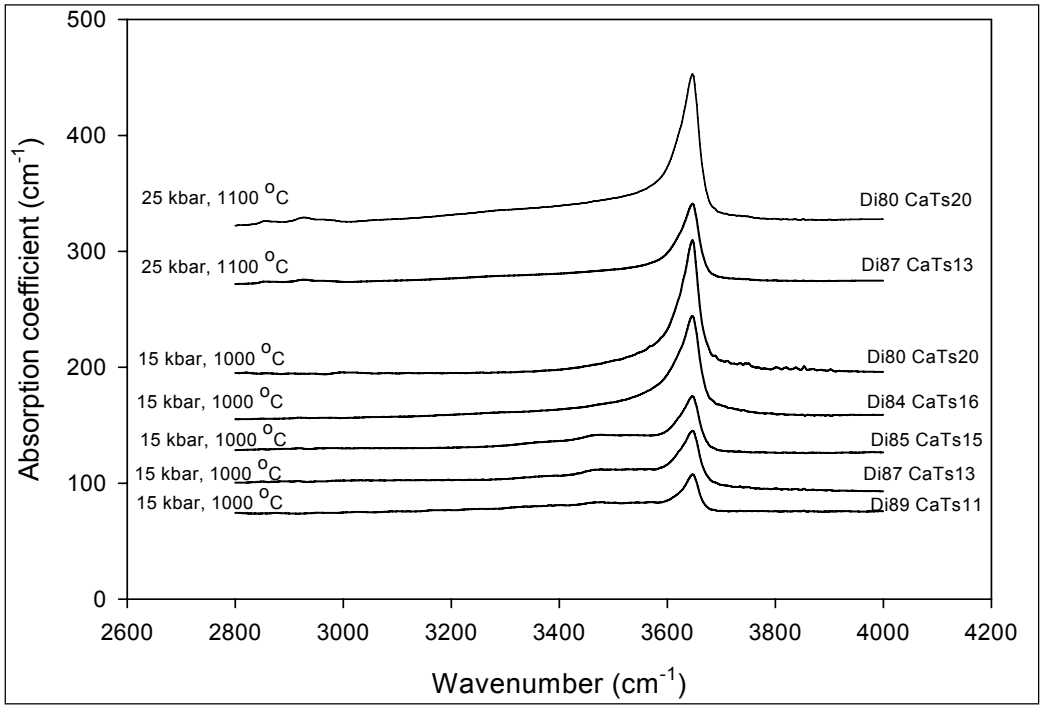

Fig. 3.5-6: Unpolarized FTIR spectra for Al-bearing diopside of different composition. Only one band is seen implying one distinct substitution mechanism for water.

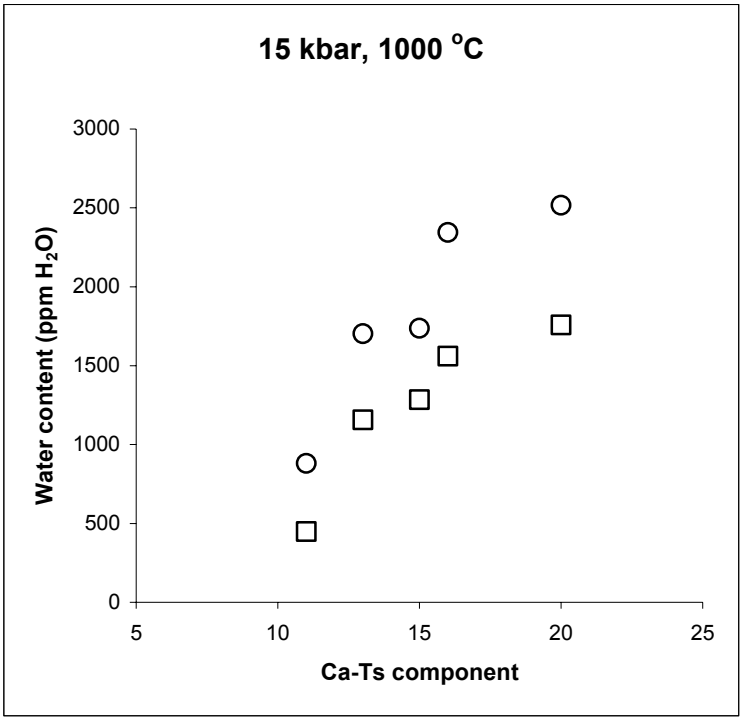

Fig. 3.5-7: Correlation between water solubility and Al content in diopside, expressed as mol.% calcium Tschermak component. Circles and squares correspond to water contents calculated with two different infrared extinction coefficients (circles: Paterson 1982; squares: Bell *et al.*, 1995).

3.6 Physics and Chemistry of Melts and Magmas

The production of magma by partial melting in the Earth's interior has been occurring throughout the history of the planet. The transport of magmas within the Earth, for example towards the surface, and magma crystallisation are major processes by which the Earth has differentiated throughout its evolution. During the early history of the Earth, partial or complete melting of the planet was required for iron alloy and silicate to separate gravitationally to form the metallic core and silicate mantle. Subsequently, ongoing melting, magma transport and crystallisation have been the main processes by which differentiation has produced the current crust and mantle. The physical and chemical properties of magmas control how transport and differentiation occur and also play a major role in controlling the nature of volcanic eruptions at the Earth's surface. The most violent and destructive eruptions involve magmas that have a high content of volatiles, such as CO_2 and H_2O. The solubility of volatiles in silicate melts and the details of how they are incorporated into the melt structure at the atomic scale is therefore of primary importance for understanding volcanism and volcanic processes. In addition, economically-valuable ore deposits originate primarily by precipitation from volatile-rich fluids that are derived from magmas.

In the first two contributions in this section, studies of the incorporation of fluids into magma are presented. Results on the speciation of dissolved CO_2 in a simplified basaltic melt are important because CO_2 is one of the main fluid species that are dissolved in magmas. Previous studies of this topic were performed on quenched glasses – which do not always maintain the same structure and speciation as the melt. The fact that the present study was performed on melt at high pressure using *in situ* spectroscopy is therefore a major advance which enables the temperature-dependence of speciation to be determined reliably for the first time. The second contribution is concerned with how much chlorine is contained in the fluid phase that is associated with granitic magmas - a question that is important for understanding the origin of ore deposits. The approach to answering this question involves linking analytical data for melt inclusions to experimentally-determined chlorine solubilities. In the present study, a comprehensive thermodynamic model for halogens dissolved in silicate melt has been developed for the first time. Furthermore, it is shown that natural magmas can exsolve two fluid phases, vapour + brine, simultaneously - which affects and complicates the use of element partitioning results in modelling studies. In the third contribution of this section, results of an experimental study of the origin of carbonate-rich magmas by partial melting of the Earth's mantle are presented. This topic is important for understanding the origin of a variety of extrusive volcanic rocks at the surface (*e.g.*, carbonatites and kimberlites) and the origin of diamonds. In addition, the results will eventually be used to understand the cycling of carbon between the Earth's mantle and the surface (hydrosphere, biosphere and atmosphere). In the final contribution, the properties of a system consisting of a small amount of melt dispersed in a crystalline matrix is investigated. The essential question is whether the melt can percolate through the matrix, as required for differentiation to occur. The system studied here is an analogue for metallic melt in a silicate matrix and is therefore applicable to understanding core formation in the Earth and other planets.

a. *High-temperature in situ infrared spectroscopic measurements on CO_2 speciation in an alkali silicate melt (A. Konschak and H. Keppler)*

CO_2 is one of the most abundant volatiles that is involved in magmatic processes in the Earth's interior. Particularly in basaltic magmas, CO_2 is the dominant volatile species and controls the nature and extent of volcanic eruptions. Therefore it is of fundamental importance to understand the behaviour of CO_2 dissolved in silicate melts, especially depolymerized natural basaltic melts, at high temperatures.

Raman, infrared and NMR spectroscopy on quenched CO_2-bearing silicate glasses has shown in the past that in depolymerized melts, similar to natural basaltic melts, CO_2 dissolves only as $(CO_3)^{2-}$ groups that are linked to non-bridging oxygen atoms (NBO) and to network modifying cations in the silicate network. On the other hand, annealing experiments on glasses of more polymerized silicate melt structures indicate that the equilibrium of the CO_2 species reaction

$$CO_2 + O^{2-} = CO_3^{2-}$$

shifts towards molecular CO_2 with increasing temperature. However, no *in situ* experimental data have been available concerning CO_2 speciation in silicate melts at high temperatures prior to the present study. Therefore we performed the first high-temperature *in situ* infrared spectroscopic measurements on CO_2 in a depolymerised silicate liquid that has a similar degree of polymerization as a basaltic melt, using an externally-heated diamond anvil cell (DAC).

We used an alkali silicate glass for the *in situ* experiments with a composition corresponding to the minimum melting point in the Na_2O-K_2O-SiO_2 system (700 °C at 1 atm), which has a similar degree of polymerization (NBO/T=1) to that of basaltic melts. The CO_2-bearing glass was synthesized in a piston cylinder apparatus with silver oxalate as the carbon source. All CO_2 is dissolved as $(CO_3)^{2-}$ anions in the glass structure at ambient conditions. The DAC experiments were performed at temperatures up to 1000 °C and moderate pressures of several kbars.

First results show that CO_2 speciation does not change with temperature and pressure in this depolymerised alkali silicate liquid. It can be clearly seen that carbonate is the only species and no molecular CO_2 is present at temperatures above 900 °C, although the signal to noise ratio became worse due to the increase of black body radiation intensity at temperatures above 700 °C (Fig. 3.6-1). The carbonate peak broadens slightly towards the low frequency region up to 300 °C and more clearly above 400 °C. The extinction integral of the carbonate peak decreases with temperature. This decrease may, however, be within the experimental error. Up to now there is no indication that the equilibrium of the CO_2 species reaction $CO_2 + O^{2-} = CO_3^{2-}$ shifts towards molecular CO_2 with increasing temperature in our depolymerised silicate basaltic melt analogue.

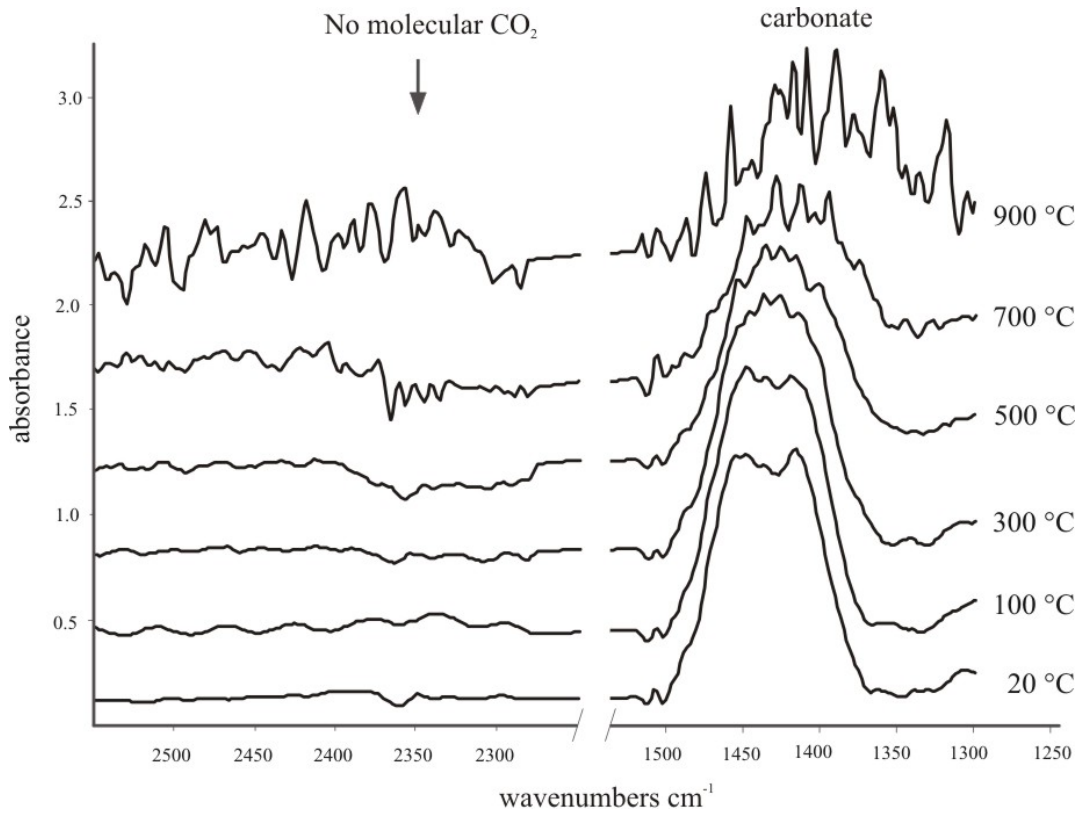

Fig 3.6-1: *In situ* FTIR spectra of the CO_2-bearing alkali silicate melt showing the frequency regions of molecular CO_2 and carbonate at temperatures up to 900 °C. A shift of the equilibrium reaction $CO_2 + O^{2-} = CO_3^{2-}$ towards molecular CO_2 with increasing temperature does not occur.

b. *Thermodynamic model of chlorine in silicic melts: A quantitative approach to magmatic devolatilization (D. Dolejš)*

Chlorine is the predominant halogen in magmatic and hydrothermal aqueous fluids. These media range from concentrated brines to dilute vapors and are responsible for metal complexing, ore deposition, various alteration styles, and constitute volcanic output to the Earth's atmosphere. From intrusive towards shallow epithermal settings, salinity and composition of hydrothermal fluids changes dramatically and this is partly due to subcritical phase separation in the H_2O-NaCl system. Outstanding questions include: (1) what is the salinity of exsolving magmatic fluids, (2) do one or two fluid phases separate simultaneously from magmas, and (3) how can analytical data from melt inclusions be linked to fluid chemistry or be used to monitor the devolatilization paths?

Quantitative modeling of magmatic devolatilization has been hindered by the lack of thermodynamic models for halogens in silicate melts. Both the conventional Margules-type formalism or the Pelton-Reddy-Blander model for chloride solubilities have disadvantages

when applied to very small chloride solubilities in highly polymerized melts. We propose a new solution model for chlorine in silica-rich melts that is based on Darken's quadratic formalism for a solute in a multicomponent solvent. In the linearly independent set of end-member melt species, chlorine is represented by NaCl whose thermodynamic properties are related to the molten-salt standard state via the Darken's increment:

$$I_{NaCl}\,(J) = \Delta_f G_{NaCl,silicate\ melt} - \Delta_f G_{NaCl,molten\ salt} = 10850 + 31.126\ T(K) - 1.333\ P(bar)$$

which was calibrated by experimental data on chlorine solubility in granitic melts at 800-1060 °C and 50-200 MPa (Fig. 3.6-2). Interaction between NaCl and H_2O in the melt structure is described by the regular solution parameter as follows:

$$W_{NaCl\text{-}H2O}\,(J) = -53385 + 42.507\ T(K) + 2.667\ p(bar)$$

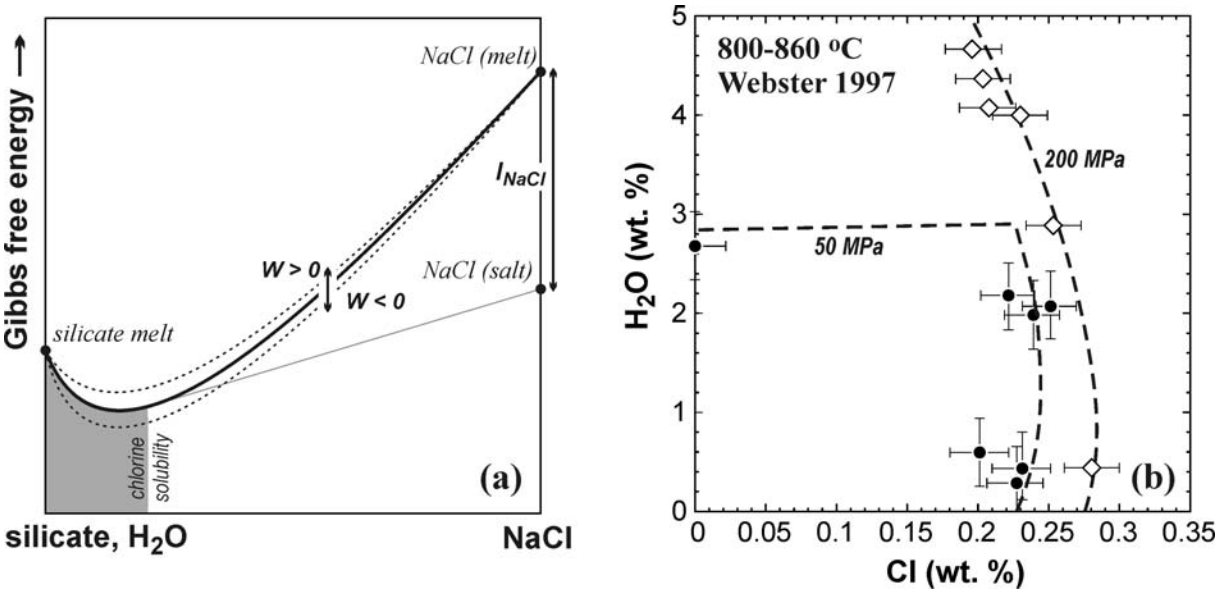

Fig. 3.6-2: (a) Graphical illustration of the model parameters, I_{NaCl} and W, in the Gibbs free energy-composition diagram; (b) comparison of experimental measurements with the thermodynamic calculations.

In the quinary system Qz-Or-Ab-H_2O-Cl_2O_{-1}, the definition of configurational properties for the silicate melt allows for substitution of Na and K on silicate and halide sites. Thermodynamic properties of silicate and aqueous components and their mixing properties are based on the Holland-Powell melt model. Activity coefficients of all melt components were obtained by differentiation of excess Gibbs free energy. Properties of H_2O-NaCl-KCl fluids are described by the Kosinski-Anderko-Pitzer equation of state. Phase equilibria in the SiO_2-Al_2O_3-Na_2O-K_2O-H_2O-Cl_2O_{-1} system were computed by Gibbs free energy

minimization using linear simplex switching, followed by second-order steepest descent refinement. This setup enables incremental calculation of proportions and compositions of coexisting solid, melt and fluid phases and predicts fluid saturation during equilibrium or fractional crystallization or decompression.

Figure 3.6-3 illustrates phase diagrams for the haplogranite-H_2O-NaCl system at 800 °C. At 200 MPa, the fluid forms a single supercritical phase ranging from 0 to 80 wt.% NaCl+KCl (Fig. 3.6-3a). H_2O solubility in the melt decreases from 5.5 to 3.2 wt.% as the chlorine concentration increases. Alkemade triangles imply the existence of a temperature minimum where tie-lines of melt-fluid and melt-crystals become colinear (5.4 wt.% H_2O and 0.13 wt.% Cl in the melt). In the vicinity of the minimum, tie-lines between coexisting melt and fluid show a strong curvature which implies that very small changes in the melt Cl/H_2O ratio produce large variations in the fluid salinity. The partition coefficient of chlorine, $D_{Cl}^{fluid/melt}$, is not constant but decreases by two orders of magnitude as the melt Cl/H_2O ratio decreases; this is a consequence of non-Henrian behavior of chlorine (as a major fluid constituent). At 800 °C and 100 MPa, the H_2O-NaCl system is subcritical and it consists of aqueous vapor and saline brine with salinities of 0-2 and 72-82 wt.% NaCl+KCl, respectively (Fig. 3.6-3b). As a result, the thermal minimum becomes an invariant point where all differentiation paths of chlorine-bearing granitic melts terminate (Cl/H_2O = 0.037). As natural silicic melts display Cl/H_2O = 0.01-0.08, these magmas will saturate with two fluids consecutively. At the invariant point, the Cl and H_2O concentrations in the melt remain constant despite the fact that the system continues to exsolve two fluid phases simultaneously. At this stage, natural melt inclusions cannot provide information on the devolatilization progress and amounts of released fluids.

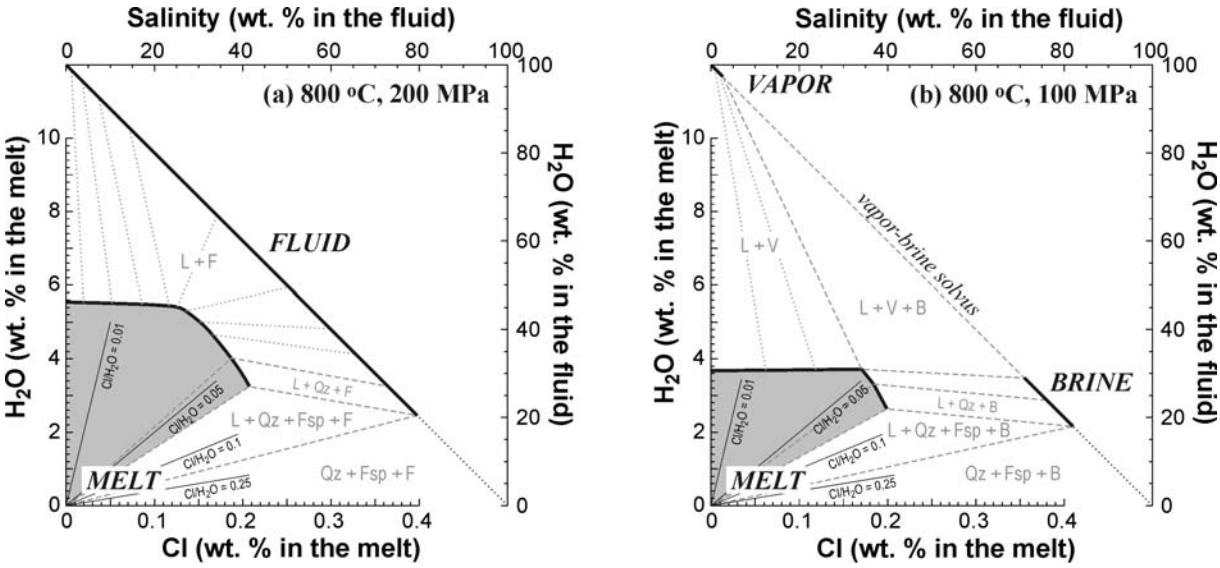

Fig. 3.6-3: Isothermal-isobaric phase diagrams showing phase assemblages, melt and fluid compositions at 800 °C and (a) 200 MPa and (b) 100 MPa.

We have modelled fractional devolatilization during isothermal decompression and isobaric crystallization. In Figure 3.6-4a, the haplogranitic minimum melt with 3 wt.% H_2O and 300 ppm Cl rises isothermally to lower pressures. At 750 MPa (~ 3 km depth), saturation with a low-salinity vapor occurs and the amount of vapor increases with magma crystallinity. At 470 MPa, the residual melt solidifies by the reaction: melt = crystals + brine. This scenario is applicable to segregation of near-eutectic melts in highly evolved plutons. The saturation with brine at the solidus only allows for incompatible enrichment of ore and minor elements in the residual melt and these elements are efficiently sequestered by the high-salinity brine upon solidification. In Figure 3.6-4b, a feldspar-saturated melt with $Cl/H_2O = 0.04$ crystallizes isobarically at 100 MPa. Over the temperature interval of 65 °C, the magma simultaneously exsolves aqueous vapor and saline brine; fluid compositions are dictated by the H_2O-NaCl+KCl solvus. At the solidus, the amounts of exsolved fluids proportionally increase but their salinities do not change. This case is applicable to crystallizing plutons after final emplacement; early saturation with brine may sequester metals and trace elements before their enrichment in the residual melt and these geological settings are likely to remain poorly mineralized or barren.

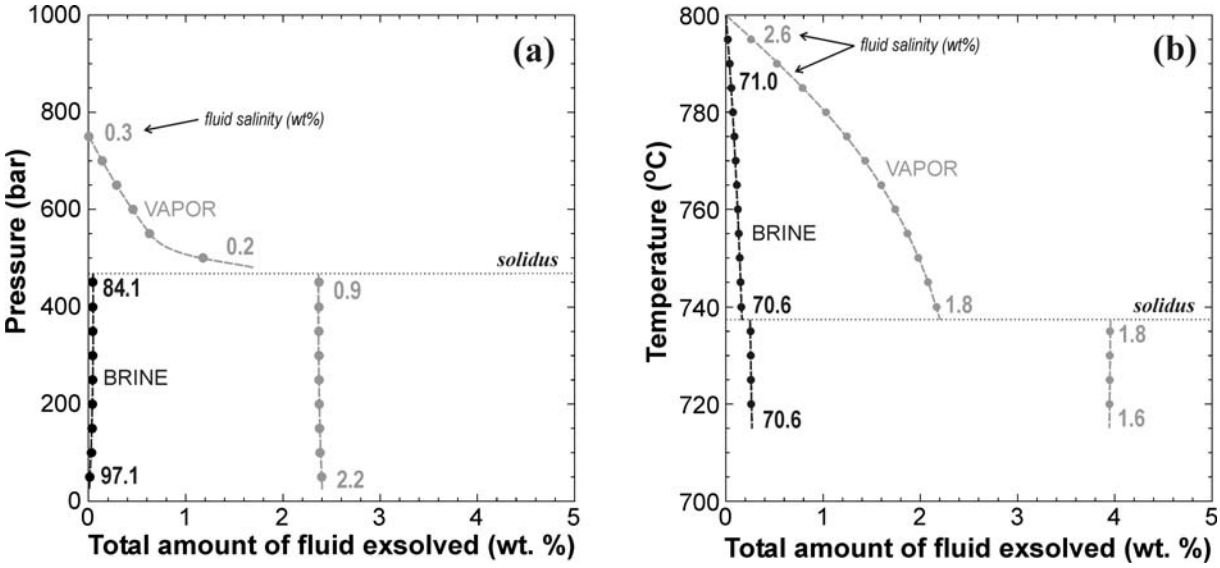

Fig. 3.6-4: Fluid release from differentiating haplogranitic melts: (a) $Qz_{38}Ab_{33}Or_{29}$ with 3.0 wt.% H_2O and 300 ppm Cl during isothermal fractional decompression at 800 °C; (b) $Qz_{15}Ab_{49}Or_{36}$ with 3.9 wt.% H_2O and 1480 ppm Cl during isobaric fractional crystallization at 100 MPa.

In summary, the new thermodynamic model demonstrates that: (1) experimental data require only minor deviations from mixing of halide and aqueous components in the melt, *i.e.*, the trends of chlorine and water solubilities can be explained by non-ideal activity-composition relationships in the aqueous fluid, (2) natural silicic magmas with $Cl/H_2O < 0.04$ first saturate

with dilute aqueous vapor and subsequently exsolve concentrated brines at the solidus, (3) the "vapor-then-brine" mechanism of exsolution promotes enrichment of incompatible and ore elements in the residual melts and their efficient removal by late-stage brines; this is an important prerequisite for the formation of economic mineralization, and (4) simultaneous exsolution of two fluids invariantly buffers the melt composition. Therefore, at this stage, melt inclusions can not provide information on the devolatilization process. The new model offers the missing link between melt and fluid chemistry that can be further used in reactive-flow modeling of ore deposition and hydrothermal alteration.

c. *Carbonated magmas in equilibrium with lherzolite in the Earth's transition zone and shallow lower mantle: Indications from experiments in the CaO-MgO-SiO_2-CO_2 system (S. Keshav and G.H. Gudfinnsson)*

Carbon is the fourth most abundant element in the solar system. On Earth, carbon is found in the atmosphere as CO_2, and in the crust and the mantle as limestone, organics, graphite, and diamond. Interstellar diamond is also ubiquitous in recovered meteorites. Diamonds are transported from the Earth's mantle in highly explosive kimberlite eruptions that have occurred in the ancient and stable parts of cratons. In the ocean basins, the presence of carbonatite and kimberlite melts has been inferred on the basis of the geochemistry of primitive alkalic basalts (ocean-island basalts) and also mantle xenoliths. Rare-earth element fractionation in continental carbonatites and kimberlites indicates that the parental melts of these volcanic rocks were produced in the presence of a significant amount of residual garnet. This observation supports the general view that these magmas are produced by a low degree of partial melting at their source region in the mantle. Recent discoveries of diamond crystals in some kimberlites containing inclusions of majoritic garnets, high-pressure clinopyroxenes, enstatite + ferropericlase, SiO_2 + ferropericlase, and $CaSiO_3$ + $MgSiO_3$ + SiO_2 suggest a deeper, transition zone and lower mantle origin for kimberlites. If this is correct, these magmas offer a previously unrecognized opportunity to understand melting processes in the Earth's interior. In addition, since kimberlites bring up diamonds, they offer unique opportunities to understand the fate of carbon, its storage in the planet, and the cycle of carbon.

Phase relations relevant to the petrogenesis of CO_2-rich magmas have previously been reported for the CaO-MgO-Al_2O_3-SiO_2-CO_2 (CMAS-CO_2) system up to 8 GPa. In this system, calcio- and magnesiocarbonatite melts are produced at the isobarically invariant solidus in equilibrium with the garnet lherzolite phase assemblage of forsterite + orthopyroxene + clinopyroxene + garnet and carbonate (dolomite up to ~ 5 GPa; magnesite at higher pressures). Above the solidus, carbonate is lost from the phase assemblage and there is a continuous gradation in melt composition from carbonatitic to kimberlitic (at pressures > 5 GPa). Along the carbonate-bearing solidus, carbonate appears to be the dominant contributor

to the melt and therefore also to have the greatest influence on the melt composition. As recent work indicates that the solubility of carbon in mantle silicates is very small and dolomite and magnesite do not dissociate at mantle conditions, it seems that carbonate is the main repository of carbon in the Earth's interior, provided oxygen fugacity is appropriate. The presence of carbon in the form of carbonate also seems to be required if carbonated magmas are produced at great depths.

From this background on the origin of carbonatites, diamonds and their high-pressure silicate inclusions, deep-seated kimberlites, and by implication the carbon cycle, one can see the need to determine the melting behaviour of the relevant mantle phase assemblages, which then can be used to model carbonatite and kimberlite magma genesis and storage of carbon in the mantle at high pressures. Therefore, we have chosen to study melting in the CaO-MgO-SiO_2-CO_2 (CMS-CO_2) system at pressures of 16-26 GPa. This pressure range corresponds to depths of ~ 500-750 km in the Earth's mantle. In this contribution, we have chosen to focus on the part of the composition space of the CMS-CO_2 system, which is analogous to the natural carbonate-bearing mantle system with peridotitic bulk composition. In contrast to previous studies that dealt with melting behaviour in the CMAS-CO_2 system, we have not included alumina in the system because at the pressures of interest the mantle contains one less main phase than at lower pressures, at the low pressure end where orthopyroxene disappears. This disappearance of a phase means that the variance of the system increases. By eliminating a component (Al_2O_3), the variance is kept the same and the amount of work needed to determine the phase relations becomes more tractable. With increasing pressure, we have determined the following isobaric invariant points that define the solidus of a carbonated mantle analogue in the CMS-CO_2 system: wadsleyite + clinopyroxene + majorite + carbonate + melt at 16 GPa; ringwoodite + majorite + Ca-perovskite + carbonate + melt at 20 GPa, and Mg-perovskite + periclase + Ca-perovskite + carbonate + melt at 26 GPa.

All the starting compositions were prepared with high-purity oxides and carbonates, fired at between 400 °C (calcium carbonate) and 1250 °C (oxides) for 16-17 hours, ground in ethanol, decarbonated, and heated to 1600-1650 °C in a platinum crucible and quenched. The resulting glass was homogeneous, optically pure and free of quench crystals. Fired magnesite (200-220 °C; 16-17 hours) was added as the source of CO_2 in the prepared silicate glasses. The experiments were performed in fired (1000 °C) 10/5 and 10/4 cells with straight $LaCrO_3$ heaters, MgO inserts, and zirconia as thermal insulating material using multianvil apparatus. Annealed platinum (Pt) was used as sample capsules. Length of the Pt capsules is in the range of 1.3-1.7 mm. Temperatures were measured using W-Re thermocouples (Type-D) in direct contact with the Pt capsule.

Preliminary experimental results indicate that at all pressures the stable carbonate phase is magnesite, and there is no evidence of dissociation of magnesite. First results indicate that the melting reactions at the solidus are of the peritectic type, where majorite is in reaction relationship with the melt at 16 and 20 GPa and Mg-perovskite at 26 GPa. Melt compositions

are carbonatitic (~ 38-42 wt.% dissolved CO_2; SiO_2 < 10 wt.%), and do not show signs of liquid immiscibility in the pressure range of interest. Additionally, the carbonate-bearing solidus appears to be flattening in the pressure range of 16-26 GPa. If this is the case, however, the relatively low-temperature solidus could be important for our understanding of mantle melting and generation of carbonated melts at these pressures, low-velocity regions indicated by seismic tomography, the enrichment processes in the source regions of kimberlites, and the relationship of carbonatites to kimberlitic melts.

d. *Liquid distribution and attainment of textural equilibrium in a partially-molten crystalline system with a high-dihedral-angle liquid phase (N.P. Walte, J.K. Becker and P.D. Bons/Tübingen, D.C. Rubie and D.J. Frost)*

The textural evolution of a high-dihedral-angle liquid in a crystalline matrix, such as Fe-S melt in an olivine matrix, is of vital importance for a range of questions including planetary core-mantle differentiation. The distribution of a low fraction of melt or fluid in a crystalline matrix is mainly determined by the dihedral-angle Θ. At low values of Θ (< 60°) the liquid forms an interconnected network that allows porous flow, while at at high values of Θ (> 60°) the liquid droplets are isolated at a low liquid fraction. Previous experiments on high-Θ systems have suggested an interconnection threshold at a melt fraction of ~ 5 vol.% so that inefficient metal-silicate separation may be possible during planetary core formation without the need to form a silicate magma ocean.

For this study we performed hydrostatic *in situ* analogue experiments with norcamphor-H_2O liquid and high-temperature experiments with olivine-FeS melt to investigate the evolution of a high-dihedral-angle liquid and the attainment of textural equilibrium (Fig. 3.6-5). The great advantage of norcamphor-H_2O is that ongoing processes of textural adjustments between liquid and matrix can be observed *in situ*.

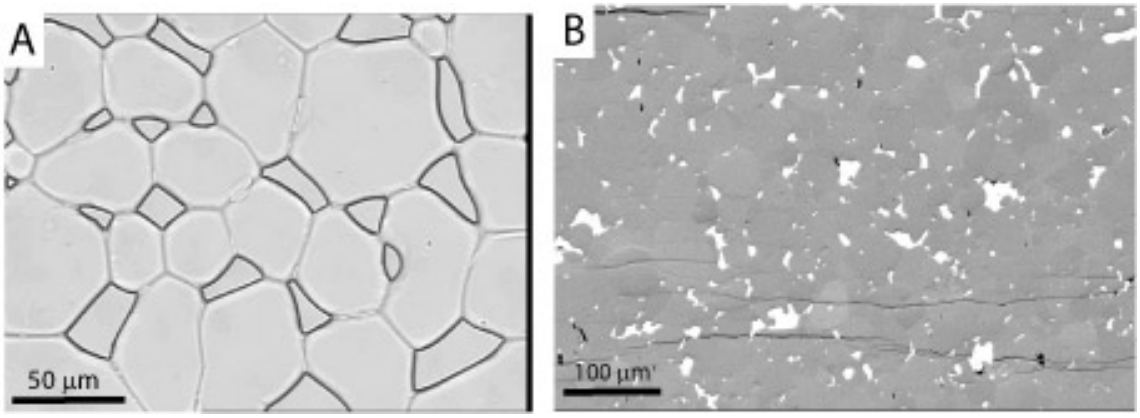

Fig. 3.6-5: (a) Liquid distribution in norcamphor-H_2O analogue experiments (optical micrograph) and (b) in olivine-FeS experiments (SEM orientation contrast). Note the uneven liquid distribution in both systems that is typical for systems with Θ > 60°.

Our experiments showed that the distribution of high-Θ liquid is more irregular than in low-dihedral-angle systems, with a high proportion of liquid occupying large irregular pools and dry triple junctions being common features (Fig. 3.6-5). *In situ* observations of textural evolution in our experiments revealed that high-dihedral-angle liquid pockets have a very low mobility during grain growth, which has several consequences:

(1) Anomalous grain growth: High-dihedral-angle liquid pockets pin the grain boundaries and triple junctions and thereby inhibit the process of normal grain growth and promote anomalous grain growth.

(2) Interaction between liquid pockets: Liquid pockets do not merge or interact with other isolated liquid pockets during grain growth but are detached from migrating grain boundaries or triple junctions and remain as isolated lenses or inclusions. At a low liquid fraction, even adjacent liquid pockets can only interact by diffusion, and energetically-favourable liquid pocket growth takes place only by Ostwald ripening and not by coalescence (Fig. 3.6-6).

(3) Stability of high-Θ melt networks and core formation: Interconnected melt networks are unstable in our experiments over longer periods of time (*e.g.*, several days) and finally pinch off (Fig. 3.6-7). This observation questions the reliability of experimentally-determined percolation thresholds at ~ 5 vol.% in high-Θ metallic melt-peridotite systems, which may not have reached liquid textural equilibrium in the experimental time. Our results indicate that an initial percolating network will likely break down before reaching the proposed connectivity threshold so that other mechanisms such as high-strain shear deformation or large-scale melting may be necessary for core formation in terrestrial planets.

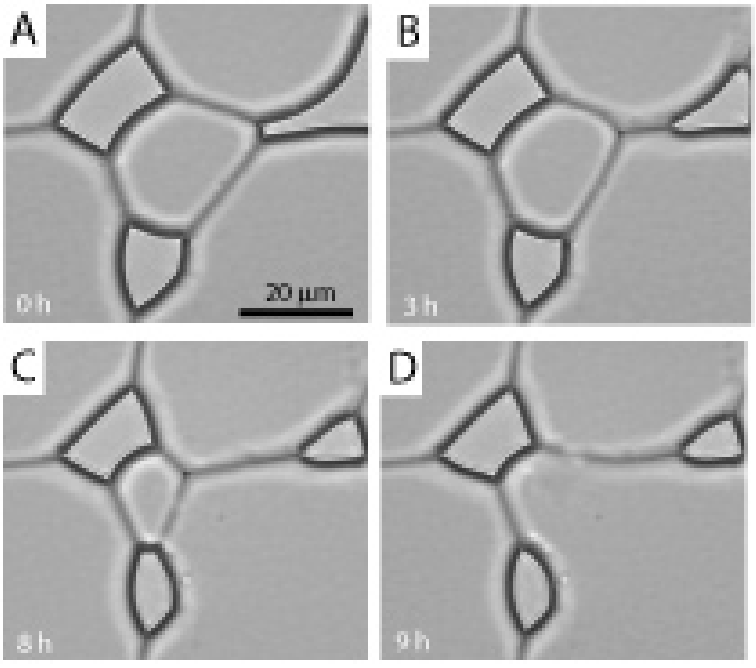

Fig. 3.6-6: Detail of a grain that is gradually disappearing during grain growth in the norcamphor-H_2O system. Note that the liquid pockets remain stationary during the topological changes in the crystalline matrix. Time in hours is listed at lower left.

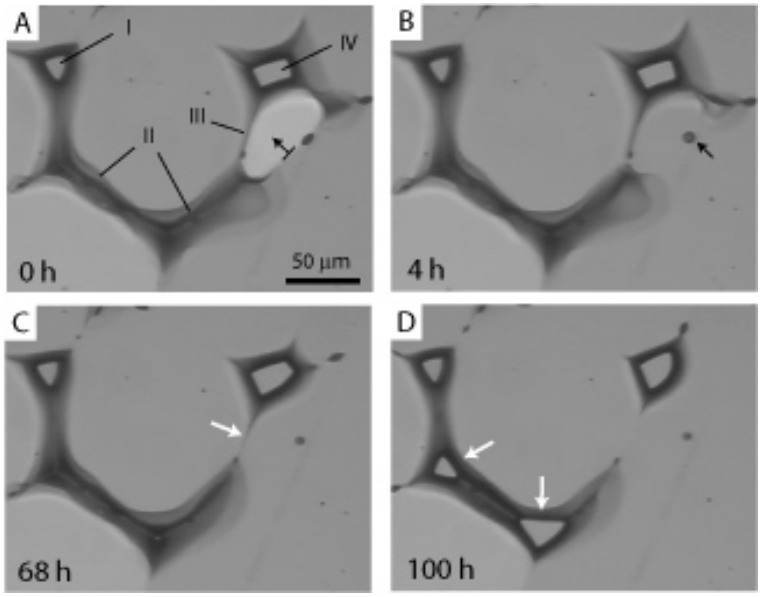

Fig. 3.6-7: Evolution of an arc-shaped liquid network in the norcamphor-H_2O system. (a) A triangular liquid pocket (I) and a rectangular liquid pocket (IV) are connected via an irregular arc-shaped liquid pocket (II) that narrows into a thin liquid grain-grain tube (III). In (b) the small grain at centre has disappeared. (c) Pinch-off of the liquid tube (III) occurs after 68 hours leaving a dry grain boundary. (d) Liquid pool (II) slowly forms two triangular liquid pockets at triple junctions (arrows). Time in hours is listed at lower left.

3.7 Rheology

The interior of the Earth is governed by dynamic processes which involve the deformation of rocks at variable spatial and time scales. At high stresses, fast strain rates and low temperatures rocks deform by brittle mechanisms (*e.g.*, ruptures triggering earthquakes) whereas at low stresses, slow strain rates and high temperatures they deform by ductile processes (*e.g.*, the convective movement of the Earth's mantle). The rheological behaviour of rocks is described by flow laws, which can be constructed by performing deformation tests in the laboratory. However, the number of external (*e.g.*, pressure, temperature, oxygen and water fugacity) and internal (*e.g.*, phase content, microstructure, texture) parameters influencing the deformation behaviour of a rock is rather large and controlled deformation experiments at pressures and temperatures pertaining to the Earth's interior remain challenging. Nevertheless, with technological developments (*e.g.*, the D-DIA multianvil apparatus) and the use of low pressure analogue materials (*e.g.*, $CaIrO_3$ as analogue for $MgSiO_3$ perovskite/post-perovskite) insights into the rheological behaviour of the Earth's deep interior can be gained. An important aspect of deformation is the fact that it may introduce microstructural changes and physical anisotropy in the deformed rock which can be detected indirectly in the deep Earth by geophysical methods (*e.g.*, seismic wave velocity or electrical conductivity).

Since the main constituents of the lower mantle, $(Mg,Fe)SiO_3$ perovskite and post-perovskite, are rather unstable at ambient conditions analogue materials such as $CaIrO_3$ are extremely valuable the characterization of their rheology and, especially, the change of rheology due to the phase transition. Deformation experiments with $CaIrO_3$ show that the transition from perovskite to post-perovskite is likely to be accompanied with a change in deformation mechanism from diffusion-assisted grain boundary sliding (perovskite) to dislocation creep (post-perovskite). This in turn means a change from an isotropic fabric (perovskite) to a strongly anisotropic fabric (post-perovskite), which is observed seismologically at the D" layer at the core mantle boundary. The second-most abundant phase of the lower mantle, magnesiowüstite, shows a particularly strong dependence of rheology on the chemical composition (Fe/Mg ratio) since the increasing Fe content is connected to a larger concentration of point defects (vacancies) which have a direct impact on the strength of the material in dislocation creep as well as the deformation mechanism.

The transition zone between upper and lower mantle is also a region where the phase transitions (*e.g.*, olivine to wadsleyite and ringwoodite) have a severe impact on plastic flow. At transition zone conditions the olivine structure of the $MnGe_2O_4$ analogue appears to be much weaker than the wadsleyite structure implying that the phase transition may impede whole mantle convection. In the upper mantle plastic flow and the resulting anisotropy of upper mantle rocks is largely governed by the deformation of olivine; whereas the deformation of pure olivine is fairly well understood, the influence of additional melt has a strong impact on the deformation behaviour and the resulting physical anisotropy. This is especially important the the interpretation of seismic data and flow patterns from the regions

beneath mid-ocean ridges, where partial melting occurs. The rheology and deformation characteristics of pyroxenes are important for the deformation of the lower crust, upper mantle and – especially – subducting oceanic slabs. Again, phase transformations (*e.g.*, proto- to orthoenstatite) as well as ordering phenomena (C2/c -> P2/n change in omphacite) have an impact on the deformation mechanisms and the resulting microstructures. Consequently, detailed analysis of the deformation features in pyroxenes allows to narrow down their p,T conditions of deformation. Upper crustal deformation is largely in the brittle field and there mostly in quartz bearing rocks; the investigation of cataclastic fault zones in quartzites therefore gives insights into the focal mechanisms that trigger earthquakes and the possible role of water in this process.

a. *Crystal morphology and dislocation microstructures of the $CaIrO_3$ phase: An analogue of the post-perovskite phase (N. Miyajima, in collaboration with K. Ohgushi, M. Ichihara and T. Yagi/Tokyo)*

$CaIrO_3$-related structure and behaviour under high pressures and high temperatures are of interest in high-pressure mineral physics, because $MgSiO_3$ perovskite transforms into a denser polymorph having the same structure as $CaIrO_3$ at 130 GPa and 2000 K. This phase is called the "post-perovskite phase" in recent studies. Some knowledge of the plastic properties of the $CaIrO_3$ phase would help constrain those of the $MgSiO_3$ post-perovskite phase, especially in relation to the polarized seismic anisotropy observed in the lowermost mantle. In the present study we report a transmission electron microscopy (TEM) of the basic crystal morphology, and type of dislocations in a synthetic $CaIrO_3$ sample. With a view to understanding better the polarization anisotropy, the preliminary results on the $CaIrO_3$ phase should trigger rheological studies of the post-perovskite phase.

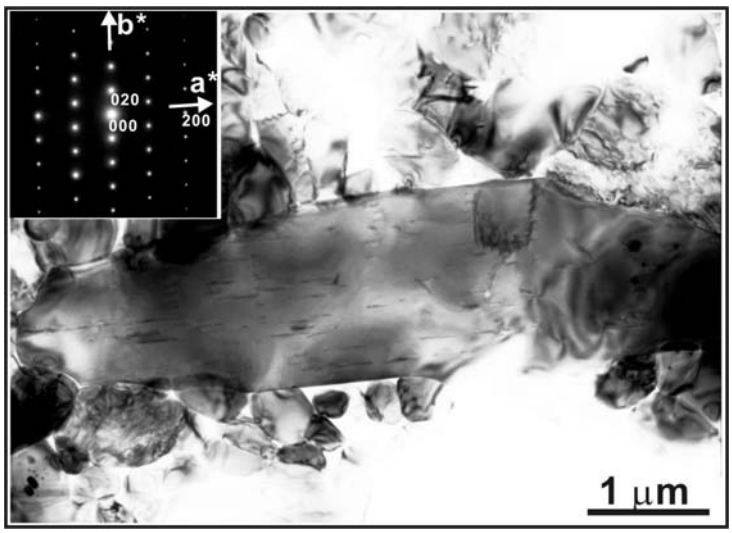

Fig. 3.7-1: Bright-field TEM micrograph of the polycrystalline $CaIrO_3$ phase, indicating a typical plate-like grain elongated to the *a*-axis. The inset is the selected area electron diffraction pattern.

A polycrystalline assemblage of the $CaIrO_3$ phase, synthesized in a multianvil apparatus at 4 GPa and 1473 K, contains many dislocations. The microstructures of the recovered sample have been investigated using TEM operating at 200 kV. The Burgers vectors of the dislocations were determined using the contrast method in weak-beam dark-field (WBDF) images. We found that the individual $CaIrO_3$ crystals have a platy habit elongated along the crystallographic *a* axis, which is the direction of the edge-shared octahedral chain (Fig. 3.7-1). A [100] screw dislocation was activated in the $CaIrO_3$ phase during the synthesis experiments (Fig. 3.7-2). The dominate slip system can be identified as (010)[100], which is the most likely slip system for a (010)-layered structure of IrO_6 octahedrons. The crystal morphology and dislocation microstructures of the $CaIrO_3$ phase should provide important constraints in discussing the source of the polarization anisotropy in the lowermost region of the Earth's lower mantle.

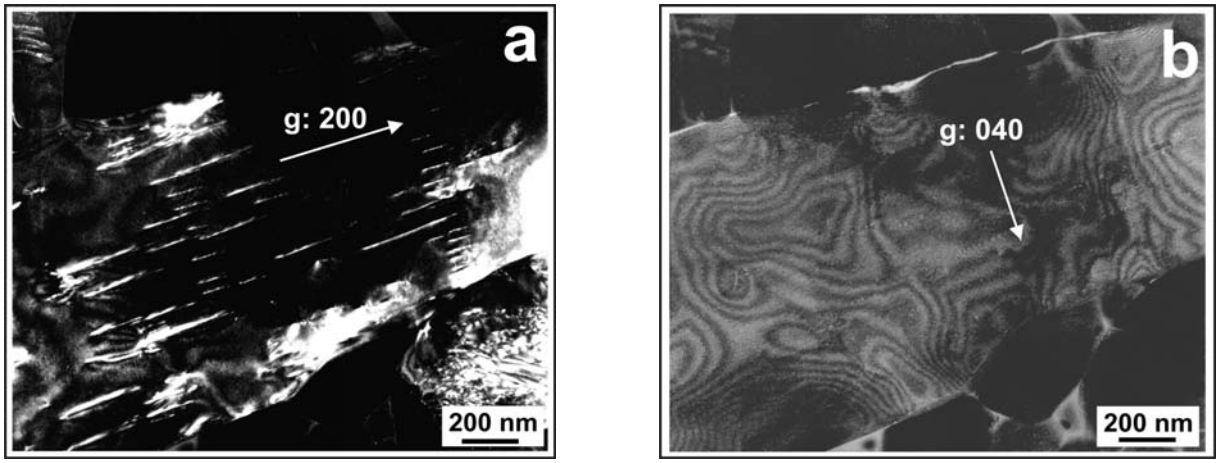

Fig. 3.7-2: Burgers vector determination of a [100] screw dislocation. (a) weak-beam dark-field TEM micrograph (g: 200). The contrast of long screw dislocations is visible. (b) weak-beam dark-field TEM micrograph (g: 040). The contrast of the dislocations is invisible.

b. *Texture development of deformed $CaIrO_3$: Implications for the D" layer at the core-mantle boundary (N. Walte, F. Heidelbach, N. Miyajima and D.J. Frost)*

$MgSiO_3$ perovskite, the major mineral phase of the lower mantle, undergoes a phase transition at approximately 125 GPa into a layered post-perovskite (pPv) structure. This phase transition coincides with the seismically distinct D" layer above the core-mantle boundary of the Earth. Thus, seismic anomalies, such as shear wave splitting that have been observed in the D" layer, might be explained by a lattice preferred orientation (LPO) of the strongly anisotropic pPv crystal structure. Since no direct deformation experiments of the pPv-phase are possible due to the extremely high pressure, isostructural analogue substances have to be used to study the deformation textures.

We performed coaxial compression and simple shear deformation experiments using the deformation-DIA with $CaIrO_3$, an analogue substance that displays a pPv-structure at ambient conditions and a perovskite (Pv) structure at temperatures > 1450 °C. The recovered samples were analysed with SEM-EBSD to obtain the LPO during compression and simple shear. The $CaIrO_3$ Pv-samples were deformed by coaxial compression at 1450 °C and 1GPa in the Pv stability field. Although several Pv-samples have been significantly shortened coaxially, EBSD analysis revealed no discernible LPO (Fig. 3.7-3 top) indicating that dislocation creep did not accommodate much of the plastic deformation. Other mechanisms such as grain boundary sliding and diffusion creep are likely to be active under the experimental conditions.

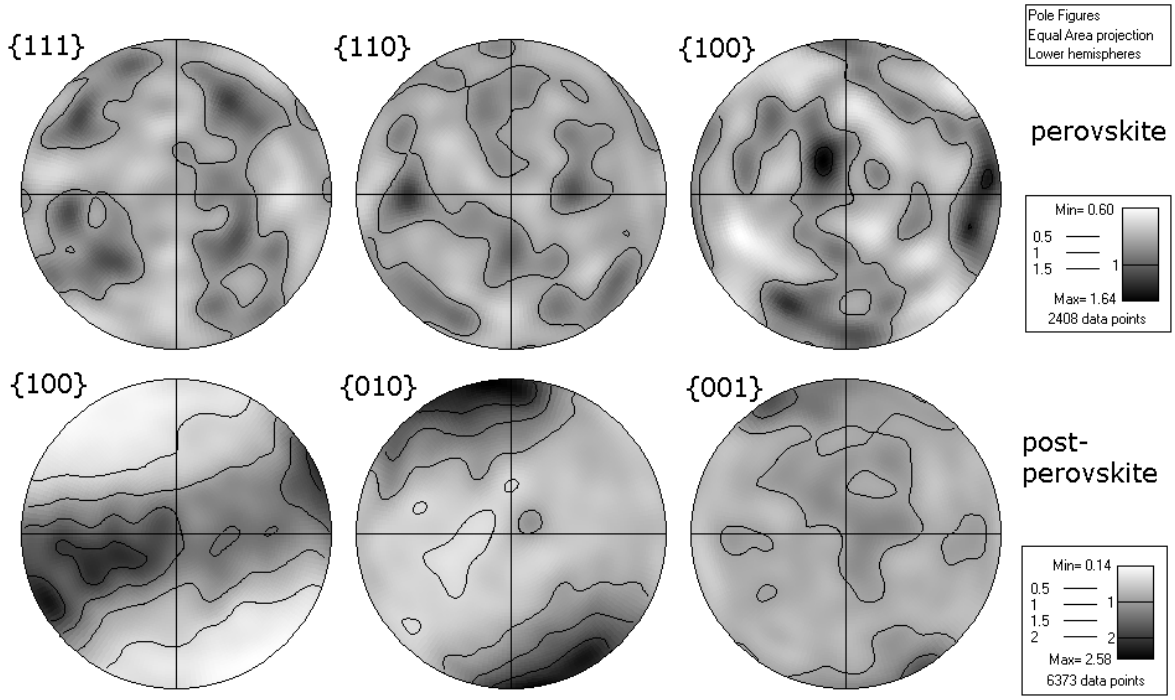

Fig. 3.7-3: Pole figures of experimentally deformed $CaIrO_3$ perovskite (top) and post-perovskite (bottom); perovskite was deformed in axial compression (compression axis vertical) and post-perovskite was deformed in dextral simple shear, trace of shear plane is horizontal and shear direction in E-W; point data for both sets of data were smoothed with a Gaussian of 15° (FWHM).

Investigation of the microstructures reveals the occurrence of diamond shaped grains, which is another indication for grain boundary sliding. The $CaIrO_3$ pPv-samples were deformed both by coaxial flattening and by simple shearing at 1000 °C and 3 GPa. The samples of simple shear deformation experiments display a preferred orientation of the b-axis sub-perpendicular to the shear zone boundary with a 10-20° back rotation of the maximum relative to the sense of shear (Fig. 3.7-3 bottom). The **a**-axis are oriented in a girdle perpendicular to the **b**-axis maximum with a pronounced maximum close to the shear direction with an offset of ca. 20°. The textures produced in axial compression as well as in simple shear of $CaIrO_3$ pPv are consistent with dislocation glide on the (010)[100] slip system.

The single crystal elastic tensor of $MgSiO_3$ post-perovskite calculated for a pressure of 136 GPa and a temperature of 3000 K, was combined with the orientation data of the pPv-samples to calculate the seismic properties of the polycrystalline aggregate. The resulting anisotropy for the pPv-sample of Fig. 3.7-3 (bottom) is shown in Fig. 3.7-4. The shear wave splitting reaches a maximum of 2.7 % near the shear direction and is generally high for shear waves traveling in the shear plane. For these waves the polarization of the fast shear wave lies subparallel to the shear plane. The minimum of the shear wave splitting is at high angles to the shear plane.

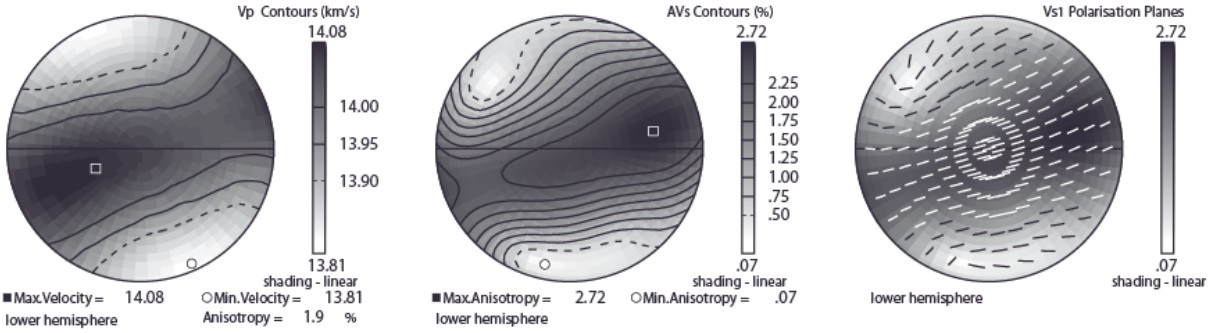

Fig. 3.7-4: Seismic wave velocity distribution of $CaIrO_3$ post-perovskite deformed experimentally in dextral simple shear; distribution of p-wave velocities (left), s-wave splitting (middle) and polarization plane of the fast s-wave (right) are shown.

The results of $CaIrO_3$ deformation experiments in the Pv- and pPv-stability field can be compared to the lower mantle and the D" layer of the Earth. The lack of seismic anisotropy of the lower mantle despite the elastic anisotropy of perovskite could be due to diffusion accommodated grain boundary sliding as the dominant deformation mechanism at lower mantle conditions. In contrast, the anisotropic seismic behaviour of the D" layer can be explained by a switch to dislocation creep after the phase transition to pPv as shown in our experiments.

c. *Lattice preferred orientation in $CaIrO_3$ formed by plastic deformation (K. Niwa, T. Yagi and K. Ohgushi/Tokyo; F. Heidelbach and N. Miyajima)*

Since the discovery of post-perovskite (pPv) phase in $MgSiO_3$ lattice preferred orientation of this phase has been suggested as a candidate of the origin of the seismic anisotropy in D" layer. However the pPv-phase of $MgSiO_3$ is unquenchable to ambient conditions and we cannot study its property using a recovered sample. Moreover, it is very difficult to perform deformation experiments within the Mbar pressure range. Therefore, deformation mechanisms of the pPv-phase under high pressures are still unclear and further experimental approaches are required. Here, we report the results of deformation experiments for $CaIrO_3$ up to 27 GPa.

At ambient condition, $CaIrO_3$ has the same structure with the pPv-phase of $MgSiO_3$ and investigations of the deformation properties of $CaIrO_3$ is important for understanding the behaviour of $MgSiO_3$ at the bottom of the lower mantle.

A diamond anvil cell combined with Nd:YAG laser was used for high pressure and temperature experiments. The initial size of the sample chamber was 180 μm in diameter and 80 μm in height. Perovskite-type (Pv) or post-perovskite-type $CaIrO_3$ was synthesized in advance using a cubic-anvil type apparatus. It was sandwiched by MgO, which works as a thermal insulator, and was loaded in the sample chamber. When Pv-$CaIrO_3$ was used as a starting material, it was compressed to about 13 GPa at room temperature and then converted into the pPv-phase by heating it to above 1500 K for 2.5 hours. After the heating, the pressure was increased gradually to 27 GPa at room temperature. When pPv-$CaIrO_3$ was used as a starting material, it was compressed to 13 GPa at room temperature and the heated to 1500 K for stress relaxation. After that it was further compressed to 27 GPa while the sample was maintained to above 1500 K by laser heating. Lattice preferred orientation of $CaIrO_3$ was studied by the high pressure *in situ* X-ray diffraction (XRD) method and EBSD-SEM observation of the recovered sample. XRD experiments were performed using conventional axial diffraction geometry, which means X-ray was irradiated to the sample parallel to the compression axis. The thickness of the recovered sample was decreased to about 30 % of the original thickness while the diameter was increased to about 140 %.

Figure 3.7-5 shows the XRD patterns of pPv-phase at elevated pressure. Before heating the sample at 13 GPa, diffraction peaks were identified as those of the perovskite phase. After heating for 2.5 hrs, the pressure was dropped to 9GPa and the Pv-phase was transformed into pPv-phase almost completely, although some weak unknown peaks remained. Intensities of the diffraction peaks of the pPv-phase were in good agreement with those of the reference data. This indicates that the crystals of pPv-phase, which were transformed from Pv-phase by heating, had random orientations in the sample chamber. During the increase of pressure up to 27 GPa at room temperature, the pPv-phase was plastically deformed and the diffraction intensities of (020) and (022) lines became relatively strong compared with those of (002) and (110) lines. Diffraction intensities of (020) and (002) lines directly reflect the degree of orientation of the b-axis and c-axis of the pPv-phase, respectively. In axial diffraction geometry, a decrease of the intensity of the (020) peak indicates that the b-axis is aligned parallel to the compression axis. Once this deformed texture is formed, it remained unchanged on release of pressure to ambient conditions.

Figure 3.7-6 shows the results of EBSD-SEM observation of two recovered samples. Secondary Electron Images (SE Images) correspond to the pressurized plane. Figure 3.7-6 (a) shows the SE Image and the pole figure of Run003, which was recovered from just after transforming Pv-phase into pPv-phase, without further deformation. On the other hand, Fig. 3.7-6 (b) shows the results of Run005, which was deformed from 13 GPa to 27 GPa at high temperature. The typical grain size of the recovered samples varied from a few micron to

more than 20 micron. In both samples some platy crystals were observed and the elongated directions correspond to the a-axis of the pPv-structure. Pole figures of Run003 indicate that there is no clear preferred orientation in this sample, while those of Run005 have clear preferred orientation that the b-axis of the pPv-phase was aligned to the compression axis. These results of EBSD-SEM observation support the change of the X-ray diffraction intensity shown in Fig. 3.7-5.

In the present study, we have deformed the pPv-type $CaIrO_3$ from 13 to 27 GPa both at room temperature and at elevated temperature (~ 1500 K) using the diamond anvil cell. In both cases, the lattice preferred orientation aligns the b-axis parallel to the compression axis, and this result can be well explained by the layered nature of the pPv-structure. All these results suggest that the deformation mechanism of such a layered structure does not change significantly with pressure and temperature.

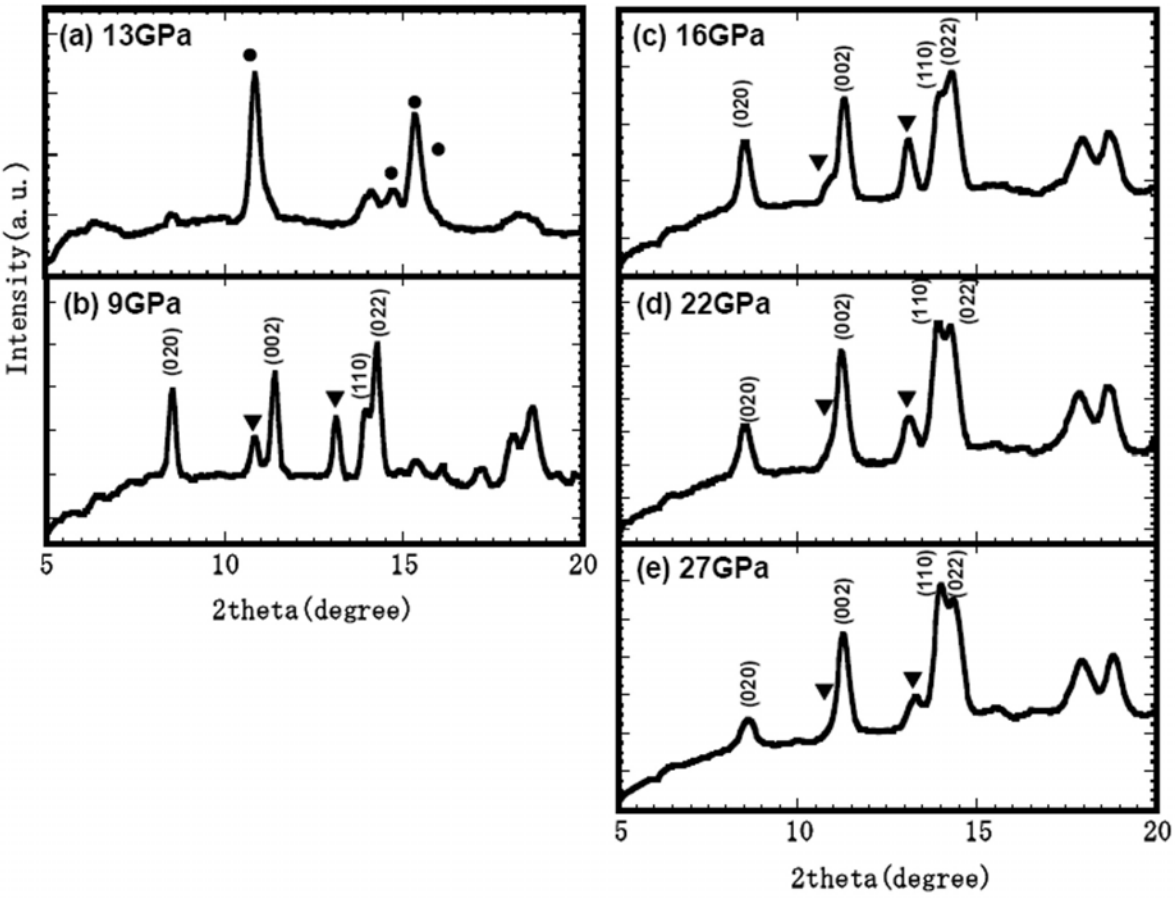

Fig. 3.7-5: Series of XRD patterns for the post-perovskite phase. (a) Before heating at 13 GPa. Solid circle indicate the diffraction from Pv-phase. (b) After heating the sample, pressure was dropped to 9 GPa. Various diffraction lines with Miller's indices were from the pPv-phase. Solid triangle indicates the diffraction from starting material of the Pv-phase or unknown phase. (c)-(e) Diffraction patterns at various pressures to 27 GPa. All patterns were taken at room temperature.

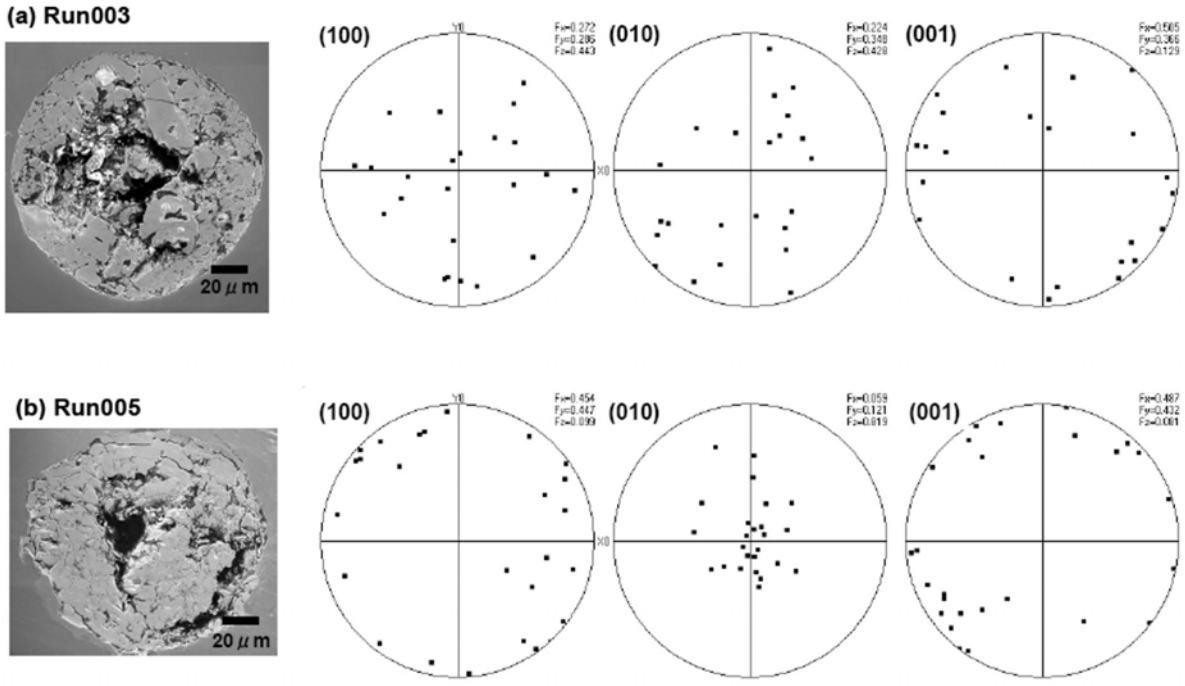

Fig. 3.7-6: Results of EBSD-SEM observation (Secondary Electron Images and pole figure). (a) Recovered from just after transition to the pPv-phase, which is heated at 13 GPa and not deformed. (b) Recovered from deformed experiments. Sample was compressed to 27 GPa accompanied by laser heating.

d. *Experimental deformation of magnesiowüstite to high shear strains: The effect of iron content (F. Heidelbach, I.C. Stretton/London and S.J. Mackwell/Houston)*

The rheology and the fabric development of polycrystalline magnesiowüstite of compositions $(Mg_{0.9\text{-}0.5}Fe_{0.1\text{-}0.5})O$ was investigated in a series of torsion tests at high temperature (1400K) and elevated pressure (300 MPa). The shear strain rates was $2x10^{-3}$ sec^{-1} and the deformation reached shear strains (γ) of up to 15. At a γ of 2 to 3 a steady state flow stress was reached in all samples. The strength of the aggregates decreases significantly with increasing Fe content except between the samples with 40 and 50 % Fe content which have similar strengths (Fig. 3.7-7). Microstructures show an increase in both starting and final grain size with Fe content and a decrease in grain size with increasing strain due to recrystallization.

Deformation tests were performed in the dislocation creep regime and characteristic crystallographic preferred orientations (CPO) developed indicating intracrystalline slip in the <110> direction (Burgers vector) on the {111}, {100} and {110} planes. This is in accordance with known slip system in the fcc crystall structure of the rocksalt type. No significant changes in CPO were detected as function of Fe content with the exception of samples with the $(Mg_{0.5}Fe_{0.5})O$ composition. In these samples texture development was slowed down considerably as a function of strain due to the increased deformation by

diffusional processes (grain boundary sliding, diffusional creep). The observations can be explained by the (absolute) increase in point defects connected with the Fe^{3+} content ($Fe^{3+}/\Sigma Fe \sim 5$ % in all samples) which facilitates climb of dislocations as well as the mobility of grain boundaries. The small change in strength between 40 and 50 % Fe content indicates that there is critical density of point defects (likely vacancies) above which they do not further facilitate dislocation movement and recovery, but enhance mainly the deformation by purely diffusional processes. Applying these results to lower mantle convective flow it appears that an increase in Fe content will additonally weaken the magnesiowüstite phase relative to the predominant perovskite, but will also decrease the amount of physical anisotropy due to magnesiowüstite CPO.

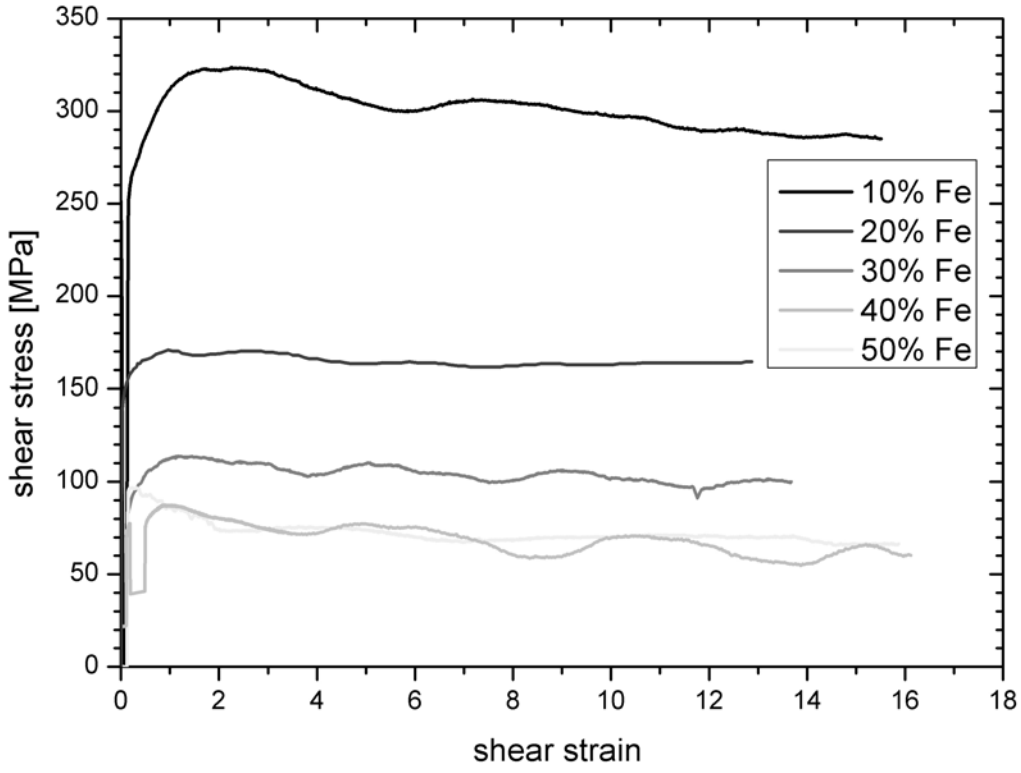

Fig. 3.7-7: Experimental shear stress- shear strain rate curves for polycrystalline magnesiowüstite samples with varying Fe content.

e. *Relative strength of olivine and wadsleyite using Mn_2GeO_4 analogs (H. Couvy, D. Weidner and J. Chen/Stony Brook; D.J. Frost)*

A major issue of modern geophysics is to understand and model the dynamics of mantle convection, which is responsible for many of the geological processes occurring at the Earth's surface. A key question is the rheological contrast between the upper mantle and the transition zone and the influence that this contrast might have on mantle convection. Although the rheological properties of the dominant upper mantle mineral olivine have been extensively

studied, our knowledge of transition zone properties (wadsleyite and ringwoodite) is lacking. Indeed, quantitative deformation experiments under pressure and temperature ranges of these phases (13 to 23 GPa at 1400 °C) are still challenging. Structural analogs of Mg_2SiO_4 phases may provide important information in this regard. Mn_2GeO_4 has been used in previous studies as an analog of Mg_2SiO_4 since it undergoes the same phase transformation of olivine to wadsleyite but at pressures low enough (4-5 GPa at 1000 °C) to allow quantitative measurements using the deformation-DIA apparatus. We have performed *in situ* rheological experiments on these analogue phases at the Advance Photon Source (Chicago) and at the National Synchrotron Light Source (Brookhaven) using a D-DIA multianvil coupled with *in situ* synchrotron X-ray diffraction and radiography measurements.

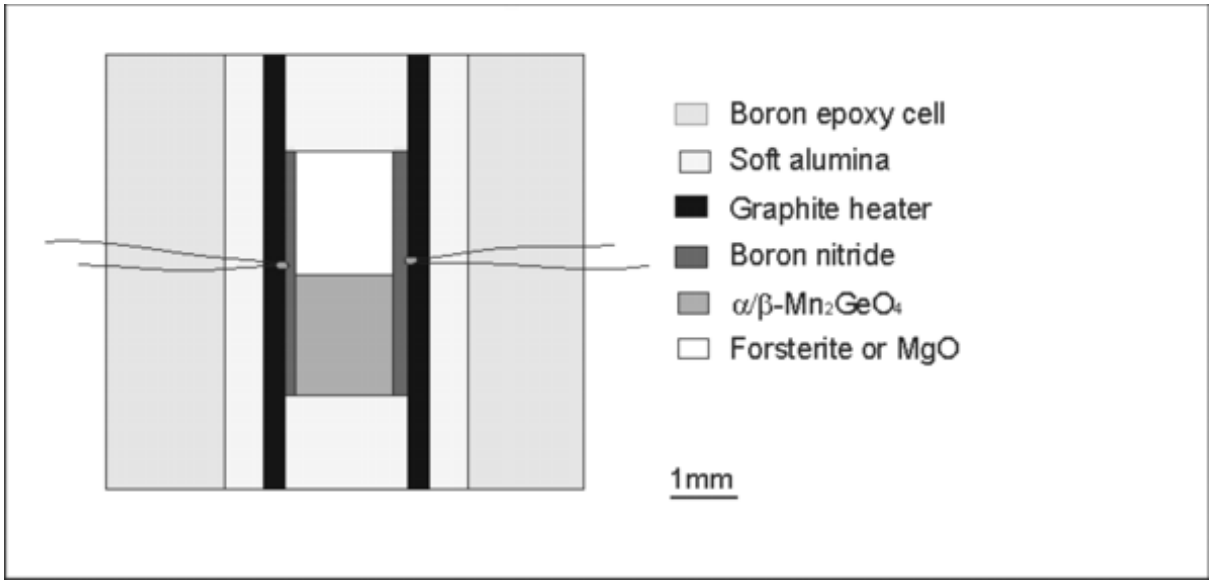

Fig. 3.7-8: Cross section of the deformation assembly in the D-DIA press.

The experiments have been performed by deforming a composite sample consisting of either olivine (α) or wadsleyite (β) structural analog and a standard material (MgO) (Fig. 3.7-8). The relative strength of α and β-Mn_2GeO_4 have been studied at 1000 °C and at 3 and 5 GPa respectively. The deformation conditions have been kept similar for each experiment. The standard has been chosen among materials that do not change substantially in strength over the pressure range studied. Moreover, this standard has provided a stress buffer in order to apply the same deviatoric stress level in those three experiments. The strength contrast can be assessed by measuring strain and strain rate of both α and β-Mn_2GeO_4 and MgO.

Figure 3.7-9 shows the evolution of the total strain of α and β-Mn_2GeO_4 while the same strain rate is applied to the MgO sample ($2*10^{-5}s^{-1}$). The α phase deforms at $2*10^{-4}s^{-1}$ and the β phase deforms at $2*10^{-5}s^{-1}$.Therefore, α-Mn_2GeO_4 seems to be weaker than β-Mn_2GeO_4 at 1000 °C. Moreover, analyses of the lattice strain using diffraction patterns of MgO shows samples have been deformed at approximately 600±200 MPa.

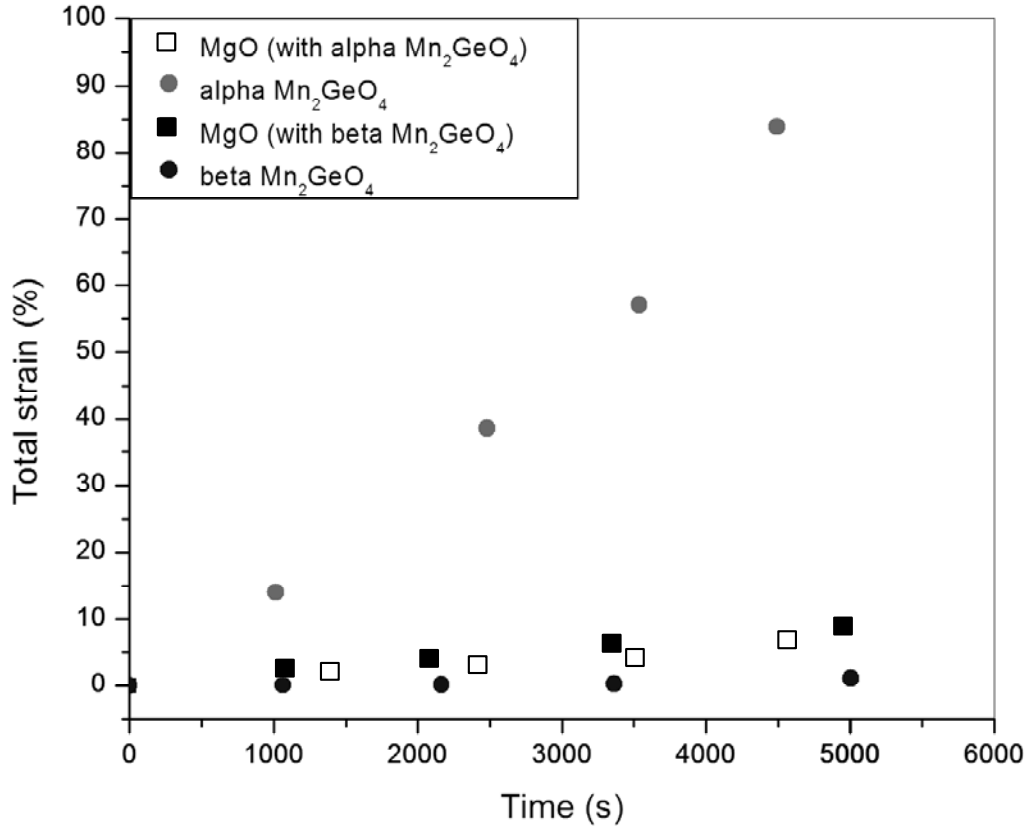

Fig. 3.7-9: Total strain versus time of α and β Mn_2GeO_4 analog (full dots) while the same strain rate ($2*10^{-5}s^{-1}$) is applied on MgO (empty squares).

Although more work is needed in order to determine precisely the deformation mechanisms involved in this study, these preliminary results show an important rheological contrast between α and β phase. Assuming that silicate olivine and these structural analogs behave similarly under mantle conditions, these rheological contrasts might cause a boundary layer in mantle convection in agreement with some seismic tomography data and convection models.

f. *The effect of melt on olivine LPO in direct shear and torsional deformation (B.K. Holtzman/New York, M.E. Zimmerman and D.L. Kohlstedt/Minneapolis; F. Heidelbach)*

In the past few years, we have been exploring the effects of small amounts of basaltic melt on the development of olivine lattice preferred orientations (LPO) in deforming aggregates. Understanding the processes that control the LPO is important because they determine the elastic and thus seismic properties of rocks. This relationship between flow direction and seismic fast direction is critical for understanding how to interpret measured seismic anisotropy in the upper mantle. Recently, a diverse suite of LPO patterns has emerged in experiments, resulting from different factor such as elevated dissolved water content, high stress, high pressure and melt localization with strain partitioning.

In direct-shear experiments in a gas-medium deformation apparatus, at 300 MPa, 1250 °C and shear stresses of 20-150 MPa, we have found that small volumes of melt (0.5-6 %) have a profound effect on the LPO. With no melt present, the LPO is characterized by intracrystalline glide on the (010)[100] slip system. When melt is present, aligned and segregated into melt-rich networks, the a-axes are either randomized or aligned 90 degrees to the shear direction. The transition to an orthogonal relationship between a-axis and shear direction alignment occurs at lower strains if melt is segregated at wavelengths longer than the grain scale than it does if melt is homogeneously distributed.

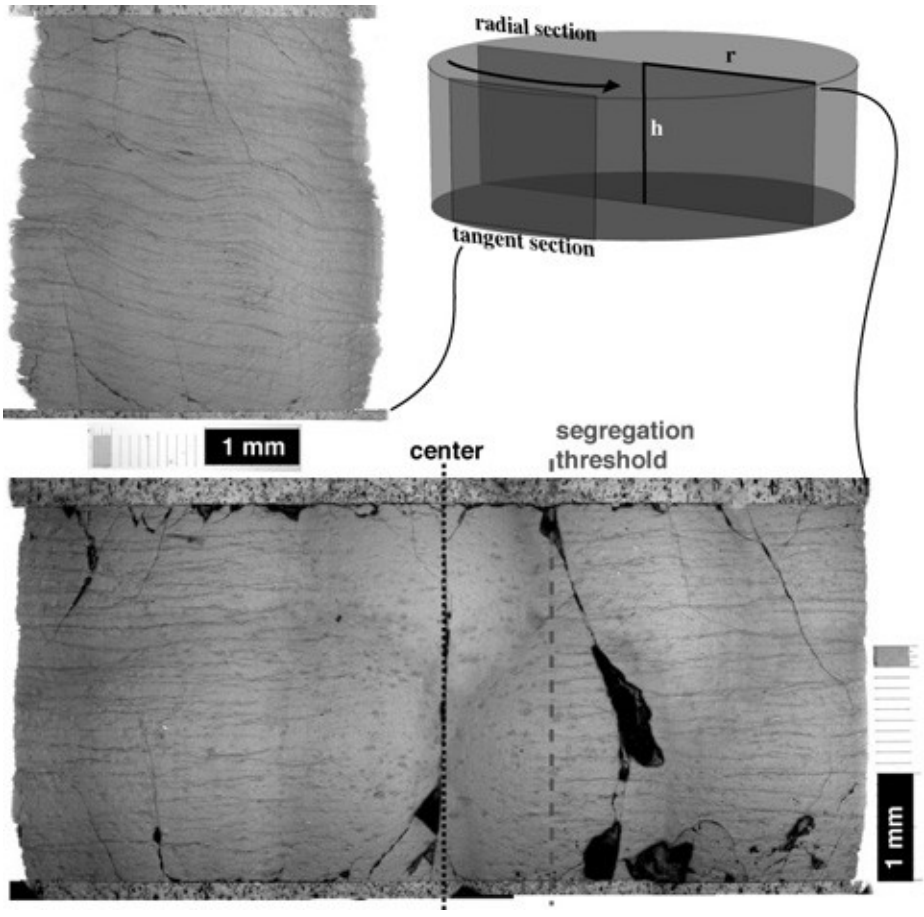

Fig. 3.7-10: Optical micrographs showing a tangential and radial section of a torsion sample containing olivine and melt; dark lines are the melt bands which form above the segregation threshold (*i.e.*, above a certain amount of strain).

This LPO pattern is usually interpreted as a change in dominant slip system, from (010)[100] to (010)[001] slip. However, we interpret it as the effect of strain partitioning: much of the strain in the shear direction is accommodated in melt-rich bands that do not produce an LPO, and the rest of the deformation, reflecting a degree of lateral extrusion, is recorded in the melt-depleted lenses, in which the LPO is produced. This hypothesis is consistent with other micro-structural evidence for strain partitioning. Also, there is no thermodynamic reason that

the intragranular micro-physical dislocation dynamics should change in the presence of melt. So these results raise the question of how the specific character of the 3-D displacement boundary conditions interact with the deformation mechanisms. Is there a critical ratio of shear to flattening required for this fabric transition to occur?

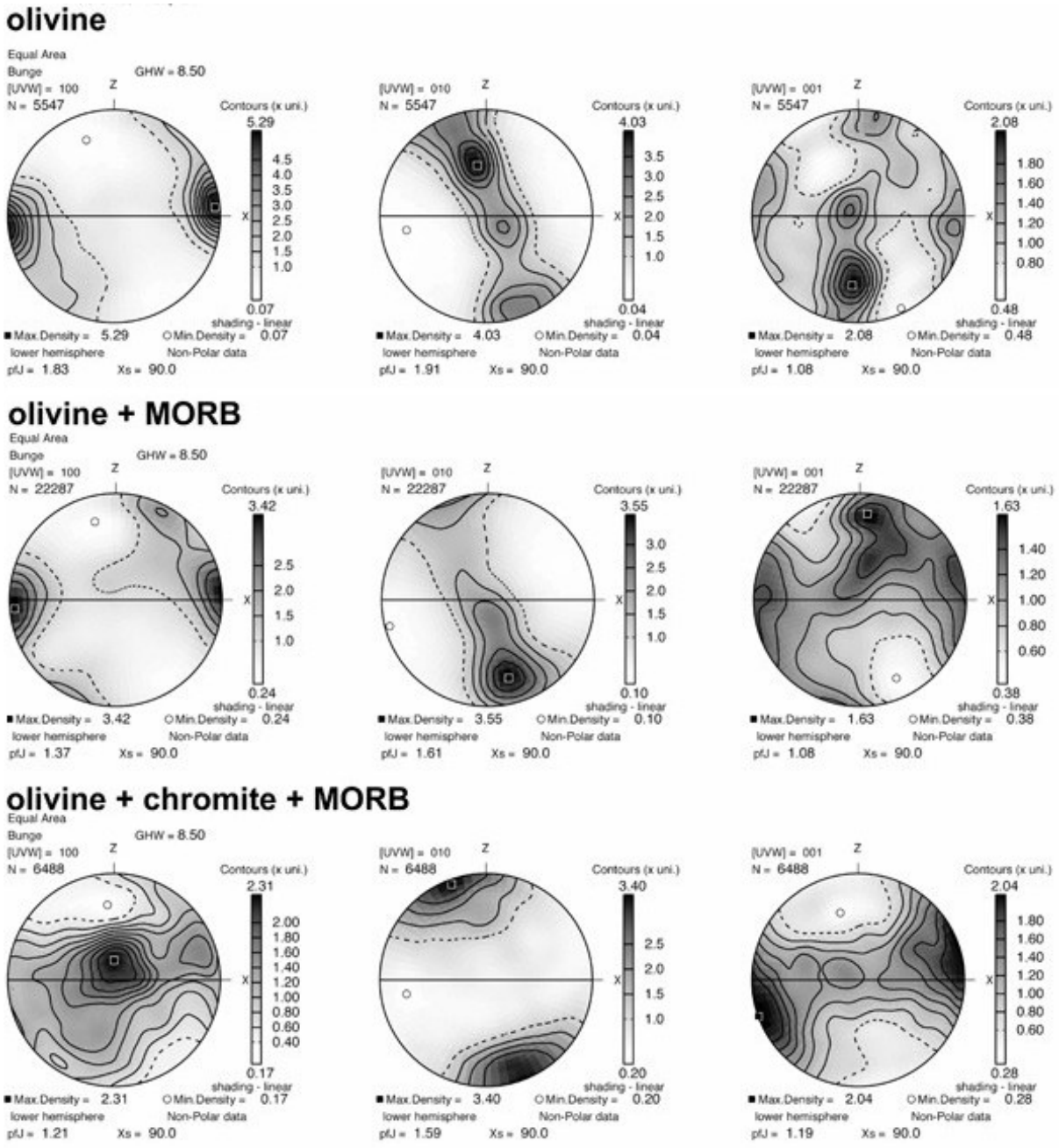

Fig. 3.7-11: Pole figures of torsion samples; pole to the shear plane is marked by Z and the shear direction by X; shear sense is dextral.

To address this question, we perform the same experiments in torsional geometry, which has the advantages that flattening strain is close to 0 % and that much larger shear strains on

larger samples can be achieved. In these experiments melt also organizes into melt-rich bands (Fig. 3.7-10), similar to those in the direct shear experiments. The melt-free olivine torsion samples have LPOs essentially with dominant slip in the [100] direction, as shown in Fig. 3.7-11 top. The samples of olivine + melt have transitional fabrics with a strong [100] maximum in the shear direction, but also a component of rotated [100] maximum and [001] close to the shear direction (Fig. 3.7-11 middle). Samples with olivine + chromite + melt are similar to those that developed in the direct shear samples with melt-rich bands, showing a almost complete rotation of the a-axes (Fig. 3.7-11 bottom). In detail, the small bulging visible on the outer edge of the lenses is evidence for strain partitioning and small components of solid flow towards and away from the center of the sample, but the overall flattening of the sample is very minimal. Thus the process that is causing the rotation to occur does not require a significant degree of flattening. We are developing an analysis and further experimental constraints on the nature and cause of these fabric transitions.

g. *Deformation experiments on omphacite at pressure and temperature conditions of high-pressure metamorphism (W.F. Müller/Darmstadt, N. Walte, N. Miyajima and D.J. Frost)*

The clinopyroxene omphacite, ideal composition $Na_{0.5}Ca_{0.5}Al_{0.5}Mg_{0.5}Si_2O_6$, is - together with garnet - the defining mineral and main component of eclogites. The rheological behaviour of eclogite is dominated by the plastic behaviour of omphacite, which is therefore most important for the geodynamic processes of subduction and exhumation of oceanic and continental crust. The lattice preferred orientation (LPO) of natural omphacite has been extensively studied, and two main fabric types were established, the S- and the L-type. Based on transmission electron microscopy (TEM) studies on omphacites the main slip systems were analysed as (100)[001], {110}[001], and {110}1/2<110>. Subsequent work attempted to simulate the LPO patterns of omphacites in deformed eclogite by means of those slip systems. This was sometimes successful, but not really convincing, because in case of the L-type one had somehow to circumvent the fact that the glide system needed, namely [001](010), was not detected by TEM.

Recently, a new discussion of the deformation behaviour of omphacite was opened by considering its crystallography and crystal chemistry. Omphacite is at temperatures above about 800 °C disordered with respect to its cations and has the space group C2/c. At lower temperatures, the cations Mg and Al convergently order on the M1 positions of the structure which leads to the space group P2/n. This has the consequence that the former “easy-slip” vector ½<110> is no longer a lattice vector and its use as Burgers vector would demand the formation of stacking faults, which is energetically not favoured. It was only consequent to correlate the S- and L-type LPO patterns to the availability or non-availability of the Burgers vector ½<110>, respectively. About at the same time, chain multiplicity faults (CMFs) || (010) were described in eclogites from the Tauern window and shown that they are part of the slip system (010)1/2<011>.

There is a growing knowledge on the deformation effects in omphacite from TEM studies on eclogites from different geologic areas. The deformation effects observed so far are free dislocations, dislocations organised in low angle grain boundaries, recrystallised grains, CMFs parallel to (010), and deformation twin lamellae on (100) (Fig. 3.7-12). The deformation mechanisms activated, however, are obviously not the same in all occurrences. *E.g.*, while the CMFs are frequent in omphacites from the Eclogite Zone and the Lower Schist Cover (Venediger Nappe) of the Tauern Window (Eastern Alps, Austria), they are very rare in the ultrahigh-pressure metamorphic omphacites from Lago di Cignana (Western Alps, Valtournenche, Italy). Deformation twin lamellae on (100) are extremely rare in omphacite from the Lower Schist Cover and have not been observed in omphacite from the Lago di Cignana, but occur in the Eclogite Zone. In order to help to attribute the specific microstructures of omphacite to the deformation conditions of the eclogite in its geologic environment, deformation experiments on omphacite have been started. We report here on our very first deformation experiment and the result of our study by TEM.

The starting material was prepared from large fibroblastic omphacite prisms from Tianshan kindly provided by Reiner Klemd, Würzburg. From this largely monomineralic sample cores of 1.5 mm diameter have been drilled. The deformation experiment was conducted using the Deformation-DIA (D-DIA) high-pressure apparatus of the BGI. The length of the cylindrical specimen was 1.3 mm. It was shortened coaxially by about 10 % at a strain rate of 10^{-5} s^{-1}, a confining pressure of 2 GPa, and a temperature of 800 °C. In future experiments, we will vary the experimental conditions and the starting materials.

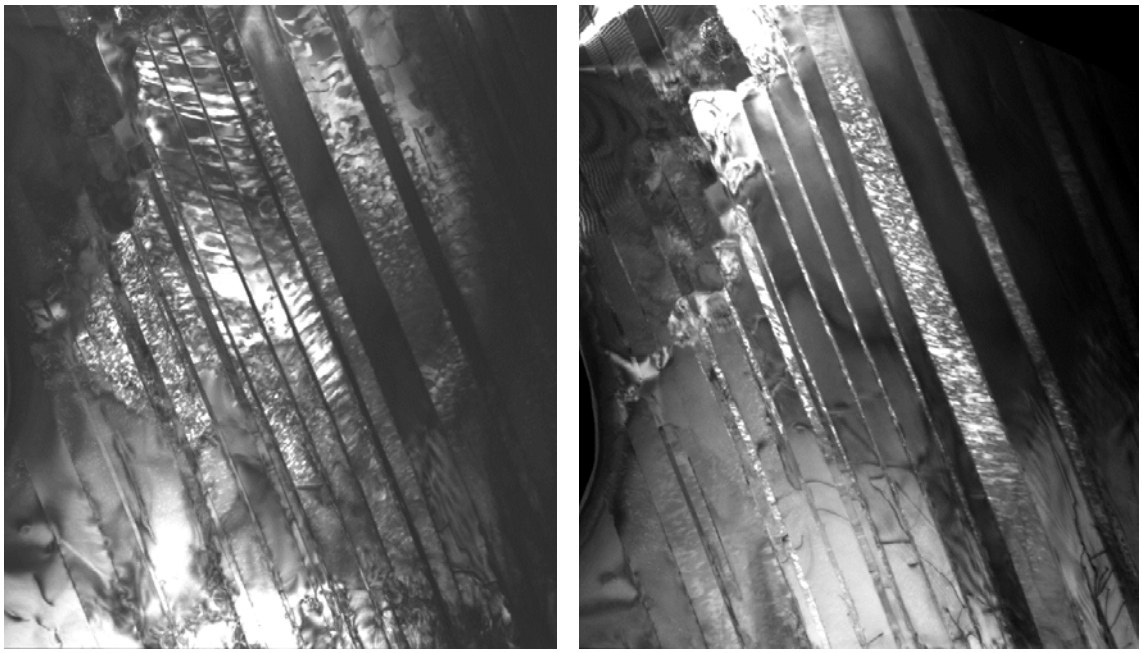

Fig. 3.7-12: TEM dark field micrographs of experimentally deformed omphacite. They are taken from the same area and show deformation twin lamellae on (100). In addition, antiphase domains (visible as black-white contrast in the lamellae) are imaged. The short lengths of the micrographs correspond each to 4 μm.

In the TEM the deformed specimen revealed a high density of submicroscopic lamellae, visible in bright field and dark field images (Fig 3.7-12). The lamellae were identified by electron diffraction as twin lamellae on (100). Although the undeformed starting omphacite has not yet been studied, it is certain that these twin lamellae were produced by the deformation experiment and are deformation twin lamellae. Polysynthetic growth twin lamellae have never been observed in omphacite. The two dark field micrographs of Fig. 3.7-12 are taken from the same area and show the matrix and the twin lamellae. The widths of the twin lamellae vary between 20 nm and 0.5 μm, their spacing are on the same order. The electron diffraction patterns contain also the reflections of the type h + k odd. That means that the omphacite is still ordered after the experiment and has the space group P2/n. Dark field images with reflections of the type h + k odd reveal antiphase domains which were obviously present in the original sample. They are also shown in both micrographs of Fig 3.7-12. From the shape of antiphase domains it can be seen that they were formed prior to the twin lamellae.

h. *High temperature deformation of polycrystalline enstatite (M. Bystricky/Toulouse, J. Lawlis/Rochester, S. Mackwell/Houston, P. Raterron/Lille and F. Heidelbach)*

Although enstatite is a significant component of the upper mantle, its rheology is still poorly understood. We have performed an experimental investigation of the mechanical properties of enstatite at high pressure and temperature in the proto- and ortho-enstatite stability fields. Synthetic enstatite powders were produced by reacting fine-grained San Carlos olivine powders with lab-grade quartz at 1430 °C in a one-atmosphere furnace under controlled oxygen fugacity. Powders were hot-pressed for up to 12 h at 1300 °C and a confining pressure of 300 MPa or 450 MPa, and were then baked at 1000 °C for 20 h under controlled oxygen fugacity conditions to remove all hydrous defect species. The polycrystalline enstatite samples were deformed in a Paterson gas-medium apparatus at temperatures of 1200-1300 °C, an oxygen fugacity buffered at Ni/NiO, and confining pressures of 300 or 450 MPa. At these temperatures, samples were in the orthoenstatite field at 450 MPa and in the protoenstatite field at 300 MPa.

At both confining pressures, the mechanical data display a progressive increase of the stress exponent n from n=1 to n~3 as a function of differential stress, suggesting a transition from diffusional to dislocation creep (Fig. 3.7-13). Non-linear least-square fits to the high-stress data yielded flow laws with a stress exponent of 3 and activation energies of 600 and 720 kJ/mol for orthoenstatite and protoenstatite, respectively.

Deformed samples were analysed using optical microscopy and scanning and transmission electron microscopy. Because enstatite reverts to clinoenstatite during quenching, the microstructures present highly twinned grains composed of thin alternating domains of

clinopyroxene and orthopyroxene. This abundant twinning makes characterization of deformation features and identification of individual dislocations problematic. Nevertheless, the microstructures show evidence of dislocation processes in the form of undulatory extinction and kink bands. Crystallographic preferred orientations measured by EBSD are axisymmetric and indicate preferential slip on (100)[001]. High resolution TEM confirm that most grains are now composed of interlayered lamellae of orthopyroxene and clinopyroxene. For samples deformed at 450MPa, these thin lamellae are bounded by partial *c* dislocations in (100) planes, suggesting that gliding of partial c dislocations on (100) was extensive in samples deformed in the orthoenstatite field (Fig. 3.7-14).

Our high-stress mechanical data for protoenstatite is in perfect agreement with the extrapolation of the flow law for dislocation creep on (100)[001], obtained for single crystals deformed in the protoenstatite stability field. This confirms that the deformation in our samples is likely controlled by slip on (100)[001], arguably the weakest slip system in enstatite. Comparison of our orthoenstatite creep law with existing flow laws for dislocation creep of olivine indicates that enstatite is almost half an order of magnitude (in strain rate) stronger than olivine at our experimental conditions. However, as enstatite has a slightly higher activation energy than olivine, the difference in strength is not likely to be as great under upper mantle conditions.

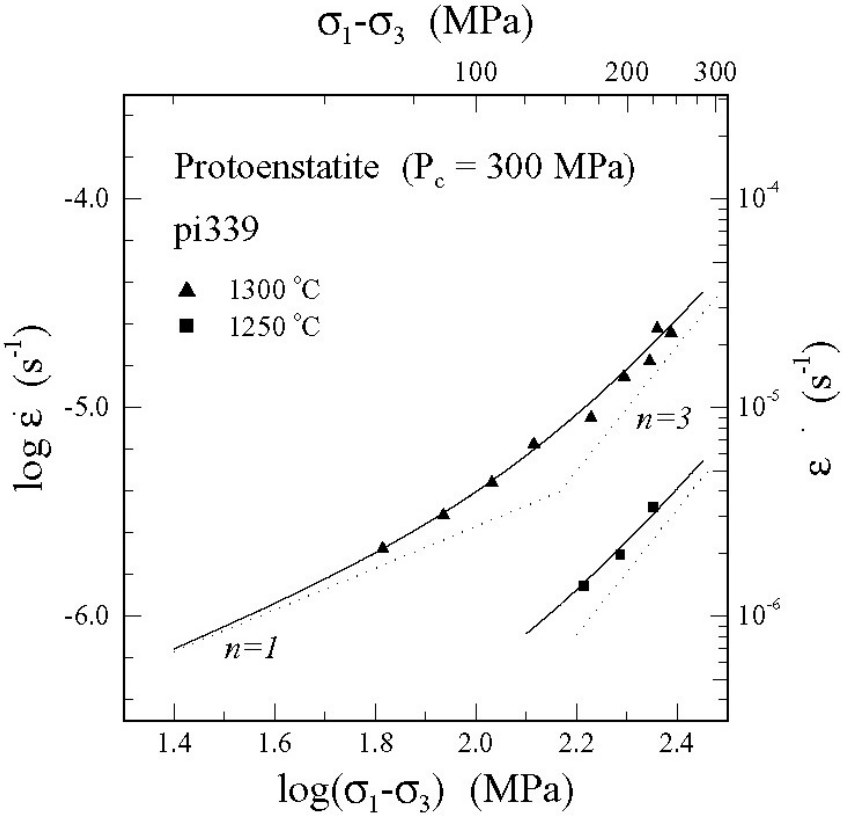

Fig. 3.7-13: Stress-strain rate diagram for a protoenstatite sample.

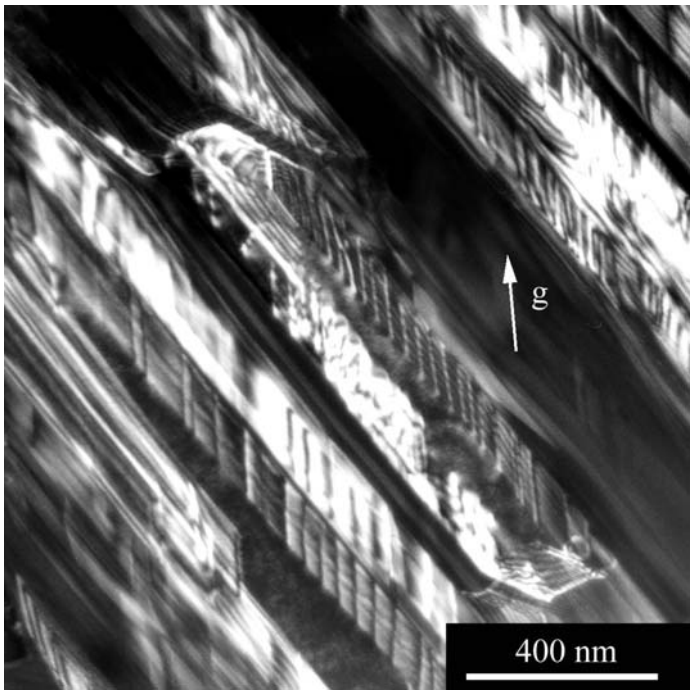

Fig. 3.7-14: TEM dark-field micrograph of deformed orthopyroxene showing thin lamellae of ortho- and clinoenstatite and partial **c** dislocations; g = 001.

i. *Microstructural characterisation of ultracataclastic deformation zones in quartzites by electron microscopy (M. Bestmann/Erlangen, H. De Wall/Würzburg and F. Heidelbach)*

An understanding of the microstructures of natural frictional fault zones is essential to interpreting and modelling fossil earthquake structures, like localized zones of ultracataclasites. Using electron microscopy (scanning electron microscopy (SEM), SEM electron backscatter diffraction (EBSD) and transmission electron microscopy (TEM)), we are investigating two fault zones in quartzites to characterise their microstructural and geochemical evolution.

To constrain the influence of possible fluid flow through the frictional deformation zones cathodoluminescence scanning electron microscopy (SEM-CL) was applied. Preliminary SEM-CL analysis revealed that the ultracataclastic zone from the "Schneeberg Zug"-Austroalpine Unit, Southern Tyrol developed under "wet" (Fig. 3.7-15), and the other from the Muth Formation, NW India, under "dry" conditions.

Since these frictional zones contain brecciated material in sub-micron scale, a TEM-CL system will be utilised for further CL imaging and spectral analysis. Such high-resolution CL-analyses will allow greater insight into grain-scale diffusion processes during deformation and cementation during inter- and/or post seismic healing in ultracataclasites. Such data are important in our understanding of the evolution of active fault-zones which are, directly or indirectly, responsible for many of the major endogenic natural catastrophes worldwide.

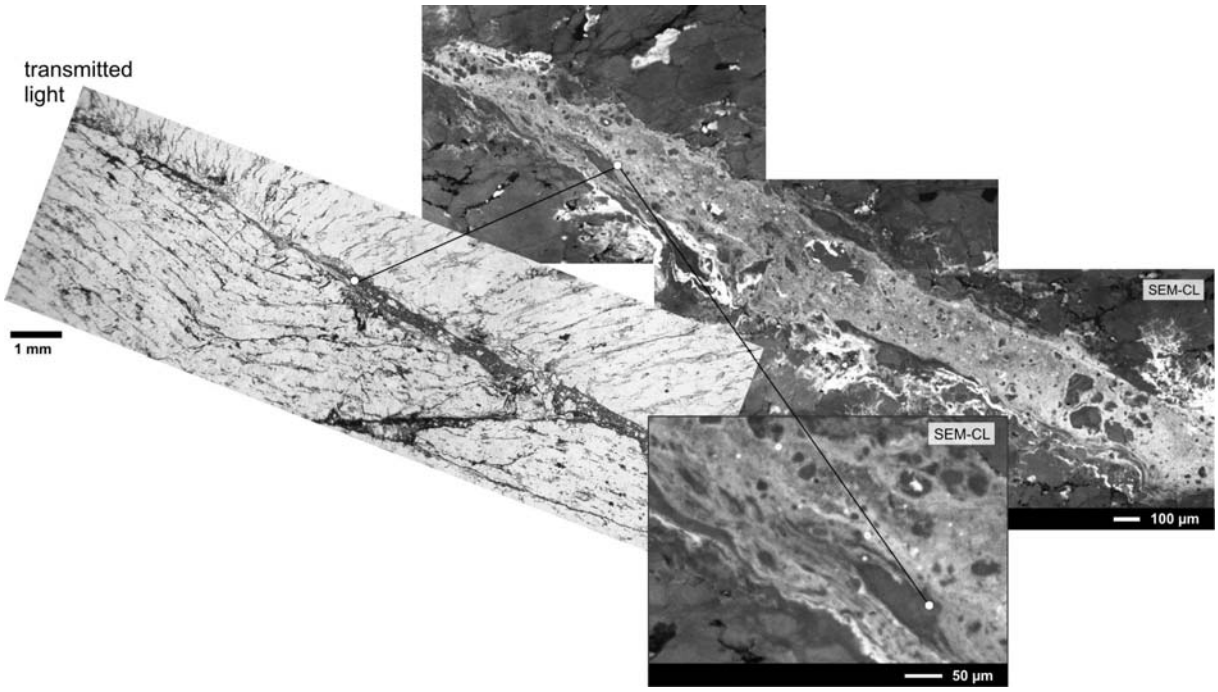

Fig. 3.7-15: Localized ultracataclasic zone in quartzite. The SEM-CL images give evidence of fluid transfer through the cataclastic deformation zone.

3.8 Metamorphism

Metamorphism is the result of changing physical and chemical conditions rocks are subjected to in active geological settings, *e.g.*, in subduction zones, during mountain building, or at rifting margins. Metamorphic reactions involve the solid state transformation of the mineral assembly in the rock that is driven by a new set of pressure, temperature and possibly fluid influx. Since these metamorphic assemblages are often preserved during exhumation, they can be used to unravel the history of the rock masses through space and time and provide a natural laboratory for understanding the processes that take place in the deep crust and upper mantle of the Earth.

The four contributions of this section reflect the diversity of metamorphism in time and space, and the range of topics that can be investigated in metamorphic rocks. The first two contributions deal with shock metamorphism, *i.e.*, metamorphic reactions that occur at very short time scales during impacts (seconds to minutes) but that often reach and record extremely high pressure and temperature, which is normally not preserved in natural settings. The first contribution presents a TEM investigation of the high-pressure nucleation of ringwoodite lammellae in olivine in a shocked chondrite sample. A new type of intergrowth orientation is reported, not previously found in high-pressure experiments. The second contribution presents the results of a high resolution TEM-EELS analysis of aluminous akimotoite ($MgSiO_3$) in shocked melt veins of a chondrite. An unusually-high ferric iron content is reported that can be explained by a coupled Fe^{3+}-Al^{3+} substitution, while coexisting majoritic garnet and ringwoodites are relatively Fe^{3+} depleted. Thus, fO_2 estimations based on these minerals have to be taken with care. The following two contributions illuminate different aspects of eclogite facies metamorphism. The third contribution investigated the importance of subgrain boundaries for diffusion in garnet during metamorphism. The chemical composition of garnet is a key for determining the PTt-paths experienced by different metamorphic rocks. The results show a decoupled diffusion of different elements depending on the occurrence and density of subgrain boundaries, which is of vital importance when modelling PTt-paths. One of the intriguing questions for geologists revolves around understanding the exhumation processes of the dense eclogite after its formation at great depths. In the last contribution the lattice preferred orientation (LPO) in omphacite in eclogites from the Tauern window/Austria was investigated. The LPO of these minerals reveal information on the intensity and direction of shear during eclogite facies metamorphism. The results suggest that current tectonic models for eclogite exhumation in that area may have to be modified.

a. *Ringwoodite lamellae in olivine in a shocked L-6 chondrite: A TEM study of the textural relations and interface growth mechanism (A. El Goresy, N. Miyajima, L.S. Dubrovinsky, T. Boffa Ballaran, F. Seifert, D.C. Rubie; P. Beck and P. Gillet/Lyon, C. Dupas-Bruzek/Lille and M. Chen/Guangzhou)*

Multianvil experiments on single olivine crystals at high pressures and temperatures induced coherent lamellar ringwoodite nucleation and growth in olivine. The experiment demonstrated

that the inversion commences with a coherent nucleation of ringwoodite platelets with their (111) oriented along (100) of olivine followed by semicoherent growth of wadsleyite at the ringwoodite-olivine interface. The coherent ringwoodite nucleation rate was found to be several orders of magnitude slower than the incoherent grain-boundary mechanism. Intracrystalline ringwoodite lamellae in olivine were reported in the last two years from several shocked L-6 chondritic meteorites and interpreted to have formed during the high-pressure regime of the natural dynamic process in the parental asteroid. This texture was thought to be reminiscent of an analogous coherent intracrystalline nucleation and growth of ringwoodite along crystallographic planes of olivine similar to the previously reported from the multianvil experiments. If proven, the intergrowth in the natural assemblage would offer a quantitative tool to estimate the time scale of the natural dynamic events in asteroids in the early history of the solar system.

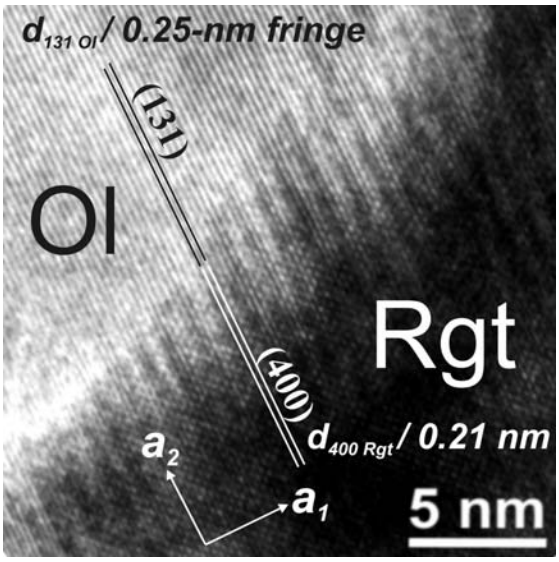

Fig. 3.8-1: High resolution TEM micrograph of an olivine (Ol) /ringwoodite (Rgt) interface.

We investigated olivine grains entrained in and adjacent to shock-melt veins in the Sixiangkou L-6 chondrite. Ringwoodite lamellae were present both in olivines entrained in the melt veins as well as in the 300 μm unmelted region outside the veins. We encountered, in comparison to the multianvil experiments, two sets of ringwoodite lamellae oriented // {101} of olivine. *In situ* microbeam X-ray diffraction indicated that the studied parental olivine grain is a single crystal with no evidence of mosaicism. TEM investigations were then conducted on this olivine crystal in order to uncover the nature of the ringwoodite lamellae and the interface relations with the olivine. The preliminary TEM studies showed that few investigated ringwoodite lamellae (≈ 900 nm) are polycrystalline with a crystallite size of ≈ 200 nm. This feature alone may feign an incoherent mechanism similar to the grain-boundary nucleation and growth experimentally produced in polycrystalline starting material. The

crystallites depict stacking faults // <110>. However, very few ringwoodite crystallites showed topotaxial intergrowth with the parental olivine at their interface (Fig. 3.8-1). The topotaxial intergrowth is: (131) of olivine is // (400) ringwoodite. Figure 3.8-2 depicts the SAED pattern at the olivine-ringwoodite interface. There is considerable lattice mismatch between ringwoodite and olivine: d_{400} ringwoodite = 0.21 nm, d_{131} olivine = 0.25 nm.

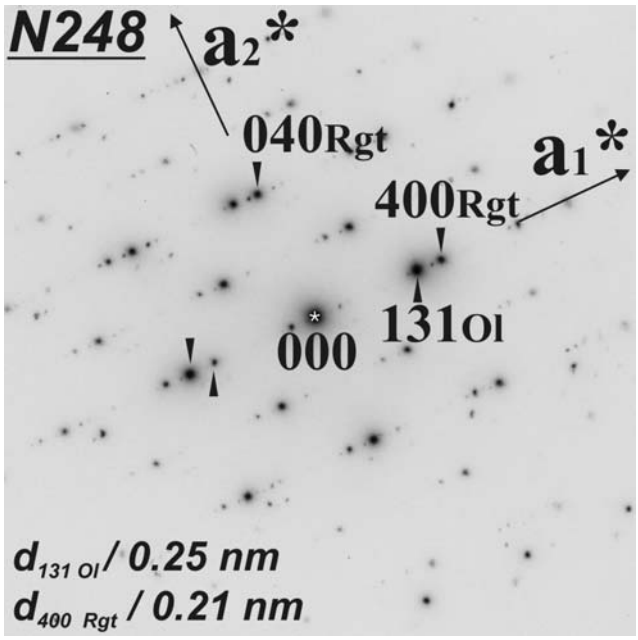

Fig. 3.8-2: Selected area electron diffraction (SAED) pattern of an olivine (Ol)/ringwoodite (Rgt) interface corresponding to the high resolution TEM.

This kind of intergrowth was not observed in natural assemblages before or produced in a laboratory high-pressure experiment on single olivine grains. One possible explanation for the topotaxial ringwoodite/olivine intergrowth could be a similarity of the atom arrangements of both polymorphs along the lattice intergrowth planes: the (400) plane of ringwoodite is constructed by oxygen atoms with distance of about 2.0 Å between the sheets. Oxygen atoms within the plane are arranged in a "squared"-lattice with a period of 4 Å and with distances of about 2.8 Å between oxygens. The (131) plane of olivine also contains oxygen sheets separated by about 2.5 Å and organized in the same manner (O-O distances vary from 2.6 to 2.9 Å) and with the same sequence as in the (400) plane of ringwoodite.

This topotaxial intergrowth is interpreted to be possibly the remnant of the original growth texture that commenced at the olivine/ringwoodite interface. This interpretation is supported by the fact that it is very unlikely to induce dual olivine/ringwoodite intergrowth mechanisms operating simultaneously in the same olivine mono-crystal at the same pressure and temperature: a topotaxial one at the olivine/ringwoodite interface and an incoherent mechanism in the lamella interior. Consequently, we interpret the absence of the topotaxial

olivine/ringwoodite intergrowth in the interior of the ringwoodite lamella to have resulted from recrystallization of the ringwoodite crystallites as the lamella grew and the residual olivine crystallites intergrown with individual ringwoodite crystallites were consumed by ringwoodite.

b. *Ferric iron in aluminous akimotoite coexisting with iron-nickel metal in a shocked L-6 chondrite (N. Miyajima, A. El Goresy, F. Seifert, D.C. Rubie, C. Dupas-Bruzek/Lille, M. Chen and X. Xie/Guangzhou)*

Coupled substitution mechanisms of aluminium and ferric iron were demonstrated in the aluminous silicate perovskite phase of the Earth's lower mantle. The substitutions can yield significant effects in the behaviour of iron during high-pressure phase transitions, element partitioning and transport properties among constituent materials during high-pressure crystallization from chondritic liquids. Akimotoite, an ilmenite-structured high-pressure mineral having the same stoichiometry as $MgSiO_3$ perovskite was reported to contain variable amounts of Al_2O_3 in shocked L-6 chondrites. This raises the question of the possibility of the presence of ferric iron in akimotoite to maintain the charge balance, as demonstrated in aluminous silicate perovskite, the substitution mechanism: $Fe^{3+} + Al^{3+} = Mg^{2+} + Si^{4+}$. In order to explore the presence of ferric iron, we have examined liquidus akimotoite in a shock-melt vein in the shocked Sixiangkou chondrite, using an analytical TEM equipped with energy dispersive X-ray spectrometer (EDXS) and electron energy-loss spectrometer (EELS).

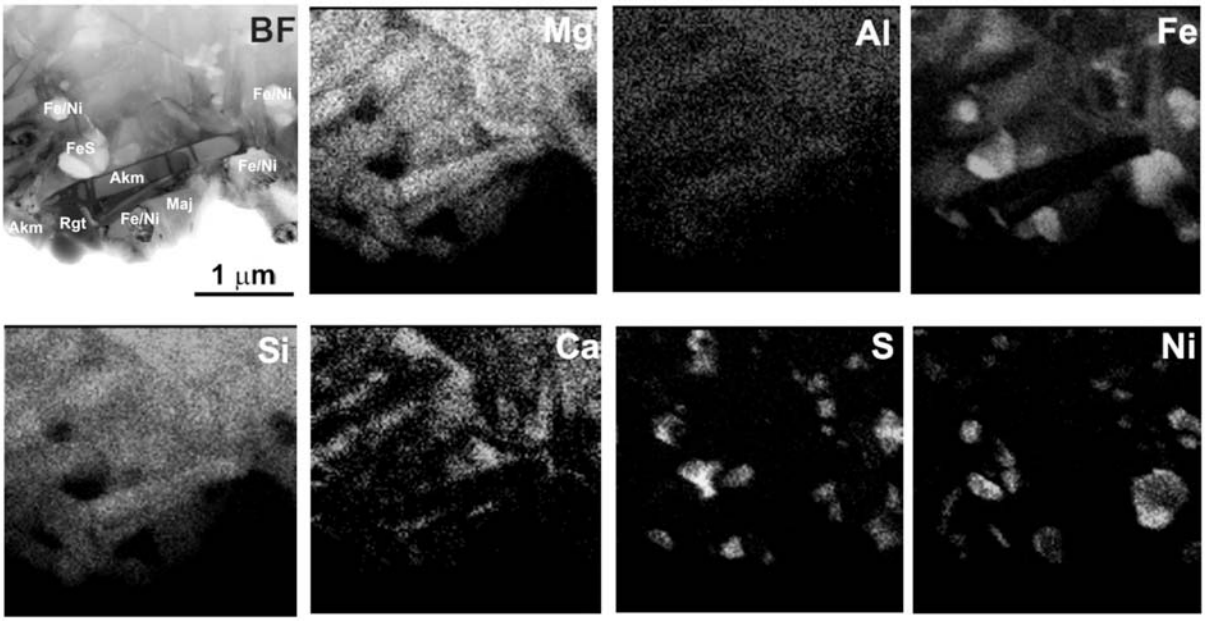

Fig. 3.8-3: Typical scanning bright-field TEM image and the EDXS-elemental mappings (*Mg-K, Al-K, Fe-K, Si-K, Ca-K, S-K, Ni-K*) of a plate-like akimotoite in a shock-melt vein. Notes: Akm: akimotoite, Rgt: ringwoodite, Maj: majoritic garnet, Fe/Ni: Fe-Ni metal, FeS: troilite.

To identify distributions of coexisting phases in a vein, elemental mappings were performed using scanning TEM mode and EDXS (Fig. 3.8-3). As a guide of the images, we measured the ferric iron to total iron ($Fe^{3+}/\Sigma Fe$) ratios in aluminous akimotoite coexisting with the other high-pressure silicate and Fe-Ni metallic phases in a melt-vein, using *Fe-$L_{2,3}$* electron energy-loss near-edge structure (ELNES) spectroscopy. The ELNES results (Fig. 3.8-4) demonstrate that akimotoite has high proportions of Fe^{3+} with $Fe^{3+}/\Sigma Fe$ ratio of 0.67(3). In contrast, the coexisting majoritic garnet and ringwoodite, which are the typical Fe-bearing phases in shock veins in meteorites, are enriched in Fe^{2+} rather than Fe^{3+} with $Fe^{3+}/\Sigma Fe$ ratio of 0.10(5) and 0.15(5), respectively. Concluding, these results suggest that the affinities of Fe^{3+} in coexisting iron-bearing minerals under the same oxygen fugacity (fO_2) and equilibrium pressure should be given attention in discussing the redox conditions of the bulk rock specimen, since Fe^{3+} / Σ Fe ratios in a particular mineral often serve as a proxy for fO_2.

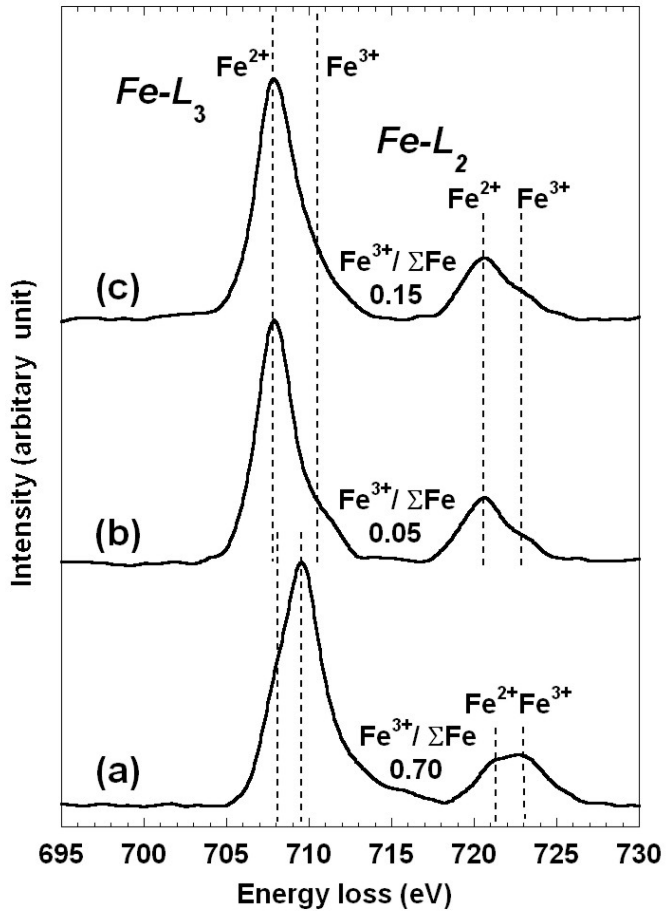

Fig. 3.8-4: *Fe-$L_{2,3}$ ELNES* of coexisting high-pressure phases: (a) akimotoite, (b) ringwoodite and (c) majoritic garnet.

c. *Compositional re-equilibration of garnet: the importance of sub-grain boundaries (M. Konrad-Schmolke and P.J. O'Brien/Potsdam; F. Heidelbach)*

Understanding compositional re-equilibration of metamorphic minerals as a response to changing pressure (P), temperature (T) and/or chemical conditions is one of the most

important aspects of metamorphic petrology. On the one hand, relaxation of T- and P-dependent gradients in chemical compositions of minerals blurs information about previous metamorphic stages, thus complicating exact determination of P-T-paths or of growth and fractionation processes during metamorphism. On the other hand, as long as the mechanism of diffusional relaxation and its parameters are known, characteristic diffusion-induced chemical zonation within mineral grains can be used to constrain temperature-time histories by calculating the effects of diffusion on pre-existing growth patterns and comparing the so-modelled profiles with those in natural samples.

In this study we investigated high-pressure garnets from the Sesia Zone, Western Alps, an area famous for its well-preserved Alpine eclogite facies mineral assemblages in continentally derived rocks. Investigations with electron microprobe and electron backscatter diffraction revealed that many garnets consist of a large number of sub-grains with irregular boundaries as well as different grain sizes and shapes. In order to test whether this sub-grain network has enhanced element mobility and compositional relaxation we also undertook detailed compositional mapping of the same garnets.

Generally, garnet shows at least three growth zones, indicated by brightness variation in back-scattered electron (BSE) images and exhibits two different types of zonation pattern. Some grains show domains with well-preserved concentric zoning whereas others parts of the same grains show an irregular, mesh-like zonation pattern (Fig. 3.8-5). An orientation contrast (OC) image (Fig. 3.8-6A) of the "cloudy" area in the garnet shown in Fig. 3.8-5C reveals a complex internal sub-grain texture. Different shades of grey in the image indicate a difference in orientation of neighbouring sub-grains. Comparison of OC images with major and trace element compositional maps (Figs. 3.8-6B-F respectively) shows that chemical modification of the originally concentric growth zonation correlates with sub-grain boundaries and also that the extent of modification is element dependent.

This observation suggests decoupling of relaxation of compositional gradients of relatively fast-diffusing elements (such as Mg) from that of slow-diffusing elements (such as Ca, Ti and Y). Further, the preservation of the original concentric zonation pattern demonstrates that the development of the sub-grain pattern postdates initial growth and that diffusional modification of the garnet interior occurs as a result of the presence of these sub-grain boundaries. The OC image (Fig. 3.8-7A) of the large garnet grain shown in Fig. 3.8-5F reveals a very complex internal microtexture. Whereas the core consists of a large number of small, mostly roundish sub-grains, the rim is made of larger elongate, sometimes palisade-like sub-grains. The close-up in Fig. 3.8-7B shows that the size of sub-grains in the fine-grained areas is between 1 and 10 μm, whereas the palisade-like grains in the rim have diameters of at least 20 to 30, sometimes up to 100 μm. The compositional variations of Mg and the X_{Mg} value (Figs. 3.8-7C and D) correspond well with the sub-grain boundary pattern in the garnet crystal *i.e.*, shows high values at garnet rim and along the sub-grain boundaries throughout the

interior. As a result of the small grain-size of sub-grains and thus high grain-boundary density, the core is almost entirely equilibrated at the same X_{Mg} level as the garnet rims.

Compositional maps of Ca (Fig. 3.8-7E) and Fe (Fig. 3.8-7F) show markedly different patterns. Whereas the Fe pattern roughly corresponds with the grain boundaries of the palisade-like sub-grains in the rim of the large garnet, there is almost no correlation between Ca-content and the sub-grain pattern in this domain. In the core, Fe and Ca exhibit a completely different compositional pattern compared to that of Mg and X_{Mg}. Ca and Fe patterns allow recognition of two core regions with slightly higher Ca and lower Fe values, one in the upper left side and one in the lower left side of the map. This suggests the existence of two garnet nuclei that amalgamated during the growth process, a structure that is obviously older than the sub-grain pattern and the Mg and X_{Mg} patterns, which equilibrated at or near peak metamorphic conditions. Differences in the diffusional re-equilibration between major elements are evident in the composition of Grt 2.1 fragments. Whereas some of the grains (arrow 1, Fig. 3.8-7) are nearly unchanged with respect to their original composition (see also Fig. 3.8-5), other, smaller sub-grains show a complete re-equilibration with respect to Mg (although the Ca and Fe content is not exactly the same as at the rim, arrow 2, Fig. 3.8-7), which leads to a complex X_{Mg} pattern that cannot be simply interpreted in terms of a P and T evolution.

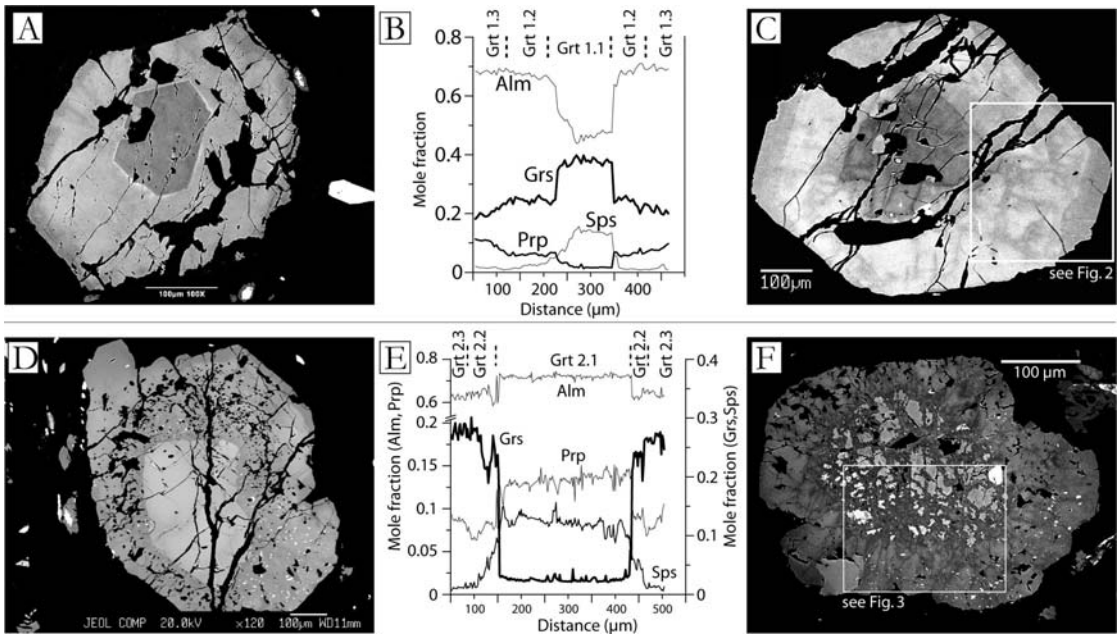

Fig. 3.8-5: Type 1 (A-C) garnets have almandine-grossular-rich cores that appear dark in the BSE image (Grt 1.1), surrounded by a 'lighter' mantle (Grt 1.2) with significantly lower Ca and higher Fe, and a 'darker' outer rim (Grt 1.3) where Mg increases at the expense of Ca. Type 2 (D-F) garnets have 'bright' almandine-rich, grossular-poor cores (Grt 2.1), overgrown by an almandine-grossular-rich mantle (Grt 2.2) and a small 'darker' rim (Grt 2.3) with slightly lower grossular and almandine and higher pyrope content.

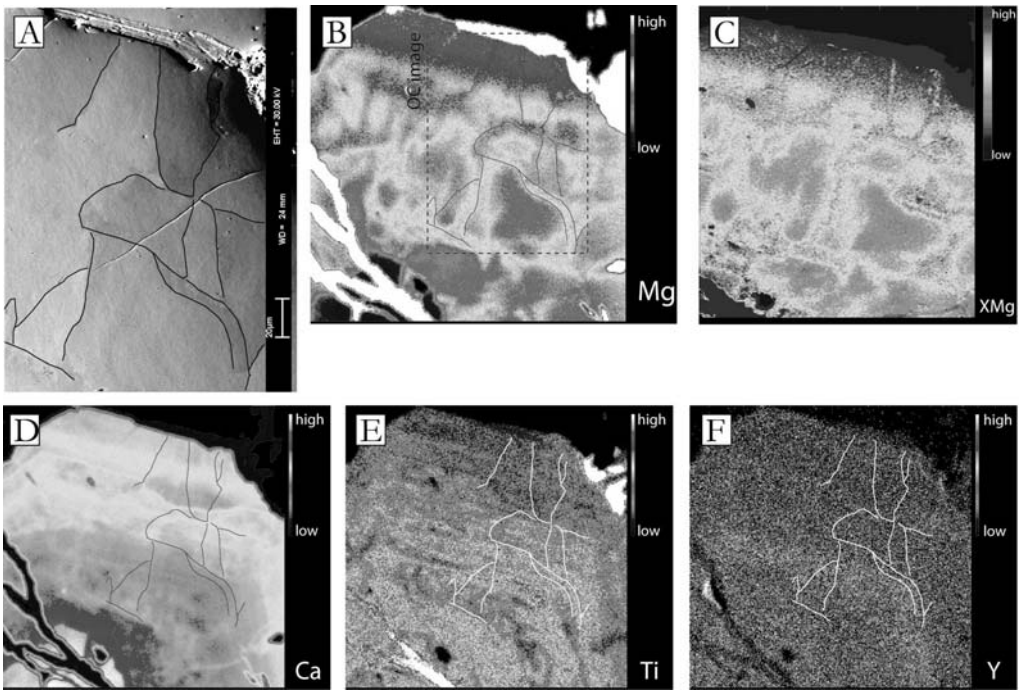

Fig. 3.8-6: Compositional patterns of Mg and X_{Mg} (=Mg/(Mg+Fe)) match the 'dark-light' pattern visible in the BSE image and largely correlate with the sub-grain pattern in the OC image. In contrast, Ca, Ti and Y concentrations (D, E, F, respectively) preserve a concentric pattern that is independent of the radially-oriented sub-grain grain-boundary network.

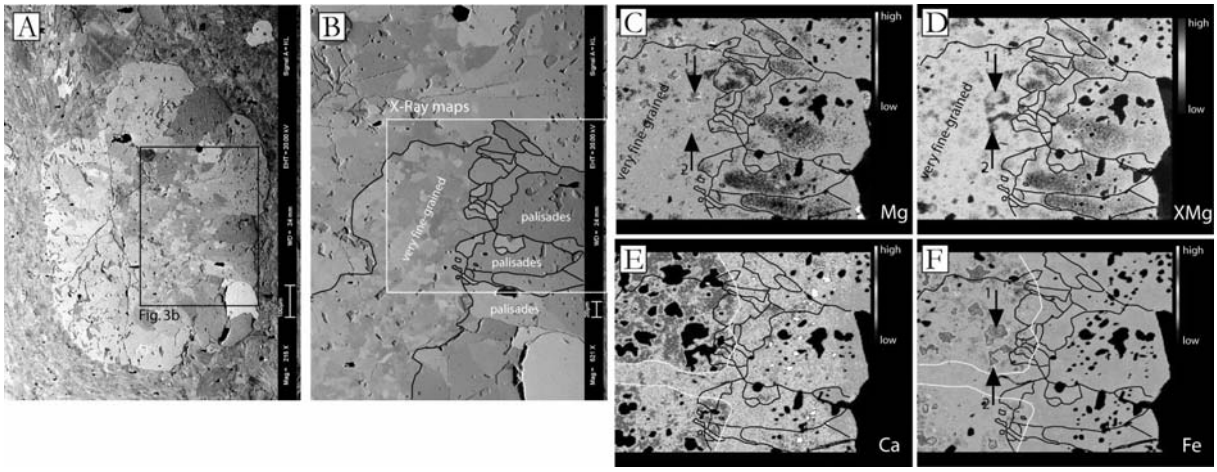

Fig. 3.8-7: OC images (A and B) show a 'core-mantle' texture of the garnet crystal in Fig. 1F with fine-grained (< 10 µm) sub-grains in the core and palisade-like, larger (> 20 µm) sub-grains forming the rim. Compositional maps show that Mg (C) and XMg (D) have highest values along sub-grain boundaries and in the fine-grained core and correspond well with the sub-grain pattern. In contrast, Ca (E) and Fe (F) allow recognition of older compositional pattern in the core (white framed regions). Differential re-equilibration between major elements (arrows) leads to a complex XMg pattern that cannot be interpreted in terms of a P-T path (see text for further explanation).

The above observations show that the patchy compositional variations visible in BSE images of many high-pressure garnets (Fig. 3.8-5C and F) are most likely the result of differential diffusive chemical re-equilibration of pre-existing zonation along sub-grain boundaries. Peak X_{Mg} values along grain and sub-grain boundaries in our samples indicate compositional re-equilibration during the prograde evolution or near peak metamorphic conditions. Further, there is a decoupling of chemical resetting between apparently fast diffusing elements, such as Mg, and slow diffusing elements such as Ca, Ti and Y during the re-equilibration process (Fig. 3.8-6). The extent of diffusional resetting is clearly dependent on the size of sub-grains, which might have severe consequences for the interpretation of diffusional relaxation timescales for garnets with a critical sub-grain size as in Fig. 3.8-5F. In this case the size of the sub-grains in the garnet interior is small enough (< 20 μm) to enable almost complete resetting with respect to X_{Mg} whereas larger sub-grains still preserve lower X_{Mg} values.

d. *Omphacite textures in eclogites of the Tauern Window: Implications for the exhumation of the Eclogite Zone, Austrian Alps (K. Neufeld/Mainz, U. Ring/Christchurch, R. Neuser/ Bochum and F. Heidelbach)*

The exhumation of extremely dense eclogites from great depths to mid-crustal levels is a lively debate in tectonics. Eclogite has a density up to 3600 kg m^{-3} and is thus much denser than any other crustal rock and also significantly denser than the lithospheric mantle. The deeply exhumed Eclogite Zone in the Tauern Window of the Austrian Alps is a superb example for addressing this problem. The Eclogite Zone is part of the Pennine nappe edifice of the Tauern Window and sandwiched between metasedimentary rocks of the Venediger Nappe below and ophiolithic rocks of the Glockner Nappe above. While maximum pressures of the surrounding units were 10-12 kbar, the Eclogite Zone was subjected to pressures of up to 20-25 kbar. Because of the adjacency of lower pressure units, different authors postulate an extrusion wedge for the Eclogite Zone with a top-N thrust fault below and a top-S normal fault above.

In this case lattice preferred orientation (LPO) in omphacite of the Eclogite Zone were analysed and compared with kinematic indicators of the Eclogite Zone and its surrounding rock units. LPO distribution along profiles across the entire Eclogite Zone were studied to review different exhumation models, assuming that the patterns should reflect the development from burial to exhumation and also deformation induced kinematic changes on both sides of the Eclogite Zone. The omphacite textures show strongly symmetric patterns across the entire Eclogite Zone. Only in few cases some asymmetries were observed. The patterns are characterized by an alignment of {110} and {010} with the foliation and a maximum of <001> close to the lineation (Fig. 3.8-8). These patterns are indicative of deformation by intracrystalline glide on the (010) [001] and (110) [001] slip systems and seem to be not affected in any way during the exhumation. The patterns are mainly transition patterns but often close to S-type LPO which is suggested to be developed during the burial of

the eclogites and therefore represent prograde textures. This is in contradiction with most of the suggested exhumation models which are based on mainly extensional processes.

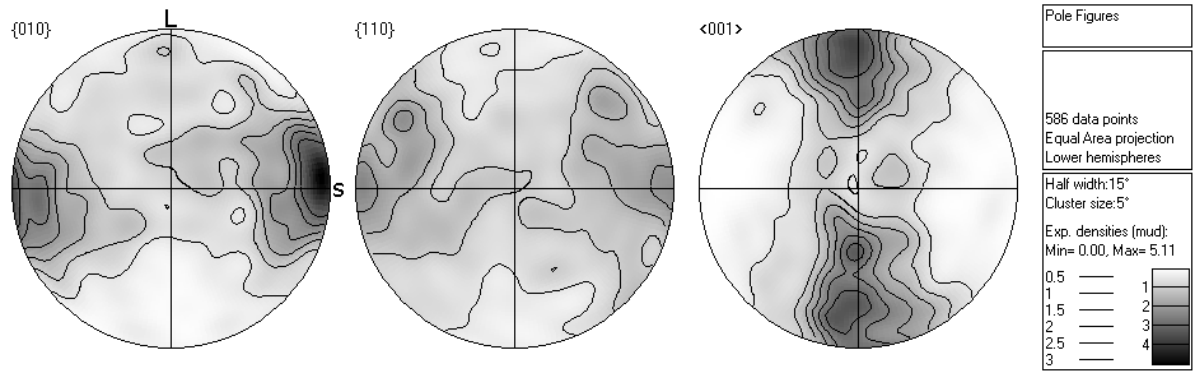

Fig. 3.8-8: Omphacite LPO from the Tauern Window, Austrian Alps. L marks the lineation and s the pole of the foliation.

Our conclusion is that the Eclogite Zone underwent an indirect exhumation process that enables the eclogites to keep a prograde signature which was preserved during the exhumation process. Kinematic indicators show top-N thrusting at the base of the Eclogite Zone and sinistral strike-slip with a modest normal faulting component at its top. Most of the kinematic indicators record blueschist- and greenschist-facies metamorphic conditions. Because of very rapid exhumation of the Eclogite Zone with rates exceeding 36 mm/yr, the kinematic indicators are interpreted to reflect the entire exhumation process from eclogite facies conditions. We suggest a model according to which the Eclogite Zone was exhumed in a strongly oblique extrusion wedge.

3.9 Materials Science

Materials science seeks to link the structure of atoms and phases in the material with the desired properties and performance for specific applications. A major influence on the structure of a material and its properties are its chemical composition and how it was processed into its final form. Applying pressure has become a common method for tuning volume, structure, and electronic properties of materials; hence Bayerisches Geoinstitut enjoys a strong advantage in the development, synthesis and characterisation of new materials with unique and useful properties. Superhard materials continue to be a focus of current research, where results from boron nitride nanocomposites show exciting promise. Nanocrystalline forms of known materials can enhance useful properties of their macrocrystalline counterparts, for example diamond, and research continues in the synthesis and characterisation of nanocrystalline diamond. A further method to enhance the useful properties of diamond is through boron doping, which modifies its electronic structure, and ongoing high-pressure synthesis experiments and theoretical calculations provide insight into its superconducting behaviour. Applications of nanocrystalline titania, zirconia and their solid solutions include use as pigments, electronics and catalysts, and studies continue to characterise their compression behaviour and phase transitions in order to understand the link between composition, microstructure, and physical properties. This theme is continued in the remaining studies reported in this section that encompass a diverse range of materials and properties.

a. *Superhard nanocomposite of dense polymorphs of boron nitride: Noncarbon material has reached diamond hardness (N.A. Dubrovinskaia, L.S. Dubrovinsky and N. Miyajima; V.L. Solozhenko and O.O. Kurakevych/Paris; V. Dmitriev/Grenoble)*

In 1957 the high-pressure high-temperature (HPHT) synthesis of cubic boron nitride (cBN) opened a field of important technical applications similar to those of diamond. With regard to thermal stability and resistance to reaction, which reaches 1650 K, cBN is superior to diamond (the latter is thermally and chemically stable only up to 950 K); hence cBN is the superabrasive of choice for machining hard ferrous steels. However, cBN cannot completely replace diamond because its hardness is only half that of diamond: single crystal diamond has a Vickers hardness (Hv) of ~ 100 GPa, while the hardest single crystal cBN has a value of ~ 50 GPa, and for commercially used polycrystalline cBN and polycrystalline diamond (PCD) the corresponding values are even lower. Many researchers and industrialists have concentrated on the synthesis of novel superhard phases in the B-C-N ternary system as thin films and bulk materials to fill this “hardness gap”, but the results obtained in the triple system are controversial.

Experimental observations and simulations suggest that for many polycrystalline materials there is an optimal grain size (usually in the range of dozens of nm, *i.e.*, nanocrystalline)

which results in a significant (up to 20-30 %) increase of hardness of the material compared to their coarse grain counterparts. Nanocrystalline diamond and aggregated diamond nanorods (ADNRs) have been successfully synthesised at high pressure and temperature and demonstrate some noticeable improvement of hardness.

We conducted a series of HPHT synthesis experiments on nanocrystalline BN phases using a multianvil press and various precursors in a broad range of pressures and temperatures. The results of HPHT synthesis in the BN system depend strongly on the nature of the precursor. Starting from pyrolytic p-BN, we synthesised unique superhard aggregated boron nitride nanocomposites (ABNNCs) showing a unique Raman spectrum (Fig. 3.9-1) and an enhancement of hardness up to 100 % compared to single crystal cBN (Fig. 3.9-2). Decrease of the grain size down to 14 nm and simultaneous formation of two dense BN phases with hexagonal and cubic structures within the grains at nano and sub-nanoscales produce an enormous enhancement of mechanical properties with a maximum hardness of 85(5) GPa.

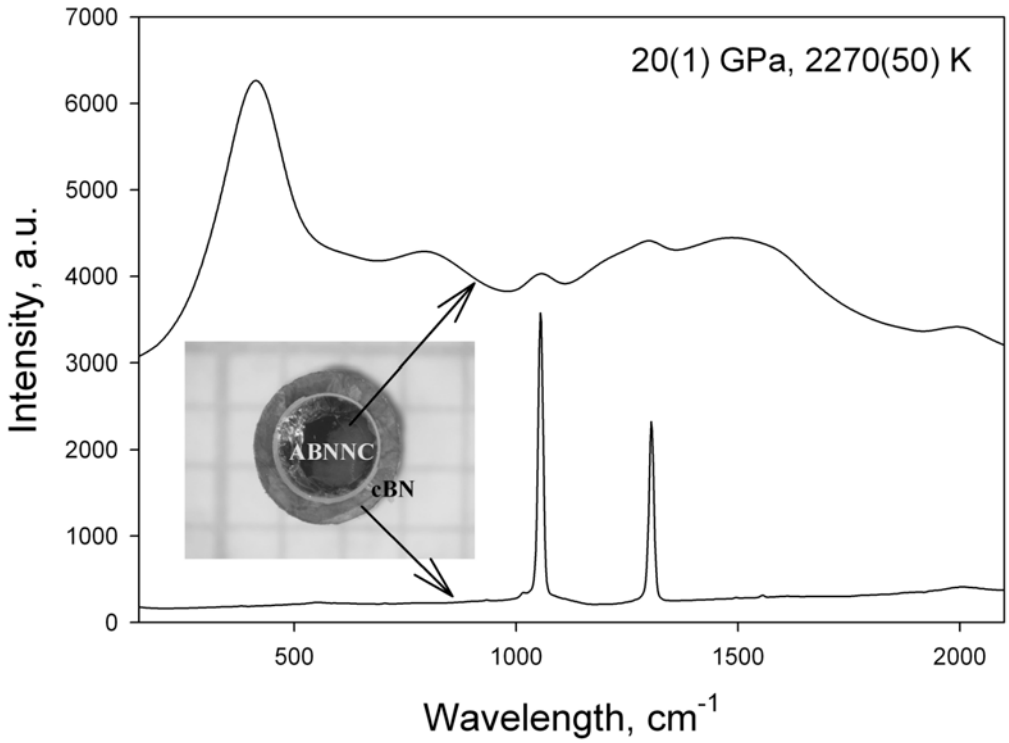

Fig. 3.9-1: Raman spectra of the materials synthesised simultaneously at P = 20(1) GPa and T = 2270 K from different precursors. A cross-section of the sample chamber after the experiment is shown in the inset (millimetre paper in the background indicates the scale). The outer layer of the sample was prepared from hexagonal BN, which transformed to cBN (grey) at HPHT conditions. The central part of the sample, made of pyrolytic p-BN and isolated by platinum foil, transformed to ABNNC (highly reflective black). Always when graphite-like hBN (Goodfellow Inc. or Aldrich Inc.) was used as a starting material, only sphalerite structured cBN with various crystallite sizes (ranging from 25 nm to > 100 nm) was produced.

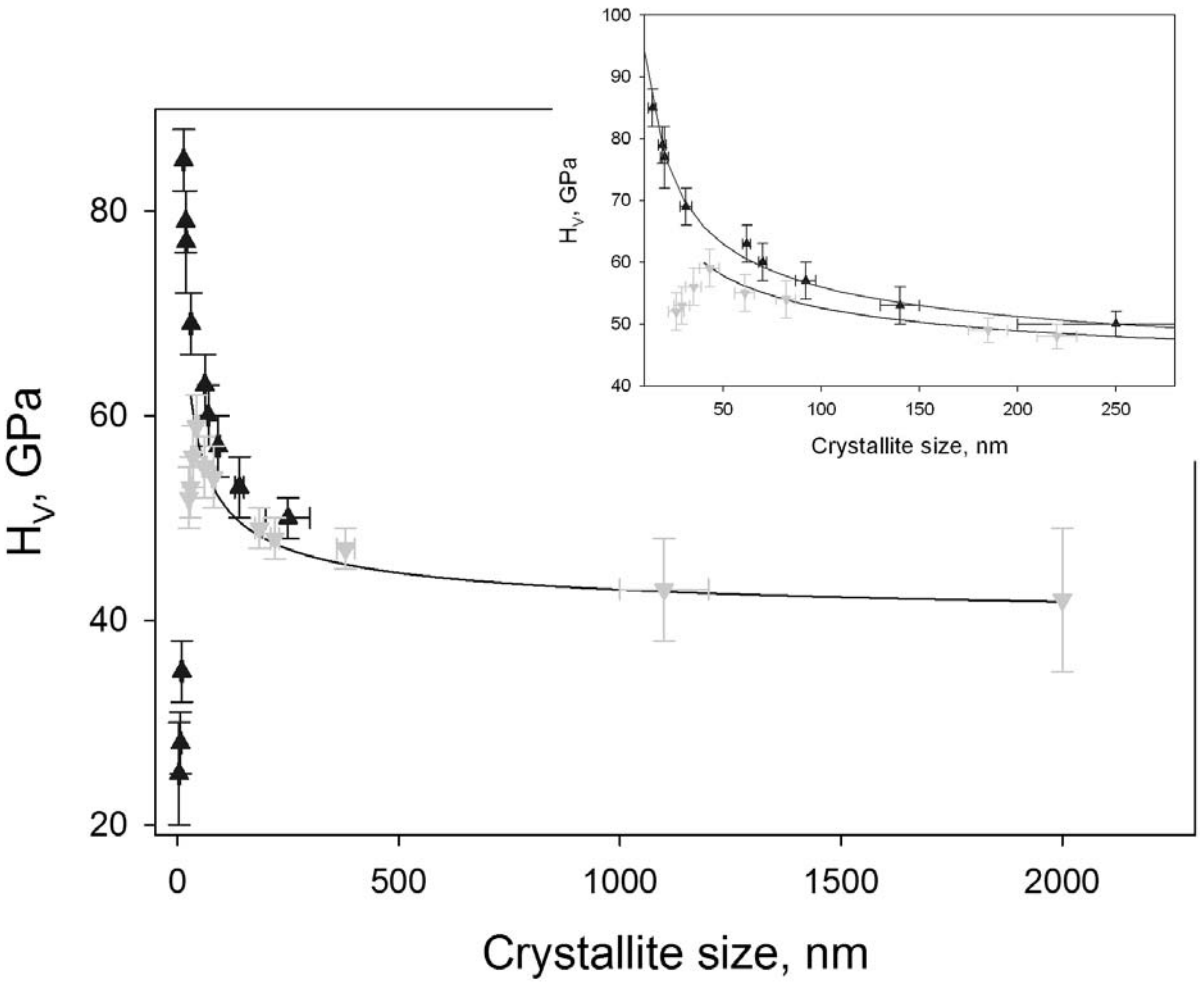

Fig. 3.9-2: Vickers hardness (Hv) as a function of crystallite size. Triangles and inverted triangles indicate the data for ABNNC and cBN, respectively. The solid curve is a fit of the experimental data for cBN using the Hall-Petch equation: $H = H_0 + K/\sqrt{d}$ with H_0 = 39 GPa and K = 126 GPa nm$^{1/2}$ (enlarged in inset). The experimental data for ABNNC can be fitted only using the Hall-Petch equation with correction for the quantum confinement effect: $H = H_0 + K_1/\sqrt{d} + K_2/d$ with H_0 = 40 GPa, K_1 = 155 GPa nm$^{1/2}$, K_2 = 50 GPa nm (upper curve in inset).

The hardening effect of grain boundaries can be expressed through the Hall-Petch equation showing the grain size (d) dependence of hardness (H): $H = H_0 + K/\sqrt{d}$. With H_0 = 39 GPa and K = 126 GPa nm$^{1/2}$ this equation fully describes the dependence of cBN hardness as a function of crystallite size (Fig. 3.9-2, solid curve). For ABNNC, however, the simple inverse square root relationship is not adequate. Based on the results of *ab inito* calculations, it has been suggested that hardness of nanocrystals depends on the "effective" bandgap, which, in turn, is inversely proportional to the size of crystallites. In other words, the combined Hall-Petch and quantum confinement effects $H = H_0 + K_1/\sqrt{d} + K_2/d$ perfectly describe the observed relations between hardness and crystallite size in ABNNC (Fig. 3.9-2, inset, upper curve: H_0 = 40 GPa,

K_1 = 155 GPa nm$^{1/2}$, K_2 = 50 GPa nm). Thus, the twofold increase of hardness of ABNNC (H_V = 85 GPa) compared to conventional polycrystalline cBN (H_V ~ 40 GPa) can be described as the result of a unique combination of two factors: (1) nanosize effect, which restricts dislocation propagation through the material, and (2) two-phase composition on the nano and sub-nanoscales which, due to quantum confinement, increases the hardness of individual crystallites. It makes ABNNC the first non-carbon-based bulk material with a hardness higher than that of PCD and approaching that of single crystal and nanocrystalline diamonds and ADNRs. The 50 GPa gap in hardness between the hardest known materials can be filled by BN nanocomposites by tuning their properties through changes in grain size and constituent structure; hence indicating the synergetic effect of nanocrystallinity and the composite nature of materials in improving their mechanical properties.

b. *In situ synthesis of nanodiamond (A. Shushkanova, L.S. Dubrovinsky and N.A. Dubrovinskaia)*

Diamond is an important mineral which has numerous industrial and commercial applications as a superhard and gem material as well as prospective applications in electronics. Nanocrystalline forms of diamond enhance their useful mechanical properties and their high-pressure high-temperature synthesis as bulk samples has been recently realised using a multianvil press. Studies of rare natural meteoritic nanodiamonds and grains of cosmic dust that predate the Sun are of great scientific importance, because they provide insight into their formation around other stars and into the early evolution of the Solar System.

Here we report the *in situ* synthesis of nanodiamonds using a diamond anvil cell (DAC) with laser heating. The experiments were conducted at pressures of approximately 21.5 GPa, and specpure graphite and sodium silicate Na_2SiO_3 were used as starting materials. Raman spectra were collected upon heating using a Dilor XY spectrometer equipped with a “superhead” and an Ar laser (514 nm excitation light). Raman spectra of temperature-quenched samples were also collected using a LabRam system (632 nm He-Ne excitation laser).

Upon heating at high pressure the Raman spectra changed their shape: at 1200-1400 K we observed the appearance of a broad feature centred at about 1400-1600 cm^{-1} (Figs. 3.9-3,4). At further temperature increase to 1800-2000 K the spectra developed a shape characteristic of nanodiamond, and on gradual decompression we observed a blue shift of the broad features of the spectra of nanodiamond (Fig. 3.9-5). Raman spectra of the recovered samples (Fig. 3.9-6) showed characteristic peaks of graphite in the area that was not heated, newly formed bulk diamond in the areas heated over 2400 K, and the Raman features of nanodiamond in areas heated at 1800-2200 K.

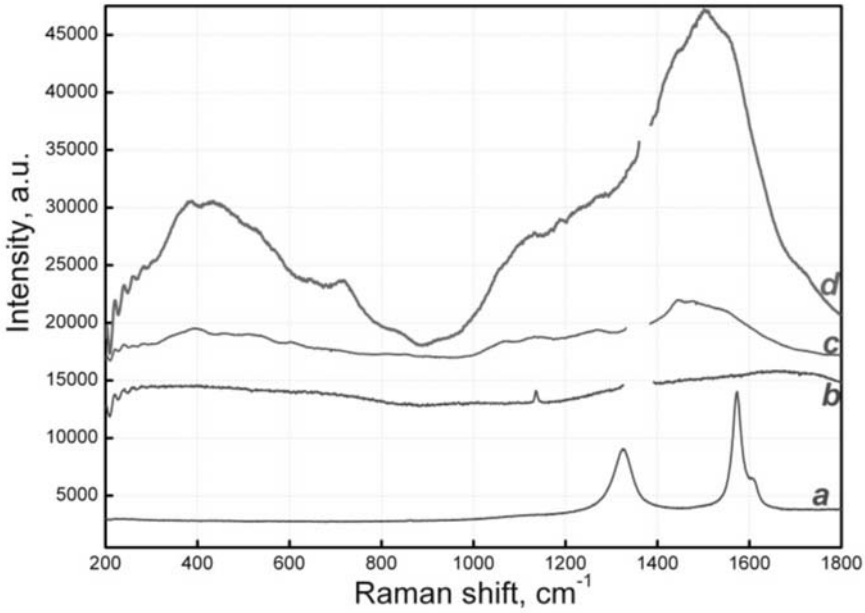

Fig. 3.9-3: Examples of Raman spectra (632 nm excitation laser) collected in the DAC at room temperature and 21.5 GPa. Spectra are shifted along the intensity-direction for clarity, and the Raman band of diamond anvils is not shown (hence some curves are interrupted). (a) spot of initial graphite collected out of the DAC; (b) spot heated to less than 1500 K; (c) spot heated at 1500-1800 K; (d) spot heated to more than 1800 K. The latter spectrum demonstrates features characteristic of nanodiamond.

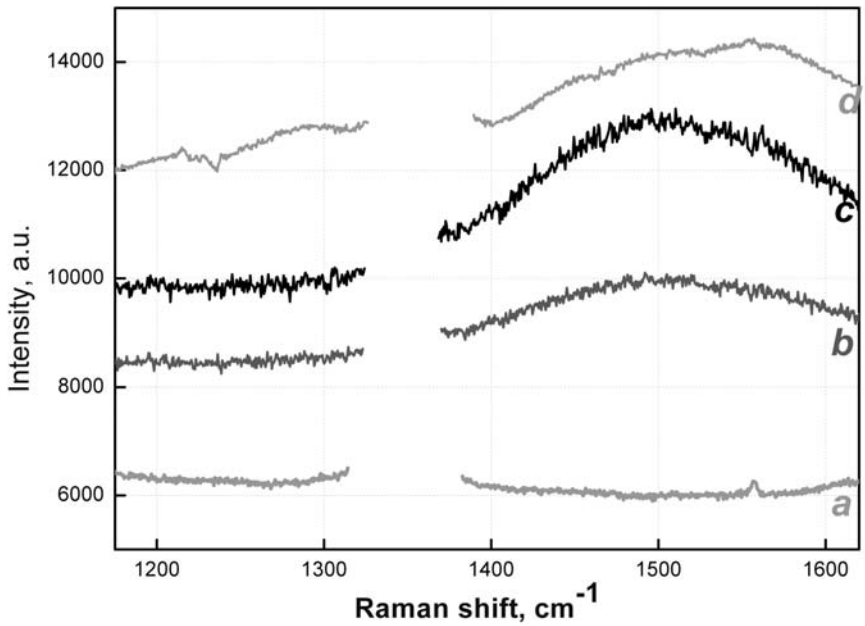

Fig. 3.9-4: Examples of Raman spectra (514 nm excitation laser) collected at 21.5 GPa. (a) nonheated spot; (b) spot heated *in situ* at ~ 1500 K; (c) spot heated *in situ* at ~ 1800 K; (d) spectrum of temperature-quenched nanodiamond, where the spot was heated to more than 1800 K.

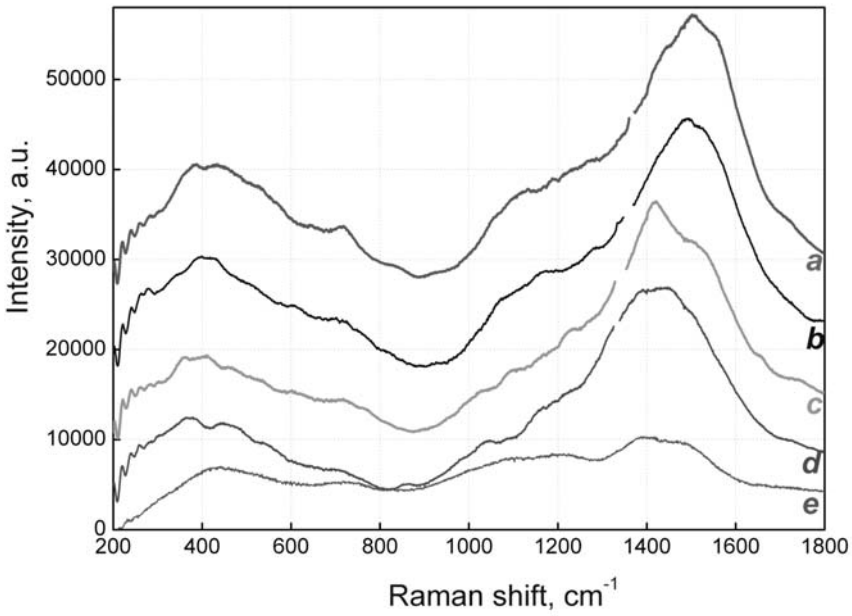

Fig. 3.9-5: Raman spectra (632 nm excitation laser) of nanodiamond after decompression. (a) nanodiamond at 21.5 GPa; (b) nanodiamond at 19.3 GPa; (c) nanodiamond at 3.2 GPa; (d) nanodiamond at ambient pressure; (e) nanodiamond at ambient pressure and heated at 1800 K from literature data [Dubrovinskaia *et al.*, Diamond & Related Materials, 14, 16, 2005].

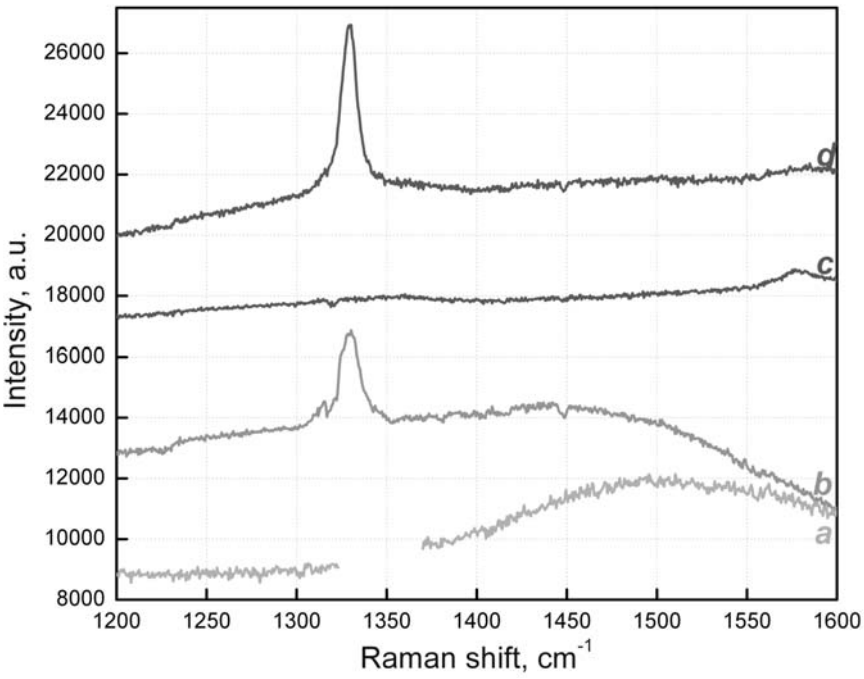

Fig. 3.9-6: Raman spectra (514 nm excitation laser) of samples after decompression. (a) spot heated to more than 1800 K at 21.5 GPa - nanodiamond; (b) quenched sample - nanodiamond and normal diamond; (c) quenched sample, nonheated spot - graphite; (d) quenched sample, spot heated at 1500-1800 K - normal diamond.

c. *Spectroscopic study of defects and inclusions in bulk poly- and nanocrystalline diamond aggregates (A.A. Shiryaev/Moscow, K. Iakoubovskii/Leuven, D. Grambole/Dresden and N.A. Dubrovinskaia)*

Recently a novel form of nanodiamond, aggregated diamond nanorods (ADNRs), exhibiting unusual mechanical properties has been synthesised by high-pressure high-temperature (HPHT) treatment of C_{60} fullerene, amorphous carbon and diamond powder. In this study, we have characterised the dominant defects in this nanodiamond by a combination of optical absorption, luminescence, Raman, electron spin resonance and elastic recoil detection techniques.

All characterisation was performed at room temperature, except for photoluminescence (PL), which was measured at 80 K. Infrared (IR) absorption spectra were obtained using a Bruker IFS 120 spectrometer equipped with a nitrogen-purged IR microscope (aperture > 50 μm) with a resolution of 1 cm^{-1}. Every sample was studied at several points in order to assess its homogeneity. Visible absorption, PL and Raman spectra were recorded with home-built spectrometers. In the so-called 'visible' absorption measurements (spectral range 1.6-5 eV), the sample was mounted on top of a photomultiplier detector in order to reduce light scattering. Luminescence was excited by a N_2 (337 nm or 3.68 eV) laser and detected with a 0.5 m double-grating spectrometer. Raman spectra were recorded under 457.9 nm Ar^+ laser excitation with resolution of 3 cm^{-1}. This excitation line was chosen out of other available Ar^+ lines in order to reduce background PL. Electron spin resonance (ESR) was measured with a commercial Bruker Q-band spectrometer (microwave frequency ~ 33 GHz). The signal positions (*g* values) and concentrations were deduced using a thoroughly calibrated LiF:Li standard, co-mounted with the studied sample. In order to increase accuracy in the signal concentrations, the ESR spectrum was first simulated using a powder-pattern routine. Then the fitting curves were double integrated and compared with the LiF:Li signals. The total hydrogen concentration in the samples was measured by elastic recoil detection using a microbeam setup (μERD). For the μERD 12 MeV C^{4+} ions at the nuclear microprobe installed at the 3 MeV tandetron accelerator were employed. The beam size was ~ 100 × 100 μm^2.

Most of the results were obtained from the sample prepared from C_{60}. Its Raman and visible absorption spectra are presented in Fig. 3.9-7. The first-order diamond Raman line at ~ 1330 cm^{-1} has not been detected previously in the material synthesised from C_{60}, when spectra were recorded under 514.5 nm laser excitation. In the present study, Raman spectra were recorded using 457.9 nm laser excitation, and a weak diamond peak was observed. It becomes more pronounced after subtracting a linear background (Fig. 3.9-7a, lower curve). It is clear from the figure that the diamond peak is significantly broadened (FWHM ~ 40 cm^{-1}) as compared to conventional HPHT diamond crystals (typical FWHM ~ 2 cm^{-1}). This broadening could originate from large strain due to small grain size and numerous grain boundaries in the nanodiamond aggregate, as well as due to the high concentration of point defects found in the sample. The presence of structural point defects and impurities is seen in

the PL spectrum (left curve in Fig. 3.9-7b). The spectrum is dominated by two broad bands centred at ~ 1.9 and 2.8 eV. Those two bands are universally observed in all synthetic diamonds. They are commonly attributed to the nitrogen-vacancy (N-V) pairs and structural (possibly dislocation related) defects. Note that the PL intensity was relatively weak; considering the very high sensitivity of this technique (up to single defects), we can conclude that the corresponding concentrations are low (ppm level).

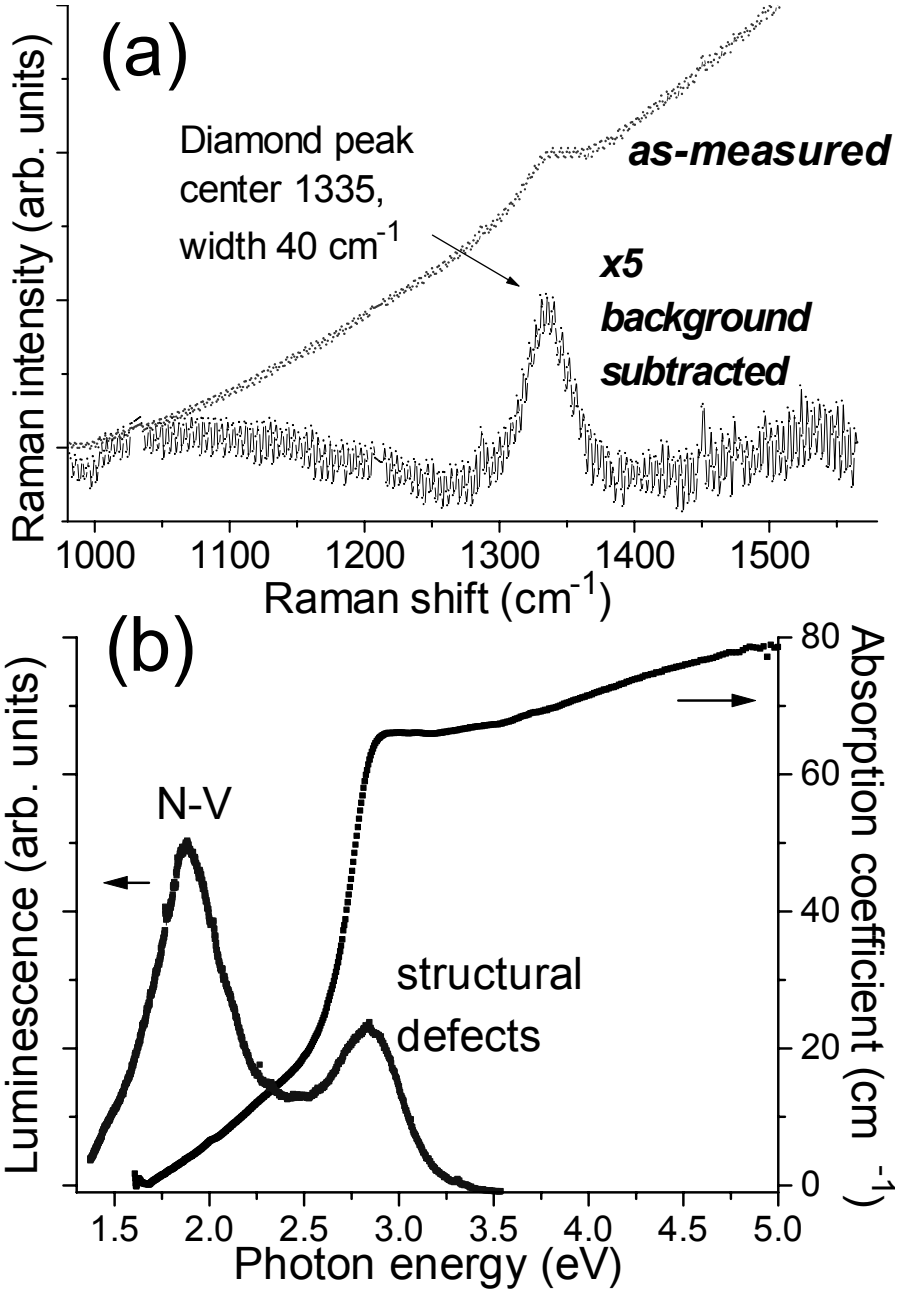

Fig. 3.9-7: (a) Raman and (b) optical absorption and PL spectra of diamond aggregate made from C_{60}. Raman and PL spectra were recorded under 457.9 and 337.1 nm laser excitation, respectively. A linear background is subtracted from the Raman spectrum.

Figure 3.9-8 presents ESR spectra from the studied nanodiamond samples. The spectra were recorded with a low microwave power (1 μW) and modulation amplitude (0.1 mT) in order to avoid signal distortions. No other significant signals were observed in the magnetic field range 30-1500 mT. The spectrum of the nanodiamond grown from C_{60} is dominated by a strong signal *d* at $g = 2.0024$ characteristic of a carbon dangling bond. Magnification reveals a number of weak satellites, labelled as *a, a', b, b', c* and *c'* on both sides of the central peak. Signals *c, c'* and *d* are commonly observed in CVD diamond, but to the best of our knowledge they have never been reported for HPHT diamond. The intensity, line shape and position of the satellite signals were studied here as a function of microwave power and compared with well-characterised CVD samples. As a result, the signals *c, c'* and *d* were unambiguously assigned to the H1 centre (electron spin $S = 1/2$, nuclear spin $I = 1/2$ due to one hydrogen atom), and signals *a, a', b* and *b'* to the P1 centre ($S = 1/2$, $I = 1$, one nitrogen atom). The central line of the P1 centre could not be identified due to the overlap with the *d* line. The unusual weakness of the hydrogen-related satellites *c* and *c'* in the H1 centre originates from the forbidden nature of the corresponding transitions. The corresponding concentrations were estimated as 75 parts per million (ppm) for the H1, and 0.1 ppm for the P1 centres.

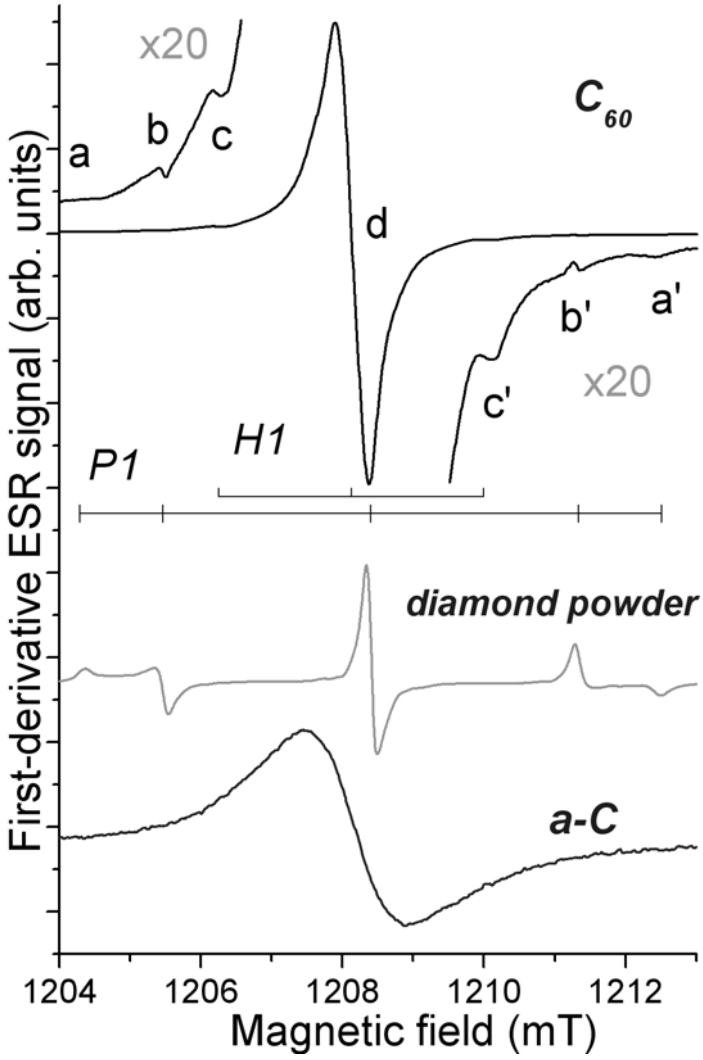

Fig. 3.9-8: Central part of the Q-band (~ 33 GHz) ESR spectra from the nanodiamonds produced from C_{60}, microcrystalline diamond powder and amorphous carbon.

Unusually high concentrations (~ 0.4 at.%) of hydrogen and very low concentrations of nitrogen (~ 5-10 at.%) compared to conventional diamond have been detected in diamond grown from C_{60}. Although most of hydrogen is shown to originate from inclusions of foreign phases, such as water, significant concentrations (~ 0.01 at.%) of hydrogen were also detected as a point defect in the nanodiamond grains. Observed structural differences between the samples made from various carbonaceous materials are attributed to different behaviour of the starting compounds during HPHT treatment.

d. *High-pressure high-temperature synthesis and characterisation of boron-doped diamond (N.A. Dubrovinskaia, L.S. Dubrovinsky and N. Miyajima, in collaboration with H.F. Braun/Bayreuth, F. Langenhorst/Jena and W. Crichton/Grenoble)*

There is an increasing interest in studies of doped diamonds due to the drastic influence of dopants on their physical properties, in particular on the metal-insulator transition. Diamond can be artificially doped using several methods: (a) during growth by high pressure-high temperature (HPHT) method or chemical vapour deposition (CVD) technique; (b) by ion implantation; or (c) by thermal diffusion. Ion implantation is problematic because of the thermal instability of diamond, because high annealing temperatures (above 1700 °C) are needed after implantation to eliminate the damage and to activate the implanted ions (*i.e.*, to move them to substitutional sites). Diffusion processes are slow, so only very thin layers with high resistance have been produced using the thermal diffusion method. Methods of doping during crystal growth are the most promising. The HPHT technique has an advantage due to the high speed of the process and the possibility to produce bulk homogeneous samples through the control of components in the initial mixture.

Polycrystalline HPHT boron-doped diamond (BDD) attracts special attention due to the discovery of superconductivity and the strong interest to investigate and explain this physical phenomenon more deeply. However, little is known about the mechanism and the upper limit of doping achievable by this technique. The purpose of the present study was to synthesise B-doped polycrystalline diamonds using a multianvil apparatus at various PT conditions and carefully investigate their phase composition and structure in order to shed light on the mechanism of boron incorporation into diamond. As starting materials in different experiments we used graphite and $B_{13}C_2$. The pure powders ($B_{13}C_2$+C-graphite) were mixed in the ratio C:B = 13:1 (~ 7 at.% B) for the BDD synthesis. Pure $B_{13}C_2$ was also treated under the same PT conditions as for the BDD synthesis. HPHT experiments were conducted in the pressure range 9-20 GPa at 2500-2700 K using the 5000-ton multianvil press at Bayerisches Geoinstitut. Quenched samples were studied by X-ray powder diffraction using a high-brilliance diffractometer at Bayerisches Geoinstitut and synchrotron radiation facilities at ESRF (ID30). Raman spectra were collected using two Raman spectrometers operating with a 514 nm laser and a 632 nm laser, and the chemical composition and texture of the samples were studied using a scanning electron microscope (SEM) and an analytical transmission electron microscope (TEM).

In house and synchrotron X-ray diffraction data revealed the presence in BDD of a small amount of a highly B-enriched phase ($B_{50}C_2$) and traces of the $B_{13}C_2$ used as an initial material (Figs. 3.9-9,10). Boron carbide was also observed by TEM and its presence was also detected by electron diffraction (Fig. 3.9-11). The absence of $B_{50}C_2$ in the product of treatment of pure $B_{13}C_2$ under the same HPHT conditions suggests that B-rich carbides exsolve from diamond on quenching, leading to boron depletion of the diamond matrix. These observations imply that boron solubility in diamond increases at high pressure and high temperature. This result may have important implications for understanding the mechanism of boron incorporation into diamond during HPHT synthesis and interpretation of the superconductivity data of polycrystalline BDD.

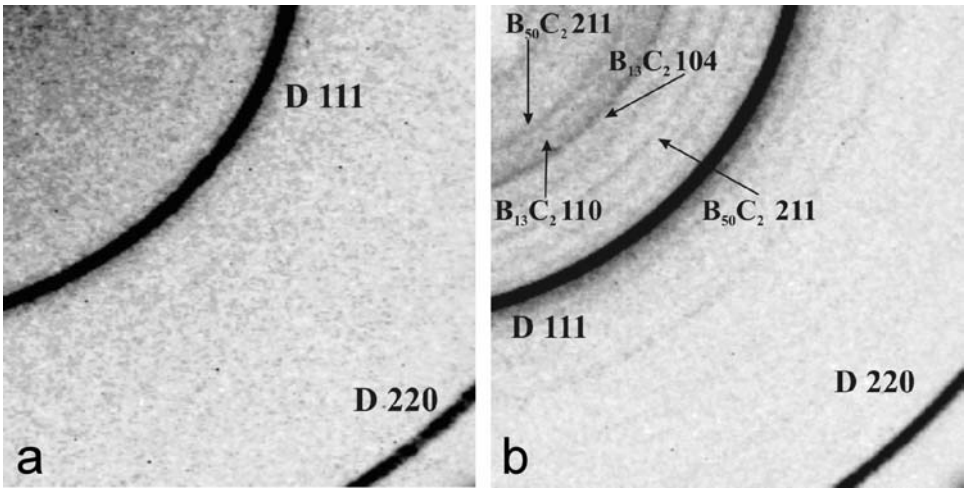

Fig. 3.9-9: Parts of the 2D diffraction images of the sample recovered after an experiment at 20 GPa and 2700 K obtained after (a) 30 s and (b) 1800 s exposure. D indicates diamond diffraction lines, and $B_{13}C_2$ and $B_{50}C_2$ denote diffraction lines of additional B-rich phases.

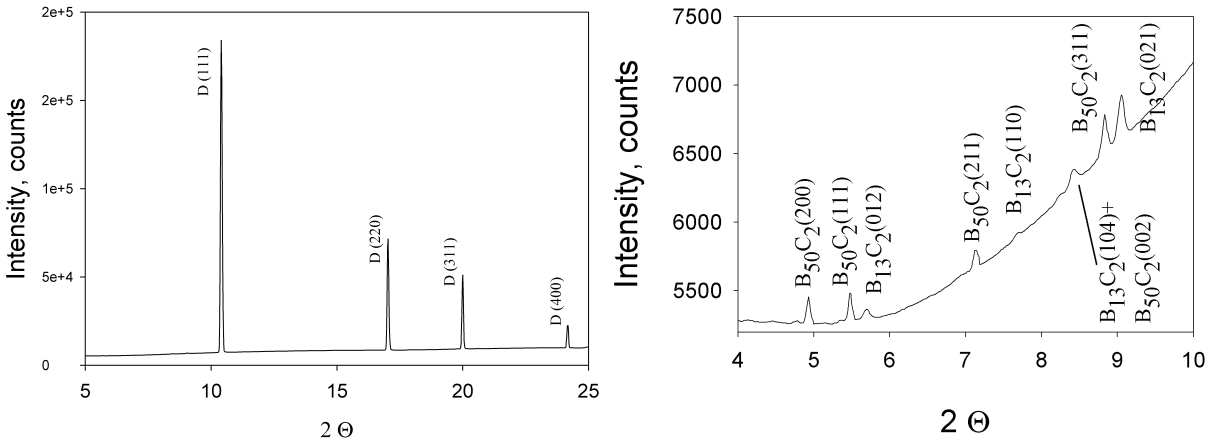

Fig. 3.9-10: (a) Synchrotron X-ray diffraction pattern of the sample synthesised at 20 GPa. (b) The enlarged area between 4 and 10 degrees 2Θ with reflections of B-rich phases ($B_{50}C_2$ and $B_{13}C_2$) clearly visible.

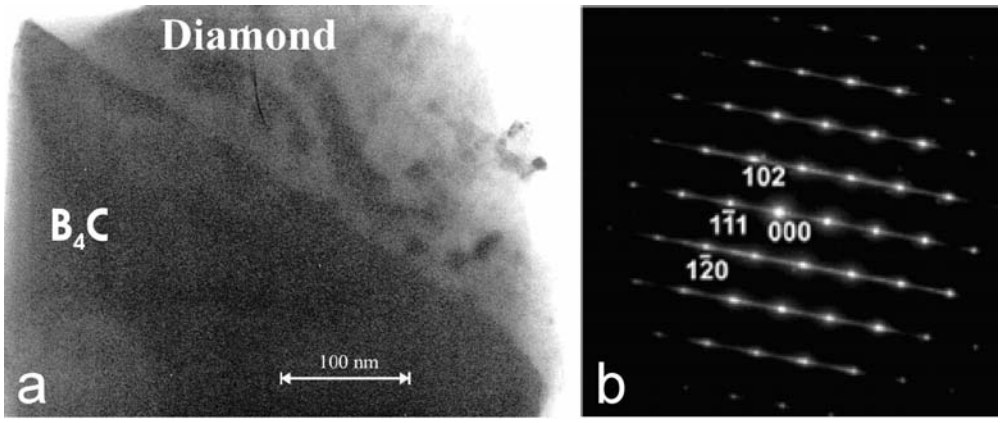

Fig. 3.9-11: (a) Bright field TEM image of a grain containing boron-doped diamond and B_4C. (b) An electron diffraction pattern of B_4C confirms the presence of this carbide in the BDD samples.

e. *Ground state properties of boron-doped diamond (E.Yu. Zarechnaya, E.I. Isaev and Yu.Kh. Vekilov/Moscow; S.I. Simak and I.A. Abrikosov/Linköping; L.S. Dubrovinsky, N.A. Dubrovinskaia and G. Steinle-Neumann)*

The basic properties of diamond suggest that it is an ideal material for electronics. It has a wide bandgap (5.5 eV, indirect), high saturated carrier velocities and carrier mobilities with similar values for both electrons and holes, high electric field breakdown strength, low dielectric constant, high thermal conductivity, and transparency to electromagnetic radiation in the visible and IR range. Many potential applications have been proposed, including high power and high frequency electronic devices. The semiconducting behaviour of diamond can be described in terms of one acceptor. Therefore, boron appears as a likely candidate for the acceptor centre. The recent experimental discovery of superconductivity of boron-doped diamond (BDD) has increased interest in further theoretical investigations of BDD. Here we present results of our *ab initio* studies of the variations of equilibrium lattice parameters and bulk moduli of B-doped diamond at different B concentration, and compare our theoretical results to available experimental data, with the conclusion that a model where B atoms occupy substitutional positions is in better agreement with experiment.

In our studies on doping of diamond by boron was simulated using a number of supercells with up to 64 atoms in a unit cell, where one C atom was substituted by one B atom (B_S) or one B atom was located in an interstitial position (B_I). Total energy calculations for the supercells were performed using an *ab initio* all-electron projector augmented waves (PAW) method as implemented in the VASP package. For reproducing the lattice parameter in good agreement with the experimental value, ENCUT = 400 eV was found to be sufficient. Exchange-correlation effects were treated by means of the generalised gradient approximation (GGA) of Perdew and Wang. Integration over the Brillouin zone was performed via the linear tetrahedron method with the Blöchl correction. The Hellman-Feynman force theorem was

used in order to minimise the total energy with respect to internal relaxations. Forces acting on each atom were converged with a tolerance of 10^{-3} eV/Å.

From our *ab initio* calculations we obtained a lattice parameter a = 3.573 Å and a bulk modulus B = 429 GPa of pure diamond, in good agreement with experimental values (a = 3.567 Å and B = 443 GPa, respectively). Our calculations show an increase of the lattice parameter with increasing B concentration (Fig. 3.9-12). The lattice parameter of interstitially B-doped diamond tends to be larger compared to the substitutional case, irrespective of supercell size at a given B concentration. Unfortunately, computational results on the unit cell parameter cannot be compared with the available experimental data, because of the inconsistency of previous experimental results. The effect of ionic relaxation on the lattice parameter for all supercells under consideration was found to be negligible.

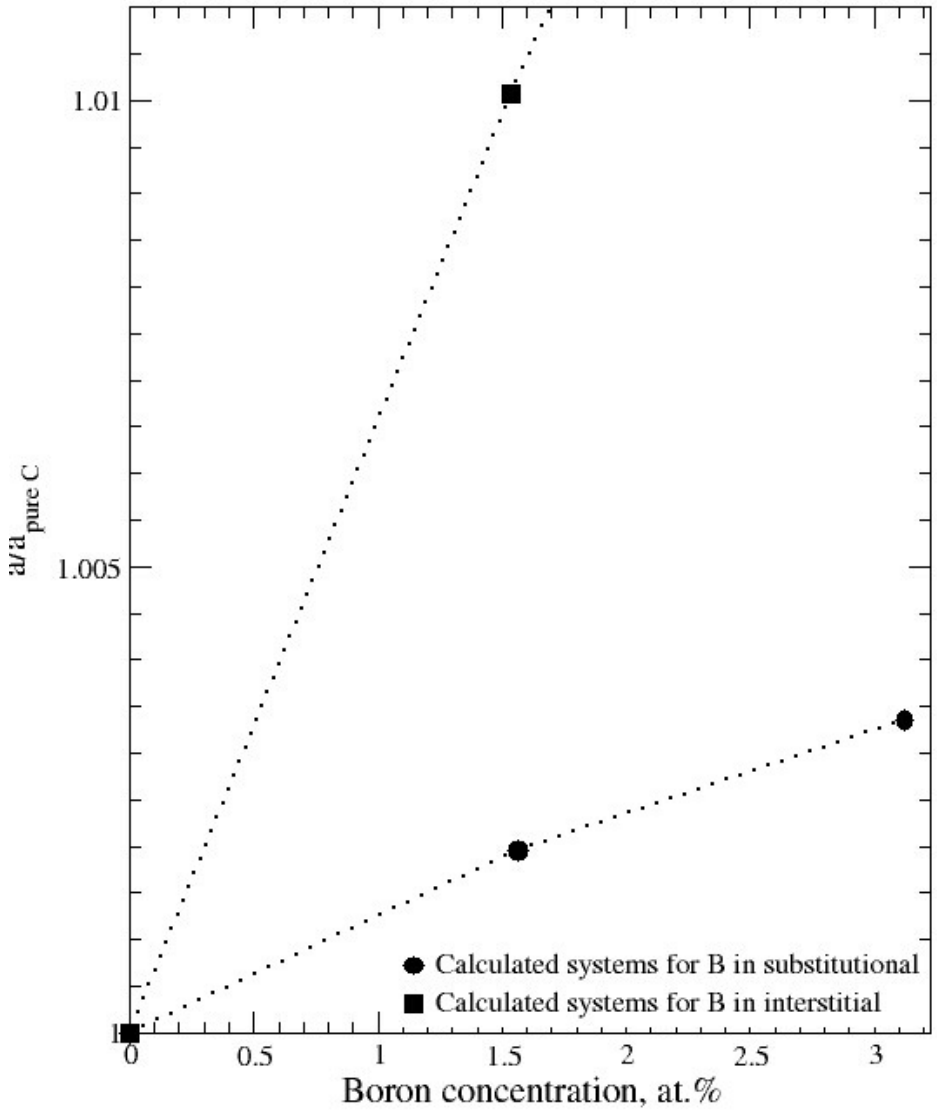

Fig. 3.9-12: Dependence of the lattice parameter in diamond on boron concentration. Solid squares and solid circles correspond to calculated supercells with interstitial and substitutional B atoms, respectively.

For substitutional incorporation we found a linear dependence of the bulk modulus on B concentration in diamond (Fig. 3.9-13). Recent experimental observations suggested small changes in bulk modulus in BDD in comparison with pure diamond, and the calculated values of the bulk modulus obtained in the substitutional B model are in better agreement with experiment. The decrease of the bulk moduli might be explained by the influence of B-doping on the bonding states of diamond (the antibonding component is enhanced with increased B concentration).

The computed dependence of the ground state parameters on dopant concentration will provide important insight into the experimental results. Based on the analysis of our theoretical results and experimental studies we conclude that B atoms substitute for C atoms in diamond rather than occupy interstitial positions. We note that the presence of other defects could substantially modify this behaviour; thus studies of more complex chemical and structural defects involving interstitial B atoms would be of interest.

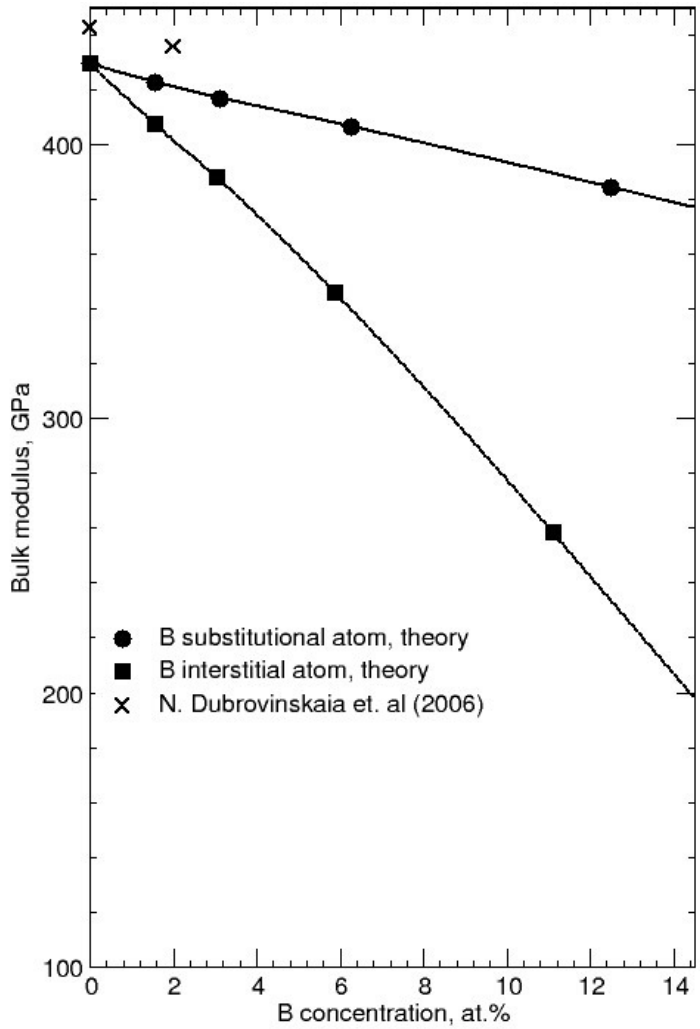

Fig. 3.9-13: Dependence of the bulk modulus on boron concentration from computations and experiments. The crosses indicate experimental data from the literature [Dubrovinskaia *et al.*, High Pressure Research, 26, 79, 2006].

f. *High-pressure Raman study of the phase transition behaviour of rutile nanocrystals (V. Swamy, Q. Dai and B.C. Muddle/Clayton; E.S. Holbig, A.V. Kurnosov and L.S. Dubrovinsky)*

Pressure-induced phase transitions of nanocrystalline systems have attracted significant interest in recent years. The Monash University-Bayerisches Geoinstitut collaborative research programme on the high-pressure phase transition behaviour of nanoscale TiO_2 has thus far investigated the size-dependent phase transitions starting with anatase nanocrystals at ambient temperature. Combined high-pressure Raman spectroscopy and angle-dispersive synchrotron X-ray diffraction experiments in diamond anvil cells have produced a detailed picture of the size-dependent phase transitions of anatase TiO_2 under pressure (see BGI Annual Report 2005). Principal results include: (i) the observation of size-dependent pressure-induced amorphisation of extremely small (< 10 nm) anatase nanocrystals; (ii) size-dependent structure selectivity of larger anatase nanocrystals undergoing pressure-induced crystal-crystal transformations to baddeleyite (monoclinic ZrO_2) or α-PbO_2 structures; and (iii) a high-density-low-density polymorphic transition in nanoscale TiO_2. Furthermore, our previous work has established an enhanced metastability and larger bulk modulus for nanocrystalline anatase compared to the bulk material.

A comparable detailed picture of the nature and size-dependence of pressure-induced phase transitions in rutile (the other most important TiO_2 polymorph) nanocrystals is unavailable. The published work on nanocrystalline rutile phase transitions includes: (i) an ambient temperature X-ray diffraction study of a 30 nm anatase-rutile mixture to ~ 35 GPa, (ii) an ambient temperature X-ray diffraction study of rutile nanocrystals (~ 10 nm size) to ~ 47 GPa, and (iii) a high-temperature, high-pressure X-ray diffraction study using ~ 10 nm-sized rutile nanocrystals to examine the relative stability of nanoscale rutile and α-PbO_2-structured TiO_2. The results obtained in the ambient temperature experiments are contradictory: the 30 nm-sized rutile nanocrystals in the anatase-rutile mixture were interpreted to transform to the baddeleyite structure at ~ 8.7 GPa (less than the bulk transition pressure of 12 GPa); whereas the 10 nm-sized rutile in the second study was reported to transform to the baddeleyite structure at pressures of 20-30 GPa. High-pressure high-temperature results obtained in the third study, however, suggested a lowering of rutile stability at the nanoscale with a distinctly curved rutile/α-PbO_2 phase boundary. The aim of the present project was to investigate the size-dependent pressure-induced phase transition behaviour of rutile nanocrystals at ambient temperature using the diamond anvil cell (DAC) technique and Raman spectroscopy.

Phase-pure rutile nanocrystals with average crystallite sizes of 5, 7, and 24 nm (determined using the Scherrer formula) were synthesised using a hydrothermal method. High-pressure Raman scattering data were obtained with four-pin type DACs at the Bayerisches Geoinstitut using a Dilor spectrometer and Ar^+ laser (514 nm) to about 35 GPa. Pressure was determined using the ruby fluorescence technique. The E_g (~ 447 cm^{-1}) and A_{1g} (~ 610 cm^{-1}) modes as well as the second-order (multi-phonon) features approximately at 237 cm^{-1} and 700 cm^{-1} are the major features of the Raman spectra of the nanocrystalline samples; the B_{1g} (~ 143 cm^{-1}) and B_{2g} (~ 826 cm^{-1}) modes are either very weak or missing in the spectra (Fig. 3.9-14). We have traced the pressure dependence of the E_g and A_{1g} modes to ~ 35 GPa for the three samples as depicted in Fig. 3.9-15, where two pressure data points for bulk rutile from the literature are shown for comparison.

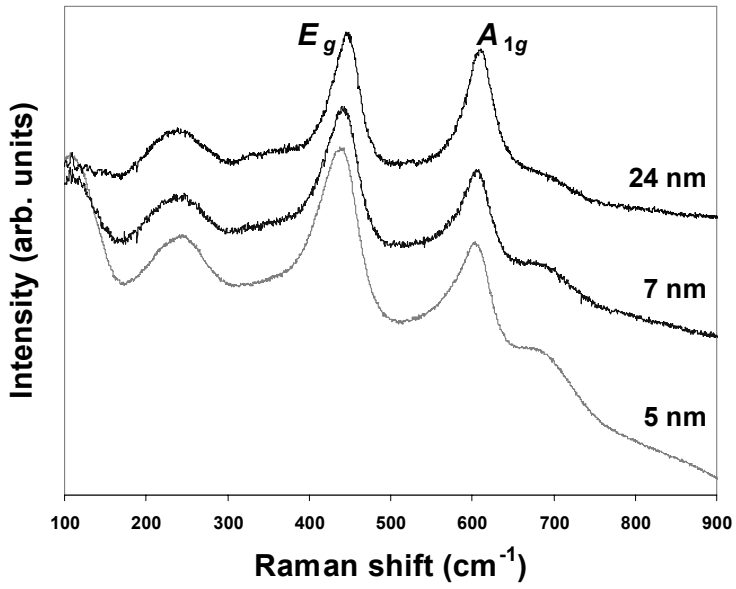

Fig. 3.9-14:
Raman spectra of nanocrystalline rutile TiO_2 recorded under ambient conditions. The average crystallite sizes obtained with the Scherrer method are indicated on the right.

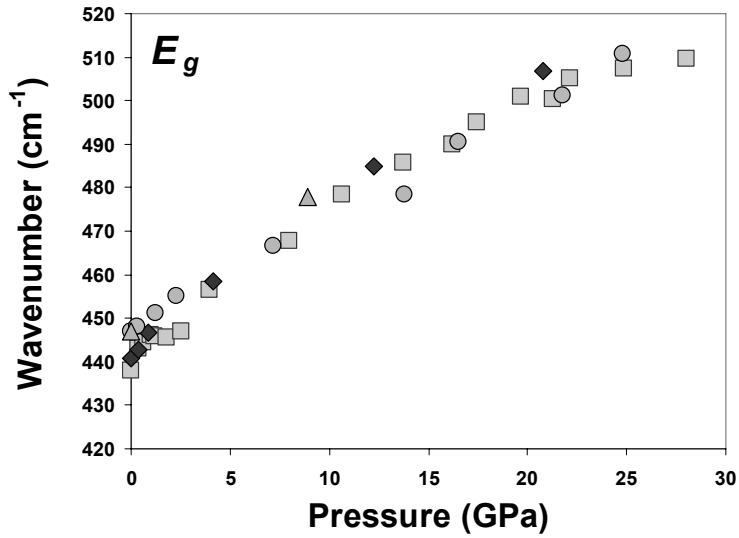

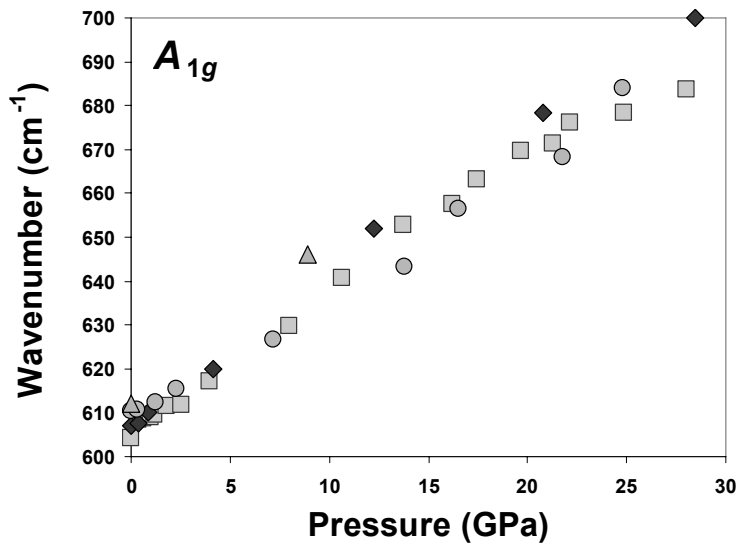

Fig. 3.9-15: Pressure dependence of the E_g and A_{1g} modes of rutile TiO_2. Symbols:
squares (5 nm rutile), diamonds (7 nm rutile), circles (24 nm rutile), triangles (bulk rutile).

As with bulk rutile, the pressure dependence of the two Raman modes are approximately linear for the nanocrystalline samples with slopes similar to that of the bulk material. As reported earlier, the pressure dependence of some of the anatase Raman modes show distinct size dependence, consistent with the observed size-dependent bulk modulus variation. The apparent lack of variation with crystallite size for the pressure dependence of Raman modes observed for rutile is consistent with the similar bulk modulus obtained for nanocrystalline and bulk rutile. Our results suggest that, as in the case of anatase, rutile also exhibits size-dependent enhanced pressure metastability at ambient temperature, with smaller crystallites persisting to higher pressures.

g. *Compression behaviour of Zr-doped nanoanatase (E.S. Holbig, L.S. Dubrovinsky and G. Steinle-Neumann; V. Prakapenka/Washington DC; V. Swamy/Clayton)*

Titania TiO_2, zirconia ZrO_2, as well as zirconium-titanium oxides and zirconium titanate-based materials are functional ceramics used for *e.g.*, pigments, composite materials, catalysts and catalyst support. The investigation of $(Ti,Zr)O_2$ solid solutions at high pressures and temperatures (HPHT) is promising for creating new materials with high bulk moduli, and we plan to systematically study the variation of mechanical properties with composition at HPHT. In this study, we focus on the variation of compressibility of anatase in response to doping with Zr. Previous experiments on the system have shown that the compressibility varies with microstructure and chemical composition: the bulk moduli of high-pressure polymorphs of TiO_2 are systematically higher than for isostructural ZrO_2 polymorphs and a decrease in crystallite size leads to a higher bulk modulus of anatase, and the bulk modulus of nanoanatase is about 35 % larger than for the macrocrystalline counterpart.

We carried out diamond anvil cell (DAC) experiments at the GSE-CARS 13 BMD at the Advanced Photon Source (APS), Argonne, Illinois, using a MAR345 detector and an X-ray beam with a wavelength of 0.31 Å. As starting material we used a 1:1 mixture of nanocrystalline Zr-doped anatase $Ti_{0.90}Zr_{0.10}O_2$ (15±5 nm), synthesised with the sol-gel process, and LiF (99.99 % purity). We observed Zr-doped nanoanatase as a pure phase up to 13 GPa, but X-ray diffraction analysis showed a significant change in compression behaviour at pressures > 4 GPa: the *a*/*c* slope strongly increases (Fig. 3.9-16), the slope of the bond length M-O2 of the octahedra changes from negative to positive, and the *z*-coordinate of the oxygen atom, the only free atomic coordinate, changes its trend. A third order Birch-Murnaghan equation-of-state (EoS) of the X-ray diffraction data revealed that Zr-doped nanoanatase is less compressible than bulk and nanoanatase (Fig. 3.9-17). This is opposite to the expectation from the comparison of elastic constants for TiO_2 and ZrO_2 polymorphs: while ZrO_2 polymorphs show a smaller bulk modulus than the corresponding TiO_2 forms, the incorporation of Zr into TiO_2 anatase results in a higher bulk modulus.

In addition to the experiments we also performed *ab initio* density functional electronic structure simulations using the VASP code (PAW method and GGA exchange correlation potential). We calculated ground state energetics (zero temperature) of Ti_8O_{16} and $Zr_1Ti_7O_{16}$ supercells for varying volumes and explored the variation of cell parameters, energies and

atomic positions. In order to gain insight into the Zr distribution in $Zr_1Ti_7O_{16}$ and to investigate the possible tendency of clustering of zirconium atoms we performed computations on supercells with different distances of neighbouring Zr atoms. The computations showed that Zr atoms at close distances are energetically favoured, hinting at possible cluster formation of Zr in the $(Ti,Zr)O_2$ compounds. The change in compression behaviour at ~ 4 GPa observed in the experiments is not reproduced by the computations for the perfect bulk crystal, suggesting that the anomalous compression behaviour is caused by the nanocrystallinity of the samples. The cluster formation and resulting structural distortions can further augment the change in compression behaviour.

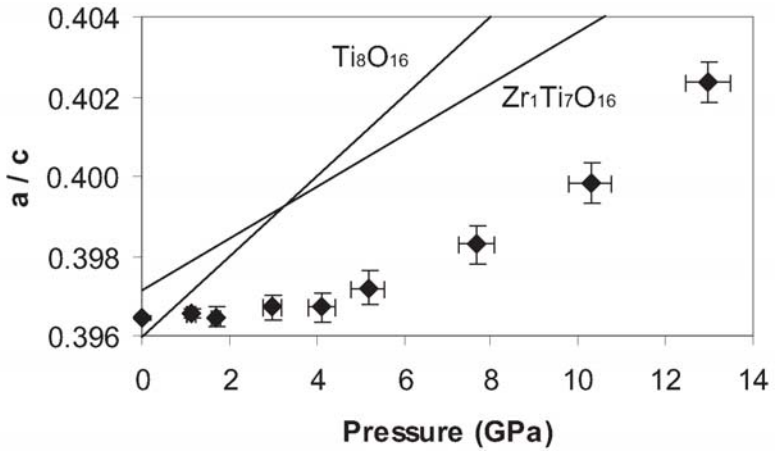

Fig. 3.9-16: Pressure influence on the lattice parameter ratio *a*/*c* of Zr-doped nanoanatase (experiments: diamonds) as well as anatase Ti_8O_{16} and $Zr_1Ti_7O_{16}$ (computed: lines).

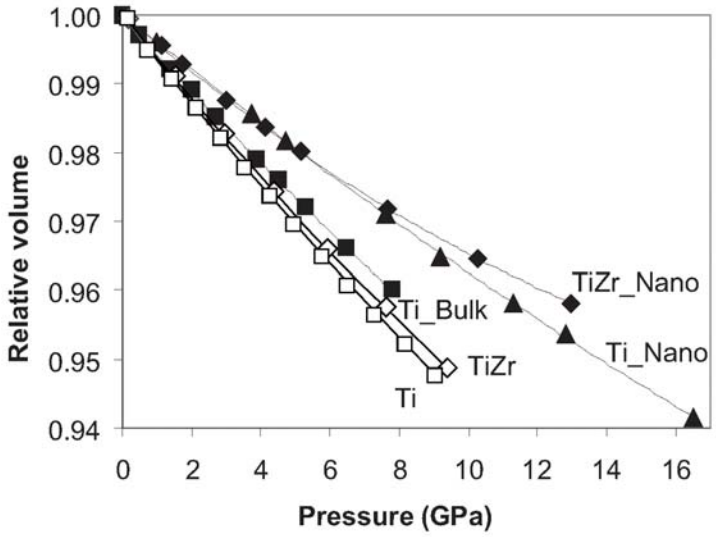

Fig. 3.9-17: Various Birch-Murnaghan equation of state fits of experimental (solid) and computational (open) pressure-volume data on anatase: Ti_Bulk = TiO_2 bulk anatase, Ti_Nano = TiO_2 nanoanatase, TiZr_Nano = $Ti_{0.90}Zr_{0.10}O_2$ nanoanatase, Ti = computational Ti_8O_{16} anatase and TiZr = computational $Ti_7Zr_1O_{16}$.

h. *Synthesis of a sodium rhenium nitride phase and the stability of copper nitride at high pressures and temperatures (C. Guillaume and G. Serghiou/Edinburgh; D.J. Frost)*

Technologically, high-density nitrides show promise for both ceramic and electronic applications ranging from cutting tools and turbines to passivating layers and optoelectronic components. In a laser-heated diamond cell we have prepared high-density metal-nitrides by reaction of the nitrogen pressure medium with an elemental substrate. Two of our objectives are to develop criteria governing whether denser than ambient nitride phases will form, and, in particular, to establish the parameters required for large volume synthesis in a multianvil press using elemental starting materials.

To date we have been able to synthesise several transition metal nitrides in a multianvil press using elemental starting materials. We were, for example, able to synthesise hexagonal nickel nitride by heating Ni together with NaN_3 using a rhenium foil capsule. On the other hand, experiments in the copper nickel nitrogen system that also employed NaN_3 as a nitrogen source show that Cu does not form a nitride at 2000 K and 20 GPa (Fig. 3.9-18a). Using this observation we can recognise factors that may aid in identifying likely systems where high-pressure nitrides may form. At ambient conditions, for example, Cu_3N has an extremely low heat of formation, low dissociation temperature and limited thermal stability. Further, it is a semiconductor exhibiting weak directional bonds; whereas the immediately adjacent lower atomic number systems are metallic interstitial nitrides. As Cu_3N does not form a high-pressure nitride it may also be useful as a nitrogen source in future experiments. The Cu metal product observed in the recovered charges was relatively pure while a Cu-free nitride was produced. Although poorer in N, Cu_3N may be superior to NaN_3 as a nitrogen source in some experiments as nitrides formed from the breakdown of NaN_3 tend also to contain Na.

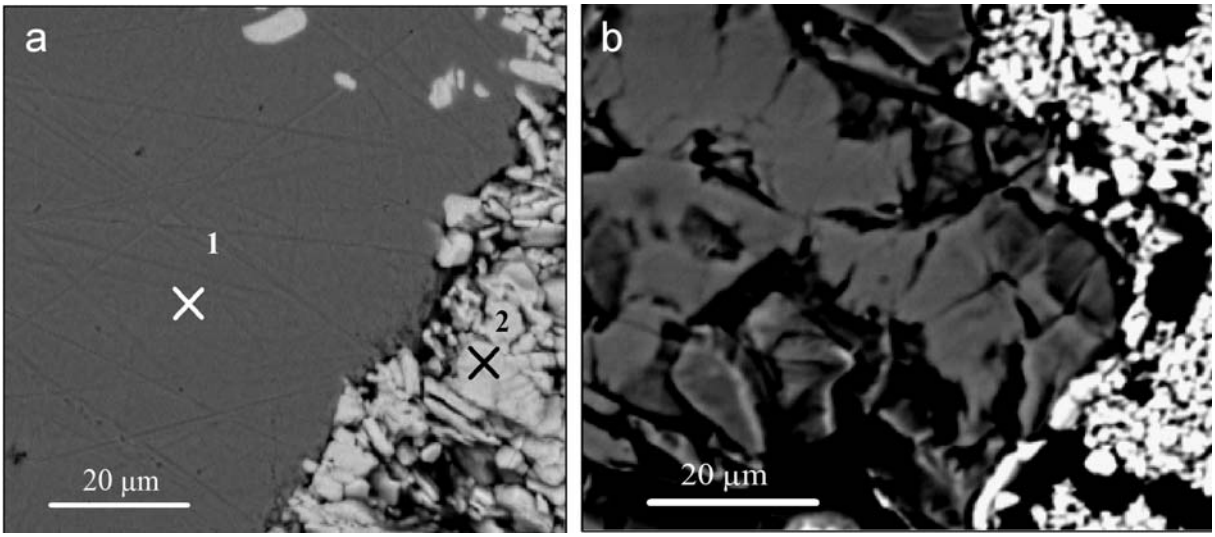

Fig. 3.9-18: Backscattered scanning electron microscopy images of (a) Cu (spot 1) and Na-Re-N (spot 2) and (b) Ni_3N and Na-Re-N recovered after heating Cu and Ni, respectively, with sodium azide at 20 GPa and 2000 K.

During the synthesis of nickel nitride, sodium azide also reacted with rhenium to form a ternary rhenium nitride (Fig. 3.9-18b). Only one other sodium rhenium nitride phase is currently known and this was prepared at ambient pressure. In addition to our measured electron diffraction patterns, we also noted a basic physical property of our dense ternary nitride phase that differs from that of the known one. In particular, while the ambient pressure prepared phase is very water and air sensitive, the dense modification is stable in both of these environments as well as in ethanol. We are now focusing on a detailed evaluation of the structure, and preliminary high-resolution electron microscopy images reveal a degree of structural disorder.

i. *Pressure-induced monoclinic distortion, charge and orbital ordering in $La_{0.5}Ca_{0.5}MnO_3$ (D.P. Kozlenko and B.N. Savenko/Dubna; L.S. Dubrovinsky; I.N. Goncharenko/Gif-sur-Yvette; V.I. Voronin/Ekaterinburg)*

Perovskite manganites $R_{1-x}A_xMnO_3$ (R - rare earth element, A - alkaline earth element) exhibit a rich variety of fascinating physical phenomena extensively studied during the past years – colossal magnetoresistance, charge and orbital ordering, and mesoscopic phase separation. Recently a pressure-induced suppression of the insulating charge-ordered (CO) orbitally-ordered (OO) CE-type antiferromagnetic (AFM) ground state in favour of the metallic A-type AFM state was observed in $Nd_{0.5}Sr_{0.5}MnO_3$ at $P \sim 3.5$ GPa. In $Pr_{0.5}Sr_{0.5}MnO_3$ the metallic A-type AFM state stability region is enhanced due to a substantial increase of T_N under pressure. The metallisation at $P \sim 32$ GPa and suppression of orbital ordering at $P \sim 18$ GPa occur in undoped $LaMnO_3$. In contrast, the shear strain evolution in $Nd_{0.5}Ca_{0.5}MnO_3$ up to 15 GPa, observed from X-ray diffraction, assumes the stability of the CO OO insulating state under pressure. These observations imply the presence of competing charge delocalisation and localisation tendencies in half-doped manganites with different $\langle r_A \rangle$ at high pressures.

For further clarification of the pressure-induced behaviour of half-doped manganites, we studied $La_{0.5}Ca_{0.5}MnO_3$ with intermediate $\langle r_A \rangle$ between $Nd_{0.5}Sr_{0.5}MnO_3$ and $Nd_{0.5}Ca_{0.5}MnO_3$ using X-ray, neutron diffraction and Raman spectroscopy up to 31 GPa. At pressures up to 17 GPa, $La_{0.5}Ca_{0.5}MnO_3$ exhibits strongly anisotropic compression of a pseudo-tetragonal character with the b axis of the orthorhombic structure of *Pnma* symmetry being the most compressible as seen from evolution of splitting of the peak formed by (202) and (040) reflections and located at $2\theta = 21.5°$ (Fig. 3.9-19). At $P \sim 17$ GPa an additional splitting of the peak located at $2\theta \approx 26.5°$ appears in X-ray diffraction spectra. With further pressure increase the peak becomes more significant and results in considerable redistribution of diffraction intensity in the 2θ range 26-28°. Such changes in diffraction patterns could not be reproduced consistently in the orthorhombic *Pnma* symmetry and indicate a pressure-induced structural phase transition. The results of the neutron diffraction experiment show that the CO OO CE-type AFM structure of $La_{0.5}Ca_{0.5}MnO_3$ is stable under pressure and the Néel temperature increases with pressure ($dT_N/dP \approx 4$ K/GPa; $T_N \sim 190$K at $P = 0$). This value suggests that the observed structural transformation may originate from the onset of the CO CE-type AFM state at ambient temperature and high pressure, which is accompanied by development of a

monoclinic distortion and doubling of the *a* axis with respect to the initial orthorhombic structure. The relevant structural model of $P2_1/m$ symmetry is consistent with X-ray diffraction data above 17 GPa (Fig. 3.9-19), supporting the proposed origin of the phase transition.

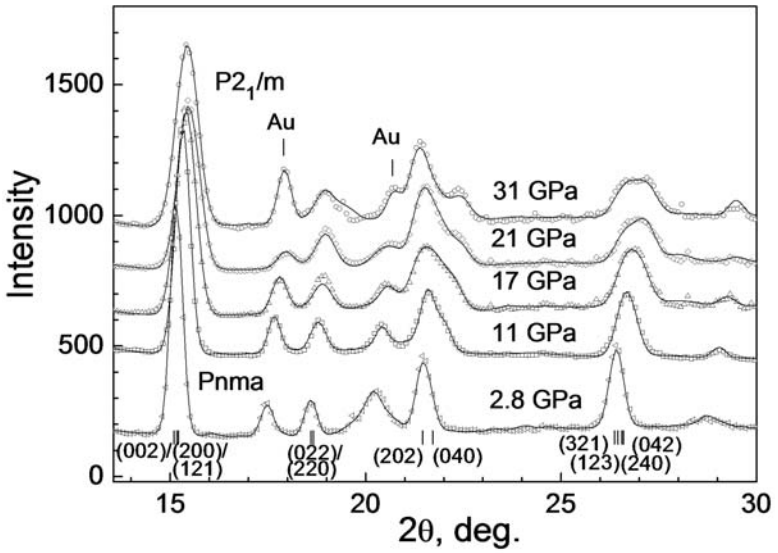

Fig. 3.9-19: X-ray diffraction patterns of $La_{0.5}Ca_{0.5}MnO_3$ measured at selected pressures and ambient temperature and processed by the Rietveld method.

Raman spectra of $La_{0.5}Ca_{0.5}MnO_3$ at high pressures (Fig. 3.9-20) exhibit peaks located at ~ 227, 245, 420 and 445 cm^{-1}. They can be assigned to the in-phase rotational mode of MnO_6 octahedra around the *b* axis with A_g character, mixed out-of-phase rotational mode of MnO_6 octahedra – the so called "tilt" mode, contributions with A_g and B_{1g} character, and out-of-phase apical oxygen bending modes of B_{1g} and A_g character, respectively. At the orthorhombic-monoclinic phase transition a splitting of the tilt mode and noticeable change of the slope of the bending and rotational modes occur (Fig. 3.9-20).

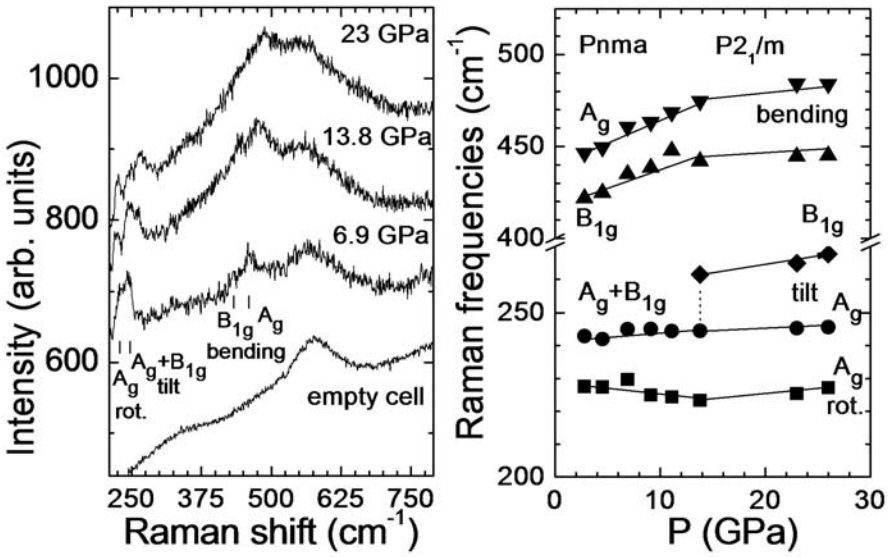

Fig. 3.9-20: Raman spectra at selected pressures (left) and pressure dependence of rotational, tilt and bending modes (right) in $La_{0.5}Ca_{0.5}MnO_3$ at ambient temperature.

j. *Effect of annealing on novel group IV alloy synthesis (C. Guillaume, G. Serghiou and J.P. Morniroli/Edinburgh; D.J. Frost)*

Group IV alloys have attracted considerable interest due to their wide tunability in both structural and electronic properties. This study focuses on forming new alloys from group IV elements (C-Si-Ge-Sn) at high pressures and high temperatures. In previous investigations in the Ge-Sn system, equimolar starting mixtures were melted at 1500 K at numerous pressures and recovered after rapid temperature quenching from the melt. Two main regions showing different chemical compositions were observed in the samples recovered from pressures above 9 GPa using scanning electron microscopy (SEM) in backscattered electron (BSE) mode. Energy dispersive X-ray (EDX) analysis showed these two main regions to both contain Ge and Sn, one region being Ge-rich (bright contrast region in Fig. 3.9-21) and the other Sn-rich (dark contrast region in Fig. 3.9-21). We employed focused ion beam (FIB) methods in order to selectively perform electron diffraction from each of the two regions (Fig. 3.9-22). Microanalysis and electron diffraction measurements showed that individual small crystallites containing both Ge and Sn were present in this sample. The zone axis diffraction pattern of these crystals did not match any of the known Ge or Sn endmember structures. Nevertheless, despite the presence of only two principal compositional regions, these two regions themselves were not of uniform composition and the individual micro to nanocrystallites within these regions were intimately mixed. This made detailed analysis including multiple zone axis diffraction from individual crystallites extremely difficult.

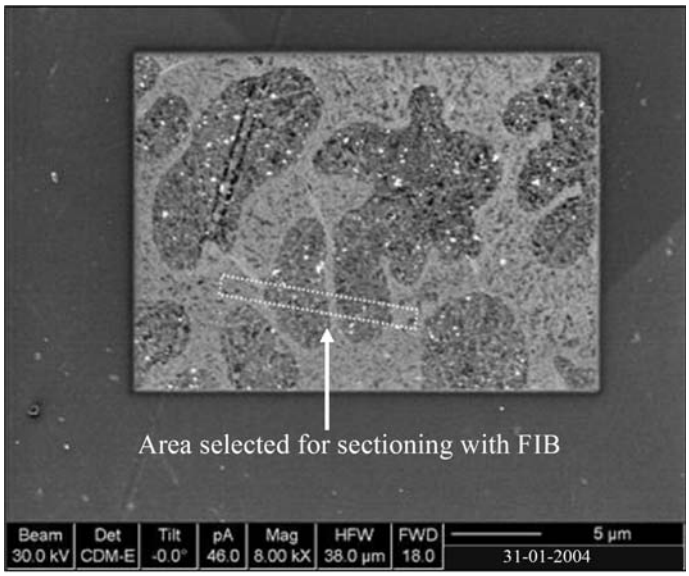

Fig. 3.9-21: Image of a sample recovered from high pressure after temperature quenching from the melt. Both contrast regions exhibited Ge and Sn, with the dark contrast region containing more Sn than Ge. The area selected for preparing a thin section is shown by the arrow.

Following these rapid quench experiments, we embarked on a set of annealing experiments to prepare more homogeneous samples, with considerable success. At 10 GPa we produced a chemically homogeneous GeSn region extending throughout the capsule. Several crystallites from that sample have already been investigated with electron diffraction and scanning transmission electron microscopy (STEM), confirming the chemical homogeneity of the

sample with very high resolution. Here we present a sample recovered from 24 GPa after melting at 1500 K followed by annealing at 770 K before quenching. Two contrast regions, a Ge-rich and a Sn-rich one were observed using SEM images acquired in BSE mode together with EDX analysis (Fig. 3.9-23). The effects of annealing were clearly observed in this sample, with the Ge-rich and Sn-rich regions being more chemically homogeneous and distinctly separated than in our previous experiments. These results are being further investigated with diffraction measurements.

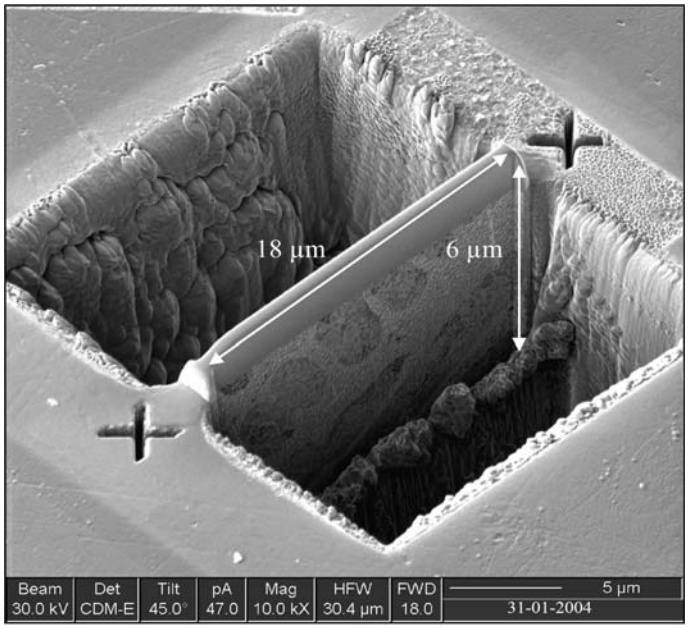

Fig. 3.9-22: Overview of the FIB section before cutting. The Ge-rich and Sn-rich regions can clearly be identified by their different contrast across the FIB section.

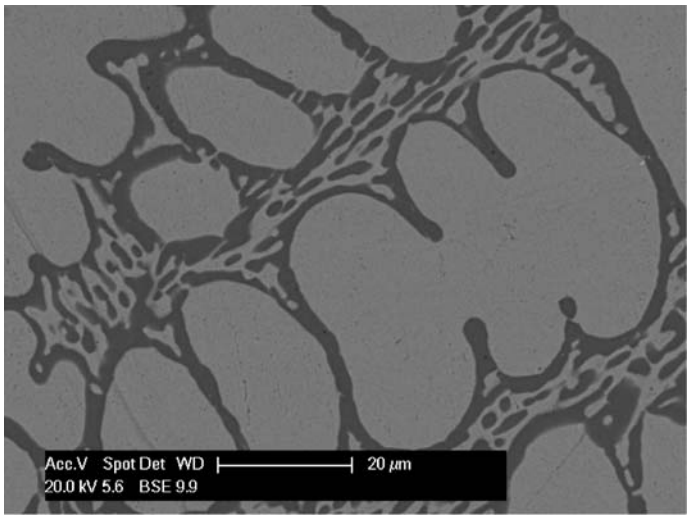

Fig. 3.9-23: SEM image in backscattering mode of a recovered sample after heating a starting mixture of Ge and Sn at 24 GPa and 1500 K for 2 minutes and then annealing at 770 K for three hours. The dark and the bright regions both contain Ge and Sn, with the dark regions containing a greater Ge proportion than the bright regions.

k. *Preparation of new lithium-nickel-manganese oxides under high pressure (R. Stoyanova, E. Shinova and M. Yoncheva/Sofia; C.A. McCammon and T. Boffa Ballaran)*

Lithium-nickel-manganese oxides, $LiNi_{1/2}Mn_{1/2}O_2$, have been considered as an alternative to the currently used $LiCoO_2$ cathode materials as lithium ion batteries since they deliver higher

reversible capacity at room and elevated temperatures. The crystal structure of $LiNi_{1/2}Mn_{1/2}O_2$ is composed of a consecutive arrangement of lithium and transition metal ions in close-packed oxygen arrays leading to the formation of discrete lithium and transition metal layers. In contrast to the ideal layered structure, some structural peculiarities can be outlined for $LiNi_{1/2}Mn_{1/2}O_2$. First, there is a mixing of Li and Ni between the layers, leading to the following cation distribution: $[Li_{1-\delta}Ni_{\delta}][Ni_{1/2-\delta}Mn_{1/2}]O_2$ with $\delta \approx 0.10$. Second, the Li^+ and Mn^{4+} ions in the layers display a tendency for ordering. In order to stabilise the layered structure, over-lithiated oxides of the type $Li[Ni_xLi_{(1-2x/3)}Mn_{(2-x)/3}]O_2$, which can be considered as solid solutions between Li_2MnO_3 and $LiNi_{1/2}Mn_{1/2}O_2$, have been proposed. The aim of this work was to synthesise new lithium-nickel-manganese oxides under high pressure: $Li_{1+x}(Ni_{1/2}Mn_{1/2})_{1-x}O_2$ with $x = 0$ and 0.2.

Under high pressure (3 GPa) and an oxygen-rich atmosphere to control the oxidation state of the nickel ions, the solid state reaction between $NiMnO_3$ and lithium oxide (Li_2O) yielded a new structural variety of $LiNi_{0.5}Mn_{0.5}O_2$ characterised with a disordered rock-salt type structure (Fig. 3.9-24). However, the low-intensity peak at 21° demonstrates that some degree of cationic order still remains in this composition. From an analysis of the X-ray diffraction patterns of $LiNi_{0.5}Mn_{0.5}O_2$ synthesised under high pressure, the following chemical composition could be extracted: $[Li_{0.63}Ni_{0.37}][Li_{0.37}Ni_{0.13}Mn_{0.5}]O_2$. Note that when the reaction between $NiMnO_3$ and Li_2O proceeds under atmospheric pressure, $LiNi_{0.5}Mn_{0.5}O_2$ with a layered structure is obtained with a chemical composition of $[Li_{0.91}Ni_{0.09}][Li_{0.09}Ni_{0.41}Mn_{0.5}]O_2$. The appearance of nickel ions in the lithium site is consistent with the close ionic radii of Li^+ and Ni^{2+}: 0.76 and 0.69, respectively. This means that under high pressure a new structural variety of $LiNi_{0.5}Mn_{0.5}O_2$ is obtained.

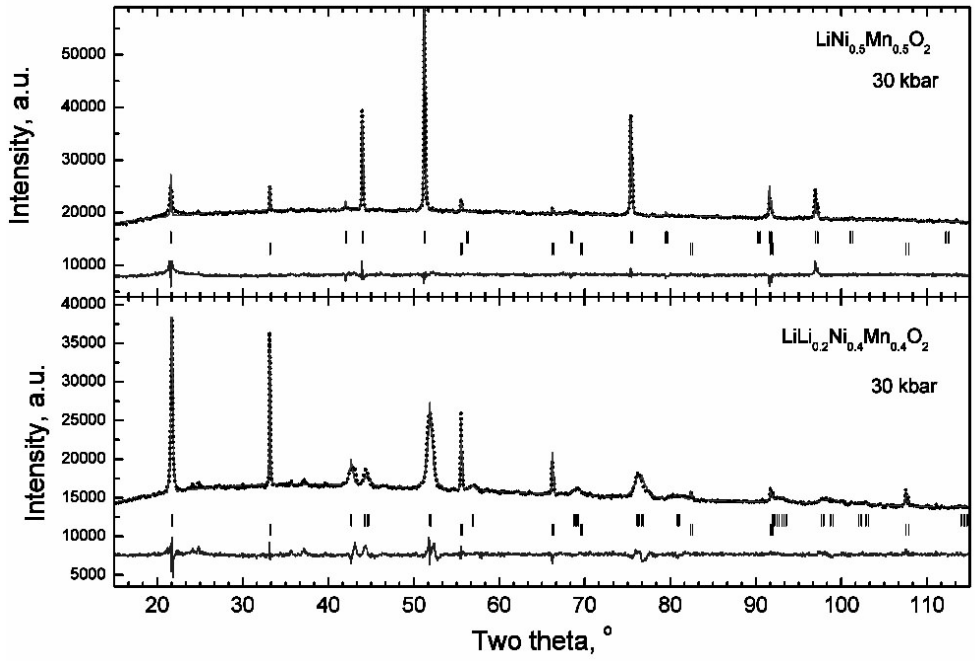

Fig. 3.9-24: X-ray diffraction patterns of ordered $Li[Li_{0.2}Ni_{0.4}Mn_{0.4}]O_2$ and disordered $Li[Ni_{0.5}Mn_{0.5}]O_2$.

When Ni and Mn are maintained in equal amounts, the solid state reaction between $NiMnO_3$ and lithium peroxide (Li_2O_2) under high pressure (3 GPa) yielded $Li_{1.2}Ni_{0.4}Mn_{0.4}O_2$ with a layered structure (Fig. 3.9-24). The appearance of Ni ions in a higher oxidation state due to the high oxygen pressure likely contributes to the stabilisation of the layered modification. The cationic distribution determined from X-ray diffraction peak analysis corresponds to $[LiNi_{0.087}][Li_{0.287}Ni_{0.313}Mn_{0.4}]O_2$. At atmospheric pressure the reaction between $NiMnO_3$ and Li_2O_2 leads to the formation of mixture of NiO and $Li_{1.2}Ni_{0.2}Mn_{0.6}O_2$. Rietveld analysis of X-ray diffraction data showed that the cationic disorder is more significant for the oxide prepared under high pressure. An important feature of the X-ray diffraction pattern of $Li_{1.2}Ni_{0.4}Mn_{0.4}O_2$ is the significant broadening of peaks compared to that of the $Li_{1.2}Ni_{0.2}Mn_{0.6}$ oxide; however no selective broadening is observed.

l. *Structural, electronic and magnetic properties of high-pressure phases of the spin-frustrated Mott insulator $CuFeO_2$ delaffosite (G.Kh. Rozenberg and M. Kertser/Tel Aviv; A.V. Kurnosov and L.S. Dubrovinsky)*

The present investigation stems from our recent extensive high-pressure magnetic (Mössbauer effect) and electronic (conductivity) studies in spin-frustrated Mott insulator $CuFeO_2$ delafossite. Recent studies to 19 GPa revealed: (*i*) a striking two-fold increase in T_N caused by the pressure-induced (PI) enhancement of the intraplanar (*a*-*a*) direct exchange, and (*ii*), the transition from a spin-frustrated system to one with long-range magnetic ordering. Above 19 GPa additional dramatic changes took place both in the electronic and magnetic framework of Fe^{3+} (and possibly of Cu^{1+}), namely, a portion of Fe^{3+} is transformed into Fe^{2+}, *e.g.*, a pressure-induced *reduction* process. Both the Fe^{2+} and Fe^{3+} high-spin states coexist to 40 GPa after which an insulator-metal (IM) transition occurs concurrent with correlation breakdown. In general our objectives have been to study possible structural changes corresponding with the above-mentioned novel phenomena using XRD and Raman spectroscopy. In particular we have emphasised the following: *(i)* structural identification, equations of state and thorough Raman studies in the three crucial pressure regimes: 0-19 GPa (collapse of the spin-frustration), 22-50 GPa (changes in Fe valence, probably Cu also), P > 50 GPa (insulator-metal transition); *(ii)* careful XRD and Raman spectroscopy studies and data analysis to investigate the structural consequences of the valence transformations in Fe ($Fe^{3+} \rightarrow Fe^{2+}$) and verify the consequential reversed transformation in Cu ($Cu^{1+} \rightarrow Cu^{2+}$), particularly by analysis of the Cu-O and Fe-O bonding distances alterations; *(iii)* the effect of the PI-induced Mott transition above 50 GPa. This transition may result in an appreciable volume reduction and vibrational spectra alterations.

Here we studied the pressure evolution of the vibrational properties of $CuFeO_2$ delafossite by Raman spectroscopy at 300K. The Raman spectra were measured using a LabRaman system spectrometer equipped with a microscope and charge-coupled device detector with an Ar laser operating at 632 nm wavelength and power of ~ 30 mW for excitation. The samples were loaded in opposed-plate diamond anvil cells into cavities of 100 μm in diameter and 30-40 μm thickness drilled in Re gaskets. High-pressure Raman studies were performed up to 60

GPa. Spectra were collected over the range 150-1800 cm^{-1}. Four slots of measurements including compression and decompression cycles were performed, and several X-ray diffraction experiments were performed after pressure release to ambient conditions.

Raman studies revealed a significant pressure evolution of the Raman spectra (Fig. 3.9-25). The modes shift towards higher energy and broaden with pressure up to ~ 15 GPa. At P ~ 15 GPa the low energy mode (~ 380 cm^{-1}) splits, and a new mode at ~ 405 cm^{-1} starts to grow, moving towards lower energy; whereas the low-pressure mode disappears gradually (Fig. 3.9-26). The slope with pressure of the high energy mode (~ 730 cm^{-1}) also changes to be negative. Above 21 GPa the intensity of the Raman modes decrease and they nearly disappear at ~ 24 GPa. These observations are in good agreement with XRD studies which revealed two structural phase transitions at P ~ 15 and 23 GPa. According to preliminary data analysis, the new high-pressure phase (P > 23 GPa) can be fitted well with a monoclinic (*C*12/*m*1) structure. This is also a layered but slightly distorted hexagonal structure which, in contrast to the low-pressure phase, accommodates two different types of Fe and Cu sites (1/3 of the Fe and Cu positions are occupied by Fe^{2+} and Cu^{2+}, respectively). The Cu environment changes significantly at this transition from dumbbell-like to distorted octahedra. With further pressure increase a significant volume drop is observed at ~ 55 GPa, concurrent with the onset of the Mott transition.

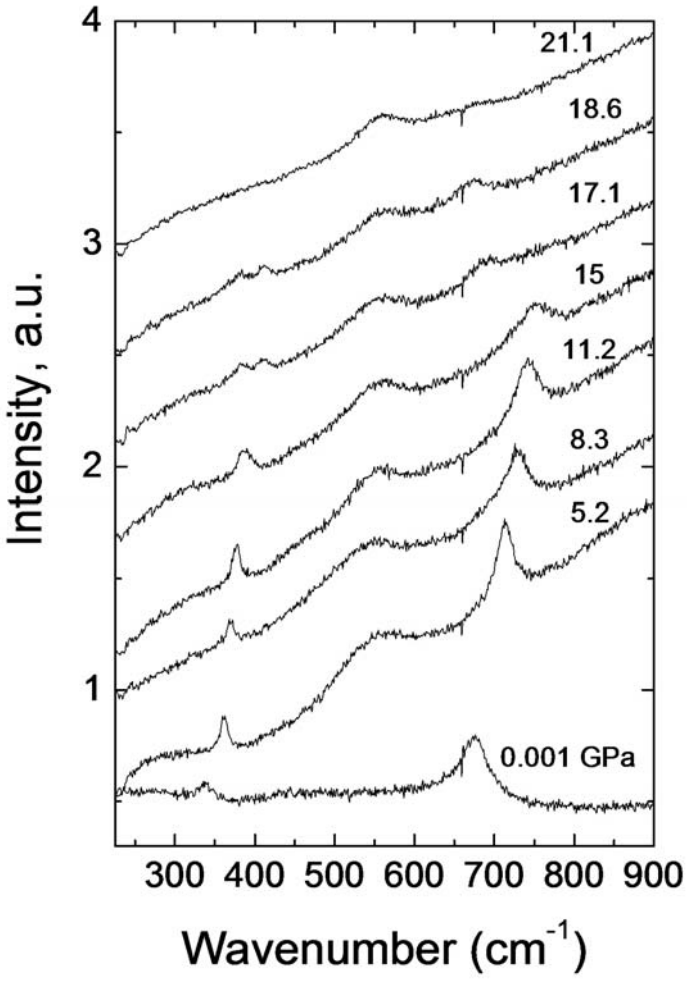

Fig. 3.9-25: Raman spectra of $CuFeO_2$ recorded at 300 K and various pressures.

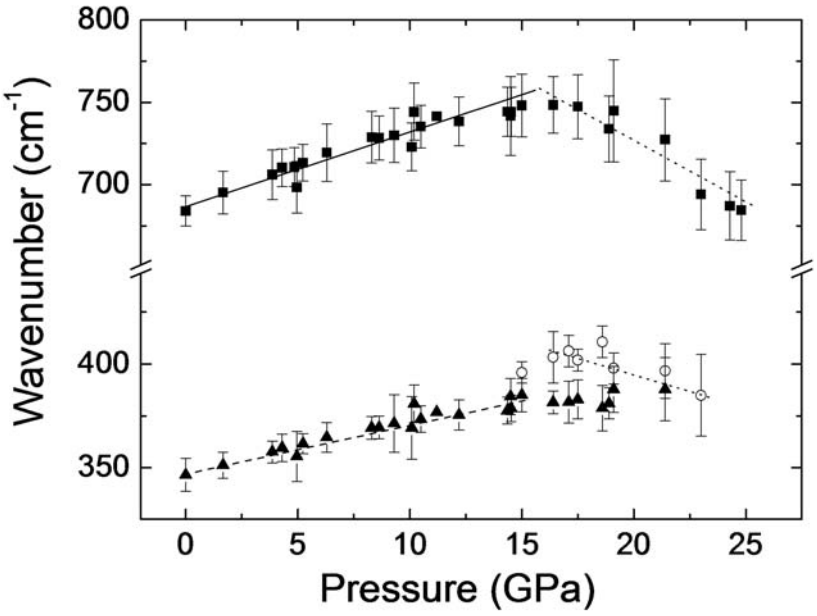

Fig. 3.9-26: Pressure dependence of the Raman mode positions. Note that up to ~ 15 GPa the modes shift towards higher energy with pressure. At ~ 15 GPa the spectra show a significant change: the low-frequency mode (~ 350 cm^{-1}) splits (triangles, open circles) while the high-frequency mode (~ 700 cm^{-1}) (squares) broadens and starts to move towards lower energy; mode intensities decrease. Both modes disappear at ~ 24 GPa.

m. *Phase transformations in potassium niobiosilicate glasses (P. Bergese, I. Alessandri, E. Bontempi and L.E. Depero/Brescia; A. Aronne, E. Fanelli and P. Pernice/Napoli; T. Boffa Ballaran and N. Miyajima; V.N. Sigaev/Moscow)*

Second harmonic generation (SHG) in isotropic materials, such as glasses based on ferroelectric or other highly polarisable phases, have been shown to be an appealing route to nanophotonics. Potassium niobium silicate (KNS) nanostructured glasses belong to this promising class of materials. In our recent experiments nanostructuring (formation of nanosized inhomogeneities) on the scale of 5-20 nm was induced in the bulk of these glasses by isothermal annealing at the glass transition temperature, T_g. For these systems the relative maximum of SHG efficiency took place at the initial stage of nanostructuring. This unusual behaviour formed the basis of a novel interpretation of the SHG mechanism as due to a combination of third-order non-linearity with a spatial modulation of linear polarisability.

Bulk nanostructuring and optical behaviour are therefore subtly intertwined and further investigations are demanded. On one side, they are of basic interest, since they can reveal intriguing mechanisms of SHG due to local (nanoscale) atomic arrangements. On the other side, they are of technological interest, as they are compulsory in manufacturing of glasses with tailored SHG.

Here we report a study of the structural and microstructural features of KNS nanostructured glasses which is focused on the growth/nucleation of the coherent domains/nanocrystals in the amorphous matrix. Previous studies showed that nanostructuring occurs by binodal phase separation and subsequent segregation of nanosize niobium-rich regions. However, the picture was still incomplete. In other words, does nanostructuring mean nucleation in the matrix of nanocrystals, or does it mean organisation of atoms in shorter coherent domains which

provide local structure seeds whose order fades out in the matrix, thus lacking crystalline periodicity?

To answer this question we combined our previous information with high resolution transmission electron microscopy (HRTEM) and *in situ* high-temperature resolved X-ray diffraction (HTXRD) experiments (all performed at Bayerisches Geoinstitut). We investigated KNS glasses of two molar compositions, namely $x\mathrm{K_2O}\cdot y\mathrm{Nb_2O_5}\cdot(100\text{-}x\text{-}y)\mathrm{SiO_2}$ with $x = 20/ y = 25$, and $x = 23/y = 27$, hereafter referred to as glasses 20-25-55 and 23-27-50, respectively. These compositions were chosen as potentially representative of different nanostructuring behaviours. HRTEM imaging, integrated with data from selected area electron diffraction (SAED) and energy dispersive X-ray spectroscopy (EDXS), indicated that in both glasses the nanostructuring process induced by annealing at T_g evolves by continuous nucleation of nanocrystals which reach a maximum size of a few tenths of nanometres. These nanocrystals are uniformly distributed in the matrix, irrespective of the glass composition. They are more numerous and slightly larger in the 20-25-55 composition, namely 10-20 nm for the 20-25-55 glass and < 10 nm for the 23-27-50 glass (Fig. 3.9-27). Finally, in both glasses the nanocrystals are richer in niobium than the matrix and (very likely) belong to the same crystallographic phase.

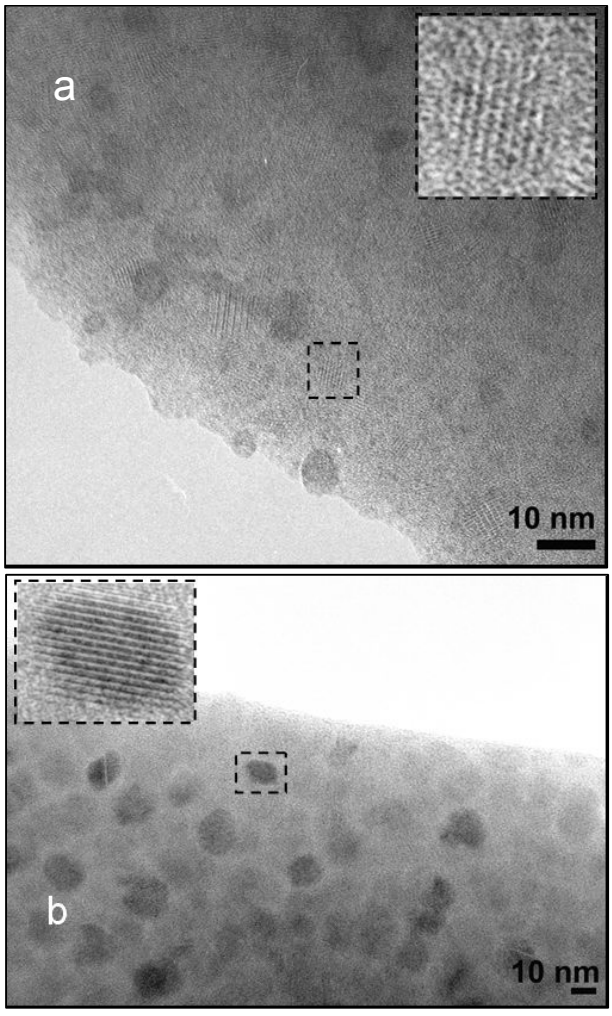

Fig. 3.9-27: HRTEM micrographs of the samples which were treated by annealing for 24 hours at T_g. The samples of compositions 23-27-50 and 20-25-55 are shown in the micrograph (a) and (b), respectively. Insets: magnifications of the black dashed regions.

HTXRD showed that upon heating the nanocrystals of both glasses transform to the same crystalline phase, NP (to date still unresolved). However, they reach NP in a different fashion, which is mainly related to the glass bulk composition. In the case of the 23-27-50 glass the nanostructure attained during annealing gradually transforms with temperature into NP (Fig. 3.9-28a), while in contrast the 20-25-55 glass maintains a stable nanostructure until 765 °C where it then transforms within 20 °C to NP (Fig. 3.9-28b). Such trends suggest that the nanocrystals of the 23-27-50 composition transform into NP by a continuous (structural and microstructural) change, *viz*. by a second order (or kinetic) transformation. In contrast, the nanocrystals of the 20-25-55 composition transform into NP by a discontinuous change, *viz*. by a first order (or thermodynamic) transformation.

HRTEM and HTXRD experiments also hinted that the 23-27-50 glass presents slower and more complex nanostructuring kinetics, suggesting that the process in the 23-27-50 glass occurs by rearrangement of the amorphous matrix which drives nucleation of niobium-rich nanocrystals, while in the 20-25-50 glass it may directly undergo the nucleation route, skipping the step of phase separation.

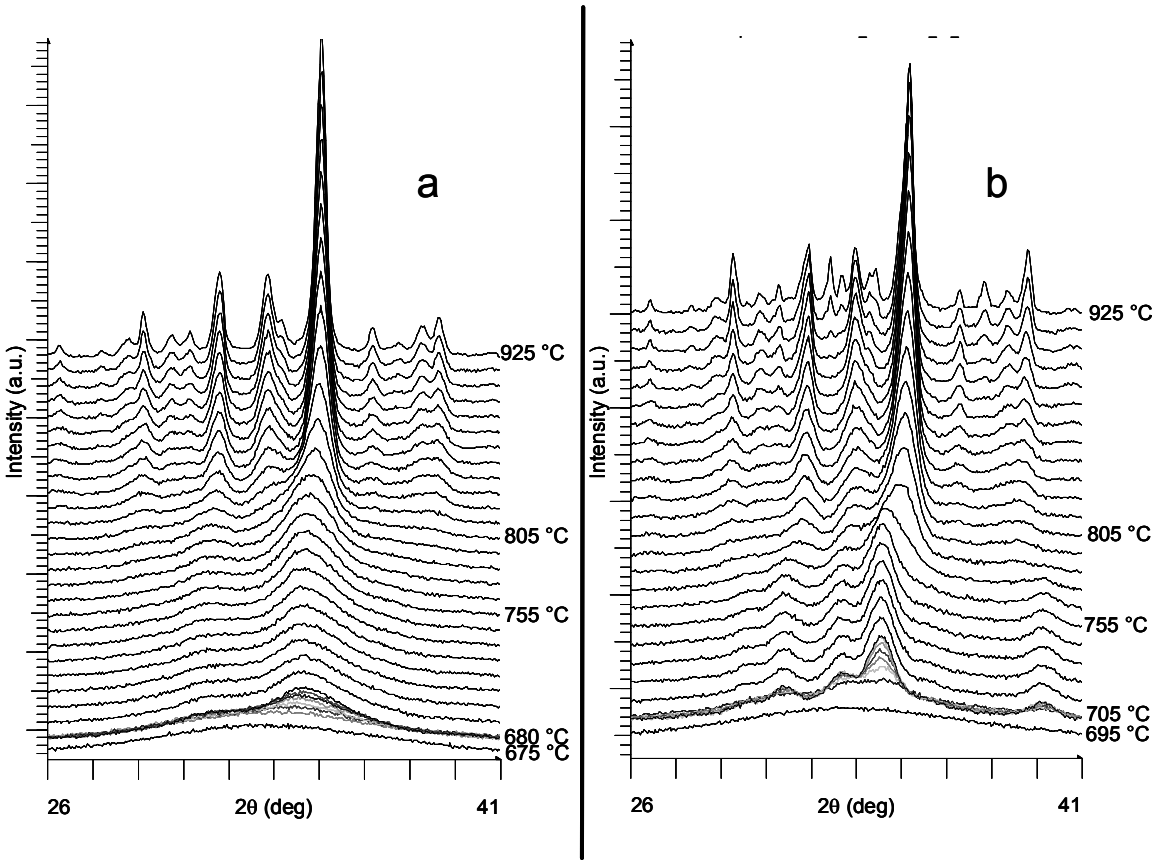

Fig. 3.9-28: HTXRD profile series of the (a) 23-27-50 as-quenched glass and (b) 20-25-55 as-quenched glass. The samples were annealed *in situ* for 10 hours at T_g. During annealing they were scanned each 0.5 hours (only the most representative ones were reported).

n. *High-pressure behaviour of Li_2VOSiO_4, a frustrated 2D quantum Heisenberg antiferromagnet (S. Tarantino and M. Zema/Pavia; T. Boffa Ballaran)*

The search for novel quantum states in low-dimensional antiferromagnets (AFs) has triggered significant activity in recent times. A remarkable amount of theoretical studies has concerned the phase diagram of AFs where long-range magnetic order is suppressed by enhanced quantum fluctuations. Such a scenario can be established when the magnetic lattice dimensionality and the spin value are reduced or when the disorder is increased, either by means of heterovalent substitutions or by spin dilution. Further enhancement of quantum fluctuations can occur when the exchange interactions can not be simultaneously satisfied in a two-dimensional S = 1/2 Heisenberg AF (2DQHAF) on a square-lattice, with nearest neighbour (J_1) and next-nearest neighbour (J_2) AF couplings of the same order of magnitude. Although the phase diagram of this system, the so-called J_1-J_2 phase diagram, has been extensively studied theoretically there are several aspects still under debate. In particular, it is not even established how the ground state should change upon increasing the frustration ratio J_2/J_1 towards the critical value $J_2/J_1 = 0.5$, namely if upon increasing J_2 there is a first order phase transition from a Néel to a collinear order or if there is a wide region in the phase diagram where the ground state is a spin liquid. Recently it has been possible to start to explore this phase diagram experimentally thanks to the discovery of two prototypes of frustrated two-dimensional S = 1/2 Heisenberg AFs (2DQHAF) on a square-lattice: Li_2VOSiO_4 and $VOMoO_4$. In these materials vanadium ions are in the V^{4+} configuration, giving rise to a two-dimensional lattice (weakly coupled in the perpendicular planes) of interacting spin 1/2. The former compound, which has been more extensively studied, is characterised by $J_2/J_1 > 1$ and recently its ground state, studied by means of RXS and neutron diffraction, has been found to be characterised by a collinear order.

Li_2VOSiO_4 under ambient conditions shows a natisite-type structure, space group $P4/nmm$ with $a \sim 6.37$ Å, $c \sim 4.45$ Å. The general network of this structure, with two formulae per unit cell, is formed by piling up parallel $[VOSiO_4]_n^{2-}$ layers of VO_5 square pyramids sharing corners with SiO_4 tetrahedra and held together by intercalated Li cations.

The goal of this project is to investigate the high-pressure elastic behaviour of Li_2VOSiO_4 by means of *in situ* single-crystal diffraction and to characterise how the applied external pressure modifies the vanadium coordination, and therefore could modulate the J_2/J_1 ratio.

Accurate lattice parameters were measured with a Huber four-circle diffractometer up to 8.5 GPa with the crystal in a BGI-type diamond anvil cell. The evolution of the lattice parameters with P shows that no phase transition occurs within the pressure range investigated (Fig. 3.9-29). Unit-cell volume data were fitted with a third-order BM-EOS. The third-order BM-EOS parameters, simultaneously refined using the data weighted by the uncertainties in V, are: V_0 = 181.29(3) Å^3, K_{T0} = 99(1) GPa and K' = 3.8(3). After 8.5 GPa severe line broadening of the crystal reflections have been observed, which may indicate either non-hydrostatic conditions

or a first order phase transition. Another set of experiments has therefore been undertaken with a crystal with opportune orientation loaded in a DAC to perform data collection at high pressure. The structural refinements of such data should give insight into the high-pressure behaviour of the VO_5 square pyramids and into a possible phase transformation.

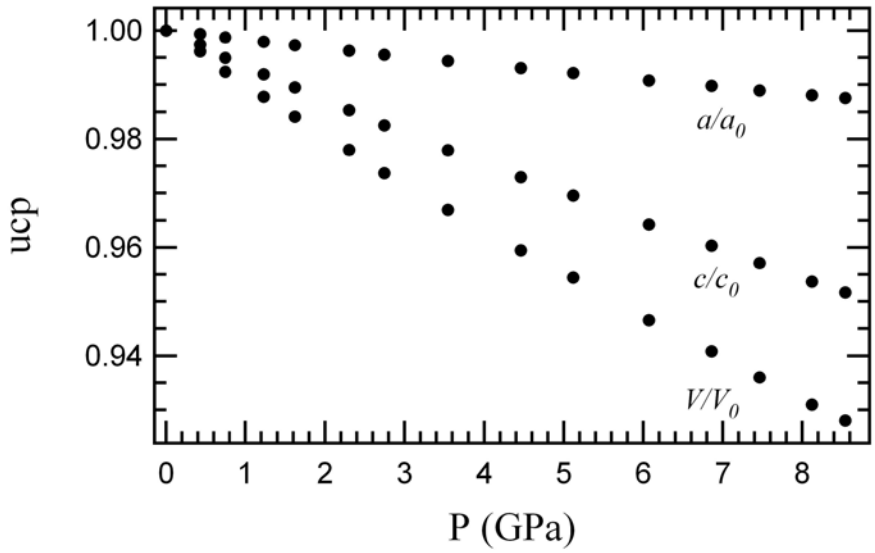

Fig. 3.9-29. Variation of the unit-cell parameters (ucp) of Li_2VOSiO_4 with pressure.

o. *Theoretical determination of precursor phases for polymeric nitrogen (R. Caracas and R.J. Hemley/Washington DC)*

The phase diagram of nitrogen is extremely complex for apparently such a simple molecular system. At low pressures several partially disordered structures are known, where the N_2 molecules freely rotate in spheres or disks (α and β phase). With increasing pressure more compact structures develop, and the freedom of movement of the molecules decreases. The search for polymeric or atomic structure has raised much interest both theoretically and experimentally. The polymeric phase was later observed and the predicted cubic gauche structure was found. Other structures have been proposed as well, but they appear to be metastable. The structures of the higher-pressure molecular phases are not known, although there are constraints from X-ray diffraction and vibrational spectroscopy. There is now evidence for new high-P-T phases prior to the transition to the atomic phase, but their structures and physical properties have not been identified or are not fully understood, which has prompted additional theoretical study. Indeed the phase diagram of nitrogen is more interesting and complex than previously thought.

In this study we predict the existence of new structures of nitrogen based on new observations in analogue systems. We perform first-principles density-functional calculations on a series of structures. A structure with *Immm* symmetry and two molecules per unit cell (Fig. 3.9-30)

was found to be stable relative to the ε and cubic gauche phases. The structure is dynamically stable from ambient pressure to at least 90 GPa. The computed physical properties and two transition path models suggest that this phase is a plausible intermediate step between the low-pressure molecular structures and the high-pressure atomic structures of nitrogen.

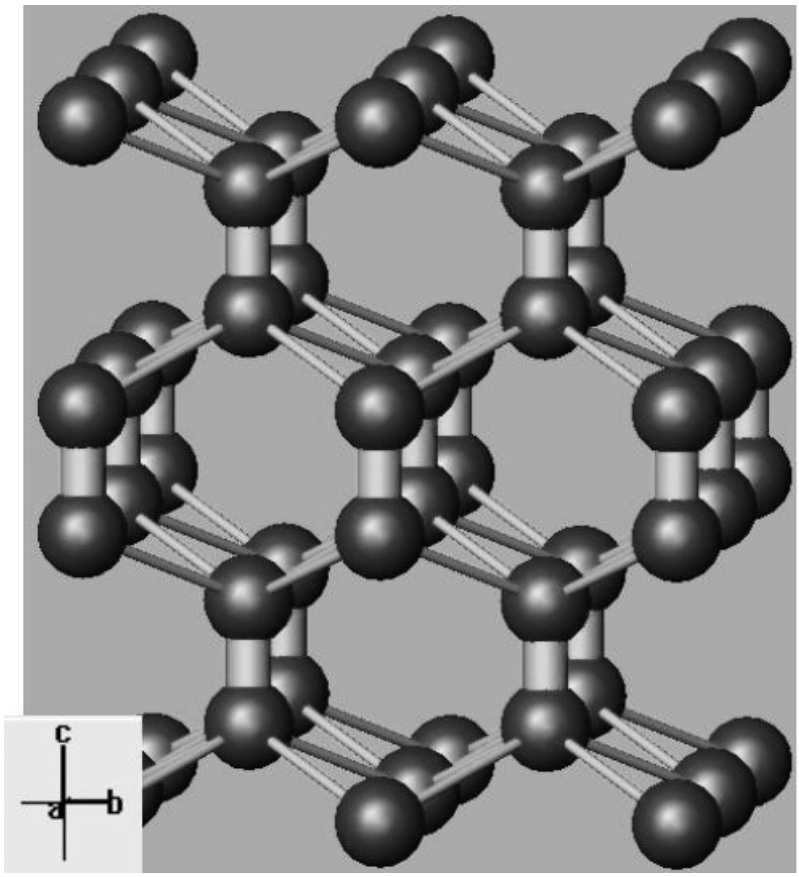

Fig. 3.9-30: Crystal structure of the newly proposed *Immm* phase of nitrogen.

3.10 Methodological Developments

New developments in experimental and analytical techniques form the backbone of any scientific research, hence their importance cannot be overemphasized. The Bayerisches Geoinstitut has a long tradition of participating at the highest level in this discipline, with many of its innovations having been adapted by labs worldwide. The design, fabrication and testing of new experimental and analytical methods is a time-consuming challenge that requires a high technical and financial support, both of which is provided at the Bayerisches Geoinstitut. In the last year, new developments were made in Micro X-ray Absorption Spectroscopy as well as in the pressure calibration and the pressurization routine of diamond anvil cells. A newly designed energy dispersive spectrometer with fixed optics and a spatial resolution of 5 μm allows for the first time generation of 2D-images from samples within the diamond anvil cell covering areas of up to 500x500 μm. A new study on the equation of state of LiF provides urgently needed data for a pressure calibrant that combines good pressure transmittance with low X-ray absorption and a lack of phase transitions up to 32 GPa and 720 °C. Finally, the controlled buildup (and release) of pressure in diamond anvil cells has become much faster and safer by a set of displacement sensors mounted into the cell. The ability to adjust pressure without having to move the cell and perform time-consuming length measurements is particularly advantageous for spatial *in situ* experiments.

a. *2D Micro-XAS mapping in a diamond anvil cell (L.S. Dubrovinsky, O. Narygina and I.Yu. Kantor, in collaboration with S. Pascarelli, G. Aquilanti and M. Munoz/Grenoble)*

Energy Dispersive X-ray Absorption Spectroscopy (EDXAS) is now a well-established method which has been used to a broad range of applications. The energy dispersive spectrometer employs a bent crystal to focus and disperse a diverging polychromatic X-ray beam onto the sample. The beam passing through the sample then diverges towards a position sensitive detector, where beam position is correlated to energy. The advantages of an energy dispersive spectrometer, that features no movement of optics during acquisition leading to an enhanced stability of energy scale, spot size and position, combined with a micron sized spot and the option of fluorescence detection, has made it possible to address 2-dimensional mapping with micron resolution on heterogeneous samples, providing full XAS information on each pixel. It is worth noting that due to the absence of mechanical scanning of the monochromator, the spatial resolution is not affected by the energy scan and remains fixed to the dimensions of the probe. In addition, the energy scale is preserved. Moreover, the dwell time per pixel is short enough to make it practically possible to acquire 100 x 100 pixel images in a few hours.

The information collected, intrinsically complete, is also too complex to be directly visualized. The extraction of the relevant information, spanning from simple oxidation state

identification (from XANES) to local structural parameters (from EXAFS), requires specific software developments for data reduction, image reconstruction and visualization, providing a targeted reduced XAS information on each pixel.

We tested 2D mapping in transmission mode to perform *in situ* investigations in the diamond anvil cell. Maps of redox and speciation at extreme conditions of pressure and temperature yield information on possible phase transitions and/or chemical reactions that occur at P and T conditions in the Earth's interior. As test sample, we chose a major component of the Earth's transition zone, ringwoodite [γ-$(Mg,Fe)_2SiO_4$]. Samples were synthesized at BGI in a large-volume press at 19 GPa and 1700 °C from natural olivine $(Mg_{0.88},Fe_{0.12})_2SiO_4$. They were polished, loaded into the DAC, compressed to the desired pressure (monitored by the unit cell volume of gold), and laser-heated (Fig. 3.10-1). We acquired Fe K-edge XANES maps at different pressures, up to ~ 40 GPa, before and after laser heating, covering for each map an area of 200 x 200 μm at 5 μm resolution.

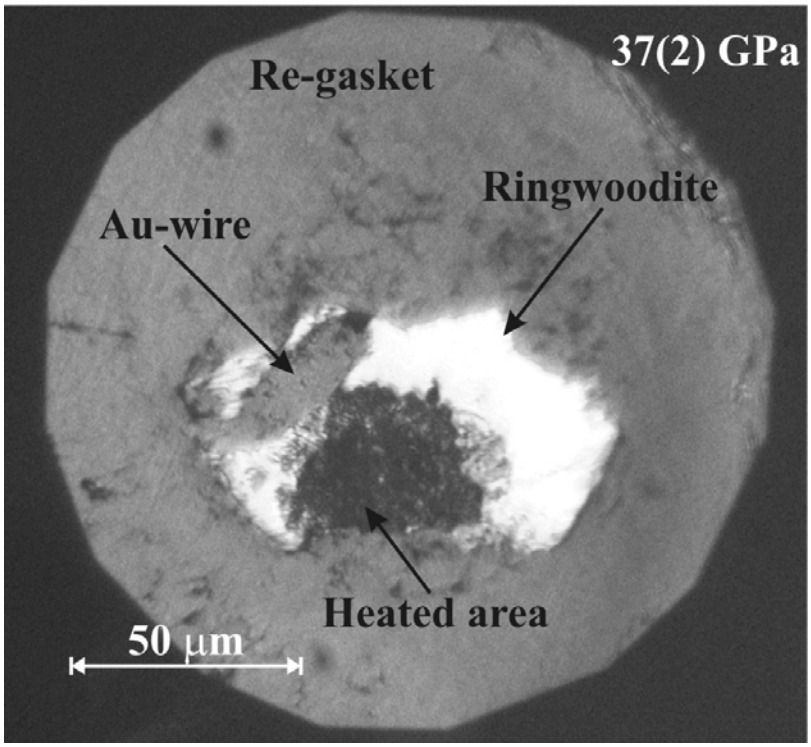

Fig. 3.10-1: Photograph of the ringwoodite γ-$(Mg_{0.88},Fe_{0.12})_2SiO_4$ sample compressed to 37(2) GPa and partially laser-heated between 1900 K and 2100 K.

Figure 3.10-2 illustrates maps of normalized absorbance at a defined energy (E = 7125 eV) at 26 GPa (top) and at 37 GPa (bottom), before (left) and after (right) laser heating. Analysis of the modifications in the spectra from the hot spot region will allow to extract quantitative Fe redox at high P and T, yielding key information for modeling Earth's mantle processes.

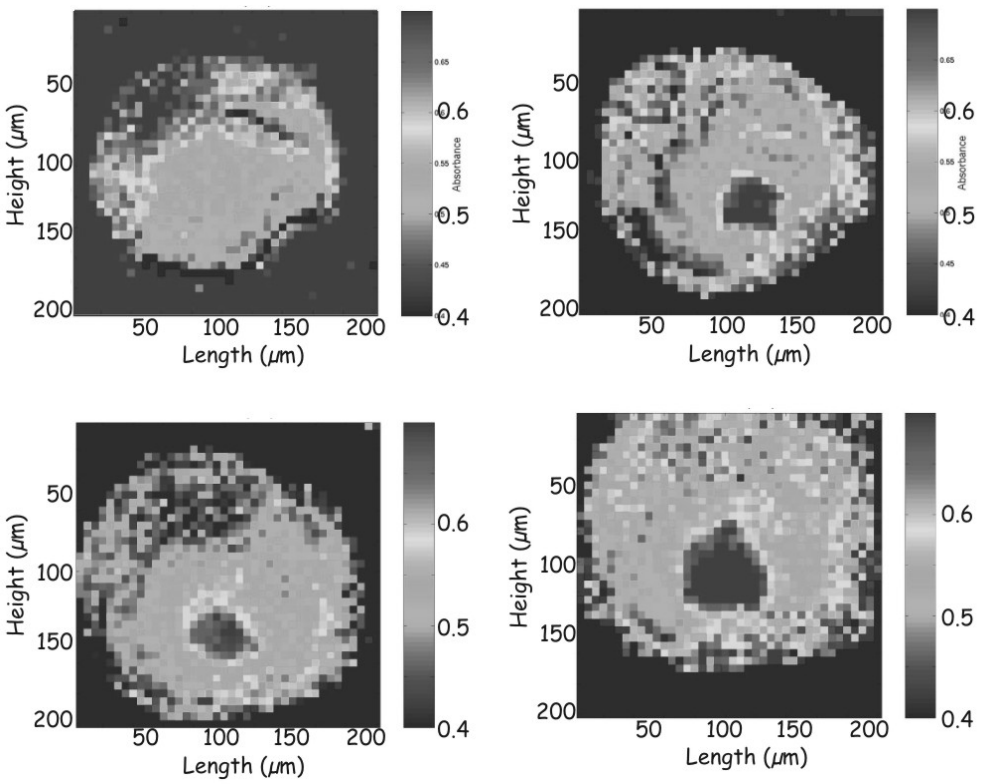

Fig. 3.10-2: Fe K-edge normalized absorbance at E=7125 eV on γ-$(Mg_{0.88},Fe_{0.12})_2SiO_4$ at 26 GPa (top) and 37 GPa (bottom) before (left) and after (right) laser heating. Laser heating at 37 GPa was performed at the same spot as previously at 26 GPa.

b. *A sensors-based inset for remote control of parallelism and micro-displacement of the plates for the opposing-plates DAC (A.V. Kurnosov, S. Linhardt, L.S. Dubrovinsky)*

Opposing-plate diamond anvil cells (OP DAC) have a number advantages compared with piston-cylinder types of DAC's. They allow mounting of internal resistive heaters and allow better access to the sample during diffraction measurement experiments. Another important advantage is the fact that the loading procedure in many cases is simpler (*e.g.*, gas + liquid loading). Opposing-plate cell furthermore are easier to produce and therefore noticeably cheaper than their piston-cylinder analogs. The price of these advantages of OP DAC is one serious disadvantage – a complicated procedure of pressurization is required in order to maintain parallelism of the diamonds. In most OP DAC's pressure is increased by tightening screws (usually 4-6 screws; depending on the model). In order to maintain a homogeneous stress distribution around the diamonds and keep them parallel one has to control the displacement of the plates after each tightening at 3-4 points. This can be done most precisely by micrometer. It requires dismounting and mounting back the cell onto the experimental stage. Often, *in situ* experiments have to be done with step-by-step pressure increase without disturbing of alignment of the cell. Displacement measurements by micrometer are in such cases impossible.

Here we report the first results of an automated displacement monitor using an inset containing force-sensors suitable for 50mm 4-pin OP DAC. The current inset model contains two force sensors, each of them being calibrated for displacement vs. applied force. The sensors elasticity of compression(~ 50 μm for maximal loading) allows them to be used as micro-displacement sensors. In future models the number of sensors will be increased up to four for better control of parallelism (for example, for the purpose of indentation of a gasket or for systematic "on-site" pressure increases).

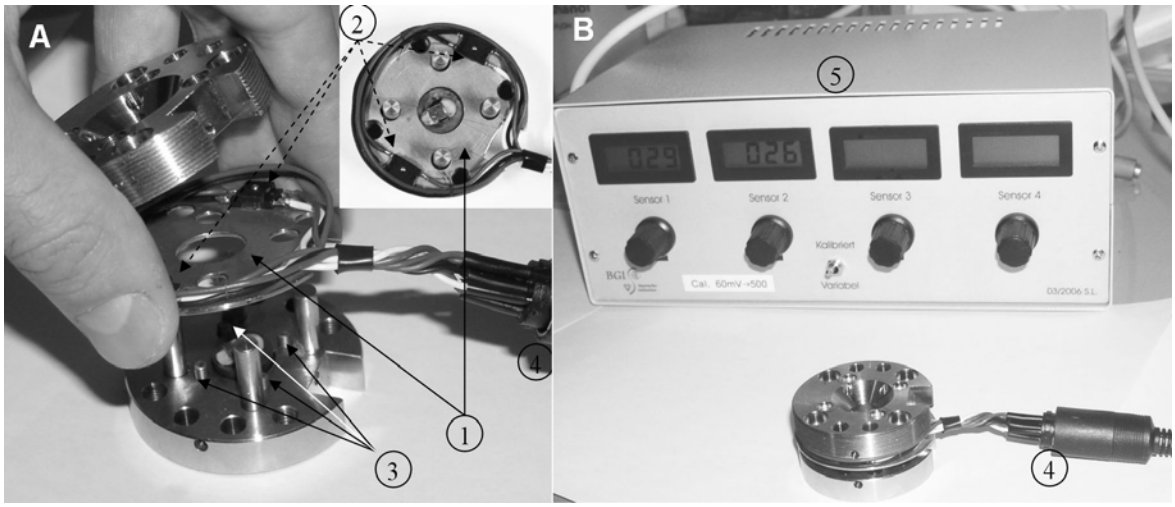

Fig. 3.10-3: (A) Assemblage of the opposing-plates DAC with two force sensors (B) Cell connected to the digital displacement indicator.

The inset is made of steel base resembling the cell geometry (1). Two sensors (2) are mounted as shown on Fig 3.10-3. Four screws (3) on the bottom plate are used for alignment of a zero displacement when the cell is assembled. The electrical connector (4) can be connected to remote controller (5). The displacement indicator has four displays - one for each sensor.

A similar setup with sensors able to be dismounted out of the assembled cell may be used in cells that are intended to be heated. Only one sensor can be used (in order to reduce electrical connections) for the purpose of controlled closing of the cell in remote devices without direct access (for example gas-loading devices).

c. *Equation of state and thermal expansivity of LiF (J. Liu, L.S. Dubrovinsky and T. Boffa Ballaran, in collaboration with M. Mezouar and W. Crichton/Grenoble)*

Lithium fluoride is an important material in the high pressure field since it is one of the substances used as pressure transmitting medium. In recent high-pressure studies there has

been an increasing use of LiF under extreme conditions in diamond anvil cell experiments. In contrast to these recent advances, no new measurements of the equation of state or the thermal expansivity of LiF were made since 1978. Moreover, the properties of LiF under high pressures and high temperatures were measured only up to 9 GPa and 800 °C. Our work presents new experimental measurements of equation of state and thermal expansivity of LiF up to 32 GPa and 720 °C.

High-pressure and high-temperature synchrotron radiation X-ray powder diffraction data of LiF were collected at the European synchrotron Radiation Facility (ESRF, Grenoble, France). LiF powder was loaded into a diamond anvil cell together with NaF powder, and a piece of gold was used for pressure calibration. During high-temperature measurements, samples were heated by an external heater attached to the DAC. Temperatures were measured by a pair of s-type thermocouples. The samples were compressed at room temperature up to 32 GPa, and then slowly heated to ~ 700 °C with some adjustments of pressure. After reaching 720 °C and 20 GPa, the samples were then decompressed to ambient pressure at same temperature. The obtained diffraction pattern were integrated by Fit2d software, and the lattice parameters of LiF were determined by full profile (GSAS package) refinements. Figure 3.10-4 shows an example of experimental data fitted with GSAS. Equation of state and thermal expasivity of LiF were calculated with the third order Birch-Murnaghan equation using the software Eos fit written by Ross Angel.

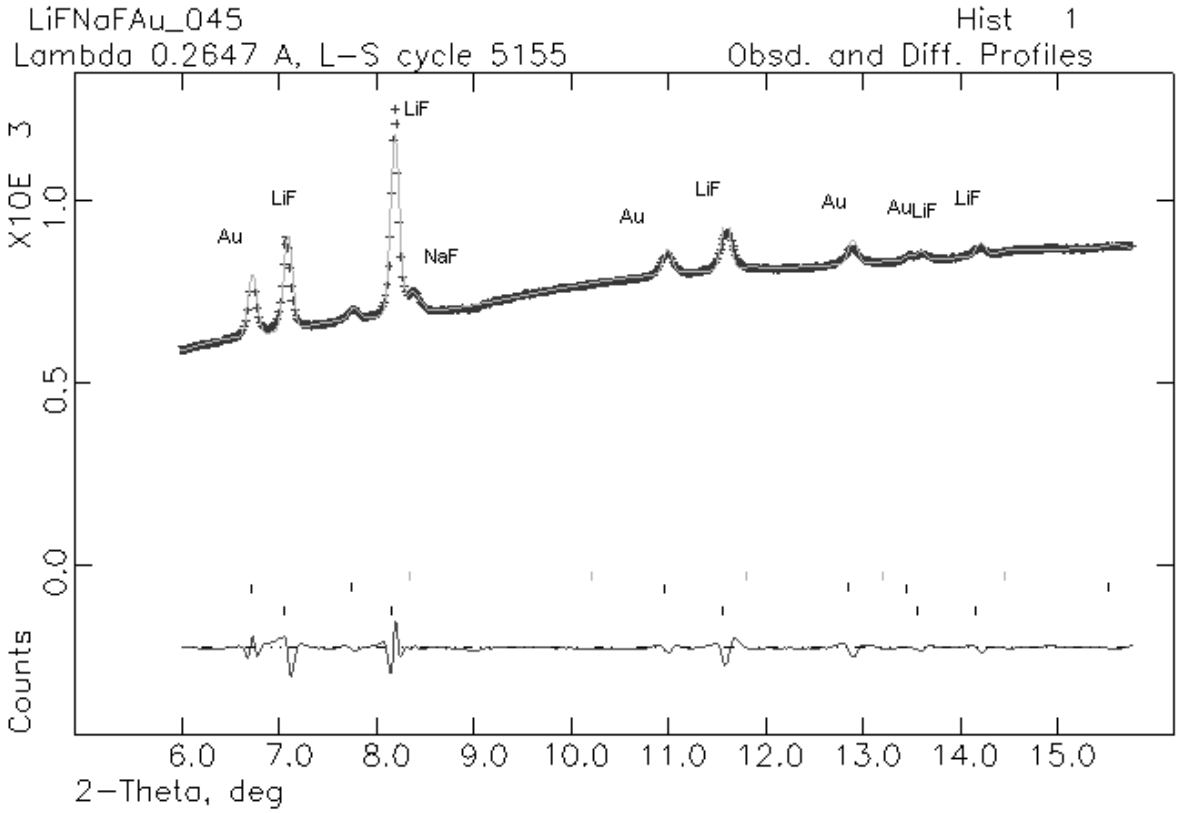

Fig. 3.10-4: GSAS fitting of experimental data at 31GPa, room temperature.

At ambient temperature, the calculated Murnaghan EOS parameters of the equation of state are: $V_0 = 65.61$ (3) Å^3, $K_0 = 74.4$ (8) GPa, and K' = 3.69 (7). A p-v-t fit of our data with high pressure and high temperature gave thermal expansivity parameters of $\alpha_0 = 1.05$ (3) $\times 10^{-4}$ and dK/dT = -0.025 (2) GPa/K, with $V_0 = 65.65$ (10) Å^3, $K_0 = 72.5$ (2.2) GPa, K' = 3.87 (18). The obtained K_0 and α_0 values are slightly higher than in the previous study. Figure 3.10-5 illustrates some of the experimental data plotted on calculated isothermal curves.

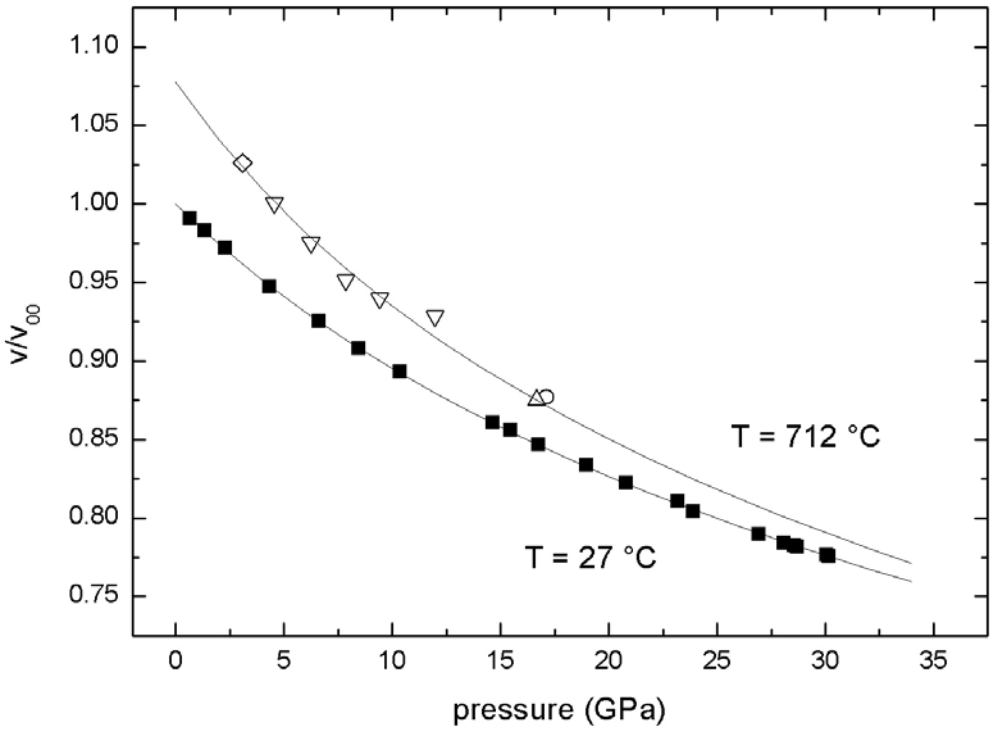

Fig 3.10-5: Isothermal compressions of LiF at 27 °C and 712 °C. The solid squares indicate data from temperature of 27 °C, and open symbols are data from around 712 °C. The solid lines indicate the third order Birch-Murnaghan equations fitted to the data.

4. International Graduate School
"Structure, Reactivity and Properties of Oxide Materials"

The interdisciplinary Graduate School is funded by the State of Bavaria and it encompasses three cooperating institutes: Bayerisches Geoinstitut (BGI), Institute of Inorganic Chemistry I (LAC), both in Bayreuth, and the Fraunhofer Institute for Silicate Research (ISC) in Würzburg. These institutes provide their research facilities, complementary expertise in basic and applied material research, and commitment to capitalize on synergies as well as international contacts to other leading research institutes all over the world.

The Graduate School is chaired by Prof. David Rubie, Ph.D. (BGI). It includes seven other faculty members and one coordinator. Enrollment in 2005 was 10 doctoral students on a full-time basis at all 3 institutes (BGI, LAC, ISC) and, in addition, 12 doctoral students have associate status in the school which provides them with full access to all educational activities. Research projects include element partitioning between silicate materials and core-forming alloys at high pressures, thermodynamics of mantle phases, hydroxyl defects in minerals, synthesis of new layer silicates and mesoporous oxide substances as well as experimental and computer simulations of solid and liquid substances.

In 2006, four new students have been accepted to the program:

Lutful Arefin since 01.01.2006	*In situ* observations of liquid-phase sintering of zinc oxide Supervisors: F. Raether (ISC), G. Müller (ISC), J. Breu (LAC)
Omar Adjaoud since 15.01.2006	Transport properties of silicate liquids Supervisors: D. Rubie (BGI), G. Steinle-Neumann (BGI), F. Raether (ISC)
Xian-Liang Huang since 01.04.2006	Effects of composition on the sintering behaviour and properties of lead zirconium titanate ceramics Supervisors: F. Raether (ISC), G. Müller (ISC), J. Breu (LAC)
Suresh Kumbar since 02.11.2006	Synthesis of hybrid organic/inorganic zeolite materials Supervisors: J. Breu (LAC), G. Sextl (ISC), H. Keppler (BGI)

New associate students are Micaela Longo (BGI), Olga Narygina (BGI), Zhengning Tang (BGI) and Melanie Stöcker (LAC).

Descriptions of the student projects can be found in Chapter 3 of this report. Students participated in several international short courses: Frontiers in high-pressure research, (Ein-Guedi, Israel), Melts, glasses and magmas (Munich), Density, temperature and elastic constants of Earth's mantle (Munich), and Water in nominally anhydrous minerals (Verbania-Pallanza, Italy). In addition, students presented their research results in publications and at international conferences such as the annual Fall Meeting of the American Geophysical Union (San Francisco, USA), the 13th Meeting of the solid-tate chemistry and materials research group (Aachen), CIMTEC Conference (Acireale, Italy) and the 11th Experimental Mineralogy, Petrology and Geochemistry meeting (Bristol, UK). A list of publications and presentations is given in Chapter 5 of this yearbook.

All students undergo an intensive training program, in addition to their research project, that encompasses lectures, short courses, a research colloquium, a graduate seminar, seminars by invited leading experts and weekend seminars on soft skills such as scientific writing, ethics and team work. Six invited speakers from overseas and Europe presented new results and novel experimental techniques and methods in a series of nine lectures during last year. The following weekend seminars were held in 2006:

Diffusion modeling in earth and material sciences, University of Bayreuth, 03.-06.02.2006

This short course was organized by Prof. Sumit Chakraborty (University of Bochum) and was hosted at the University of Bayreuth. It gave overview of diffusion in solids, macroscopic and microscopic diffusion mechanisms, summary of experimental techniques as well as examples from natural materials. The lecture program was complemented by computer exercises using mathematical packages and Fortran programs.

Chemical industry in southern Bavaria, 26.-27.06.2006

This two-day excursion was guided by Profs. J. Breu (LAC) and G. Sextl (ISC). The site visit at Wacker-Siltronic in Burghausen focused on demonstration of new technical materials and presented synthesis of silicon-based semiconductors. The tour at the Degussa Construction Chemicals in Trostberg aimed at construction materials and testing of their physical and chemical properties. Participants in these site visits included graduate students from the University of Bayreuth, Fraunhofer ISC in Würzburg as well as those from the Advanced Materials and Processes program at the University of Erlangen-Nürnberg.

Communication skills, Verbania (Italy), 29.-30.09.2006

This workshop in Verbania was organized by the Kempkes-Gebhardt company and focused on techniques of professional communication. Participants were introduced to models of communication, conversation techniques, non-verbal aspects, feedback relations, methods of

conflict resolution and team work. This seminar was designed to regularly complement training of graduate students in soft skills.

Graduate students during industrial excursion in June 2006 (DEGUSSA Construction Chemicals, Trostberg)

In addition, faculty members of the graduate school organized three short courses in the last year: Finite element simulations in material sciences (F. Raether, ISC), high pressure crystallography (L. Dubrovinsky, BGI) and water in nominally anhydrous minerals (H. Keppler, BGI).

Detailed information on the Graduate School "Structure, Reactivity and Properties of Oxide Materials" can be found at http://www.uni-bayreuth.de/elitenetzwerk/oxides.

5. Publications, Conference Presentations, Seminars

5.1 Publications (published)

Supplement to **2005** (papers published at the end of 2005):

SHIRYAEV, A.A; IZRAELI, E.S.; HAURI, E.H.; ZAKHARCHENKO, O.D.; NAVON, O. (2005): Chemical, optical and isotopic investigation of fibrous diamonds from Brazil. Russian Geology and Geophysics 46, No. 12, 1207-1222

2006

a) Refereed international journals

AUDÉTAT A.; PETTKE T. (2006): Evolution of a porphyry-Cu mineralized magma system at Santa Rita, New Mexico (USA). Journal of Petrology 47, No. 10, 2021-2046

BESTMANN, M.; RICE, A.H.N.; LANGENHORST, F.; GRASEMANN, B.; HEIDELBACH, F. (2006): Subglacial bedrock welding associated with ice quakes. Journal of the Geological Society 163, 417-420

BOFFA BALLARAN, T.; WOODLAND, A.B. (2006): Local structure of ferric iron-bearing garnets deduced by IR-spectroscopy. Chemical Geology 225, 360-372

BOLFAN-CASANOVA, N.; MCCAMMON, C.A. (2006): Water in transition zone and lower mantle minerals. – In: JACOBSEN, S.; VAN DER LEE, S. (Eds.): Earth's Deep Water Cycle, American Geophysical Union, Washington D.C., 57-68

BROMILEY, G.D.; SHIRYAEV, A.A. (2006): Neutron irradiation and post-irradiation annealing of rutile (TiO_{2-x}): effects on hydrogen incorporation and optical absorption. Physics and Chemistry of Minerals 33(6), 426-425

BROMILEY, G.D.; BROMILEY, F.A. (2006): High-pressure phase transitions and hydrogen incorporation in $MgSiO_3$ enstatite. American Mineralogist 91, 1094-1101

BROMILEY, G.D.; SHIRYAEV, A.A. (2006): Neutron irradiation and post-irradiation annealing of rutile (TiO_{2-x}): effects on hydrogen incorporation and optical absorption. Physics and Chemistry of Minerals 33(6), 426-425

BYSTRICKY, M.; HEIDELBACH, F.; MACKWELL, S.J. (2006): Large-strain deformation and strain partitioning in polyphase rocks: Dislocation creep of olivine-magnesiowüstite aggregates. Tectonophysics 427, 115-132

CHEN, M.; LI, H.; EL GORESY, A.; LIU, J.; XIE, X. (2006): Fracture-related intracrystalline transformation of olivine to ringwoodite in the shocked Sixiangkou meteorite. Meteoritics and Planetary Sciences 41, No. 5, 731-738

COMODI, P.; CERA, F.; DUBROVINSKY, L.S.; NAZARRENI, S. (2006): The high-pressure behaviour of the 10 Å phase: A spectroscopic and diffractometric study up to 42 GPa. Earth and Planetary Science Letters 246, 444-457

DEMOUCHY, S.; JACOBSEN, S.D.; GAILLARD, F.; STERN, C.R. (2006): Rapid magma ascent recorded by water diffusion profiles in mantle olivine. Geology 34, 429-432

DEMOUCHY, S.; MACKWELL, S.J. (2006): Mechanisms of hydrogen incorporation and diffusion in iron-bearing olivine. Physics and Chemistry of Minerals 33, 347-355

DMITRIEV V.P.; DUBROVINSKY, L.S.; LE BIHAN, T.; KUZNETSOV, A.Yu.; WEBER, H.-P.; PONIATOVSKY, E.G. (2006): Collapsed hexagonal-phase in a compressed TiZr alloy: Angle-dispersive synchrotron-radiation X-ray diffraction study. Physical Review B 73, 094114

DOLEJŠ, D.; BAKER, D.R. (2006): Fluorite solubility in hydrous haplogranitic melts at 100 MPa. Chemical Geology 225, 40-60

DOLEJŠ, D.; BAKER, D.R. (2006): Phase transitions and volumetric properties of cryolite, Na_3AlF_6: Differential thermal analysis to 100 MPa. American Mineralogist 91, 97-103

DUBROVINSKAIA, N.A.; ESKA, G.; SHESHIN, G.A.; BRAUN, H. (2006): Superconductivity in polycrystalline boron-doped diamond synthesized at 20 GPa and 2700 K. Journal of Applied Physics 99, 033903

DUBROVINSKAIA, N.A.; DUB, S.; DUBROVINSKY, L.S. (2006): Superior wear resistance of aggregated diamond nanorods. Nano Letters 6(4), 824-826

DUBROVINSKAIA, N.A.; DUBROVINSKY, L.S. (2006): Special issue: Novel Superhard Materials – Guest editors' preface. High Pressure Research, 26, No. 2, 55-60

DUBROVINSKAIA, N.A.; DUBROVINSKY, L.S. (2006): Special issue: Novel Superhard Materials – Introduction. High Pressure Research 26 No. 2, 61-62

DUBROVINSKAIA, N.A.; DUBROVINSKY, L.S.; CRICHTON, W.A.; ZARECHNAYA, E.; ISAEV, E.; ABRIKOSOV, I.A. (2006): Compressibility of B-doped diamond. High Pressure Research 26, No. 2, 79-85

DUBROVINSKAIA, N.A.; DUBROVINSKY, L.S.; MIYAJIMA, N.; LANGENHORST, F.; CRICHTON, W.A.; BRAUN, H.F. (2006): High-pressure high-temperature synthesis and characterization of boron-doped diamond. Zeitschrift für Naturforschung 61b, 1561-1565

DUBROVINSKAIA, N.A.; DUBROVINSKY, L.S.; SOLOZHENKO, V.L. (2006): New bulk superhard semiconducting C-B composite. Proceedings of the Joint 20th AIRAPT – 43rd EHPRG International Conference on High Pressure Science and Technology

DUBROVINSKY, L.S.; DUBROVINSKAIA, N.A.; KANTOR, I.Yu.; NESTOLA, F.; GATTA, G.D. (2006): High-brilliance X-ray system for high-pressure in-house research: Applications for studies of superhard materials. High Pressure Research 26, No. 2, 137-143

FROST, D.J. (2006): The stability of hydrous mantle phases. Reviews in Mineralogy & Geochemistry 62, 243-271

GALADÍ-ENRÍQUEZ, E.; ZULAUF, G.; HEIDELBACH, F.; ROHRMÜLLER, J. (2006): Insights into the deformation history of a dyke-host association showing contrasting rheologies and inconsistent shear-sense indicators: the Saunstein granite dyke (Bavarian Forest, SE Germany, European Variscides). Journal of Structural Geology 28, 1536-1552

GANGULY, J.; FROST, D.J. (2006): Stability of anhydrous phase B: Experimental studies and implications for phase relations in subducting slab and the X discontinuity in the mantle. Journal of Geophysical Research 111, B06203

GATTA, G.D.; NESTOLA, F.; BOFFA BALLARAN, T. (2006): Elastic behavior, phase transition, and pressure induced structural evolution of analcime. American Mineralogist 91, 568-578

GATTA, G.D.; NESTOLA, F.; BOFFA BALLARAN, T. (2006): Elastic behaviour and structural evolution of topaz at high pressure. Physics and Chemistry of Minerals 33, 235-242

GLASMACHER, U.A.; LANG, M.; KEPPLER, H.; LANGENHORST; F.; NEUMANN, R.; SCHARDT, D.; TRAUTMANN, C.; WAGNER, G.A. (2006): Phase transitions in solids stimulated by simultaneous exposure to high pressure and relativistic heavy ions. Physical Review Letters 96, 195701

GOLDIN, T.J.; WÜNNEMANN, K.; MELOSH, H.J.; COLLINS, G.S. (2006): Hydrocode modeling of the Sierra Madera impact structure. Meteoritics and Planetary Science 41, 1947-1958

GOTOU, H.; YAGI, T.; FROST, D.J.; RUBIE, D.C. (2006): Opposed-anvil-type high-pressure and high-temperature apparatus using sintered diamond. Review of Scientific Instruments 77, 035113

GUILLAUME, C.; MORNIROLI, J.P.; FROST, D.J.; SERGHIOU, G. (2006): Synthesis of hexagonal Ni_3N using high pressures and temperatures. Journal of Physics: Condensed Matter 18, 8651-8660

HOLBIG, E.; DUBROVINSKY, L.S.; STEINLE-NEUMANN, G.; PRAKAPENKA, V.; SWAMY, V.: Compression behavior of Zr-doped nanoanatase. Zeitschrift für Naturforschung 61b, 1577-1585

HOLL, C.M.; SMYTH, J.R.; MANGHNANI, M.H.; AMULELE, G.M.; SEKAR, M.; FROST, D.J.; PRAKAPENKA, V.B.; SHEN, G. (2006): Crystal structure and compression of an iron-bearing Phase A to 33 GPa. Physics and Chemistry of Minerals 33, 192-199

KANTOR, A.P.; KANTOR, I.Yu.; DUBROVINSKY, L.S.; KRISCH, M.; BOSSAK, A.; DMITRIEV, V.P.; URUSOV, V. (2006): Measuring the speed of sound in an iron-nickel alloy at high pressure by inelastic X-ray scattering. Doklady Physics 51(11), 584-587

KANTOR, I.Yu.; DUBROVINSKY, L.S.; URUSOV, V. (2006): Spin transitions in ferropericlase under high pressure: Comparison of Mössbauer-spectroscopy and X-ray emission-spectroscopy data. Doklady Physics 51, 229-233

KANTOR, I.Yu.; DUBROVINSKY, L.S.; MCCAMMON, C.A. (2006): Spin crossover in (Mg,Fe)O: A Mössbauer effect study with an alternative interpretation of X-ray emission spectroscopy data. Physical Review B 73, 100101 (Rapid Communications)

KANTOR, I.Yu.; DUBROVINSKY, L.S.; MCCAMMON, C.A.; KANTOR, A.P.; PASCARELLI, S.; AQUILANTI, G.; CRICHTON, W.A.; MATTESINI, M.; AHUJA, R.; ALMEIDA, J.; URUSOV, V. (2006): Pressure-induced phase transition in $Mg_{0.8}Fe_{0.2}O$ ferropericlase. Physics and Chemistry of Minerals 33, 35-44

KEPPLER, H.; BOLFAN-CASANOVA, N. (2006): Thermodynamics of water solubility and partitioning. Reviews in Mineralogy & Geochemistry 62, 193-230

KURNOSOV, A.V.; OGIENKO, A.G.; GORYAINOV, S.V.; LARIONOV, E.G.; MANAKOV, A.Yu.; LIHACHEVA, A.Yu.; ALADKO, E.Ya.; ZHURKO, F.V.; VORONIN, V.I.; BERGER, I.F.; ANCHAROV, A.I. (2006): Phase diagram and high-pressure boundary of hydrate formation in the ethane-water system. The Journal of Physical Chemistry B 110, 21788-21792, doi: 10.1021/jp0636726

KURNOSOV, A.V.; DUBROVINSKY, L.S.; KUZNETSOV, A.Yu.; DMITRIEV, V.P. (2006): High-pressure high-temperature behavior of methane-ammonia-water system up to 3 GPa. Zeitschrift für Naturforschung 61b, 1573-1576

KUZNETSOV, A.Yu.; DE ALMEIDA, J.S.; DUBROVINSKY, L.S.; AHUJA, R.; KWON, S.K.; KANTOR I.Yu.; KANTOR, A.P.; GUIGNOT, N. (2006): High-pressure synthesis and physical properties of an orthorhombic phase of chromium dioxide. Journal of Applied Physics 99 (5), 053909

KUZNETSOV, A.Yu.; PEREIRA, A.S.; SHIRYAEV, A.A.; HAINES, J.; DUBROVINSKY, L.S. (2006): Pressure-induced chemical decomposition and structural changes of boric acid. The Journal of Physical Chemistry B 110, 13858-13865

LEE, K.K.M.; STEINLE-NEUMANN, G. (2006): High-pressure alloying of iron and xenon: 'Missing' Xe in the Earth's core? Journal of Geophysical Research 111, B02202, doi: 10.1029/2005JB003781

MACKENZIE, K.J.D.; TEMUUJIN, J.; MCCAMMON, C.A.; SENNA, M. (2006): Mechanochemical activation of wolframite, $FeWO_4$, studied by ^{57}Fe Mössbauer spectroscopy. Journal of the European Ceramic Society 26, 2581-2585

MANN, U.; MARKS, M.; MARKL, G. (2006): Influence of oxygen fugacity on mineral compositions in peralkaline melts: The Katzenbuckel volcano, Southwest Germany. Lithos 91, 262-285

MASHIKINA, E.; MAGERL, A.; OLLIVIER, J.; GOEBBELS, M.; SEIFERT, F. (2006): Oxygen mobility in the perovskite $SrTi_{1-x}Fe_xO_{3-\delta}$ (x=0.8). Physical Review B 74, 214106

MCCALLUM, I.S.; DOMENEGHETTI, M.C.; SCHWARTZ, J.M.; MULLEN, E.K.; ZEMA, M.; CÁMARA, F.; MCCAMMON, C.A.; GANGULY, J. (2006): Cooling history of lunar Mg-suite gabbronorite 76255, troctolite 76535 and Stillwater pyroxenite SC-936: The record in exsolution and ordering in pyroxenes. Geochimica et Cosmochimica Acta 70, 6068-6078

MCCAMMON, C.A. (2006): Microscopic properties to macroscopic behaviour: The influence of iron electronic state. Journal of Mineralogical and Petrological Sciences 101, 130-144

MECKLENBURGH, J.; ZHAO, Y.-H.; HEIDELBACH, F.; MACKWELL, S.J. (2006): Deformation of olivine-spinel aggregates in the system $(Mg,Ni)_2GeO_4$ deformed to high-strain in torsion: Implications for upper mantle anisotropy. Journal of Geophysical Research 111, B11209, doi: 10.1029/2006JB004285

MIYAJIMA, N.; OHGUSHI, K.; ICHIHARA, M.; YAGI, T. (2006): Crystal morphology and dislocation microstructures of $CaIrO_3$. A TEM study of an analogue of the $MgSiO_3$ post-perovskite phase. Geophysical Research Letters 33, L12302, doi: 10.1029/2005GL025001

NESTOLA, F.; BOFFA BALLARAN, T.; LIEBSKE, C.; BRUNO, M.; TRIBAUDINO, M. (2006): High-pressure behaviour along the jadeite $NaAlSi_2O_6$ – aegirine $NaFeSi_2O_6$ solid solution up to 10 GPa. Physics and Chemistry of Minerals 33, 417-425

NESTOLA, F.; GATTA, G.D.; BOFFA BALLARAN, T. (2006): The effect of Ca substitution on the elastic and structural behavior of orthoenstatite. American Mineralogist 91, 809-815

O'NEILL, H.S.C.; BERRY, A.J.; MCCAMMON, C.A.; JAYASURIYA, K.D.; CAMPBELL, S.J.; FORAN, G. (2006): An experimental determination of the effect of pressure on the $Fe^{3+}/\Sigma Fe$ ratio of an anhydrous silicate melt to 3.0 GPa. American Mineralogist 91, 404-412

PISTORINO, M.; NESTOLA, F.; BOFFA BALLARAN, T.; DOMENEGHETTI, M.C. (2006): The effect of composition and cation ordering on the compressibility of columbites up to 7 GPa. Physics and Chemistry of Minerals 33, 593-600

POE, B.T.; ROMANO, C.; LIEBSKE, C.; RUBIE, D.C.; TERASAKI, H.; SUZUKI, A.; FUNAKOSHI, K. (2006): High-temperature viscosity measurements of hydrous albite liquid using *in situ* falling-sphere viscometry at 2.5 GPa. Chemical Geology 229, 2-9

RICHTER, A.; SMITH, R.; DUBROVINSKAIA, N.A.; MCGEE, E. (2006): Mechanical properties of superhard materials synthesised at various P-T conditions investigated by nanoindentation. High Pressure Research 26, No. 2, 99-109

ROBINSON, P.; HEIDELBACH, F.; HIRT, A.; MCENROE, S.A.; BROWN, L.L. (2006): Crystallographic-magnetic correlations in single crystal hemo-ilmenite: New evidence for lamellar magnetism. Geophysical Journal International 165, 17-31

ROMANO, C.; POE, B.T.; KREIDIE, N.; MCCAMMON, C.A. (2006): Electrical conductivities of pyrope-almandine garnets up to 19 GPa and 1700 °C. American Mineralogist 91, 1371-1377

ROUQUETTE, J.; HAINES, J.; BORNAND, V.; PINTARD, M.; PAPET, Ph.; SAUVAJOL, J.L. (2006): Use of resonance Raman spectroscopy to study the phase diagram of $PbZr_{0.52}Ti_{0.48}O_3$. Physical Review B 73, 224118

ROUQUETTE, J.; HAINES, J.; BORNAND, V.; PINTARD, M.; PAPET, PH. (2006): Piezo-ferroelectrics: Pressure-induced phase transition in $Pb(Zr_{1-x}Ti_x)O_3$ (PZT). – In: GRZECHNIK, A. (Ed.): Pressure-Induced Phase Transitions, Research Signpost/ Transworld Research Network

SHAW, C.S.J.; HEIDELBACH, F.; DINGWELL, D.B. (2006): Origin and evolution of reaction textures in mantle peridotite xenoliths from Sal Island, Cape Verde. Contributions to Mineralogy and Petrology 151, 681-697

SHCHEKA, S.S.; WIEDENBECK, M.; FROST, D.J.; KEPPLER, H. (2006): Carbon solubility in mantle minerals. Earth and Planetary Science Letters 245, 730-742

SHIRYAEV, A.A.; IAKOUBOVSKII, K.; GRAMBOLE, D.; DUBROVINSKAIA, N.A. (2006): Spectroscopic study of defects and inclusions in bulk poly- and nanocrystalline diamond aggregates. Journal of Physics: Condensed Matter 18, L493-L501

SMYTH, J.R.; FROST, D.J.; NESTOLA, F.; HOLL, C.M.; BROMILEY, G.D. (2006): Olivine hydration in the deep upper mantle: Effects of temperature and silica activity. Geophysical Research Letters 33, L15301

SOLOZHENKO, V.L.; KURAKEVYCH, O.O.; DUBROVINSKAIA, N.A.; DUBROVINSKY, L.S. (2006): Synthesis of superhard composites in the B-C system. Journal of Superhard Materials 5, 3-8

SWAMY, V.; MENZIES, D.; MUDDLE, B.C.; KUZNETZOV, A.; DUBROVINSKY, L.S.; DAI, Q.; DMITRIEV, V.P. (2006): Nonlinear size dependence of anatase TiO_2 lattice parameters. Applied Physics Letters 88, 243103

SWAMY, V.; KUZNETSOV, A.Yu.; DUBROVINSKY, L.S.; MCMILLAN, P.F.; PRAKAPENKA, V.B.; SHEN, G.; MUDDLE, B.C. (2006): Size-dependent pressure-induced amorphization in nanoscale TiO_2. Physical Review Letters 96, 135702

TALYZIN, A.V.; DZWILEWSKI, A.; SUNDQVIST, B.; TSYBIN, Y.; MARSHALL, A.G.; PURCELL, J.M.; SHULGA, Y.; MCCAMMON, C.A.; DUBROVINSKY, L.S. (2006): Hydrogenation of C_{60} at 2 GPa pressure and high temperature. Chemical Physics 325, 445-451

TERRY, M.P. HEIDELBACH, F. (2006): Deformation-enhanced metamorphic reactions and the rheology of high-pressure shear zones in the Western Gneiss Region, Norway. Journal of Metamorphic Geology 24, 3-18

TEXIER, M.; CORDIER, P. (2006): TEM characterization of dislocations and slip systems in stishovite deformed at 14 GPa, 1,300 °C in the multianvil apparatus. Physics and Chemistry of Minerals 33, 394-402

WESTRAADT, J.E.; NEETHLING, J.H.; DUBROVINSKAIA, N.A.; SIGALAS, I. (2006): Characterization of the microstructure of thermally stable polycrystalline diamond sintered with calcium carbonate. Proceedings of the Microscopy Society of South Africa 36, 35

b) Monographs

KEPPLER, H.; SMYTH, J.R. (2006): Water in Nominally Anhydrous Minerals. Reviews in Mineralogy and Geochemistry 62, 478 pp.

5.2 Publications (submitted, in press)

ASAHARA, Y.; FROST, D.J.; RUBIE, D.C.: Partitioning of FeO between magnesiowüstite and liquid iron at high pressures and temperatures: Implications for the composition of the Earth's outer core. Earth and Planetary Science Letters (submitted)

BERGESE, P.; ALESSANDRI, I.; BONTEMPI, E.; DEPERO, L.E.; ARONNE, A.; FANELLI, E.; PERNICE, P.; BOFFA BALLARAN, T.; MIYAJIMA, N.; SIGAEV, V.N.: Phase transformations in potassium niobiosilicate glasses. Journal of Physics and Chemistry B (in press)

BROMILEY, F.; BOFFA BALLARAN, T.; LANGENHORST, F.; SEIFERT, F.: Order and miscibility in the otavite – magnesite solid solution. American Mineralogist (submitted)

BROMILEY, F.; BOFFA BALLARAN, T.; ZHANG, M.: An infrared investigation of the otavite – magnesite solid solution. American Mineralogist (submitted)

CARACAS, R.; HEMLEY, R.J.: Theoretical determination of precursor phases for polymeric nitrogen. Physical Review Letters (submitted)

CARTER-STIGLITZ, B.; MCENROE, S.; HARRISON, R.; ROBINSON, P.; MCCAMMON, C.A.: Nature's engineering: Giant exchange bias (> 1 T) in a natural mineral. Nature Nanotechnology (submitted)

CORGNE, A.; KESHAV, S.; FEI, Y.; MCDONOUGH, W.F.: How much potassium is in the Earth's core? New insights from new partitioning experiments. Earth and Planetary Science Letters (submitted)

DOLEJŠ, D.; BAKER, D.R.: Liquidus equilibria in the system K_2O-Na_2O-Al_2O_3-SiO_2-F_2O_{-1}-H_2O to 100 MPa: I. Silicate-fluoride liquid immiscibility in anhydrous systems. Journal of Petrology (in press)

DOLEJŠ, D.; BAKER, D.R.: Liquidus equilibria in the system K_2O-Na_2O-Al_2O_3-SiO_2-F_2O_{-1}-H_2O to 100 MPa: II. Differentiation paths of fluorosilicic magmas in hydrous systems. Journal of Petrology (in press)

DUBROVINSKAIA, N.A.; DUBROVINSKY, L.S.: Melting of Ice VII and new high-pressure high-temperature amorphous ice. – In: Ohtani, E. (Ed.): "GSA monograph" (in press)

DUC-TIN, Q.; AUDÉTAT, A.; KEPPLER, H.: Solubility of tin in (Cl,F)-bearing aqueous fluids at 700 °C, 140 MPa: a LA-ICP-MS study of synthetic fluid inclusions. Geochimica et Cosmochimica Acta (submitted)

EECKHOUT, S.G.; BOLFAN-CASANOVA, N.; MCCAMMON, C.A.; KLEMME, S.; AMIGUET, E.: XANES study of the oxidation state of Cr in lower mantle phases: periclase and magnesium silicate perovskite. American Mineralogist (in press)

EIMER, B.C.; KIEFER, B.; STEINLE-NEUMANN, G.: Elasticity and magnetism of hexagonal iron at pressures below a megabar. Physical Review B (submitted)

EL GORESY, A.; DERA, P.; SHARP, T.G.; PREWITT, C.T.; CHEN, M.; DUBROVINSKY, L.S.; WOPENKA, B.; BOCTOR, N.Z.; HEMLEY, R.J.: Seifertite, a new dense orthorhombic polymorph of silica from the Martian meteorites Shergotty and Zagami. European Journal of Mineralogy (submitted)

FROST, D.J.; DOLEJŠ, D.: Experimental determination of the effect of H_2O on the 410-km seismic discontinuity. Earth and Planetary Science Letters (in press)

GILLET, Ph.; EL GORESY, A.; BECK, P.; CHEN, M.: High-pressure mineral assemblages in shocked meteorites and shocked terrestrial rocks: Mechanisms of phase transformations and constraints to pressure and temperature histories. GSA Special Paper (in press)

HOLBIG, E.; BOCKMEYER, M.; DUBROVINSKY, L.S.; LÖBMANN, P.: Sol-gel synthesis of amorphous and nanocrystalline ZrO_2-TiO_2 powders. Journal of Alloys and Compounds (submitted)

HOLZAPFEL, C.; CHAKRABORTY, S.; RUBIE, D.C.; FROST, D.J.: Effect of pressure on Fe-Mg, Ni and Mn diffusion in $(Fe_xMg_{1-x})SiO_4$ olivine. Physics of the Earth and Planetary Interiors (submitted)

KANTOR, A.P.; KANTOR, I.Yu.; KURNOSOV, A.V.; KUZNETSOV, A.Yu.; DUBROVINSKAIA, N.A.; KRISCH, M.; BOSSAK, A.A.; DMITRIEV, V.P.; URUSOV, V.S.; DUBROVINSKY, L.S.: Sound wave velocities of *fcc* Fe-Ni alloy at high pressure and temperature by mean of inelastic X-ray scattering. Earth and Planetary Science Letters (submitted)

KANTOR, I.Yu.; DUBROVINSKY, L.S.; MCCAMMON, C.A.; DUBROVINSKAIA, N.A.; GONCHARENKO, I.; KANTOR, A.P.; KUZNETSOV, A.Yu.; CRICHTON, W.A.: FeO and MnO high-pressure phase diagrams: relations between structural and magnetic properties. Phase Transitions, Special Issue (in press)

KANTOR, I.Yu.; KANTOR, A.P.; DUBROVINSKY, L.S.; MCCAMMON, C.A.: High-pressure phase transformations in the system FeO-MgO. High Pressure Mineral Physics (in press)

KEPPLER, H.; KANTOR, I.Yu.; DUBROVINSKY, L.S.: Optical absorption spectra of ferropericlase to 84 GPa. American Mineralogist (in press)

KESHAV, S.; SEN, G.; PRESNALL, D.C.: Garnet-bearing xenoliths from Salt Lake Crater, Oahu, Hawaii: High-pressure fractional crystallization in the oceanic mantle. Journal of Petrology (submitted)

KONRAD-SCHMOLCKE, M.; O'BRIEN, P-J.; HEIDELBACH, F.: Compositional re-equilibration of garnet: the importance of sub-grain boundaries. Geology (submitted)

KURNOSOV, A.V.; DUBROVINSKY, L.S.; KUZNETSOV, A.Yu.; DMITRIEV, V.P.: High-pressure melting curve of methane hydrates and implication to Titan's interior. Earth and Planetary Science Letters (submitted)

KUZNETSOV, A.Yu.; DMITRIEV, V.P.; VOLKOVA, Y.; KURNOSOV, A.V.; DUBROVINSKY, L.S.: *In situ* combined X-ray diffraction and electrical resistance measurements of Pr and $Fe_{0.8}Ni_{0.2}$ alloy at high pressures and temperatures. Review of Scientific Instruments (submitted)

LEE, K.K.M.; STEINLE-NEUMANN, G.: Ab-initio predictions of pressure- and chemistry-dependent electron-capture radioactive decay of ^{7}Be, ^{22}Na and ^{40}K in crystalline materials. Physical Review B (submitted)

LIU, L.-G.; EL GORESY, A.: High-Pressure phase transitions of the feldspars and further characterization of lingunite. International Geology Review (in press)

MACHEK, M.; ŠPAČEK, P.; ULRICH, S.; HEIDELBACH, F.: Origin and orientation of microporosity in eclogites of different microstructure. Engineering Geology (submitted)

MARKS, M.A.; RUDNICK, R.L.; MCCAMMON, C.A.; VENNEMANND, T.; MARKL, G.: The behavior of Li and its isotopes during igneous fractionation: A case study from the peralkaline Ilímaussaq igneous complex, south Greenland. Geochimica et Cosmochimica Acta (submitted)

MIERDEL, K.; KEPPLER, H.; SMYTH, J.R.; LANGENHORST, F.: Water solubility in aluminous orthopyroxene and the origin of Earth's asthenosphere. Science (in press)

MIYAJIMA, N.; EL GORESY, A.; DUPAS-BRUZEK, C.; SEIFERT, F.; RUBIE, D.C.; CHEN, M.; XIE, X.: Ferric iron in Al-bearing akimotoite coexisting with iron-nickel metal in a shocked L-6 chondrite. American Mineralogist (submitted)

MLYNARCZYK, M.S.J.; WILLIAMS-JONES, A.E.; DOLEJŠ, D.: Geology and geochemistry of alteration at the San Rafael Sn-Cu deposit, SE Peru. Economic Geology (submitted)

PERRILAT, J.-P.; DANIEL, I.; MOSTEFAOUI, S.; EL GORESY, A.; BOHN, M.; FROST, D.J.: A novel method for chemical analysis of very small synthetic ultrahigh-pressure samples: a NanoSIMS study. Geochemistry Geophysics Geosystems (submitted)

PIAZZONI, A.S.; STEINLE-NEUMANN, G.; BUNGE, H.-P.; DOLEJŠ, D.: A mineralogical model for density and elasticity of the Earth's mantle. G-Cubed (submitted)

PRESNALL, D.C.; GUDFINNSSON, G.H.: Global Na8-Fe8 systematics of MORBs: Implications for mantle heterogeneity, temperature, and plumes. Journal of Petrology (submitted)

QIN, S.; LI, Y.; SEIFERT, F.: Phase transitions in A-site substituted perovskite compounds: The $Ca_{1-2x}Na_xLa_xTiO_3$ ($0<x<0.5$) solid solution. Journal of Solid State Chemistry (in press)

QUACH-DUC, T.; AUDÉTAT, A.; KEPPLER, H.: Solubility of tin in (Cl, F)-bearing aqueous fluids at 700 °C, 140 MPa: a LA-ICP-MS study on synthetic fluid inclusions. Geochimica et Cosmochimica Acta (submitted)

ROUQUETTE, J.; KANTOR, I.Yu.; MCCAMMON, C.A.; DUBROVINSKY, L.S.: Pressure-induced spin transition in $Mg_{1.8}Fe_{0.2}SiO_4$ olivine. Physical Review B, Rapid Communications (submitted)

RUBIE, D.C.; NIMMO, F.; MELOSH, H.J.: Formation of the Earth's core. Treatise on Geophysics, Elsevier (in press)

SHIRYAEV, A.A.; FROST, D.J.; LANGENHORST, F.: Impurity diffusion and microstructure in diamonds deformed at high pressures and temperatures. Diamond & Related Materials (in press)

SHIRYAEV, A.A.; GRAMBOLE, D.; RIVERA, A.; HERRMANN, F.: On the interaction of molecular hydrogen with diamonds: an experimental study using nuclear probes and thermal desorption. Diamond & Related Materials (accepted)

STEINBERGER, B.: Effect of latent heat release at phase boundaries on flow in the Earth's mantle, phase boundary topography and dynamic topography at the Earth's surface. Physics of the Earth and Planetary Interiors (submitted)

STOYANOV, E.; LANGENHORST, F.; STEINLE-NEUMANN, G.: The effect of valence state and site geometry on Ti $L_{3,2}$ and O K electron energy-loss spectra of Ti_xO_y phases American Mineralogist (in press)

TALYZIN, A.V.; ANDERSSON, O.; SUNDQVIST, B.; KURNOSOV, A.V.; DUBROVINSKY, L.S.: High pressure phase transition in $LiBH_4$. Journal of Solid State Chemistry (in press)

TERASAKI, H.; FROST, D.J.; RUBIE, D.C.; LANGENHORST, F.: Percolative core formation in planetesimals. Earth and Planetary Science Letters (submitted)

TERASAKI, H.; FROST, D.J.; RUBIE, D.C.; LANGENHORST, F.: The interconnectivity of Fe-O-S liquid in polycrystalline silicate perovskite at lower mantle conditions. Physics of the Earth and Planetary Interiors (in press)

TERRY, M.P.; HEIDELBACH, F.; COUVY, H.; BROMILEY, G.D.; CARSWELL, D.A.: Deformation and metamorphism of the Kvalvika peridotite, Norway: Conditions and timing for olivine c-slip and exhumation at ultrahigh pressure. Journal of Metamorphic Petrology (submitted)

WALKER, A.M.; DEMOUCHY, S.; WRIGHT, K.: Computer modelling of the energies and vibrational properties of hydroxyl groups in α- and β-Mg_2SiO_4. European Journal of Mineralogy (in press)

WALTE, N.P.; BECKER, J.K.; BONS, P.D.; RUBIE, D.C.: Liquid-distribution and attainment of textural equilibrium in a partially-molten crystalline system with a high-dihedral-angle liquid phase. Earth and Planetary Science Letters (submitted)

WENZEL, M.J.; STEINLE-NEUMANN, G.: Nonequivalence of the octahedral sites of cubic Fe_3O_4 magnetite. Physical Review B (submitted)

ZARECHNAYA, E.Yu.; ISAEV, E.I.; SIMAK, S.I.; VEKILOV, Yu.Kh.; DUBROVINSKY, L.S.; DUBROVINSKAIA, N.A.; ABRIKOSOV, I.A.: Ground state properties of boron-doped diamond. Physical Review B (submitted)

5.3 Presentations at scientific institutions and at congresses

ASAHARA, Y.; RUBIE, D.C.; FROST, D.J.; LANGENHORST, F.: 13.-17.03.2006, 37th Lunar and Planetary Science Conference, Houston, USA: "Oxygen solubility in liquid iron and consequences for the early differentiation of Earth and Mars", Abstract No. 1162

ASAHARA, Y.; FROST, D.J.; RUBIE, D.C.: 23.-28.07.2006, 19th General Meeting of the International Mineralogical Association (IMA), Kobe, Japan: "The effects of pressure and temperature on the solubility of oxygen in liquid iron and implications for the composition of the Earth's core", Abstract No. 005-15

ASAHARA, Y.; FROST, D.J.; RUBIE, D.C.; LANGENHORST, F.: 13.-15.08.2006, Joined Workshop of the 'Interior – Early Evolution – Core Formation' and 'SNC Meteorite' Groups, Max-Planck-Institut für Chemie, Mainz, Germany: "Oxygen solubility in molten iron during terrestrial planet core formation"

ASAHARA, Y.; RUBIE, D.C.; DUBROVINSKY, L.S.; MIYAJIMA, N.; FROST, D.J.; HOLZAPFEL, C.: 09.-11.11.2006, the 47th Meeting of the Japan Society of High Pressure Science and Technology, Kumamoto, Japan: "Oxygen solubility in liquid Fe at high pressures and high temperatures: Result from combined techniques of focused ion beam milling and transmission electron microscopy", Special Issue of the Review of High Pressure Science and Technology 16, 257, 2006

ASAHARA, Y.; RUBIE, D.C.; FROST, D.J.: 08.-10.12.2006, Workshop on Early Planetary Differentiation, Sonoma County, California, USA: "Partitioning of oxygen between magnesiowüstite and liquid iron: consequences for the early differentiation of terrestrial planets"

AUDÉTAT, A.; KEPPLER, H.: 24.05.2006, GEO-Kurs 2006, Universität Konstanz, Germany: "Fluide im Erdinnern"

AUDÉTAT, A.; PETTKE, T.; HEINRICH, C.A.: 23.-28.07.2006, 19th General Meeting of the International Mineralogical Association (IMA), Kobe, Japan: "The magmatic-hydrothermal transition in barren vs. mineralized intrusions", Abstract No. 90464

AUDÉTAT, A.; KEPPLER, H.: 23.-28.07.2006, 19th General Meeting of the International Mineralogical Association (IMA), Kobe, Japan: "Physical and chemical properties of subduction zone fluids - direct insights by experiments in the hydrothermal diamond anvil cell", Abstract No. 90467

AUDÉTAT, A.; PETTKE, T.: 23.-28.07.2006, 19th General Meeting of the International Mineralogical Association (IMA), Kobe, Japan: "Evolution of sulfur and copper in the magmas associated with porphyry-Cu mineralization at Santa Rita, New Mexico (U.S.A.)", Abstract No. 90427

AUDÉTAT, A.; PETTKE, T.: 25.-27.09.2006, 84. Jahrestagung der DMG, Hannover, Germany[*2]: "Evolution of sulfur and copper in the porphyry-Cu mineralized magma system at Santa Rita, New Mexico (U.S.A.)", Beihefte zum European Journal of Mineralogy 18, 10

BALI, E.; BOLFAN-CASANOVA, N.; KOGA, K.: 01.-04.10.2006, MSA Short course, Verbania, Italy[*3]: "Pressure and temperature dependence of water solubility in forsterite"

BOFFA BALLARAN, T.; BALIC-ZUNIC, T.; NESTOLA, F.; STALDER, R.: 11.-13.09.2006, EMPG XI, Bristol, U.K.[*1]: "The effect of Al and water substitution on the high-pressure behaviour of orthoenstatite", Abstract Volume, 9, 2006

BOLFAN-CASANOVA, N.; MCCAMMON, C.A.; MACKWELL, S.J.: 01.-04.10.2006, MSA Short course, Verbania, Italy[*3]: "Incorporation of water in ferropericlase as a function of pressure, temperature and composition"

BROMILEY, G.D.; BROMILEY, F.A.; BROMILEY, D.W.; SHIRYAEV, A.A.: 11.-13.09.2006, EMPG XI, Bristol, U.K.[*1]: "Water incorporation in stishovite", Abstract Volume, 12, 2006

BUNGE, H.-P.; PIAZZONI, A.S.; STEINLE-NEUMANN, G.: 11.-15.12.2006, AGU Fall Meeting, San Francisco, USA[*4]: "Fully resolved global mantle convection models", EOS Trans. AGU, 87(52), Fall Meet. Suppl., Abstract MR53A-0976, 2006

BYSTRICKY, M.; HEIDELBACH, F.; MACKWELL, S.J.: 11.-13.09.2006, EMPG XI, Bristol, U.K.[*1]: "Large-strain deformation and strain partitioning in polyphase rocks: Dislocation creep of olivine-magnesiowüstite aggregates", Abstract Volume, 12, 2006

CARICCHI, L.; ARDIA, P.; BURLINI, L.; ULMER, P.; MCCAMMON, C.A.; GERYA, T.: 02.-07.04.2006, EGU General Assembly 2006, Vienna, Austria: "Viscoscities of hydrous andesite and the effect of crystals on the rheology and relative viscosity of magmas: An experimental study"

CARICCHI, L.; BURLINI, L.; ULMER, P.; GERYA, T.; MCCAMMON, C.A.; POTUZAK, M.: 11.-13.09.2006, EMPG XI, Bristol, U.K.[*1]: "Viscoscities of hydrous andesite and rheology of crystal-bearing magmas"

COMODI, P.; CERA, F.; DUBROVINSKY, L.S.; NAZZARENI, S.: 11.-13.09.2006, EMPG XI, Bristol, U.K.[*1]: "The behaviour of 10 Å phase under H*T*-H*P* condition", Abstract Volume, 16, 2006

CORGNE, A.; KESHAV, S.; FEI, Y.; MCDONOUGH, W.F.: 27.08.-01.09.2006, 16th Annual V.M. Goldschmidt Conference, Melbourne, Australia: "How much potassium in the Earth's core? Insights from experimental petrology"

COUVY, H.; WEIDNER, D.; FROST, D.J.; CHEN, J.: 11.-13.09.2006, EMPG XI, Bristol, U.K.[*1]: "Relative strength of olivine and wadsleyite using Mn_2GeO_4 structural analog", Abstract Volume, 18, 2006

DE CARLI, P.S.; EL GORESY, A.; XIE, Z.; SHARP, T.G.: 11.-15.12.2006, AGU Fall Meeting, San Francisco, USA[*4]: "On the concordance of static high pressure phase transformation data on minerals with shock wave data", EOS Trans. AGU, 87(52), Fall Meet. Suppl., Abstract MR53D-08, 2006

DOBSON, D.P.; WOOD, I.G.; VOČADLO, L.; KNIGHT, K.S.; KOCKELMANN, W.; MCCAMMON, C.A.: 25.-27.10.2006, Humboldt-Kolleg 'Ferroics' Cambridge, U.K.: "The ground-state structure of $Fe_{0.98}O$"

DOBSON, D.; DE RONDE, A.; HEIDELBACH, F.; MEREDITH, P.; BOON, S.: 11.-15.12.2006, AGU Fall Meeting, San Francisco, USA[*4]: "Fault reactivation during the olivine to wadsleyite transition: A mechanism for deep focus earthquakes", EOS Trans. AGU, 87(52), Fall Meet. Suppl., Abstract MR24A-08, 2006

DOLEJŠ, D.: 11.-13.09.2006, EMPG XI, Bristol, U.K.[*1]: "Quartz solubility and complex formation in fluorine-bearing aqueous fluids: Key to the origin of silicothermal gels", Abstract Volume, 22, 2006

DOLEJŠ, D.: 11.-13.09.2006, EMPG XI, Bristol, U.K.[*1]: "Thermodynamics of chlorine in silicic melts: Implications for magmatic devolatilization and fluid composition", Abstract Volume, 23, 2006

DOLEJŠ, D.: 07.11.2006, Institut für Mineralogie, Universität Münster, Germany: "Chemical mass transfer in magmatic and hydrothermal systems: Insights from experiments and thermodynamic models"

DUBROVINSKAIA, N.A.; DUBROVINSKY, L.S.: 20.01.2006, "Leitz GmbH", Oberkochen, Germany: "Prospective applications of nanocrystalline materials as superabrasives"

DUBROVINSKAIA, N.A.; DUBROVINSKY, L.S.: 20.02.2006 Institute for Superhard Materials of the National Academy of Sciences of Ukraine, Kiev, Ukraine *(invited)*: "Synthesis and characterization of heavily B-doped diamonds and aggregated diamond nanorods"

DUBROVINSKAIA, N.A.: 23.02.2006, Laboratory of Crystallography, Physics Department, Universität Bayreuth: "High pressure- high temperature synthesis and X-ray characterization of various materials in the B-C system"

DUBROVINSKAIA, N.A.: 28.-30.03.2006, 'Synthesis Design and Function in New Materials Chemistry' Meeting sponsored by the Royal Society of Chemistry (Solid State Chemistry group), London, U.K. *(invited)*: "Synthesis and characterisation of new functional materials in the B-C system"

DUBROVINSKAIA, N.A.; DUBROVINSKY, L.S.: 26.04.2006, University of the Witwatersrand, Johannesburg, South Africa *(invited)*: "Novel nanocrystalline materials: their properties and prospective applications"

DUBROVINSKAIA, N.A.: 27.07.2006, Laboratory of Crystallography, Physics Department, Universität Bayreuth, Germany: "Applied nanoscience: aggregated BN nanocomposite (ABNNC) with superior mechanical properties"

DUBROVINSKAIA, N.A.; DUBROVINSKY, L.S.; MIYAJIMA, N.; KANTOR, A.P.: 03.-08.09.2006, 3rd International Workshop on Spinel-Nitrides and Related Materials, Rüdesheim am Rhein, Germany *(invited)*: "Superhard BN nanocomposites: synthesis and characterization"

DUBROVINSKAIA, N.A.; DUBROVINSKY, L.S.; MIYAJIMA, N.; KANTOR, A.P.; SOLOZHENKO, V.L.; KURAKEVYCH, O.O.; RICHTER, A.; DMITRIEV, V.P.: 17.-20.09.2006, International Specialized Workshop 'BN 2006 - Sinaia', Sinaia, Romania *(invited)*: "Synthesis and characterisation of bulk samples of nanocrystalline cBN with superior mechanical properties"

DUBROVINSKAIA, N.A.; DUBROVINSKY, L.S.: 09.11.2006, Institute of Materials Physics, University of Linköping, Sweden *(invited)*: "Enigmas of nanocrystalline matter: High pressure synthesis and characterization of nano-diamond and nano-boron nitride with superior mechanical properties"

DUBROVINSKAIA, N.A.; DUBROVINSKY, L.S.: 10.11.2006, SANDVIK AB, Stockholm, Sweden *(invited)*: "Prospective applications of novel superhard materials"

DUBROVINSKY, L.S.: 03.-08.09.2006, 3rd International Workshop on Spinel-Nitrides and Related Materials, Rüdesheim am Rhein, Germany *(invited)*: "High pressure synthesis and physical properties of chromium dioxide and oxynitride"

DUBROVINSKY, L.S.; DUBROVINSKAIA, N.A.; PAPAGEORGIOU, T.; BRAUN, H.F.: 17.-20.09.2006, International Specialized Workshop 'BN 2006 - Sinaia', Sinaia, Romania *(keynote lecture)*: "Bulk boron-doped diamonds: new developments"

EL GORESY, A.: 03.-05.08.2006, Workshop on Desert Meteorites, Casablanca, Morocco: "Native copper in Fe/Ni metal and the assemblage chromite-plagioclase in ordinary chondrites: Discarded as shock parameters"

EL GORESY, A.; FERROIR, T.; GILLET, P.; DUBROVINSKY, L.S.; CHEN, M.; SIMIONOVICI, A.: 06.-11.08.2006, 69th Annual Meeting of the Meteoritical Society, Zürich, Switzerland: "Intracrystalline and grain-boundary olivine-ringwoodite (-wadsleyite) phase transitions in shocked L6-chondrites: Evidence for diffusion controlled phase transition mechanisms involving Fe and Mn"

EL GORESY, A.: 11.-15.12.2006, AGU Fall Meeting, San Francisco, USA[*4] *(invited)*: "Olivine to ringwoodite and wadsleyte phase transformation mechanisms in naturally shocked chondritic meteorites: Clues to incoherent, coherent growths and retrograde transitions", EOS Trans. AGU, 87(52), Fall Meet. Suppl., Abstract MR54A-08, 2006

FERROIR, T.; BECK, P.; GILLET, P.; SIMIONOVICI, A.; BOHN, M.; DUBROVINSKY, L.S.; EL GORESY, A.: 11.-15.12.2006, AGU Fall Meeting, San Francisco, USA[*4]: "Polycrystalline and intracrystalline growth of akimotoite in clinoenstatite of the L-6 tenham chondrite", EOS Trans. AGU, 87(52), Fall Meet. Suppl., Abstract MR54A-06, 2006

FROST, D.J.: 01.02.2006, Institut für Geologie, Mineralogie und Geophysik, Ruhr-Universität, Bochum, Germany: "Interpreting mantle seismic discontinuities through high pressure experiments"

FROST, D.J.; SAIKIA A.: 19.04.2006, Department of Earth Sciences, University of Bristol, England: "Clues to the compositional and thermal structure of the Earth's mantle from the experimental interpretation of mantle seismic discontinuities"

FROST, D.J.: 23.-28.07.2006, 19th General Meeting of the International Mineralogical Association (IMA), Kobe, Japan: "The effect of water content and oxygen fugacity on the olivine to wadsleyite transformation"

FROST, D.J.: 01.-04.10.2006, MSA Short course, Verbania, Italy[*3] *(invited)*: "The stability of hydrous mantle phases", Reviews in Mineralogy and Geochemistry 62, 243-271

FROST, D.J.; SAIKIA A.: 19.09.2006, Bavarian Academy of Science Workshop on 'Temperature, Density and Elastic Constants in the Mantle', Munich, Germany: "The effect of bulk composition on phase transformations of mantle minerals"

FROST, D.J.: 22.-26.10.2006, MSA Awardee Lecture at the Geological Society of America Annual Meeting GSA 2006, Philadelphia, USA: "Calibrating the effect of water on seismic discontinuities in the Earth's mantle"

FROST, D.J.: 11.-15.12.2006, AGU Fall Meeting, San Francisco, USA[*4]: "C-O-H fluid processes at the 410 km seismic discontinuity", EOS Trans. AGU, 87(52), Fall Meet. Suppl., Abstract MR21D-05, 2006

GAVRILENKO, P.; KEPPLER, H.: 01.-04.10.2006, MSA Short course, Verbania, Italy[*3]: "Water solubility in pure diopside"

GAVRILENKO, P.; BOFFA BALLARAN, T.; KEPPLER, H.: 01.-04.10.2006, MSA Short course, Verbania, Italy[*3]: "The compressibility of water-saturated diopside"

GOLDIN, T.J.; MELOSH, H.J.: 08.-14.06.2006, 'Impact craters as indicators for planetary environmental evolution and astrobiology' Meeting, Östersund, Sweden: "Interactions between impact ejecta and the atmosphere: Implications for Chicxulub"

GOLDIN, T.J.; MELOSH, H.J.: 06.-11.08.2006, 69th Annual Meeting of the Meteoritical Society, Zürich, Switzerland: "Effects of falling impact ejecta on the post-Chicxulub atmosphere"

GUDFINNSSON, G.H.; PRESNALL, D.C.: 11.-13.09.2006, EMPG XI, Bristol, U.K.[*1]: "Generation of kimberlite and carbonatite melts at 3-14 GPa", Abstract Volume, 31, 2006

HAUNES, J.; FRAYSSE, G.; ROUQUETTE, J.; BORNAND, V; PINTARD, M.; PAPET, Ph.: 24.-29.09.2006, 7th International Conference of Solid State Chemistry 2006 (SSC 2006), Pardubice, Czech Republic: "Structural phase transitions in lead perovskites at high pressure"

HEIDELBACH, F.: 19.09.2006, SIMP Summer School 'Microstructures in the Earth Sciences', Campiglia, Italy: "Microstructures in the Earth"

HOLL, C.M.; SMYTH, J.R.; FROST, D.J.: 11.-15.12.2006, AGU Fall Meeting, San Francisco, USA[*4]: "Cation ordering in hydrous wadsleyite", EOS Trans. AGU, 87(52), Fall Meet. Suppl., Abstract MR11A-0111, 2006

JACOBSEN, S.D.; JIANG, F.; SMYTH, J.R.; DUFFY, T.S.; MAO, Z.; HOLL, C.M.; FROST, D.J.: 11.-15.12.2006, AGU Fall Meeting, San Francisco, USA[*4] *(invited)*: "Sound velocities of hydrous olivine and the effects of water on the equation of state of nominally anhydrous minerals", EOS Trans. AGU, 87(52), Fall Meet. Suppl., Abstract V53F-03, 2006

KANTOR, A.P.; KANTOR, I.Yu.; KURNOSOV, A.V.; KUZNETSOV, A.Yu.; DUBROVINSKAIA, N.A.; KRISCH, M.; BOSSAK, A.; DMITRIEV, V.P.; URUSOV, V; DUBROVINSKY, L.S.: 28.09.-01.10.2006, International Workshop 'Crystallography at High Pressures' 2006, Dubna, Russia: "Sound wave velocities in *fcc* Fe-Ni alloy at high pressure and temperature by mean of inelastic X-ray scattering"

KANTOR, A.P.; DUBROVINSKY, L.S.; KANTOR, I.Yu.; KURNOSOV, A.V.; KUZNETSOV, A.Yu.; DUBROVINSKAIA, N.A.; KRISCH, M.: 11.-15.12.2006, AGU Fall Meeting, San Francisco, USA[*4]: "Sound wave velocities of Fe-Ni alloy at high pressure and temperature", EOS Trans. AGU, 87(52), Fall Meet. Suppl., Abstract MR53B-0982, 2006

KANTOR, I.Yu.: 06.-10.02.2006, High Pressure and Synchrotron Radiation workshop at ESRF User Meeting, Grenoble, France: "Ferropericlase at high pressures: probing structural and electronic properties at synchrotron and in-house facilities"

KANTOR, I.Yu.; KANTOR, A.P.; DUBROVINSKY, L.S.; MCCAMMON, C.A.; KURNOSOV, A.V.; STEINLE-NEUMANN, G.: 28.09.-01.10.2006, International Workshop 'Crystallography at High Pressures' 2006, Dubna, Russia: "Monoclinic FeO under High Pressure"

KANTOR, I.Yu.; DUBROVINSKY, L.S.; MCCAMMON, C.A.; KURNOSOV, A.V.; STEINLE-NEUMANN, G.: 11.-15.12.2006, AGU Fall Meeting, San Francisco, USA[*4]: "Monoclinic FeO under high pressure", EOS Trans. AGU, 87(52), Fall Meet. Suppl., Abstract MR53B-0990, 2006

KEGLER, Ph.; HOLZHEID, A.; FROST, D.J.; RUBIE, D.C.; PALME, H.: 11.-13.09.2006, EMPG XI, Bristol, U.K.[*1]: "Is a magma ocean really needed to explain the Earth mantle siderophile element abundances?", Abstract Volume, 36, 2006

KEPPLER, H.: 03.02.2006, ETH Zürich, Switzerland: "Water in the Earth"

KEPPLER, H.: 14.07.2006, Workshop 'Neutrons in Geoscience', TU München, Germany: "High-pressure research in geoscience with neutrons"

KEPPLER, H.; BOLFAN-CASANOVA, N.: 01.-04.10.2006, MSA Short course, Verbania, Italy[*3] *(invited)*: "Thermodynamics of water solubility and partitioning"

KESHAV, S.; GUDFINNSSON, G.H.; PRESNALL, D.C.: 11.-13.09.2006, EMPG XI, Bristol, U.K.[*1]: "Majoritic-garnets and clinopyroxenes in cratonic diamonds: Precipitates from CO_2-rich melts", Abstract Volume, 36, 2006

KONSCHAK, A.; KEPPLER, H.: 25.-27.09.2006, 84. Jahrestagung der DMG, Hannover, Germany[*2]: "First high-temperature and high-pressure *in situ* infrared spectroscopic measurements on CO_2 in silicate melts", Beihefte zum European Journal of Mineralogy 18, 78

KONZETT, J.; FROST, D.J.: 11.-13.09.2006, EMPG XI, Bristol, U.K.[*1]: "Experimental constraints on the transport and storage of phosphorus in the Earth's upper mantle", Abstract Volume, 36, 2006

KURNOSOV, A.V.; DUBROVINSKY, L.S.: 22.02.2006, Nikolaev Institute of Inorganic Chemistry, Novosibirsk, Russia *(invited)*: "Methane hydrates in Titan's interior"

KURNOSOV, A.V.; DUBROVINSKY, L.S.: KUZNETSOV, A.Yu.; DMITRIEV, V.P.: 28.09.-01.10.2006, International Workshop 'Crystallography at High Pressures' 2006, Dubna, Russia: "Clathrate hydrates in methane-ammonia-water system at high pressures and temperatures"

LEE, K.K.M.; STEINLE-NEUMANN, G.; AKBER-KNUTSON, S.: 11.-15.12.2006, AGU Fall Meeting, San Francisco, USA[*4] *(invited)*: "Is potassium really in the core? Ab-initio predictions of potassium partitioning between (Mg, Fe)SiO_3 perovskite and iron", EOS Trans. AGU, 87(52), Fall Meet. Suppl., Abstract MR51C-07, 2006

LEE, K.K.M.; STEINLE-NEUMANN, G.: 11.-15.12.2006, AGU Fall Meeting, San Francisco, USA[*4]: "Pressure- and chemistry-dependent electron-capture radioactive decay of ^{7}Be, ^{22}Na and ^{40}K in crystalline materials", EOS Trans. AGU, 87(52), Fall Meet. Suppl., Abstract MR53A-0978, 2006

LIU, J.; DUBROVINSKY, L.S.; BOFFA BALLARAN, T.; FROST, D.J.: 11.-13.09.2006, EMPG XI, Bristol, U.K.[*1]: "Effect of Na substitution into $KAlSi_3O_8$ hollandite type structure and high-pressure behavior of $K_{0.6}Na_{0.4}AlSi_3O_8$ hollandite", Abstract Volume, 45, 2006

LONGO, M.; NESTOLA, F.; BOFFA BALLARAN, T.; KEPPLER, H.; MCCAMMON, C.A.: 11.-13.09.2006, EMPG XI, Bristol, U.K.[*1]: "Cation vacancies in mantle-derived omphacitic clinopyroxenes and their relation with OH concentration", Abstract Volume, 45, 2006

LONGO, M.; NESTOLA, F.; BOFFA BALLARAN, T.; KEPPLER, H.; MCCAMMON, C.A.: 01.-04.10.2006, MSA Short course, Verbania, Italy[*3]: "Cation vacancies in mantle-derived omphacitic clinopyroxenes and their relation with OH concentration"

MANN, U.; FROST, D.J.; RUBIE, D.C.; SHEARER, C.K.; AGEE, C.B.: 13.-17.03.2006, 37th Lunar and Planetary Science Conference, Houston, USA: "Is silicon a light component in the Earth's core? - Constraints from liquid metal - liquid silicate partitioning of some lithophile elements", Abstract No. 1161

MAO, Z.; JIANG, F.; JACOBSEN, S.D.; SMYTH, J.R.; HOLL, C.M.; DUFFY, T.S.; FROST, D.J.: 11.-15.12.2006, AGU Fall Meeting, San Francisco, USA[*4]: "Single-crystal elasticity of hydrous wadsleyite by Brillouin scattering", EOS Trans. AGU, 87(52), Fall Meet. Suppl., Abstract MR14A-08, 2006

MARKS, M.A.W.; MANN, U.; SCHMITT, A.K.; MARKL, G.: 25.-27.09.2006, 84. Jahrestagung der DMG, Hannover, Germany[*2]: "New geochronological and petrological information on the igneous rocks of the Katzenbuckel, Southwest Germany", Beihefte zum European Journal of Mineralogy 18, 89

MCCAMMON, C.A.: 23.-26.05.2006, 2006 Joint Assembly, Baltimore, USA *(invited)*: "Mantle properties and processes from the perspective of Mössbauer spectroscopy", EOS Trans. AGU, 87(36), Jt. Assem. Suppl., Abstract M22A-03, 2006

MCCAMMON, C.A.: 23.-28.07.2006, 19th General Meeting of the International Mineralogical Association (IMA), Kobe, Japan: "Microscopic properties to macroscopic behaviour: The influence of iron electronic state"

MCCAMMON, C.A.: 16.11.2006, Eberhard-Karls-Universität Tübingen, Institut für Geowissenschaften, Tübingen, Germany: "The paradox of mantle redox and consequences for the Earth's history"

MCCAMMON, C.A.; DUBROVINSKY, L.S.: 31.10-01.11.2006, DFG Schwerpunkt-programm 1236: Workshop I, Hünfeld, Germany: "High-P,T ^{57}Fe Mössbauer spectroscopy in laser-heated DACs: Applications for the mineralogy of Earth's lower mantle and core"

MCCAMMON, C.A.; KANTOR, I.Yu.; DUBROVINSKY, L.S.: 11.-15.12.2006, AGU Fall Meeting, San Francisco, USA[*4] *(invited)*: "Constraints on mantle dynamics from studies of iron electronic state", EOS Trans. AGU, 87(52), Fall Meet. Suppl., Abstract MR13A-01, 2006

MCENROE, S.A.; CARTER-STIGLITZ, B.; HARRISON, R.J.; ROBINSON, P.; MCCAMMON, C.A.: 11.-15.12.2006, AGU Fall Meeting, San Francisco, USA[*4]: "Nature's engineering: Giant magnetic exchange bias > 1 T in a natural mineral", EOS Trans. AGU, 87(52), Fall Meet. Suppl., Abstract GP31C-0098, 2006

MECKLENBURGH, J.; ZHAO, Y.; HEIDELBACH, F.; MACKWELL, S.J.: 11.-15.12.2006, AGU Fall Meeting, San Francisco, USA[*4]: "Deformation of olivine-spinel aggregates in the system $(Mg,Ni)_2GeO_4$ deformed to high-strain in torsion: Implications for upper mantle anisotropy", EOS Trans. AGU, 87(52), Fall Meet. Suppl., Abstract GP31C-0098, 2006

MELOSH, H.J.; THE DEEP IMPACT TEAM: 02.-07.04.2006, EGU General Assembly 2006, Vienna, Austria *(invited Keynote talk)*: "Deep Impact: The first second", Geophysical Research Abstracts 8, 06798, 2006

MELOSH, H.J.: 08.-12.05.2005, 1st International Conference on Impact Cratering in the Solar System, ESTEC, Noordwijk, The Netherlands *(Keynote talk)*: "The physics and chemistry of impact cratering"

MELOSH, H.J.; RUBIE, D.C.: 08.-10.12.2006, Workshop on Early Planetary Differentiation, Sonoma County, California, USA: "A numerical model for Ni partitioning in the terrestrial magma ocean"

MIYAJIMA, N.; EL GORESY, A.; DUPAS, C.; SEIFERT, F.; RUBIE, D.C.; CHEN, M.; XIE, X.: 06.-11.08.2006, 69th Annual Meeting of the Meteoritical Society, Zürich, Switzerland: "Ferric iron in Al-bearing akimotoite coexisting with iron-nickel metal in a shocked L-6 chondrite"

MIYAJIMA, N.; EL GORESY, A.; DUPAS, C.; SEIFERT, F.; RUBIE, D.C.; CHEN, M.; XIE, X.: 14.11.2006, Kolloquium Angewandte Geowissenschaften, Technische Universität Darmstadt, Germany: "Ferric iron in Al-bearing akimotoite coexisting with iron-nickel metal in a shocked L-6 chondrite"

MIYAJIMA, N.; MARTON, F.C.; FROST. D.J.; LANGENHORST, F.H.; RUBIE. D.C.: 11.-15.12.2006, AGU Fall Meeting, San Francisco, USA[*4]: "Aluminium diffusion in $MgSiO_3$ perovskite and majoritic garnet", EOS Trans. AGU, 87(52), Fall Meet. Suppl., Abstract MR32A-07, 2006

NAKASHIMA, D.; HERRMANN, S.; OTT, U.; EL GORESY, A.; NAKAMURA, T.: 25.-27.09.2006, 84. Jahrestagung der DMG, Hannover, Germany[*2]: "Noble gases and nitrogen in the KLE98300 EH3 chondrite", Beihefte zum European Journal of Mineralogy 18, 98

NESTOLA, F.; BOFFA BALLARAN, T.; PRINCIVALLE, F.; BALIC-ZUNIC, T.; DAL NEGRO, A.: 11.-13.09.2006, EMPG XI, Bristol, U.K.[*1]: "The effect of the degree of order on $MgAl_2O_4$ at high-pressure", Abstract Volume, 55, 2006

PERRILLAT, J.; NESTOLA, F.; SINOGEIKIN, S.V.; BASS, J.D.: 11.-15.12.2006, AGU Fall Meeting, San Francisco, USA[*4]: "Single-crystal elastic properties of $Ca_{0.07}Mg_{1.93}Si_2O_6$ orthopyroxene", EOS Trans. AGU, 87(52), Fall Meet. Suppl., Abstract MR11B-0123, 2006

PETFORD, N.; RUSHMER, T.; YUEN, D.; WALTE, N.P.: 11.-15.12.2006, AGU Fall Meeting, San Francisco, USA[*4]: "Can deformation help us to explore the chemical nature of the CMB region?", EOS Trans. AGU, 87(52), Fall Meet. Suppl., Abstract U41A-0802, 2006

PIAZZONI, A.; BUNGE, H.-P.; STEINLE-NEUMANN, G.: 02.-07.04.2006, EGU General Assembly 2006, Vienna, Austria: "Linking mineral physics and geodynamic mantle models", Geophysical Research Abstracts 8, 03928, 2006

PIAZZONI, A.S.; STEINLE-NEUMANN, G.; BUNGE, H.-P.: 25.-27.09.2006, 84. Jahrestagung der DMG, Hannover, Germany[*2]: "Towards driving mantle convection by mineral physics", Beihefte zum European Journal of Mineralogy 18, 104

PIAZZONI, A.S.; STEINLE-NEUMANN, G.; BUNGE, H.-P.: 01.-04.10.2006, MSA Short course, Verbania, Italy[*3]: "Temperature and compositional effects on the adiabatic bulk modulus in the Earth's mantle: Does a wet mantle require a cold transition zone?"

PIAZZONI, A.S.; STEINLE-NEUMANN, G.; BUNGE, H.-P.: 11.-15.12.2006, AGU Fall Meeting, San Francisco, USA[*4]: "Linking mineral physics and geodynamic mantle models", EOS Trans. AGU, 87(52), Fall Meet. Suppl., Abstract MR14A-04, 2006

POE, B.T.; ROMANO, C.; NESTOLA, F.; RUBIE, D.C.: 11.-13.09.2006, EMPG XI, Bristol, U.K.[*1]: "Complex impedance spectroscopy of hydrous single crystal olivine", Abstract Volume, 59, 2006

ROUQUETTE, J.; KANTOR, I.Yu.; MCCAMMON, C.A.; DUBROVINSKY, L.S.: 04.-08.09.2006, 44th EHPRG International Conference, Prague, Czech Republic: "Electronic configuration of iron in cold compressed olivine $Mg_{1.8}Fe_{0.2}SiO_4$"

ROUQUETTE, J.; DOLEJŠ, D.; KANTOR, I.Yu.; MCCAMMON, C.A.; FROST, D.J.; DUBROVINSKY, L.S.: 11.-15.12.2006, AGU Fall Meeting, San Francisco, USA[*4]: "Iron-carbon interactions at high pressures and temperatures", EOS Trans. AGU, 87(52), Fall Meet. Suppl., Abstract MR51C-03, 2006

RUBIE, D.C.: 29.07.06-02.08.2006, Kumamoto International Symposium on Recent Advancement of Mineralogy and Petrology, Kumamoto, Japan: "Process of core formation on terrestrial planets"

RUBIE, D.C.: 13.11.2006, Planet-Z Workshop, ETH Zürich, Switzerland: "Chemical and physical constraints on the mechanisms of core formation in terrestrial planets"

RUBIE, D.C.; ASAHARA, Y.; FROST, D.J.: 11.-15.12.2006, AGU Fall Meeting, San Francisco, USA[*4] *(invited)*: "Oxygen content of the Earth's core and chemical interaction at the core mantle boundary", EOS Trans. AGU, 87(52), Fall Meet. Suppl., Abstract U42A-04, 2006

SAIKIA, A.; BOFFA BALLARAN, T.; FROST, D.J.; RUBIE, D.C.: 11.-13.09.2006, EMPG XI, Bristol, U.K.[*1]: "Equation of state of (Al, Fe)-$MgSiO_3$ lower mantle perovskite" Abstract Volume, 62, 2006

SAIKIA, A.; ROUQUETTE, J.; KANTOR, I.Yu.; MCCAMMON, C.A.; DIMITRIEV, V.; DUBROVINSKY, L.S.: 11.-15.12.2006, AGU Fall Meeting, San Francisco, USA[*4]: "Pressure-induced spin crossover in olivine $Mg_{1.8}Fe_{0.2}SiO_4$", EOS Trans. AGU, 87(52), Fall Meet. Suppl., Abstract MR53B-0983, 2006

SCHUBERTH, B.; PIAZZONI, A.; BUNGE, H.-P.; IGEL, H.; STEINLE-NEUMANN, G.: 02.-07.04.2006, EGU General Assembly 2006, Vienna, Austria: "Global seismic wave field effects of geodynamically derived 3-D mantle structures", Geophysical Research Abstracts 8, 07722, 2006

SCHUBERTH, B.; PIAZZONI, A.; IGEL, H.; BUNGE, H.; STEINLE-NEUMANN, G.: 11.-15.12.2006, AGU Fall Meeting, San Francisco, USA[*4]: "The role of forward modeling of seismic waveforms for interpretation of mantle structure, physics and composition", EOS Trans. AGU, 87(52), Fall Meet. Suppl., Abstract S53C-08, 2006

SHINOVA, E.; ZHECHEVA, E.; STOYANOVA, R.; BROMILEY, G.D.; BOFFA BALLARAN, T.; ALCANTARA, R.; TIRADO, J.L.: 25.-27.05.2006, Workshop on Size-Dependent Effects in Materials for Environmental Protection and Energy Application (SizeMat), Varna, Bulgaria: "Influence of the synthesis conditions on the formation of solid solution $LiNiO_2$-$\alpha LiAlO_2$ in the whole concentration range"

SHIRYAEV, A.A.; DUBROVINSKAIA, N.A.; IAKOUBOVSKII, K.; GRAMBOLE, D.: April 2006, Annual Condensed Matter Physics Conference, Moscow, Russia: "Defects and inclusions in bulk nano- and polycrystalline diamonds"

SMYTH, J.R.; HOLL, C.M.; JACOBSEN, S.D.; FROST, D.J.: 11.-15.12.2006, AGU Fall Meeting, San Francisco, USA[*4]: "Volumes of hydration in forsterite, wadsleyite, and ringwoodite", EOS Trans. AGU, 87(52), Fall Meet. Suppl., Abstract V53F-02, 2006

STEINLE-NEUMANN, G.: 02.-07.03.2006, German-Israeli Minerva School 'Frontiers in High Pressure Research', Kibbutz Ein-Guedi, Dead-Sea, Israel *(invited)*: "Computing properties in the deep Earth – potentials and limitations"

STEINLE-NEUMANN, G.; 14.03.2006: Department of Earth Sciences, University College London, U.K.: "Bananas for the planet – the role of potassium in the Earth"

STEINLE-NEUMANN, G.; AKBER-KNUTSON, S.; ASIMOW, P.: 25.-27.09.2006, 84. Jahrestagung der DMG, Hannover, Germany[*2]: "On the sharpness of the perovskite to post-perovskite transition", Beihefte zum European Journal of Mineralogy 18, 136

STEINLE-NEUMANN, G.; WENZEL, M.J.: 11.-15.12.2006, AGU Fall Meeting, San Francisco, USA[*4] *(invited)*: "Nonequivalence of the octahedral sites of cubic Fe_3O_4 magnetite", EOS Trans. AGU, 87(52), Fall Meet. Suppl., Abstract MR43D-06, 2006

STEINLE-NEUMANN, G.; LEE, K.K.M.; AKBER-KNUTSON, S.: 11.-15.12.2006, AGU Fall Meeting, San Francisco, USA[*4]: "Ab-initio predictions of potassium partitioning between $MgSiO_3$ perovskite and $MgSiO_3$ post-perovskite", EOS Trans. AGU, 87(52), Fall Meet. Suppl., Abstract MR53A-0977, 2006

STOYANOV, E.; LANGENHORST, F.; STEINLE-NEUMANN, G.: 21.-23.04.2006, DFTEM, International Conference on Density Functional Theory (DFT) and Transmission Electron Microscopy (TEM), Vienna, Austria: "Cr L_3 electron energy loss near-edge structures of Cr-bearing compounds: comparison between experiment and computation"

TRØNNES, R.G.; FROST, D.J.; BOFFA BALLARAN, T.; STOLEN, S.: 11.-15.12.2006, AGU Fall Meeting, San Francisco, USA[*4]: "The perovskite to post-perovskite transition in $CaIrO_3$", EOS Trans. AGU, 87(52), Fall Meet. Suppl., Abstract MR11A-0097, 2006

VAN ORMAN, J.A.; KESHAV, S.; FEI, Y.: 27.08.-01.09.2006, 16th Annual V.M. Goldschmidt Conference, Melbourne, Australia: "High-pressure solid-metal/liquid-metal partitioning of Os, Re, and Pt in the Fe-S system"

WAGNER, T.; DOLEJŠ, D.: 14.-17.05.2006, GAC-MAC Annual Meeting, Montreal, Canada: "Hydrothermal alteration of granitic rocks: Insights from thermodynamic modeling of non-ideal mineral-aqueous systems", Abstract Volume, 158, 2006

WALTE, N.P.; MIYAJIMA, N.; HEIDELBACH, F.; FROST, D.J.: 25.-27.09.2006, 84. Jahrestagung der DMG, Hannover, Germany[*2]: "Deformation and texture development in $CaIrO_3$: Implications for the seismic properties of the D" layer", Beihefte zum European Journal of Mineralogy 18, 150

WALTE, N.P.; MIYAJIMA, N.; HEIDELBACH, F.; FROST, D.J.: 11.-15.12.2006, AGU Fall Meeting, San Francisco, USA[*4]: "Deformation and texture development in $CaIrO_3$: Implications for the seismic properties of the D" Layer", EOS Trans. AGU, 87(52), Fall Meet. Suppl., Abstract MR11B-0131, 2006

WESTRAADT, J.E.; NEETHLING, J.H.; DUBROVINSKAIA, N.A.; SIGALAS, I.: 29.11.-01.12.2006, The 45th Annual Conference of the Microscopy Society of Southern Africa (MSSA), Nelson Mandela Metropolitan University, Port Elizabeth, South Africa: "Characterization of thermally stable polycrystalline diamond"

YANG, H.; KONZETT, J.; FROST, D.J.: 11.-13.09.2006, EMPG XI, Bristol, U.K.[*1]: "The crystal chemistry and elastic properties of clinopyroxenes with 6-coordinated silicon", Abstract Volume, 62, 2006

[*1] **EMPG XI: 11th International Conference on Experimental Mineralogy, Petrology and Geochemistry, 11.-13.09.2006, Bristol, U.K. – Lithos, Supplement to Volume XX, No. X, 2006**

[*2] **DMG: 84. Jahrestagung der Deutschen Mineralogischen Gesellschaft, 25.-27.09.2006, Hannover, Germany – Beihefte zum European Journal of Mineralogy 18**

[*3] **MSA Short course "Water in Nominally Anhydrous Minerals", 01.-04.10.2006, Verbania, Lago Maggiore, Italy**

[*4] **AGU: American Geophysical Union Fall Meeting, 11.-15.12.2006, San Francisco, USA – EOS Transactions, American Geophysical Union, 87(52), AGU Fall Meeting 2006 Supplement**

5.4 Lectures and seminars at Bayerisches Geoinstitut

ARIMA, H., Osaka University, Japan: "Local structural change of germanate melts under high pressure", 02.11.2006

AUBAUD, C., University of Minnesota, USA: "Experimental determination of water partitioning between basaltic melts and nominally anhydrous minerals: analytical developments and geochemical implications", 09.03.2006

BALI, E., Eötvös University, Department of Petrology and Geochemistry, Budapest, Hungary: "Silicate melt inclusion study on a quartz-bearing orthopyroxene-rich websterite xenolith western Hungary, Pannonian Basin: Evidence for melting of the subducted slab", 08.03.2006

GAO, Y., Westfälische Wilhelms-Universität Münster, Institut für Physikalische Chemie und SFB 458, Münster, Germany: "Mixed alkali effect in glasses with two and three types of alkali ions", 01.02.2006

GOLDIN, T., University of Arizona, USA: "Interactions between falling impact ejecta and the post-Chicxulub atmosphere", 20.07.2006

HANSEN, U., Westfälische Wilhelms-Universität Münster, Institut für Geophysik, Münster, Germany: "Plates and plumes in models of mantle convection", 26.01.2006

HARTMANN, K., GeoForschungsZentrum Potsdam, Germany: "Element transport in granulites from the Lofoten Islands, Norway", 23.08.2006

HOLL, C., University of Colorado at Boulder, USA: "Structure and compression of hydrous wadsleyite: implications for water storage and cycling in the Earth's mantle", 27.04.2006

IRIFUNE, T., Ehime University, Geodynamics Research Center, Matsuyama, Japan: "Combined *in situ* X-ray and ultrasonic measurements and mineralogy of the mantle transition region", 16.06.2006

JAMBON, A., Université Pierre et Marie Curie, Laboratoire Magie, Paris, France: "Angrites, meteorites from Venus?", 30.11.2006

JAPEL, S., New Mexico State University, Department of Physics, Las Cruces, USA: "Iron and nickel phosphides at high temperature and pressure", 27.07.2006

KANTOR, A.P., Bayerisches Geoinstitut, Bayreuth, Germany: "Elasticity of FeNi alloy measured by inelastic X-ray scattering", 22.06.2006

KOENDERS, C., Kingston University, London, U.K.: "Deformation of and flow through granular aggregates", 06.07.2006

KURNOSOV, A.V., Bayerisches Geoinstitut, Bayreuth, Germany: "Study of methane-ammonia-water system at high pressures and temperatures: current state and perspectives", 19.10.2006

LAKSHTANOV, D., University of Illinois at Urbana-Champaign, USA: "Brillouin scattering in geologic materials. Elasticity and phase transitions", 03.07.2006

LEE, K.K.M., New Mexico State University, Las Cruces, USA: "Pressure and chemical-dependent electron-capture radioactivity", 06.07.2006

LOWENSTEIN, T., State University of New York at Binghamton, Department of Geological Sciences and Environmental Studies, Binghamton, USA: "High pCO_2 in the Eocene Greenhouse world from Green River Na-carbonates", 06.12.2006

MAO, W., Los Alamos National Laboratory, Los Alamos, USA: "Viewing planetary interiors through a diamond window", 21.09.2006

MIYAJIMA, N., Bayerisches Geoinstitut, Bayreuth, Germany: "Crystal morphology and dislocation microstructures of the $CaIrO_3$ phase. TEM study of an analogue of the post-perovskite phase", 12.01.2006

MÜLLER, W.F., TU Darmstadt, Institut für Angewandte Geowissenschaften, Darmstadt, Germany: "Microstructures of minerals in the Transmission Electron Microscope", 08.06.2006

MYDEEN, K., Bharathidasan University, School of Physics, India: "A simple uniaxial pressure generating device for electrical resistivity measurements: Suitable for closed cycle refrigerator system", 11.01.2006

PETFORD, N., Kingston University, School of Earth Sciences, Surrey, U.K.: "Deformation of granular magma mushes", 11.05.2006

PETRY, W., TU München, Physik Department und FRM-II, München, Germany: "Light in the dark: Neutrons for basic and applied research, industry and medicine", 23.02.2006

PRESNALL, D., The University of Texas at Dallas, Department of Geosciences, Richardson, USA: "Cool MORBs and a hot Hawaii – Implications for the existence of plumes", 22.02.2006

ROSE, L., University of Toronto, Department of Geology, Toronto, Canada: "Is a 'late veneer' necessary? Answers from metal-silicate partitioning of Te, Se, and S", 27.04.2006

ROUQUETTE, J., Bayerisches Geoinstitut, Bayreuth, Germany: "Influence of iron in mineral physics at high pressure and high temperature: From chemical reactions to phase transitions", 07.12.2006

SITNIKOVA, M., RWTH Aachen, Germany: "Evolution of Nb and REE minerals in multistage carbonatites – a test to experimental petrology", 11.10.2006

SKORODUMOVA, N., Uppsala University, Sweden: "Theoretical study of Mg(Fe)O under pressure", 29.06.2006

SPEZIALE, S., GeoForschungsZentrum Potsdam, Germany: "Spin transition of Fe in (Mg,Fe)O: Consequences for the lower mantle modeling?", 09.11.2006

SU, W., Chinese Academy of Sciences: "Water in UHP NAM's and its implications", 03.08.2006

TSUNO, K., Tohoku University, Institute of Mineralogy, Petrology and Economic Geology, Sendai, Japan: "Liquid immiscibility in the Fe-O-S system at high pressure", 16.11.2006

WEIGEL, C., Institut de Minéralogie et de Physique des Milieux Condensés (IMPMC), Paris, France: "Local environment around ferric iron in sodo-silicate glasses", 23.11.2006

Lectures and poster presentations during the 20th Anniversary Bayerisches Geoinstitut and the EU User Workshop 'Structure and Properties of Materials at High Pressure', Bayreuth, Germany, 12.-13.06.2006

Lectures:

IRIFUNE, T., Geodynamic Research Center, Ehime University, Matsayuma, Japan: "Synthesis of ultrahard nano-polycrystalline diamond and its potential application to high pressure generation"

KEPPLER, H., Bayerisches Geoinstitut, Bayreuth, Germany: "Water in the Earth"

MCCAMMON, C.A., Bayerisches Geoinstitut, Bayreuth, Germany: "Oxygen in the Earth"

MCENROE, S., Geological Survey of Norway: "Predicting the magnetic behavior of ilmenite-hematite exsolutions at lower crustal conditions: Experimental constraints and TEM observations"

MÜNKER, C., Mineralogisch-Petrologisches Institut, Universität Bonn, Germany: "The chronology of early planetary differentiation processes"

POE, B.T., Università degli Studi "G. d'Annunzio", Chieti, Italy: "Electrical conductivity of hydrous minerals in the Earth's mantle"

RUBIE, D.C., Bayerisches Geoinstitut, Bayreuth, Germany: "Core formation in terrestrial planets"

WALTER, M., University of Bristol, U.K.: "Phase relations and compressibility of aluminous perovskite in Earth's lower mantle"

YAGI, T., Institute for Solid State Physics, University of Tokyo: "Mineralogy of the lower mantle"

Poster presentations:

ASAHARA, Y.; FROST, D.J.; RUBIE, D.C.; DUBROVINSKY, L.S.; MIYAJIMA, N.; LANGENHORST, F.: "Partitioning of FeO between magnesiowüstite and liquid iron at high pressures and temperatures: Implications for the composition of the Earth's outer core"

BLÄß, U.W.; LANGENHORST, F.; BOFFA BALLARAN, T.; FROST, D.J.; MCCAMMON, C.A.; SEIFERT, F.; ANGEL, R.: "Exchange of silicon by trivalent cations of iron or aluminium in $CaSiO_3$-perovskite"

COMODI, P.; CERA, F.; DUBROVINSKY, L.S.; NAZZARENI, S.: "The high pressure and high temperature behaviour of 10 Å phase: a spectroscopic and diffractometric study up to 42 GPa"

DE RONDE, A.: "3D location and waveform analysis of micro-seismicity in multianvil experiments"

DEMOUCHY, S.: "Diffusivity of water in the deep Earth: Reports from the lab, highlights from Patagonia"

DOLEJŠ, D.: "Quartz solubility and complex formation in fluorine-bearing aqueous fluids: Key to the origin of silicothermal gels"

DOLEJŠ, D.; WAGNER, Th.: "Fluid-rock interactions in the temperature-composition space: Thermodynamic modelling of non-ideal mineral-aqueous systems"

DUBROVINSKAIA, N.A.; DUB, S.; DUBROVINSKY, L.S.: "Superior wear resistance of aggregated diamond nanorods"

DUPAS, C.: "Transformation of $(Mg,Fe)_2SiO_4$ olivine under excimer laser irradiation"

DUPAS, C.; ROBBE, O.; ADDAD, A.; TURRELL, S.; DEROZIER, D.: "Transformation of silicone rubber under YAG laser irradiation: first results towards a new miniaturised nerve electrode fabrication process"

DZWILEWSKI, A.: "Structural and magnetic characterization of phases synthesized close to the boundary of C60 collapse at high temperature high pressure conditions"

ESCUDERO, A.; PAVON, E.: "High pressure-temperature transformation of β-$Sc_2Si_2O_7$"

HIRAI, H.: "Phase changes of methane hydrates up to 86 GPa and a reason for its stability under high pressure"

HOLBIG, E.; DUBROVINSKY, L.S.: "Compression behaviour of nanocrystalline anatase $Ti_{0.90}Zr_{0.10}O_2$"

KANTOR, A.P.; KANTOR, I.Yu.; DUBROVINSKY, L.S.: "Sound wave velocities of Fe-Ni alloy at high pressure and temperature by mean of inelastic X-ray scattering"

KANTOR, I.Yu.; DUBROVINSKY, L.S.; KURNOSOV, A.V.: "Monoclinic FeO at high pressure"

KOMABAYASHI, T.: "Phase transition in $CaSiO_3$ perovskite"

KONSCHAK, A.; KEPPLER, H.: "First high temperature and high pressure *in situ* infrared spectroscopic measurements on CO_2 in silicate melts"

KONZETT, J.; YANG, H.; FROST, D.J.: "High P-T stability and crystal chemical properties of pyroxenes with 6-coordinated silicon"

KURNOSOV, A.V.; DUBROVINSKY, L.S.; KUZNETSOV, A.Yu.; DMITRIEV, V.P.: "High-pressure melting curve of methane hydrates: Implication to Titans interior"

LEE, K.K.M.; STEINLE-NEUMANN, G.: "Pressure and chemistry-dependent electron-capture radioactivity"

LIU, J.; BOFFA BALLARAN, T.; DUBROVINSKY, L.S.; FROST, D.J.: "High-pressure study of K-Na hollandite solid solution"

LONGO, M.; NESTOLA, F.; BOFFA-BALLARAN, T.; KEPPLER, H.; MCCAMMON, C.A.: "Cation vacancies in mantle-derived omphacitic clinopyroxenes and their relation with OH concentration"

MANN, U.; FROST, D.J.; SHEARER, C.K.; AGEE, C.B.: "Is silicon a light component in the Earth's core? Constraints from liquid metal – liquid silicate partitioning of some lithophile elements"

MCENROE, S.; ROBINSON, P.; LANGENHORST, F.; BROMILEY, G.D.; TERRY, M.P.; HEIDELBACH, F.; HIRT, A.: "High- and low-T magnetic properties and mineral chemistry before and after experiments at deep crust conditions on hemo-ilmenite, Allard Lake, Quebec: Persistence of uncompensated spins associated with microscale phase interfaces"

MIYAJIMA, N.; ASAHARA, Y.; DUBROVINSKY, L.S.; RUBIE, D.C.; HOLZAPFEL, C.: "A preparation method of TEM specimens using combined techniques of Focus Iron Beam milling and conventional Ar-milling"

NESTOLA, F.; BOFFA BALLARAN, T.; LIEBSKE, C.: "Elastic properties and high-pressure crystal structure behaviour along the jadeite-hedembergite solid solution"

NOWAK, M.: "Diffusion of argon and carbon dioxide in aluminosilicate melts"

PIAZZONI, A.; STEINLE-NEUMANN, G.; BUNGE, H.-P.: "Mantle convection with self-consistent formulation of mineral physics"

ROUQUETTE, J.; KANTOR, I.Yu.; DOLEJŠ, D.; MCCAMMON, C.A.; FROST, D.J.; DUBROVINSKY, L.S.: "Electronic state of iron in diamond inclusions"

ROUQUETTE, J.; KANTOR, I.Yu.; MCCAMMON, C.A.; DUBROVINSKY, L.S.: "Electronic configuration of iron in cold compressed olivine $Mg_{1.8}Fe_{0.2}SiO_4$"

ROZENBERG, G.; PASTERNAK, M.; AMIEL, Y.; KERTZER, M.; XU, W.; KURNOSOV, A.V.; DUBROVINSKY, L.S.; HANFLAND, M; MUNOZ, M.: "Structural features related to pressure-induced valence transformation and charge transfer in delafossite ($CuFeO_2$) and magnetite (Fe_3O_4)"

SAIKIA, A.; FROST, D.J.; RUBIE, D.C.: "The formation of calcium perovskite from majorite garnet: Implications for splitting of the 520 km seismic discontinuity"

SERGHIOU, G.: "Phase relations and stability of group IV alloys and of transition metal nitrides at high pressures and temperatures"

SHINOVA, E.; ZHECHEVA, E.; STOYANOVA, R.; BROMILEY, G.D.; BOFFA BALLARAN, T.: "High-pressure synthesis of new layered $Li[Li_xNi_{1-x}]O_2$ and $Li[Li_xNi_{1-x-y}Al_y]O_2$ oxides for cathode materials in lithium-ion batteries"

SOLOZHENKO, V.; KURAKEVYCH, O.; DUBROVINSKAIA, N.A.; DUBROVINSKY, L.S.: "HP-HT synthesis of bulk superhard materials in the B-C system"

STOYANOV, E.; FROST, D.J.; BOFFA BALLARAN, T.; MASSONE, H-J.; LANGENHORST, F.: "Influence of Ti^{3+} on the α-PbO_2 structure of rutile"

STOYANOV, E.; LANGENHORST, F.; STEINLE-NEUMANN, G.: "Cr L_3 electron energy loss near-edge structures of Cr-bearing compounds: Comparison between experiment and computation"

TALYZIN, A.: "Hydrogenation of C60 at high pressure and high temperature"

TERASAKI, H.: "Development of high pressure X-ray micro-tomography and measurement of interfacial energy of liquid Fe-alloy at high pressure"

WALTE, N.P.; FROST, D.J.; RUBIE, D.C.: "Behaviour of high dihedral angle melts during annealing and deformation"

WENZEL, M.; STEINLE-NEUMANN, G.: "Absence of charge localization in Fe_3O_4 under pressure"

5.5 Conference organization

03.-04.08.2006, The Meteoritical Society Desert Meteorites Workshop, Hassan II Casablanca University, Faculty of Sciences, Casablanca, Morocco (Co-Organizer: EL GORESY, A.)

01.-04.10.2006, MSA Workshop "Water in Nominally Anhydrous Minerals", Verbania, Lago Maggiore, Italy (KEPPLER, H.; SMYTH, J.R.)

6. Visiting scientists

6.1 Visiting scientists funded by the Bayerisches Geoinstitut

AUBAUD, C., University of Minnesota, Minneapolis, USA: 07.-12.03.2006

ARIMA, H., Osaka University, Japan: 30.10.-04.11.2006

BALI, E., Eötvös University, Department of Petrology and Geochemistry, Budapest, Hungary: 06.-10.03.2006

BUREAU, H., Laboratoire Pierre Süe UMR 9956 CEA-CNRS, Gif sur Yvette, France: 11.-13.06.2006

CHAKRABORTY, S., Ruhr-Universität Bochum, Institut für Geologie, Mineralogie & Geophysik, Bochum, Germany: 18.-20.06.2006

CHENNAOUI, H., Université Hassan II Aïn Chock, Faculté des Sciences, Département de Géologie, Casablanca, Morocco: 27.11.-01.12.2006

DE RONDE, A., Universität Basel, Department of Earth Sciences, Basel, Switzerland: 19.-21.01.2006

DEMOUCHY, S., University of Minnesota, Department of Geology and Geophysics, Minneapolis, USA: 08.-14.06.2006

DEON, F., Università degli Studi di Roma "La Sapienza", Italy: 15.-19.07.2006

DRIESNER, T., ETH Zürich, Institut für Mineralogie und Petrographie, Zürich, Switzerland: 19.-21.06.2006

GAO, Y., Westfälische Wilhelms-Universität Münster, Institut für Physikalische Chemie und SFB 458, Münster, Germany: 30.01.-02.02.2006

HANSEN, U., Westfälische Wilhelms-Universität Münster, Institut für Geophysik, Münster, Germany: 26.-27.01.2006

HARTMANN, K., GeoForschungsZentrum Potsdam, Germany: 22.-23.08.2006

HIROSHI, A., Osaka University, Graduate School of Science, Earth and Space Science, Osaka, Japan: 30.10.-04.11.2006

HOLL, C., University of Colorado at Boulder, USA: 24.-30.04.2006

HOWELL, D., University College London, Department of Earth Sciences, London, U.K.: 19.06.-02.07.2006

IRIFUNE, T., Ehime University, Geodynamics Research Center, Matsuyama, Japan: 12.-17.06.2006

JACOBSEN, S.D., Carnegie Institution of Washington, Geophysical Laboratory, Washington DC, USA: 27.01.-09.02.2006

JAMBON, A., Université Pierre et Marie Curie, Laboratoire Magie, Paris, France: 28.11.-01.12.2006

JAPEL, S., New Mexico State University, Department of Physics, Las Cruces, USA: 30.06.-05.08.2006

KOZLENKO, D.; Frank Laboratory of Neutron Physics, Joint Institute for Nuclear Research, Dubna, Russia: 20.11.-20.12.2006

LINNEN, R., University of Waterloo, Department of Earth Sciences, Waterloo, Canada: 10.-14.06.2006

LOWENSTEIN, T., State University of New York at Binghamton, Department of Geological Sciences and Environmental Studies, Binghamton, USA: 05.-07.12.2006

MAO, W., Los Alamos National Laboratory, Los Alamos, USA: 21.-24.09.2006

MARTEL, C., UMR 6113 - CNRS/Université d'Orléans, Institut des Sciences de la Terre d'Orleans, France: 11.-13.06.2006

MÜLLER, W., TU Darmstadt, Institut für Angewandte Geowissenschaften, Darmstadt, Germany: 01.05.-15.06.2006

MÜNKER, C., Universität Bonn, Mineralogisch-Petrologisches Institut, Bonn, Germany: 12.-13.06.2006

MYDEEN, K., Bharathidasan University, School of Physics, India: 09.-13.01.2006

NESTOLA, F., Università degli Studi di Padova, Dipartimento di Mineralogia e Petrologia, Padova, Italy: 11.-13.06.2006

OKUBE, M., Tokyo Institute of Technology, Materials and Structures Laboratory, Yokohama, Japan: 21.-23.08.2006

ONO, S., Institute for Research on Earth Evolution, Kanagawa-ken, Japan: 18.-21.06.2006

PETRY, W., TU München, Physik Department und FRM-II, München, Germany: 23.02.2006

PRESNALL, D., The University of Texas at Dallas, Department of Geosciences, Richardson, USA: 18.-25.02.2006, 01.06.-31.07.2006

ROSE, L.A., University of Toronto, Department of Geology, Toronto, Canada: 22.-28.04.2006

SITNIKOVA, M., RWTH Aachen, Germany: 09.-13.10.2006

SPEZIALE, S., GeoForschungsZentrum Potsdam, Germany: 08.-10.11.2006

SCHOLLENBRUCH, K., Universität Tübingen, Institut für Geowissenschaften, Tübingen, Germany: 25.-26.10.2006

SU, W., Chinese Academy of Sciences, Institute of Geology and Geophysics, Beijing, China: 31.07.-06.08.2006

TANG, Z., Katholieke Universiteit Leuven, Belgium: 21.07.2006

TERASAKI, H., Tohoku University, Institute of Mineralogy, Petrology and Economic Geology, Sendai, Japan: 10.-15.06.2006

TOMMASEO, C.E., Johannes Gutenberg-Universität Mainz, Institut für Geowissenschaften, Mainz, Germany: 01.-03.03.2006

TSUNO, K., Tohoku University, Institute of Mineralogy, Petrology and Economic Geology, Sendai, Japan: 12.-17.11.2006

ZARECHNAYA, E., Moscow State Institute of Steel and Alloys, Theoretical Physics Department, Moscow, Russia: 16.-20.07.2006

6.2 Visiting scientists supported by other externally funded BGI projects

ALESSANDRI, I., Università degli Studi di Brescia, Italy: *"Crystallization and nanostructuring in glasses for second harmonic generation (SHG)"*, 19.02.-03.03.2006 (RITA^{*B})

ARMSTRONG, L., University of Bristol, Department of Earth Sciences, Bristol, U.K.: *"Perovskite phase relations in the system Si-Al-Fe-Mg-O at lower mantle conditions"*, 23.-30.04.2006 (RITA^{*B})

ASIMOW, P., California Institute of Technology, Pasadena, USA: *"Effects of trace water on upper mantle melting and fractionation in the oceanic crust", "Thermodynamics of lower mantle minerals and melts from shock experiments"*, 15.-18.01.2006 (ENB^{*A})

AUBAUD, C., IPGP, Paris, France: *"Role of oxygen fugacity on the solubility and speciation of hydrogen in olivine at high pressure"*, 28.07.-29.08.2006 (RITA^{*B})

BALDINI, M., Università degli Studi di Roma "La Sapienza", Dipartimento di Fisica, Roma, Italy: *"High pressure properties of VO_2 (X-ray diffraction, vandatates, high-pressure)"*, 13.-22.02.2006 (RITA^{*B})

BOLFAN-CASANOVA, N., University of Clermont-Ferrand, Laboratoire Magmas et Volcans, Clermont-Ferrand, France: *"Effect of temperature, MgO and SiO_2 activities on the water solubility in mantle perovskite"*, 11.-19.03.2006, 22.-31.07.2006 (RITA^{*B})

BORGHINI, G., Università degli Studi di Genova, Italy: *"The subsolidus spinel to plagioclase transition in mantle peridotites: Experimental constraints at 0.3-0.5 GPa, 1000-1100 °C"*, 13.-27.11.2006 (RITA^{*B})

BRENAN, J., University of Toronto, Department of Geology, Toronto, Canada: *"Fractionation of highly siderophile elements by sulfide-silicate partitioning: A new spin"*, 05.-10.09.2006 (ENB^{*A})

BROMILEY, G., University of Cambridge, Department of Earth Sciences, Cambridge, U.K.: *"Slab-derived melts from the Earth's lower mantle: possible plume sources and the global"*, 06.-17.05.2006, 22.-24.05.2006 (RITA^{*B})

BROMILEY, G., University of Cambridge, Department of Earth Sciences, Cambridge, U.K.: 10.-13.06.2006 (RITA^{*B})

BURTON, B., National Institute of Standard and Technology (NIST), Gaithersburg, USA: *"First principles phase diagram calculations I"*, *"First principles phase diagram calculations II"*, 21.-28.02.2006 (ENB^{*A})

CARACAS, R., Carnegie Institution of Washington, Geophysical Laboratory, Washington DC, USA: *"First-principles calculations of incommensurate materials"*, 28.05.-02.06.2006 (ENB^{*A})

CHAKRABORTY, S., Ruhr-Universität Bochum, Institut für Geologie, Mineralogie & Geophysik, Bochum, Germany: *"Diffusion modeling in Earth and material sciences"*, 02.-06.02.2006 (ENB^{*A})

CERA, F., Università degli Studi di Perugia, Dipartimento di Scienze della Terra, Perugia, Italy: *"The phlogopite-10 Å phase solid solution: a high pressure/high temperature Raman study"*, 02.-12.07.2006 (RITA^{*B})

CERA, F., Università degli Studi di Perugia, Dipartimento di Scienze della Terra, Perugia, Italy: 11.-13.06.2006 (RITA^{*B})

COMODI, P., Università degli Studi di Perugia, Dipartimento di Scienze della Terra, Perugia, Italy: 11.-13.06.2006 (RITA^{*B})

COMODI, P., Università degli Studi di Perugia, Dipartimento di Scienze della Terra, Perugia, Italy: *"The phlogopite-10 Å phase solid solution: a high pressure/high temperature Raman study"*, 02.-06.07.2006 (RITA^{*B})

CORDIER, P., Université des Sciences et Technologies de Lille, Laboratoire de Structure et Propriétés de l'Etat Solide, Villeneuve d'Ascq, France: *"Plastic deformation experiments of garnets and pyroxenes at high pressure using the D-DIA"*, 09.-21.07.2006 (RITA^{*B})

CORDIER, P., Université des Sciences et Technologies de Lille, Laboratoire de Structure et Propriétés de l'Etat Solide, Villeneuve d'Ascq, France: 11.-14.06.2006 (RITA^{*B})

DE RONDE, A., University College London, Department of Earth Sciences, London, U.K.: 10.-14.06.2006 (RITA^{*B})

DEMENET, J.-L., CNRS/University of Poitiers, UFR Sciences SP2MI, Chasseneuil Futuroscope, France: *"Unusual slip systems in α-SiC"*, 04.-11.02.2006, 19.-25.11.2006 (RITA^{*B})

DOBSON, D., University College London, Department of Earth Sciences, London, U.K.: 10.-14.06.2006 (RITA^{*B})

DOBSON, D., University College London, Department of Earth Sciences, London, U.K.: *"The ground state structure of $Fe_{0.98}O$"*, 15.-20.06.2006 (RITA^{*B})

DUPAS-BRUZEK, C., Université des Sciences et Technologies de Lille 1, Centre d'Etudes et de Recherches et Applications, Villeneuve d'Ascq, France: 11.-14.06.2006 (RITA^{*B})

DZWILEWSKI, A., Umeå University, Experimental Physics, Umeå, Sweden: 10.-14.06.2006 (RITA^{*B})

ESCUDERO, A., Universidad de Sevilla, Instituto de Ciencia de Materiales de Sevilla, Spain: 10.-14.06.2006 (RITA^{*B})

GALUSKIN, E., University of Silesia, Faculty of Earth Sciences, Chair of Geochemistry, Mineralogy and Petrography, Division of Mineralogy, Sosnowiec, Poland: *"Structure of new mineral with composition $MnTi_2(OH)_2xH_2O(?)$ from altered skarn rocks of Wiluy River, Yakutia, Russia"*, 03.-10.12.2006 (RITA^{*B})

GALUSKIN, I., University of Silesia, Faculty of Earth Sciences, Chair of Geochemistry, Mineralogy and Petrography, Division of Mineralogy, Sosnowiec, Poland: *"Structure of new mineral with composition $MnTi_2(OH)_2xH_2O(?)$ from altered skarn rocks of Wiluy River, Yakutia, Russia"*, 03.-10.12.2006 (RITA^{*B})

GAUTRON, L., Université de Marne-la-Vallée, Laboratoire des Géomatériaux, Marne-la-Vallée, France: *"Location of uranium and thorium in a pyrolitic lower mantle"*, 25.06.-02.07.2006 (RITA^{*B})

GEORGIEVA GEORGIEVA, M., Bulgarian Academy of Sciences, Geological Institute, Sofia, Bulgaria: *"Composition and crystallographic orientation of mineral inclusions in garnets from metapelites, Central Rhodope, Bulgaria"*, 23.-30.04.2006 (RITA^{*B})

GREAUX, S., Université de Marne-la-Vallée, Laboratoire des Géomatériaux, Marne-la-Vallée, France: *"Location of uranium and thorium in a pyrolitic lower mantle"*, 25.06.-02.07.2006 (RITA^{*B})

GUILLAUME, C., The University of Edinburgh, School of Engineering and Electronics, Edinburgh, U.K.: *"Synthesis of alloys and ceramics at high pressures and temperatures"*, 21.-27.05.2006 (RITA^{*B})

HERNÁNDEZ, E., CSIC, Campus de la Universidad Autonoma de Barcelona, Bellaterra, Spain: *"Calculation of phase diagrams, melting points, and coexisting lines"*, 13.-22.05.2006 (ENB^{*A})

HUNT, S., University College London, Department of Earth Sciences, London U.K.: *"Rheology of garnets"*, 01.-10.01.2006 (EU Marie Curie Training Site)

KONZETT, J., Universität Innsbruck, Institut für Mineralogie und Petrographie, Innsbruck, Austria: 10.-14.06.2006 (RITA[*B])

KUMBAR, S., National Chemical Laboratory, Catalysis Division, Pune, India: 05.-16.08.2006 (ENB[*A])

KURAKEVYCH, O., Université Paris Nord, LPMTM-CNRS, Institut Galilée, Villetaneuse, France: 01.-14.05.2006 (Bayerisch-Französisches Hochschulzentrum)

KURAKEVYCH, O., Université Paris Nord, LPMTM-CNRS, Institut Gelilée, Villetaneuse, France: 10.-14.06.2006 (RITA[*B])

KUZNETSOV, O., The University of Chicago, CARS, Argonne, USA: 22.-28.07.2006 (ENB[*A])

LORD, O., University of Bristol, Department of Earth Sciences, Bristol, U.K.: *"Perovskite phase relations in the system Si-Al-Fe-Mg-O at lower mantle conditions"*, 23.-30.04.2006 (RITA[*B])

MALAVASI, L., Università degli Studi di Pavia, Dipartimento di Chimica Fisica *M. Rolla*, Pavia, Italy: *"High pressure properties of VO_2 (X-ray diffraction, vandatates, high-pressure)"*, 13.-22.02.2006 (RITA[*B])

MARTONAK, R., ETH Zürich, Department of Chemistry and Applied Biosciences, USI Campus, Lugano, Switzerland: *"Theoretical methods in high-pressure crystallography"*, 24.-27.07.2006 (ENB[*A])

MCENROE, S., Geological Survey of Norway: 11.-14.06.2006 (RITA[*B])

MISITI, V., Istituto Nazionale di Geofisica e Vulcanologia, Roma, Italy: *"Experimental study and modelisation of the decarbonation process at the magma/carbonatic sediments interface in the Colli Albani Volcanic District"*, 09.-23.07.2006 (RITA[*B])

MOLLO, S., Istituto Nazionale di Geofisica e Vulcanologia, Roma, Italy: *"Experimental study and modelisation of the decarbonation process at the magma/carbonatic sediments interface in the Colli Albani Volcanic District"*, 09.-23.07.2006 (RITA[*B])

ORSINGHER, L., Università degli Studi di Trento, Dipartimento di Fisica, Povo, Italy: *"Densification of germanium dioxide*", 12.-20.11.2006 (RITA[*B])

PALASYUK, T., Polish Academy of Sciences, Institute of Physical Chemistry, Warsaw, Poland: *"The high-pressure resitrometric and optical studies of rare earth trihydrides"*, 13.-27.04.2006 (RITA[*B])

PETFORD, N., Kingston University, School of Earth Sciences, Surrey, U.K.: *"Dilatancy in granular materials at high confining pressures"*, 08.-14.05.2006, 03.-06.07.2006 (RITA[*B])

POE, B., Università degli Studi "G. d'Annunzio", Chieti, Italy: *"Effect of dissolved H_2O on the electrical conductivity of single crystal olivine"*, 27.06.-15.07.2006 (RITA[*B])

POE, B., Università degli Studi "G. d'Annunzio", Chieti, Italy: 11.-13.06.2006 (RITA[*B])

POMPILIO, M., Istituto Nazionale di Geofisica e Vulcanologia, Pisa, Italy: *"Experimental constraints on the interaction between high- and low- porhyricty magmas of Stromboli volcano"*, 20.-29.06.2006, 30.07.-11.08.2006 (RITA[*B])

RABIER, J., CNRS/University of Poitiers, UFR Sciences SP2MI, Chasseneuil Futuroscope, France: *"Unusual slip systems in α-SiC"*, 04.-10.02.2006 (RITA[*B])

ROBINSON, P., Geological Survey of Norway: 11.-14.06.2006 (RITA^{*B})

ROMANO, C., Università degli Studi "G. d'Annunzio", Chieti, Italy: 11.-13.06.2006 (RITA^{*B})

ROMANO, C., Università degli Studi "G. d'Annunzio", Chieti, Italy: *"Effect of dissolved H_2O on the electrical conductivity of single crystal olivine"*, 27.06.-15.07.2006 (RITA^{*B})

ROZENBERG, G., Tel Aviv University, School of Physics & Astronomy, Tel Aviv, Israel: 11.-14.06.2006 (RITA^{*B})

SANLOUP, C., Université Paris 6, France: *"Preparation and investigation of solid rare gases compounds with planetary materials"*, 02.-13.04.2006, 17.-24.09.2006 (RITA^{*B})

SERGHIOU, G., University of Edinburgh, The School of Engineering and Electronics, Edinburgh, U.K.: 11.-14.06.2006 (RITA^{*B})

SHINOVA, E., Bulgarian Academy of Sciences, Sofia, Bulgaria: *"Novel compositions in the "$LiFeO_2$-$Li[Li_{1/3}Ti_{2/3}]O_2$" system obtained under high-pressure"*, 25.04.-05.05.2006, 11.-16.05.2006 (RITA^{*B})

SHINOVA, E., Bulgarian Academy of Sciences, Sofia, Bulgaria: 10.-13.06.2006 (RITA^{*B})

SKÁLA, R., Academy of Sciences of the Czech Republic, Institute of Geology, Prague, Czech Republic: *"Thermal expansions of $(Fe_{1-x}Ni_x)_3P$ compounds: Application to iron meteorites"*, 19.-25.11.2006 (RITA^{*B})

SKORODUMOVA, N., Uppsala University, Phxsics Department, Uppsala, Sweden: 26.06.-01.07.2006 (ENB^{*A})

SMYTH, J.R., University of Colorado at Boulder, USA: 21.02.-05.03.2006 (RITA^{*B})

SMYTH, J.R., University of Colorado at Boulder, USA: 10.-14.06.2006 (RITA^{*B})

SOLOZHENKO, V., Université Paris Nord, LPMTM-CNRS, Institut Galilée, Villetaneuse, France: 01.-14.05.2006 (Bayerisch-Französisches Hochschulzentrum)

TALYZIN, A., Umeå University, Experimental Physics, Umeå, Sweden: *"High pressure structural study of $LiAlH_4$, $NaAlH_4$, and $NaBH_4$ using DAC"*, 22.-28.01.2006 (RITA^{*B})

TALYZIN, A., Umeå University, Experimental Physics, Umeå, Sweden: *"High pressure structural study KBH_4 using DAC"*, 19.-25.11.2006 (RITA^{*B})

TALYZIN, A., Umeå University, Experimental Physics, Umeå, Sweden: 10.-14.06.2006 (RITA^{*B})

TARANTINO, S., Università degli Studi di Pavia, Dipartimento di Scienze della Terra, Pavia, Italy: *"Pressure effect on crystal structure of Li_2VOSiO_4, a frustrated 2D quantum Heisenberg antiferromagnet"*, 16.-29.07.2006 (RITA^{*B})

TRØNNES, R.G., University of Oslo, Natural History Museum, Department of Geology, Oslo, Norway: *"The perovskite to post-perovskite transition in $CaIrO_3$ and $CdTiO_3$"*, 19.06.-05.07.2006 (RITA^{*B})

URUSOV, V.S., Moscow State University, Department of Crystallography, Moscow, Russia: 16.-26.11.2006 (ENB^{*A})

VAN WESTRENEN, W., Vrije Universiteit Amsterdam, Department of Petrology, Amsterdam, The Netherlands: *"Exploring Fe and Si isotopic fractionation during metal-silicate equilibration"*, 24.-29.09.2006 (RITA^{*B})

VERROCCHIO, P., Università degli Studi di Trento, Dipartimento di Fisica, Povo, Italy: *"Densification of germanium dioxide"*, 12.-16.11.2006 (RITA^{*B})

VROON, P., Vrije Universiteit Amsterdam, Department of Petrology, Amsterdam, The Netherlands: *"Exploring Fe and Si isotopic fractionation during metal-silicate equilibration"*, 24.-29.09.2006 (RITA[*B])

WALTER, M.J., University of Bristol, Department of Earth Sciences, Bristol, U.K.: *"Perovskite phase relations in the system Si-Al-Fe-Mg-O at lower mantle conditions"*, 23.-30.04.2006 (RITA[*B])

WALTER, M.J., University of Bristol, Department of Earth Sciences, Bristol, U.K.: 11.-13.06.2006 (RITA[*B])

WEIGEL, C., Institut de Minéralogie et de Physique des Milieux Condensés (IMPMC), Paris, France: *"Structural behaviour of ferric iron in glasses"*, 09.09.-15.12.2006 (EUMC[*C])

YONCHEVA, M., Bulgarian Academy of Sciences, Sofia, Bulgaria: *"Novel compositions in the "$LiFeO_2$-$Li[Li_{1/3}Ti_{2/3}]O_2$" system obtained under high-pressure"*, 25.04.-05.05.2006, 11.-16.05.2006 (RITA[*B])

ZAHN, D., Max-Planck-Institut für Chemische Physik fester Stoffe, Dresden, Germany: *"Exploring the atomistic mechanisms of crystal nucleation from computer simulation"*, 24.-25.04.2006 (ENB[*A])

ZALITE, I., Riga Technical University, Institute of Inorganic Chemistry, Riga, Latvia: *"Use of high pressure hot pressing equipment for fabricating of nanostructured ceramic materials"*, 19.-27.11.2006 (RITA[*B])

ZARECHNAYA, E., Moscow State Institute of Steel and Alloys, Theoretical Physics Department, Moscow, Russia: *"Ab initio computations on B-doped diamonds"*, 01.09.-31.12.2006 (EUMC[*C])

ZEMA, M., Università degli Studi di Pavia, Dipartimento di Scienze della Terra, Pavia, Italy: *"Pressure effect on crystal structure of Li_2VOSiO_4, a frustrated 2D quantum Heisenberg antiferromagnet"*, 16.-23.07.2006 (RITA[*B])

[*A)] ENB: International Graduate School under the Elitenetzwerk Bayern

[*B)] RITA: EU "Research Infrastructures: Transnational Access" Programme

[*C)] EUMC: EU Marie Curie Actions "Atomic to Global" Training Programme

6.3 Visitors (externally funded)

ABRIKOSOV, I., Linköping University, Department of Physics, Chemistry, and Biology (IFM), Linköping, Sweden: 14.-16.09.2006

BARSUKOVA, T., TU Bergakademie Freiberg, Germany: 21.-24.08.2006

BAUER, M., Johann Wolfgang Goethe-Universität Frankfurt/M., Institut für Geowissenschaften, Frankfurt/M., Germany: 27.02.-05.03.2006

BAYARJARGAL, L., Johann Wolfgang Goethe-Universität Frankfurt/M., Institut für Geowissenschaften, Frankfurt/M., Germany: 24.-25.10.2006

DOLLASE, W., University of California, Department of Earth and Space Sciences, Los Angeles, USA: 04.09.-13.10.2006

FRIEDRICH, A., Johann Wolfgang Goethe-Universität Frankfurt/M., Institut für Geowissenschaften, Frankfurt/M., Germany: 24.-25.10.2006

GOLDIN, T., University of Arizona, Lunar and Planetary Laboratory, Tucson, USA: 01.01.-14.08.2006

GREGORYANZ, E., University of Edinburgh, School of Physics, Edinburgh, U.K.: 20.-21.12.2006

GROSS, T., Technische Universität Darmstadt, Fachbereich Materialwissenschaft, Darmstadt, Germany: 16.-20.01.2006

HASEGAWA, M., Tohoku University, Institute for Materials Research, Sendai, Japan: 08.-10.09.2006

ISAEV, E., Linköping University, Department of Physics, Chemistry, and Biology (IFM), Linköping, Sweden: 14.-16.09.2006

JIN, C., Chinese Academy of Science, China: 17.07.2006

KEGLER, P., Universität Köln, Germany: 27.04.-03.05.2006

KOENDERS, C., Kingston University, Surrey, U.K.: 02.-07.07.2006

KONRAD-SCHMOLKE, M., Universität Potsdam, Institut für Geowissenschaften, Germany: 12.-15.05.2006, 07.-10.07.2006

KONZETT, J., Universität Innsbruck, Institut für Mineralogie und Petrographie, Innsbruck, Austria: 13.-26.02.2006, 25.09.-08.10.2006

LAKSHTANOV, D., University of Illinois, USA: 29.06.-05.07.2006

LANG, M., Gesellschaft für Schwerionenforschung mbH, Darmstadt, Germany: 06.-10.03.2006, 01.-04.08.2006

LOCHERER, T., Technische Universität Darmstadt, Fachbereich Materialwissenschaft, Darmstadt, Germany: 16.-20.01.2006

MARKS, M., Universität Tübingen, Institut für Geowissenschaften, Tübingen, Germany: 14.-16.02.2006

NAKASHIMA, D., Max-Planck-Institut für Chemie, Mainz, Germany: 06.-09.06.2006

NEUFELD, K., Universität Mainz, Institut für Geowissenschaften, Mainz, Germany: 10.-13.02.2006

NIWA, K., University of Tokyo, Institute for Solid State Physics, Tokyo, Japan: 20.-29.09.2006

OHGUSHI, K., University of Tokyo, Japan: 14.-15.07.2006

OTT, U., Max-Planck-Institut für Chemie, Mainz, Germany: 06.-09.06.2006

SCHMIDT, B., Universität Göttingen, Abteilung Experimentelle und Angewandte Mineralogie, Göttingen, Germany: 02.-13.04.2006, 17.-24.09.2006

SCHWARZ, M., TU Bergakademie Freiberg, Germany: 18.-20.01.2006

SHUSHKANOVA, A., Russian Academy of Sciences, Institute of Experimental Mineralogy, Chernogolovka, Russia: 01.09.-30.11.2006

SIMAK, S., Linköping University, Department of Physics, Chemistry, and Biology (IFM), Linköping, Sweden: 14.-16.09.2006

SWAMY, V., Monash University, School of Physics & Material Engineering, Victoria, Australia: 08.-14.10.2006

TARANTINO, S., Università degli Studi di Pavia, Dipartimento di Scienze della Terra, Pavia, Italy: 11.-15.12.2006

WOODLAND, A., Johann Wolfgang Goethe-Universität Frankfurt/M., Institut für Geowissenschaften, Frankfurt/M., Germany: 27.02.-05.03.2006

WOSYLUS, A., TU Bergakademie Freiberg, Germany: 18.-19.01.2006

YAMAUCHI, T., University of Tokyo, Japan: 14.-15.07.2006

ZEMA, M., Università degli Studi di Pavia, Dipartimento di Scienze della Terra, Pavia, Italy: 11.-15.12.2006

7. Additional scientific activities

7.1 Patents

DUBROVINSKAIA, N.A.; DUBROVINSKY, L.S.; MIYAJIMA, N.: Superhard aggregated boron nitride nanocomposites (ABNNCs): synthesis and applications. Submitted October 2006

7.2 Honours and awards

Andreas AUDÉTAT	received the Victor Moritz Goldschmidt award of the German Mineralogical Society for outstanding young scientists
Andreas AUDÉTAT	received the research award of the Bayreuth University Association (Bayreuther Hochschulverein)
Dan FROST	2006 MSA Award of the Mineralogical Society of America 2006 James B. Macelwane Medal of the American Geophysical Union
Tamara GOLDIN	was awarded the "Best Student Presentation" prize at the conference on "Impact Craters as Indicators for Planetary Environmental Evolution and Astrobiology", Östersund, Sweden, 08.-14.06.2006
Catherine MCCAMMON	was elected a Fellow of the American Geophysical Union

7.3 Editorship of scientific journals

DUBROVINSKAIA, N.A.	Guest Editor for a special issue of the "High Pressure Research-International Journal"
DUBROVINSKY, L.S.	Guest Editor for a special issue of the "High Pressure Research-International Journal"
FROST, D.J.	Associate Editor "Geophysical Research Letters"
HEIDELBACH, F.	Associate Editor "American Mineralogist"
MCCAMMON, C.A.	Editor "Physics and Chemistry of Minerals"
RUBIE, D.C.	Editor-in-Chief "Physics of the Earth and Planetary Interiors"
SEIFERT, F.	Editorial Advisory Board of "Physics and Chemistry of Minerals"

7.4 Membership of scientific advisory bodies

KEPPLER H.	Chairman, Section for Crystallography, Physics and Chemistry of Minerals, German Mineralogical Society

MCCAMMON, C.A.	MSA Lecture Program Committee of the Mineralogical Society of America
	VGP Fellows Committee of the American Geophysical Union
	Advisory Board of "Mössbauer Information Exchange"
	International Advisory Board of the Mössbauer Effect Data Center
RUBIE, D.C.	Member of AGU Mineral and Rock Physics Executive Committee
	Chair of AGU Mineral and Rock Physics Awards Committee
	Member of Forschungskollegium Physik des Erdkörpers (FKPE)
SEIFERT, F.	Committee for Glaciology, Bavarian Academy of Sciences
	Forschungskollegium Mineralogie
	Mitglied des Kuratoriums des Geo-Zentrums an der KTB e. V. (bis Mai 2006)
	Academia Europaea, London
	Deutsche Akademie der Naturforscher Leopoldina, Halle (Senate 2003-2006)
	Bayerische Akademie der Wissenschaften, München
	Akademie der Wissenschaften, Göttingen

8. Scientific and Technical Personnel

Name		Position	Duration in 2006	Funding source
ADJAOUD, Omar	M.Sc. (Physics)	Wiss. Mitarbeiter	from 17.01.	BGI/IGS
AREFIN, Mohammad Lutful	M.Sc. (Nanomaterials)	Wiss. Mitarbeiter	from 01.01.	BGI/IGS[6]
ASAHARA, Yuki	Dr.	Wiss. Angestellte	to 31.07.	DFG
AUDÉTAT, Andreas	Dr.	Wiss. Assistent		BGI
BALI, Enikö	Dr.	Wiss. Angestellte	from 01.07.	BGI/VP
BAUMGARTNER, Alexander	Dipl.-Chem.	Wiss. Mitarbeiter		BGI/IGS[7]
BÖHM, Ulrich		Mechaniker		BGI
BÖSS, Wolfgang	RAR	Verwalt. Beamter		BGI
BOFFA BALLARAN, Tiziana	Dr.	Akad. Rätin		BGI
BUCHERT, Petra		Fremdsprachen-sekretärin		BGI
CARACAS, Razvan	Dr.	Wiss. Angestellter	from 01.10.	BGI/VP
DOLEJŠ, David	Dr.	Wiss. Angestellter		BGI/IGS
DUBROVINSKAIA, Natalia	Dr.	Wiss. Angestellte	01.03.-31.07. 01.08.-31.12.	BGI[5] DFG[1]
DUBROVINSKY, Leonid	PD Dr.	Akad. Oberrat		BGI
EL GORESY, Ahmed	Prof. Dr.			BGI/VP[2]
FISCHER, Heinz		Mechaniker		BGI
FROST, Daniel	Dr.	Akad. Oberrat		BGI
GAVRILENKO, Polina	Dipl.-Geol.	Wiss. Mitarbeiterin		BGI/IGS
GOLLNER, Gertrud		Chem.-Techn. Assistentin		BGI
GUDFINNSSON, Gudmundur	Dr.	Wiss. Angestellter	09.01.-31.01., 01.02.-30.06. 01.07.-31.08. 01.09.-31.12.	EU BGI EU BGI/VP
HEIDELBACH, Florian	Dr.	Wiss. Assistent		BGI
HOLBIG, Eva	Dipl.-Min.	Wiss. Mitarbeiterin		BGI/IGS
HUANG, Xianliang	M.E. (Material Science)	Wiss. Mitarbeiter	from 01.04.	BGI/IGS[6]
KANTOR, Anastasia	Dipl.-Geol.	Wiss. Angestellte		DFG
KANTOR, Innokenty	Dipl.-Geol.	Wiss. Angestellter		DFG
KEPPLER, Hans	Prof. Dr.	Leiter		BGI
KESHAV, Shantanu	Dr.	Wiss. Angestellter	from 09.01.	BGI/VP
KEYSSNER, Stefan	Dr.	Akad. Oberrat		BGI
KISON-HERZING, Lydia		Sekretärin		BGI
KLASINSKI, Kurt	Dipl.-Ing. (FH)	Techn. Angestellter		BGI
KONSCHAK, Alexander	Dipl.-Geol.	Wiss. Angestellter	01.01.-30.09 from 01.10.	DFG[3] BGI/VP

KRAUßE, Detlef	Dipl.-Inform. (FH)	Techn. Angestellter		BGI
KRIEGL, Holger		Haustechniker		BGI
KUMBAR, Suresh	M.Sc. (Inorg. Chem.)	Wiss. Mitarbeiter	from 02.11.	BGI/IGS[7]
KURNOSOV, Alexander	Dr.	Wiss. Angestellter		BGI/VP
KUZNETSOV, Oleksii	Dr.	Wiss. Angestellter	to 14.04.	BGI/VP
LEE, Kanani	Dr.	Stipendiatin	27.05.-12.08.	AvH[4]
LEITNER, Oskar		Präparator	to 31.08.	BGI
LINHARDT, Sven		Elektrotechniker		BGI
LIU, Jun	Dipl.-Min.	Wiss. Angestellte		DFG
LONGO, Micaela	Dipl.-Min.	EU-Gastwissenschaftlerin	from 18.04.	EU
MANN, Ute	Dipl.-Geol.	Wiss. Mitarbeiterin		BGI/IGS
MCCAMMON, Catherine	Dr.	Akad. Oberrätin		BGI
MELOSH, Jay	Prof. Dr.	Forschungspreisträger	to 20.09.	AvH
MIYAJIMA, Nobuyoshi	Dr.	Akad. Rat a.Z.		BGI
NARYGINA, Olga	M.Sc. (Phsics)	Wiss. Angestellte	from 15.07.	DFG
NÖTH, Andreas	Dipl.-Min.	Wiss. Mitarbeiter	to 31.05.	BGI/IGS[6]
POTZEL, Anke		Chem.-Techn.	to 30.09.	DFG[3]
		Assistentin	from 01.10.	BGI
RAMMING, Gerd		Elektroniker		BGI
RAUSCH, Oliver		Mechaniker		BGI
ROUQUETTE, Jérôme	Dr.	Wiss. Angestellter	to 20.12.	BGI/VP
RUBIE, David C.	Prof. Dr.	Stellvertr. Leiter		BGI
SAIKIA, Ashima	M.Sc. (Geol.)	Wiss. Mitarbeiterin		BGI/IGS
SCHMAUß-SCHREINER, Deborah	Dipl.-Geophys.	Wiss. Angestellte	to 30.06.	DFG[3]
SCHULZE, Hubert		Präparator		BGI
SEIFERT, Friedrich	Prof. Dr.	Stellvertr. Leiter	to 30.09.	BGI
SHCHEKA, Svyatoslav	Dr.	Wiss. Angestellter	01.01.-30.09.	DFG[3]
			01.10.-31.12.	BGI/VP
STEINLE-NEUMANN, Gerd	Dr.	Akad. Rat z.A.		BGI
TANG, Zhengning	M.E. (Material Science)	Wiss. Angestellter	01.09.-31.10.	BGI/VP
		HWHK	01.11.-28.11.	BGI[8]
		EU-Gastwissenschaftler	from 29.11.	EU
TERRY, Michael	Dr.	Wiss. Angestellter	to 31.03.	BGI/VP
ÜBELHACK, Stefan		Mechaniker		BGI
WALTE, Nicolas	Dipl.-Geol.	Wiss. Angestellter	01.01.-30.04.	BGI/VP
			01.05.-30.09.	DFG
			01.10.-31.12.	BGI/VP
XIONG, Xiaolin	Dr.	Wiss. Angestellter	01.10.-31.12.	BGI/VP
YELAMANCHILI, Ram Sai	Dipl.-Chem.	Wiss. Mitarbeiter		BGI/IGS[7]

Abbreviations/explanations:

AvH	Alexander von Humboldt Foundation
BGI	Staff Position of Bayerisches Geoinstitut
BGI/VP	Visiting Scientists' Program of Bayerisches Geoinstitut
DFG	German Science Foundation
EU	European Union
IGS	International Graduate School under the Elitenetzwerk Bayern "Structure, Reactivity and Properties of Oxide Materials"

[1] project granted to Prof. H.F. Braun, Bayreuth

[2] partially funded by the Visiting Scientists' Program of Bayerisches Geoinstitut

[3] Leibniz award Prof. Keppler

[4] Summer Research Fellowship for U.S. Scientists and Scholars

[5] Cooperation with Element Six

[6] Fraunhofer ISC Würzburg

[7] Chair Inorganic Chemistry I, Prof. Breu

[8] Funds from the Department for Biology, Chemistry and Earth Sciences

Index